Chapter 2

JET PHYSICS

Convenors: *R. Baier* [6], *A. Morsch* [4], *I.P. Lokhtin* [8], *X.N. Wang* [14], *U.A. Wiedemann* [4]

Editor: *U.A. Wiedemann* [4]

Contributors: *A. Accardi* [1,2], *F. Arleo* [3], *N. Armesto* [4,5], *R. Baier* [6], *D. d'Enterria* [1], *R.J. Fries* [7], *O.L. Kodolova* [8], *I.P. Lokhtin* [8], *A. Morsch* [4], *A. Nikitenko* [9], *S.V. Petrushanko* [8], *J.W. Qiu* [10], *C. Roland* [11], *C.A. Salgado* [4], *L.I. Sarycheva* [8], *S.V. Shmatov* [12], *A.M. Snigirev* [8], *S. Tapprogge* [13], *I.N. Vardanian* [8], *I. Vitev* [10], *R. Vogt* [14,15], *E. Wang* [16], *X.N. Wang* [14], *U.A. Wiedemann* [4], *P.I. Zarubin* [12], *B. Zhang* [16]

[1] Columbia University, New York, NY, USA
[2] University of Heidelberg, Heidelberg, Germany
[3] ECT* and INFN, Trento, Italy
[4] CERN, Geneva, Switzerland
[5] University of Cordoba, Cordoba, Spain
[6] University of Bielefeld, Bielefeld, Germany
[7] Duke University, Durham, NC, USA
[8] Moscow State University, Moscow, Russia
[9] Imperial College, London, UK
[10] Iowa State University, Ames, IA, USA
[11] Massachusetts Institute of Technology, Cambridge, MA, USA
[12] Joint Institute of Nuclear Research, Dubna, Russia
[13] University of Helsinki, Helsinki, Finland
[14] Lawrence Berkeley National Laboratory, Berkeley, CA, USA
[15] University of California, Davis, CA, USA
[16] Huazhong Normal University, Wuhan, China

Abstract
We discuss the importance of high-p_T hadron and jet measurements in nucleus–nucleus collisions at the LHC.

1. INTRODUCTION

U.A. Wiedemann

This report summarizes the current understanding of how the production of high-p_T partons in nucleus–nucleus collisions at the LHC can be used as a 'hard probe', i.e. as a diagnostic tool for the produced QCD matter either in thermalized (quark gluon plasma) or in other non-equilibrated but dense forms.

The production of high-p_T partons (observed as high-p_T hadrons or jets) involves a 'hard' perturbative scale $Q \gg \Lambda_{\rm QCD}$. This report mainly considers the case when this scale is harder than any momentum scale characterizing the medium produced in the nucleus–nucleus collision. Momentum scales proposed to characterize the medium (such as the initial temperature T or the saturation momentum Q_s) may be perturbatively large themselves, in which case $Q \gg T, Q_s$ and $T, Q_s \gg \Lambda_{\rm QCD}$. This restriction aims at insuring that *hard* partonic production processes are not part of the 'bulk matter': they occur in the primary partonic collisions on temporal and spatial scales $\Delta\tau \sim 1/Q$, $\Delta r \sim 1/Q$ which are sufficiently small to be unaffected by the properties of the produced matter. This makes them promising candidates of processes whose primary partonic production process is unaffected by the presence of a medium, while the development of the final (and possibly initial) state parton shower leaving (entering) the hard partonic subprocess is sensitive to the medium. If collinear factorization is applicable in nucleus–nucleus collisions, then inclusive cross sections of high-p_T partons measured in proton–proton collisions or calculated in perturbative QCD can be used as benchmark against which one can search for the actual signals and properties of the hot and dense matter created in nucleus–nucleus collisions at the LHC.

Section 2. discusses benchmark calculations for jet spectra and identified high-p_T hadronic spectra in nucleus–nucleus collisions at LHC, calculated in the framework of collinear factorized QCD. The question to what extent collinear factorization can be expected to hold in nucleus–nucleus collisions, and how its validity can be tested experimentally, is discussed elsewhere in this workshop report [1].

Section 3. addresses the main theoretical arguments for strong final state medium-modifications in jet production at the LHC. A jet is the hadronized remnant of a final state parton shower related to a produced highly virtual parton. Sections 3.1. and 3.2. focus mainly on the modification of this final state parton shower due to multiple parton scattering in a spatially extended dense medium. The current understanding of the additional medium-induced radiative contributions and the transverse momentum broadening of the parton shower is discussed. Section 3.3. compares radiative and collisional modifications of the parton shower. Section 3.4. discusses calculations of the main observables in which these medium-modifications are expected to show up. Related results obtained in the formalism of medium-enhanced higher twist expansion are summarized in Section 3.5. Finally, Section 3.6. on other potentially large medium-modifications discusses medium effects which may become important at moderate scales, Q up to $\sim$ 10 GeV.

Once medium-modifications of hard probes are determined, the question arises to what extent the properties of the hot and dense matter produced in nucleus–nucleus collisions differ from those of normal cold nuclear matter. To this end, Section 3.1.4. summarizes what is known about the medium-modifications of hard probes in cold nuclear matter.

The remainder of this report summarizes the experimental situation. Section 4. gives a short overview of the data available for AuAu collisions at $\sqrt{s}$ = 200 GeV from the Relativistic Heavy Ion Collider RHIC at Brookhaven. Several measurements at RHIC indicate that strong final state medium-modifications of the hadron production in central AuAu collisions persist at RHIC up to the highest transverse momenta explored ($p_T < 15$ GeV). This further supports the theoretical expectations of strong final state medium-modifications in nucleus–nucleus collisions at LHC where a much wider range in transverse energy is experimentally accessible. Finally, Section 5. discusses the current status of how the

LHC experiments ALICE, ATLAS and CMS will measure jets and their medium-modifications in the high-multiplicity background of a heavy ion collision.

In summary:

- Jets and high-p_T hadrons are the most abundant hard probes produced in nucleus–nucleus collisions at LHC. Within one month of running at design luminosity and in the absence of strong medium-modifications, jet spectra up to at least E_T = 200 GeV and leading hadron spectra up to p_T = 100 GeV are accessible (Section 2.).
- Both theoretical arguments (Section 3.) and data at lower center of mass energy (Section 4.) suggest large medium-modifications of hadronic high-p_T spectra in nucleus–nucleus collisions at LHC.
- A variety of theoretical approaches (comparison with benchmark calculations, Section 2.) and experimental techniques (comparison to benchmark measurements, dependence of medium-modifications on nuclear geometry, Section 3.4.6., etc.) are available to quantify the medium-dependence of jet production at LHC. The mutual consistency of these different approaches is a prerequisite for any characterization of the produced hot and dense medium from the medium-dependence of hard probes (see also Ref. [2, 3]). We emphasize that data from pA collisions at the LHC are an important part of this program [1].

2. BENCHMARK CROSS SECTIONS

2.1. Jet and Dijet Rates in Nucleus–Nucleus Collisions

A. Accardi, N. Armesto and I.P. Lokhtin

Jet studies will play a central role as a proposed signature of the formation of QGP in AB collisions. Energy loss of energetic partons inside a medium where color charges are present, the so-called jet quenching [4], has been suggested to behave very differently in cold nuclear matter and in QGP. It has been postulated as a tool to probe the properties of this new state of matter [5–8].

On the other hand, jet calculations at NLO have been successfully confronted with experimental data in hadron–hadron collisions [9]. Monte Carlo codes have become available: among them, we will use that of [10–12] adapted to include isospin effects and modifications of nucleon pdf inside nuclei, see the section on jet and dijet rates in pA collisions [1] for more information. Here we will present the results of 'initial' state effects, i.e. no energy loss of any kind will be taken into account. These results can be considered as the reference, hopefully to be tested in pA, whose failure should indicate the presence of new physics. As in pA collisions, we will work in the LHC lab frame, which for symmetric AB collisions coincides with the center-of-mass one, and the accuracy of our computations, limited by CPU time, is the same as in the pA case:

- For the transverse energy distributions, 2% for the lowest and 15% for the highest E_T-bins.
- For the pseudorapidity distributions, 3%.
- For the dijet distributions of the angle between the two hardest jets, 20% for the least populated and 3% for the most populated bins.

All the energies will be given per nucleon and, in order to compare with the pp case, all cross sections will be presented per nucleon–nucleon pair, i.e. divided by AB.

Unless explicitly stated and as in the pA case, we will use as nucleon pdf MRST98 central gluon [13] modified inside nuclei using the EKS98 parameterizations [14, 15], a factorization scale equal to the renormalization scale $\mu = \mu_F = \mu_R = E_T/2$, with E_T the total transverse energy of all the jets in the generated event, and for jet reconstruction we will employ the k_T-clustering algorithm [16, 17] with $D = 1$. The kinematic regions we are going to consider are the same as in the pA case:

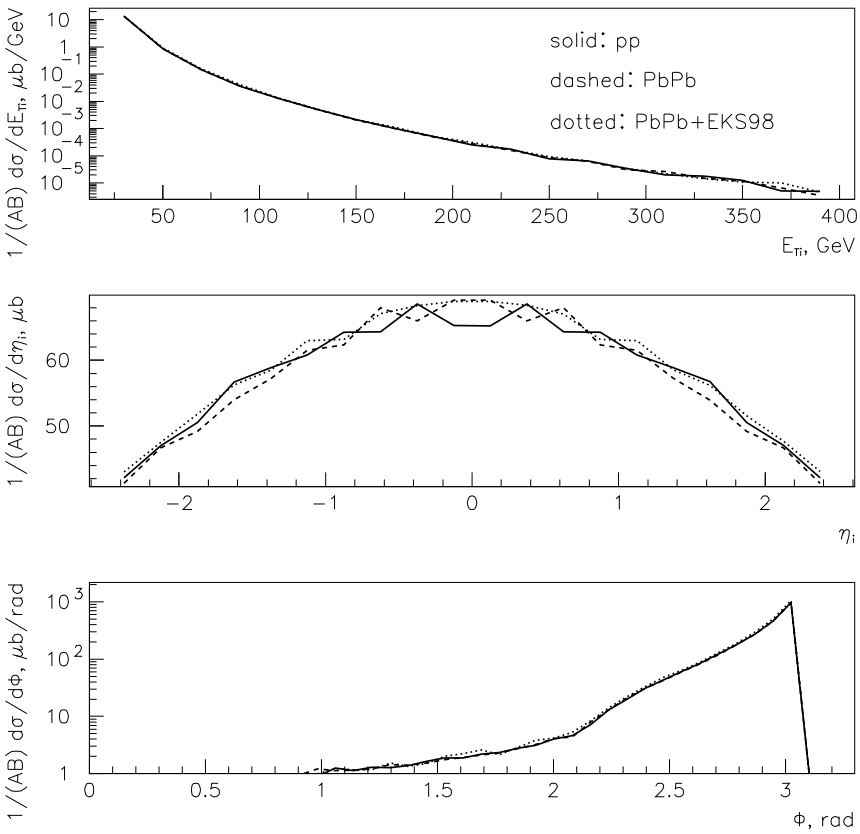

Fig. 2.1: Isospin and nuclear pdf dependence of jet cross sections (pp results: solid lines; PbPb results without modification of nucleon pdf inside nuclei: dashed lines; PbPb results with EKS98 modification of nucleon pdf inside nuclei: dotted lines) versus transverse energy of the jet (for $|\eta_i| < 2.5$, upper plot) and pseudorapidity of the jet (for $E_{Ti} > 20$ GeV, middle plot), and dijet cross sections (lower plot) versus angle between the two hardest jets for $E_{T1} >$20 GeV, $E_{T2} > 15$ GeV and $|\eta_1|, |\eta_2| < 2.5$, for collisions at 5.5 TeV. Unless otherwise stated default options are used, see text.

- $|\eta_i| < 2.5$, with η_i the pseudorapidity of the jet; this corresponds to the acceptance of the central part of the CMS detector.
- $E_{Ti} > 20$ GeV in the pseudorapidity distributions, with E_{Ti} the transverse energy of the jet; this will ensure the validity of perturbative QCD.
- $E_{T1} > 20$ GeV and $E_{T2} > 15$ GeV for the ϕ-distributions, with E_{T1} (E_{T2}) the transverse energy of the hardest (next-to-hardest) jet entering the CMS acceptance, and ϕ the angle between these two jets.

For more information, we refer to the chapter [1] of this report. The centrality dependence is not studied in either contribution.

The words of caution about our results which were given in the pA Section are even more relevant in AB collisions, as our ignorance on soft multiparticle production in this case is even larger than in pA collisions. For example, the number of particles produced at midrapidity in a central PbPb collision at the LHC may vary as much as a factor 3 [18, 19] among different models which, in principle, are able to reproduce the available experimental data on multiplicities at SPS, RHIC and TeVatron. Therefore, these issues of the underlying event [20, 21] and multiple hard parton scattering [22–26] demand extensive Monte Carlo studies including full detector simulation. Preliminary analysis, based on the developed sliding window-type jet finding algorithm (which subtracts the large background from the

underlying event) and full GEANT-based simulation of the CMS calorimetry, shows that even in the worst case of central PbPb collisions with maximal estimated charged particle density at mid-rapidity $dN^{\pm}/dy|_{y=0}$ = 8000, jets can be reconstructed with almost 100% efficiency, low noise and satisfactory energy and spatial resolution starting from $E_{Ti} \sim 100$ GeV (see the Section on Jet Detection at CMS). In the case of more realistic, lower multiplicities, the minimal threshold for adequate jet reconstruction could even decrease.

As in the pA case, see the previously mentioned section on pA collisions, the influence of disconnected collisions on jet production in AB collisions may be studied using simple estimates on the number $\langle n \rangle$ of nucleon–nucleon collisions involved in the production of jets with E_{Ti} greater than a given E_{T0}, which can be obtained in the Glauber model [27, 28] in the optical approximation: $\langle n \rangle(b, E_{T0}) = ABT_{AB}(b)\sigma(E_{T0})/\sigma_{AB}(b, E_{T0})$, with b the impact parameter, $T_{AB}(b) = \int d^2s T_A(s) T_B(b-s)$ the convolution of the nuclear profile functions of projectile and target normalized to unity, $\sigma(E_{T0})$ the cross section for production of jets with E_{Ti} greater than E_{T0} in pp collisions, and $\sigma_{AB}(b, E_{T0}) = 1 - [1 - T_{AB}(b)\sigma(E_{T0})]^{AB}$. Taking $\sigma(E_{T0})$ = 294, 0.463 and 0.0012 μb as representative values in PbPb collisions at 5.5 TeV for E_{T0} = 20, 100 and 200 GeV respectively (see results in Fig. 2.2 below), the number of nucleon–nucleon collisions involved turns out to be respectively 3.5, 1.0 and 1.0 for minimum bias collisions (i.e. integrating numerator and denominator in $\sigma_{pA}(b, E_{T0})$ between b = 0 and ∞), while for central collisions (integrating between b = 0 and 1 fm) the numbers are 8.9, 1.0 and 1.0, respectively. So, in AB collisions at LHC energies the contribution of multiple hard scattering coming from different nucleon–nucleon collisions seems to be negligible for transverse energies of the jets greater than $\sim$ 100 GeV, while for E_{Ti} smaller than $\sim$ 50 GeV this effect might need to be taken into account more carefully in our computations.

2.1.1. Uncertainties

Uncertainties on the renormalization/factorization scale, on the jet reconstruction algorithm and on nucleon pdf, have been discussed in the mentioned Section on pA collisions and show very similar features in the AB case, so we will discuss them no longer. Here we will focus, see Fig. 2.1, on isospin effects (obtained from the comparison of pp and PbPb without any modifications of nucleon pdf inside nuclei at the same energy per nucleon, 5.5 TeV) and on the effect of modifications of nucleon pdf inside nuclei, estimated by using EKS98 [14, 15] nuclear corrections.

On the transverse momentum distributions isospin effects are negligible, while effects of EKS98 result in a $\sim$ 3% increase. On the pseudorapidity distributions, isospin effects apparently tend to fill a small dip at $\eta \simeq 0$ present in the pp distribution, while EKS98 results in some increase, but nevertheless effects never go beyond 5% and are not very significant when statistical errors are considered. On the dijet angular distributions, isospin effects are negligible while EKS98 produces an increase of order 10% at maximum.

2.1.2. Results

The expected LHC luminosities in different collisions are collected into Table 2.1, and also shown are $\mathcal{L} \times$ (1 month) in units of $\mu\text{b}/(AB)$. Using this Table and the cross sections for inclusive one-jet production and dijet production in the Figures, it is possible to extract the number of expected jets (Figs. 2.1 and 2.2) or dijets (Fig. 2.2) in different ranges of the kinematic variables. For example, examining the solid line in Fig. 2.2 (upper-left) one can expect, within the pseudorapidity region we have considered, the following number of jets per month in PbPb collisions at 5.5 TeV with a luminosity of 5×10^{26} cm^{-2}s^{-1}: 2.2×10^7 jets with $E_{Ti} \sim 50$ GeV (corresponding to a cross section of 1 μb/(AB)), and 2.2×10^3 jets with $E_{Ti} \sim 250$ GeV (corresponding to a cross section of 10^{-4} μb/(AB)).

A detailed study of jet quenching [4–8] and of associated characteristics as jet profiles, which should be sensitive to radiation from the jet [29], should be feasible with samples of $\sim 10^3$ jets. Looking

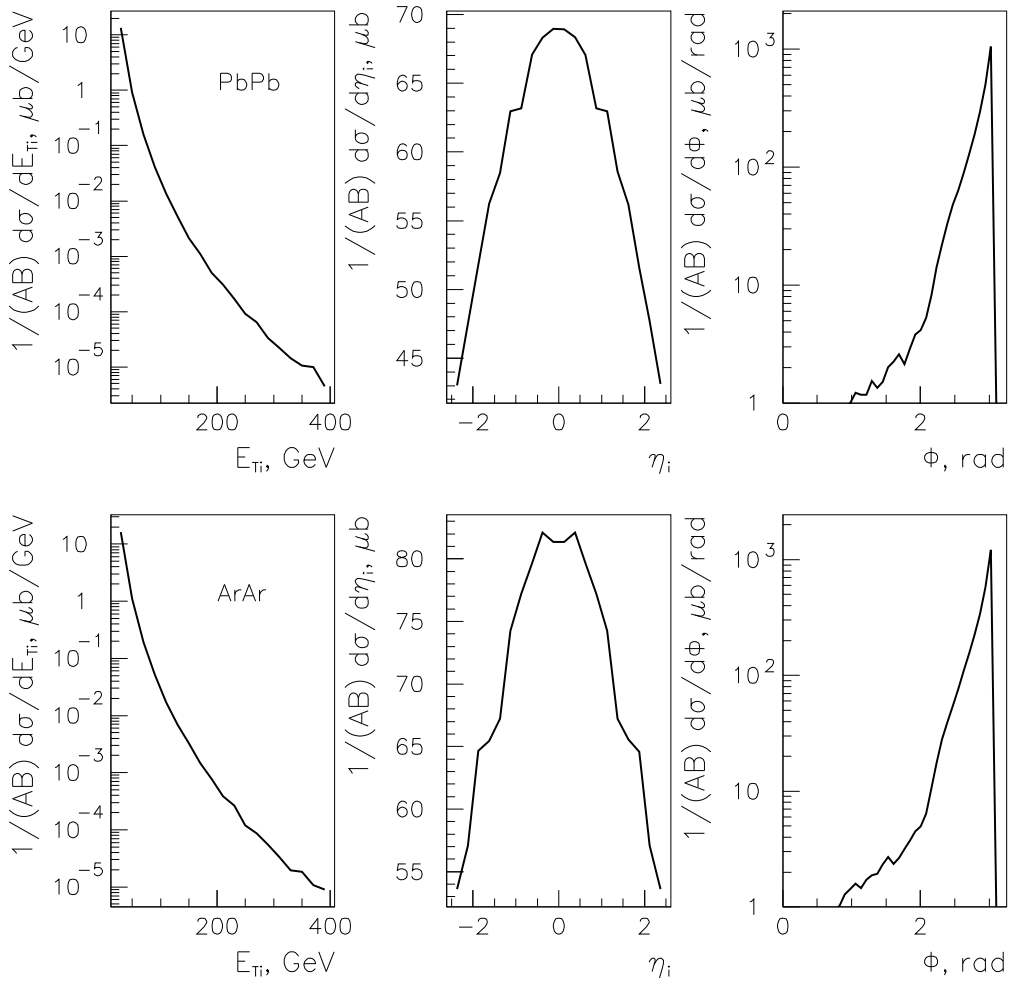

Fig. 2.2: Jet cross sections versus transverse energy of the jet (for $|\eta_i| < 2.5$, plots on the left) and pseudorapidity of the jet (for $E_{Ti} > 20$ GeV, plots in the middle), and dijet cross sections versus angle between the two hardest jets for $E_{T1} > 20$ GeV, $E_{T2} > 15$ GeV and $|\eta_1|, |\eta_2| < 2.5$ (plots on the right), for PbPb collisions at 5.5 TeV (upper plots) and ArAr collisions at 6.3 TeV (lower plots). Default options are used, see text.

Table 2.1: Luminosities $\mathcal{L}$ in units of $\mathrm{cm}^{-2}\mathrm{s}^{-1}$ and $\mathcal{L}\times 10^6$ s in units of $\mu\mathrm{b}/AB$ for different collisions at the LHC. The numbers of expected jets and dijets in a certain kinematic range are obtained by multiplying the latter column by the cross sections given in Figs. 2.1, 2.2 (jets) and 2.2 (dijets).

Collision	E_{cm} **per nucleon (TeV)**	$\mathcal{L}$ **(cm^{-2}s^{-1})**	**Number of jets/events per month per μb/(AB)**
ArAr	6.3	10^{29}	1.6×10^8
ArAr	6.3	3×10^{27}	4.8×10^6
PbPb	5.5	5×10^{26}	2.2×10^7

at the results given in Fig. 2.2, it becomes evident that, from a theoretical point of view, the study of such samples should be possible up to a transverse energy $E_{Ti} \sim 275$ GeV with a run of 1 month at the considered luminosity: indeed, from Table 2.1, 10^3 jets for PbPb would correspond to a cross section of 4.5×10^{-5} μb/(AB), which in Fig. 2.2 (upper-left) cuts the curve at $E_{Ti} \sim 275$ GeV.

The centrality dependence of the observables has not been examined due to our poor knowledge of the centrality behavior of the modification of nucleon pdf inside nuclei; if this behavior becomes clear in future experiments at eA colliders [30–32], such study would become very useful [33]. In any case, a variation of nuclear sizes should allow a systematic study of the dependence of jet spectra on the size and energy density of the produced plasma.

2.2. Benchmark Particle Cross Sections

I. Vitev

Hadron production in leading order pQCD is reviewed. The shape of the single inclusive particle spectra is well described for $p_T \geq$ 2–3 GeV at center of mass energies from 20 GeV to 2 TeV. The phenomenological K-factor is found to decrease systematically with $\sqrt{s}$. For ultra-relativistic heavy ion reactions the calculation is augmented with the effects of initial multiple parton scattering and final state radiative energy loss. Baseline CERN-LHC predictions for hadron production in pp and suppression in central PbPb reactions at $\sqrt{s}$ = 5.5 TeV are given in comparison to the corresponding results at BNL-RHIC and CERN-SPS energies.

The purpose of this section is to present a *lowest order* (LO) analysis of inclusive hadron production up to the Tevatron energies and discuss hadron differential cross sections and composition at the LHC.

2.2.1. Hadroproduction in factorized pQCD

The standard factorized pQCD hadron production formalism expresses the differential hadron cross section in $N + N \rightarrow h + X$ as a convolution of the measured parton distribution functions (PDFs) $f_{\alpha/N}(x_\alpha, Q^2_\alpha)$ for the interacting partons ($\alpha = a, b$), with the fragmentation function (FFs) $D_{h/c}(z, Q^2_c)$ for the leading scattered parton c into a hadron of flavor h and the parton–parton differential cross sections for the elementary sub-process $d\sigma^{(ab\rightarrow cd)}/d\hat{t}$:

$$E_h \frac{d\sigma^{NN}}{d^3p} = K_{NLO} \sum_{abcd} \int_0^1 dz_c \int_{x_{a\,\min}}^1 \int_{x_{b\,\min}}^1 dx_a dx_b \; f_{a/p}(x_a, Q^2_a) f_{b/p}(x_b, Q^2_b) \times D_{h/c}(z_c, Q^2_c) \frac{\hat{s}}{\pi z_c^2} \frac{d\sigma^{(ab\rightarrow cd)}}{d\hat{t}} \delta(\hat{s} + \hat{u} + \hat{t}) \; . \tag{2.1}$$

A list of the lowest order partonic cross sections can be found in Ref. [34]. In Eq. (2.1) x_a, x_b are the initial momentum fractions carried by the interacting partons and $z_c = p_h/p_c$ is the momentum fraction of the observed hadron. K_{NLO} is a phenomenological factor that is meant to account for next-to-leading order (NLO) corrections. It is $\sqrt{s}$ and scale dependent and takes typical values $\simeq$ 1–4. One usually finds that Eq. (2.1) over-predicts the curvature of the inclusive hadron spectra $|\partial_{p_T} d\sigma^h|$ at transverse momenta $p_T \leq 4$ GeV. This can be partly corrected by the introduction of a small intrinsic (or primordial) k_T-smearing of partons, transversely to the collision axis, and generalized parton distributions $\tilde{f}_\alpha(x, k_T, Q^2)$ motivated by the pQCD initial state radiation. For the corresponding modification of the kinematics in Eq. (2.1) in addition to the $\int d^2k_T^a \int d^2k_T^b \, (\cdots)$ integrations see Ref. [34]. The generalized parton distributions are often approximated as

$$\tilde{f}_\alpha(x, k_T, Q^2) \approx f_\alpha(x, Q^2) g(k_T), \qquad g(k_T) = \frac{e^{-k_T^2/\langle k_T^2 \rangle}}{\pi \langle k_T^2 \rangle} \; , \tag{2.2}$$

where the width $\langle k_T^2 \rangle$ of the Gaussian enters as a phenomenological parameter.

Perturbative QCD fits to data [35–42] use different coupled choices for K_{NLO} and $\langle k_T^2 \rangle$ and the extracted values are thus not directly comparable. However, similar agreement between data and theory at the level of spectral shapes and the $\sqrt{s}$ dependence of the corrective factors discussed above is found. In Ref. [43] the factorization and fragmentation scales were set to $Q_{PDF} = p_T/2$ and $Q_{FF} = p_T/2z_c$ and no K_{NLO} factors were employed. The extracted $\langle k_T^2 \rangle$ decreases from 2.7 GeV^2 at $\sqrt{s} \simeq 50$ GeV to 0.75 GeV^2 at $\sqrt{s} \simeq 2$ TeV. Alternatively, in Ref. [44] no primordial k_T-smearing was used and the scales in the calculation were fixed to be $Q_{PDF} = Q_{FF} = p_T$. The deduced K_{NLO} decreases from ~ 6 at $\sqrt{s} \simeq 50$ GeV to ~ 1.5 at $\sqrt{s} \simeq 2$ TeV.

In the fits shown in Fig. 2.3 we have used the GRV98 LO PDFs [45] and the BKK LO FFs [46]. Proton+antiproton fragmentation has been parameterized as in Ref. [47], inspired from PYTHIA [48] results. A fixed $\langle k_T^2 \rangle_{pp}$ = 1.8 GeV^2 has been employed, leading to a K_{NLO} parameter that naturally exhibits a smaller variation with $\sqrt{s}$. A ± 25% error band about the K_{NLO} value, fixed by the requirement to match the moderate- and high-p_T behavior of the data, is also shown. The fragmentation and factorization scales were fixed as in [44]. In the lower right panel the systematic decrease of the next-to-leading order K-factor is presented. Two fits to K_{NLO} have been used: linear $K_{NLO} = 2.7924–0.0999 \ln s$ and quadratic $K_{NLO} = 3.8444–0.3234 \ln s + 0.0107 \ln^2 s$ in $\ln s$. For center of mass energies up to 1 TeV the two parameterization differ by less than 15% but this difference is seen to grow to 30%–50% at $\sqrt{s} = 5$–10 TeV.

In Fig. 2.4 the predicted transverse momentum distribution of neutral pions and inclusive charged hadrons is shown, corresponding to the quadratic in $\ln s$ fit to K_{NLO} for energies typical of SPS, RHIC, and the LHC. The *significant* hardening of the spectra with $\sqrt{s}$ has two important consequences for pA and AA collisions: a notably reduced sensitivity to initial state kinematic effects (smaller Cronin) and larger variation of the manifested final-state multi-parton scattering (energy loss) with p_T [8]. We have also investigated the effect of isospin asymmetry between pp and p$\bar{\text{p}}$ reactions in π^0 and $h^+ + h^-$ production and found it to be small. More quantitatively, at $\sqrt{s} = 5.5$ TeV the fractional difference $|d\sigma^{\bar{p}p} - d\sigma^{pp}|/d\sigma^{pp}$ varies from 2.5% at $p_T = 5$ GeV to 4.8% at $p_T = 15$ GeV. This is insignificant as compared to the projected 50% uncertainty that comes from the extrapolation of K_{NLO} in LO calculations (see Fig. 2.3) or the choice of scale in NLO calculations. A recent study showed *no* deviation from DGLAP evolution at $Q^2 = 10$ GeV^2 down to $x = 10^{-5}$ in NN reactions [49]. The nuclear amplification effect $\propto$ A$^{1/3} \simeq 10$ for a large nucleus is still insufficient to enable measurements of high initial gluon density QCD at RHIC, but will play an important role at the LHC.

2.2.2. Perturbative QCD hadron composition

The predicted hadron composition in pp (p$\bar{\text{p}}$) reactions is plotted in the right panel of Fig. 2.4. The proton+kaon fraction is seen to increase systematically with p_T ($x_T = 2p_T/\sqrt{s}$) and is reflected in the decreasing $\pi^0/0.5(h^+ + h^-)$. At RHIC and LHC energies this ratio becomes ~ 0.5 at $p_T \simeq 15$ GeV and $p_T \simeq 75$ GeV, respectively. At transverse momenta $p_T \simeq 2$–4 GeV the contribution of baryons and kaons to $h^+ + h^-$ is $\leq 20\%$. This is significantly smaller compared to data on NN reactions, with the discrepancy being amplified in central AA. Possible explanations include: enhanced baryon production via topological gluon configurations (junctions) and its interplay with jet quenching [50,51] in AA [52,53], hydrodynamic transverse flow [54], uncertainty of the fragmentation functions $D_{p/c}(z_c, Q^2)$ into protons and antiprotons [55], and quark recombination driven by unorthodox (extracted) parton distributions inside nuclei [56]. The approaches in Refs. [52–54] also address the centrality dependence of the baryon/meson ratios in heavy ion collisions at RHIC. In Ref. [53] in has been shown that similar nuclear enhancement is expected in $\Lambda, \bar{\Lambda}$ production (as compared to kaons). The combined low-p_T baryon enhancement and the growth of the non-pionic hadron fraction in the perturbative regime may lead to an approximately constant pion to charged hadron ratio in the full measured p_T region at RHIC at $\sqrt{s_{NN}} = 200$ GeV. We propose that the LHC may play a critical role in resolving the mystery of

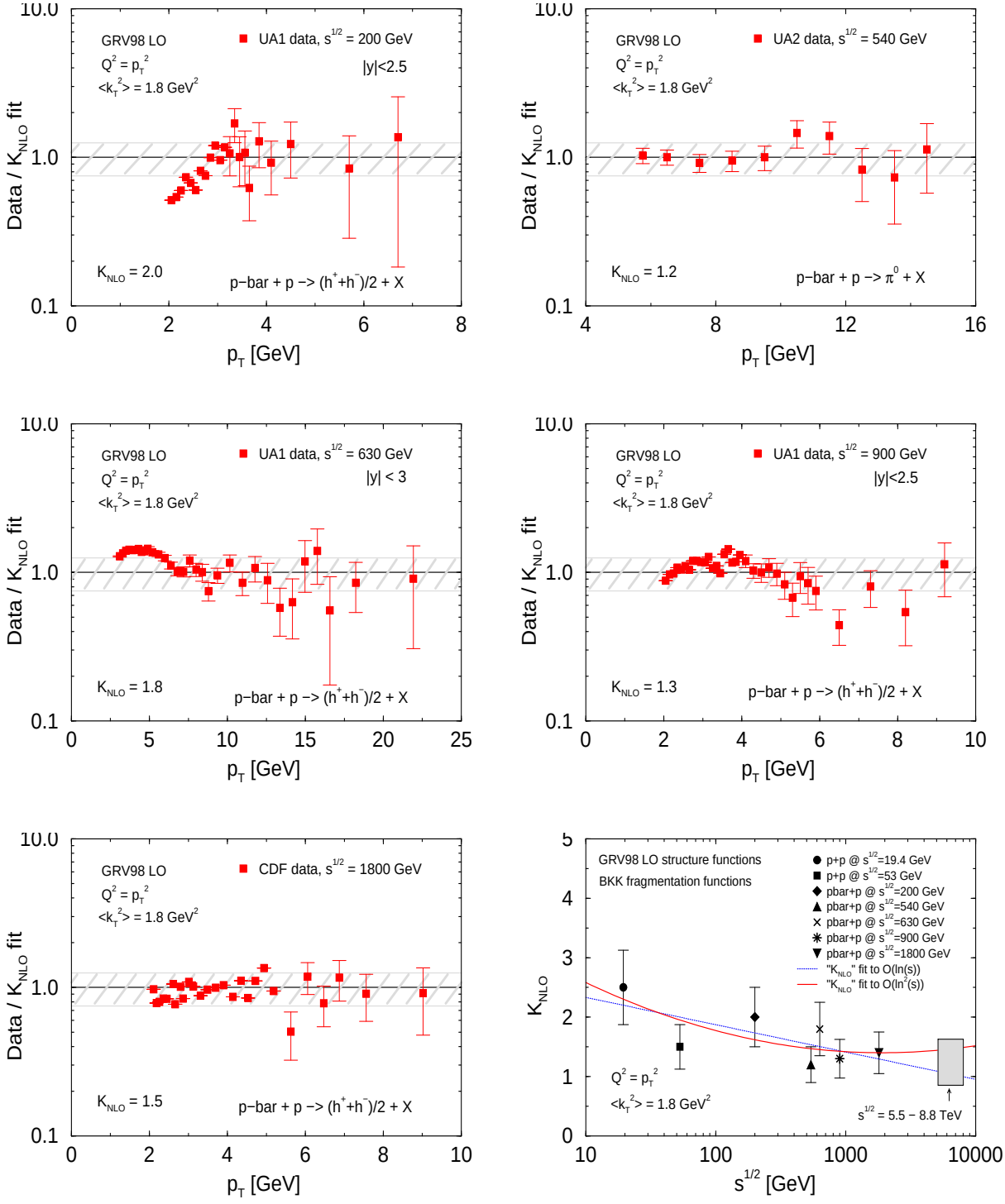

Fig. 2.3: Extracted K_{NLO} from comparison of LO pQCD calculation to data [37–42] at and about mid-rapidity in the range $2 \leq p_T \leq 25$ GeV. A systematic decrease of K_{NLO} with $\sqrt{s}$ is observed and illustrated in the bottom right panel. The projected 50% uncertainty at $\sqrt{s} = 5.5$–8.8 TeV is also shown.

enhanced baryon production in AA through the significantly larger experimentally accessible p_T range. Effects associated with baryon transport and transverse flow are not expected to extend beyond $p_T = 10$–15 GeV and may result in a detectable minimum of the baryon/meson ratio versus p_T before a secondary

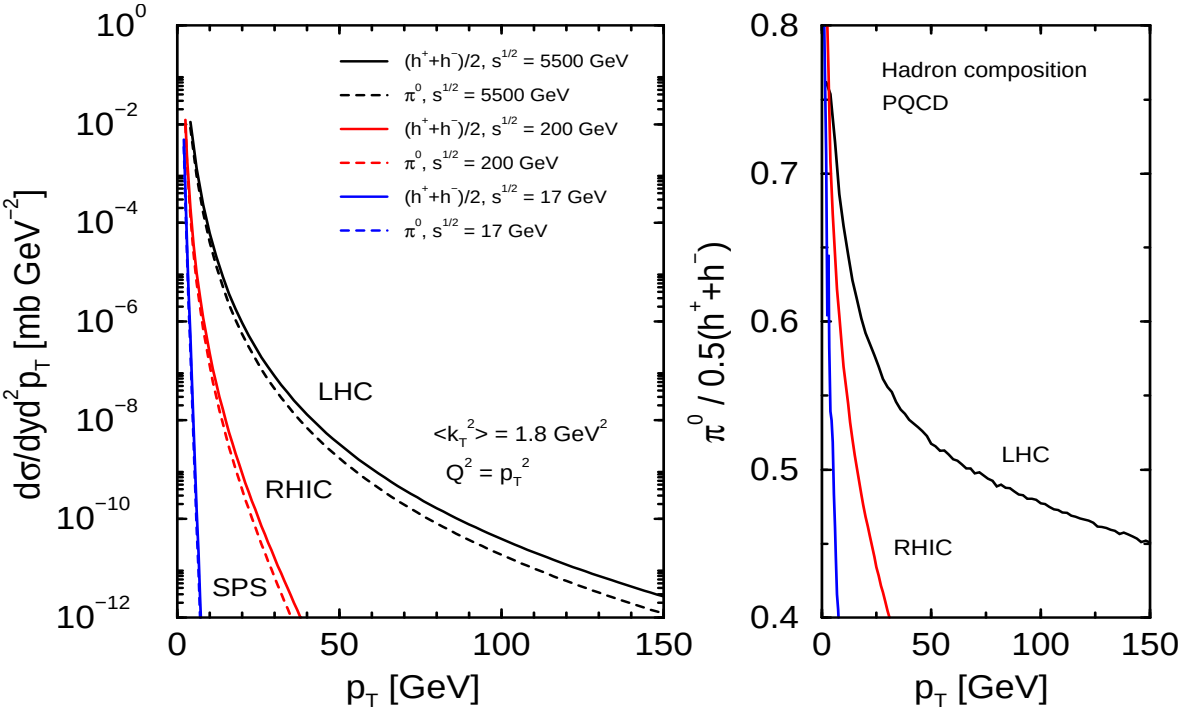

Fig. 2.4: The predicted LO differential cross section $d\sigma^{pp}/dyd^2p_T$ for inclusive neutral pion and charged hadron production at midrapidity y = 0 in pp ($\bar{\text{p}}$p) reactions is shown for $\sqrt{s}$ = 17, 200, and 5500 GeV. The ratio of neutral pions to inclusive charged hadrons versus p_T is given in the right panel.

subsequent rise. On the other hand, fragmentation functions (possibly enhanced at large z_c relative to current parameterizations) are expected to exhibit a much more monotonic behavior.

3. FINAL STATE EFFECTS IN DENSE AND HOT MATTER

Bjorken argument

In August 1982 J.D. Bjorken published a preprint [57] on 'Energy Loss of Energetic Partons in Quark-Gluon Plasma: Possible Extinction of High $p_\perp$ Jets in Hadron–Hadron Collisions', in which he discussed that high energy quarks and gluons propagating through quark-gluon plasma (QGP) suffer differential energy loss, and where he further pointed out that as an interesting signature events may be observed in which the hard collisions may occur such that one jet is escaping without absorption and the other is fully absorbed.

The arguments in this work have been based on elastic scattering of high momentum partons from quanta in the QGP, with a resulting ('ionization') loss $-dE/dz \simeq \alpha_s^2\sqrt{\epsilon}$, with ϵ the energy density of the QGP. The loss turns out to be less than the string tension of O(1 GeV/fm) [58] .

However, as in QED, bremsstrahlung is another important source of energy loss [51]. Due to multiple (inelastic) scatterings and induced gluon radiation high momentum jets and leading large $p_\perp$ hadrons become depleted, quenched [59] or may even become extinct. In [60] it has been shown that a genuine pQCD process (Fig. 2.5) is responsible for the dominant loss: after the gluon is radiated off the energetic parton it suffers multiple scatterings in the medium. Indeed, further studies [61–74] support this observation. For reviews, see Refs. [4, 75, 76].

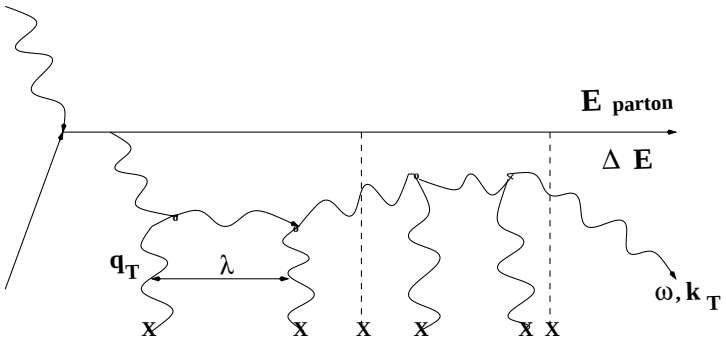

Fig. 2.5: Typical gluon radiation diagram

3.1. Radiative Energy Loss and Medium-Induced Gluon Radiation

3.1.1. Qualitative arguments

R. Baier and U.A. Wiedemann

After its production in a hard collision, the energetic parton radiates a gluon which both traverse a finite size L medium. Due to its non-abelian nature and its interaction with the medium, this gluon follows a zig-zag path (Fig. 2.5), with a mean free path $\lambda > 1/\mu$, which is the range of screened multiple gluon interactions. We estimate the medium-induced gluon radiation in two different limits, requiring that the gluon is emitted from the hard parton if it picks up sufficient transverse momentum to decohere from the partonic projectile.

In the multiple soft scattering limit, the average phase φ accumulated by the gluon due to multiple scattering is

$$\varphi = \left\langle \frac{k_T^2}{2\omega}\,\Delta z \right\rangle \sim \frac{\hat{q}\,L}{2\omega} L = \frac{\omega_c}{\omega}\,. \tag{2.3}$$

Here, the medium dependence is controlled by the transport coefficient

$$\hat{q} \simeq \mu^2/\lambda \simeq \rho \int d^2q_\perp\, q_\perp^2\, d\sigma/d^2q_\perp\,, \tag{2.4}$$

where ρ is the density of the medium (a nucleus, or partons) and σ the cross section of the gluon-medium interaction. According to Eq. (2.3), gluons are emitted from a hard parton traversing a finite path length L in the medium, if the phase $\varphi > 1$. Thus, their energy has to be smaller than the 'characteristic gluon frequency'

$$\omega_c = \frac{1}{2}\,\hat{q}\,L^2\,. \tag{2.5}$$

For an estimate of the shape of the energy distribution, consider the number $N_{\rm coh}$ of scattering centres which add coherently in the gluon phase Eq. (2.3), $k_T^2 \simeq N_{\rm coh}\,\mu^2$. Based on expressions for the coherence time of the emitted gluon, $t_{\rm coh} \simeq \frac{\omega}{k_T^2} \simeq \sqrt{\frac{\omega}{\hat{q}}}$ and $N_{\rm coh} = \frac{t_{\rm coh}}{\lambda} = \sqrt{\frac{\omega}{\mu^2\,\lambda}}$, one estimates for the gluon energy spectrum per unit path length

$$\omega\frac{dI}{d\omega\,dz} \simeq \frac{1}{N_{\rm coh}}\,\omega\frac{dI^{1\,\rm scatt}}{d\omega\,dz} \simeq \frac{\alpha_s}{t_{\rm coh}} \simeq \alpha_s\,\sqrt{\frac{\hat{q}}{\omega}}\,. \tag{2.6}$$

Again, this $1/\sqrt{\omega}$-energy dependence of the medium-induced non-abelian gluon energy spectrum is expected for sufficiently small $\omega < \omega_c$. The average energy loss of the parton (in the limit $E_{\rm parton} \to \infty$) due to gluon radiation with a spectrum $\omega dI/d\omega$ is then determined by the characteristic gluon energy ω_c as follows,

$$\Delta E = \int^{\omega_c} \frac{\omega dI}{d\omega}\,d\omega \simeq \alpha_s\,\omega_c\,, \tag{2.7}$$

It shows a characteristic quadratic dependence on the in-medium pathlength. The medium-induced BDMPS gluon spectrum (valid for finite size $L >> \lambda$ and for soft gluon energies $\omega_{GB} = \hat{q}\lambda^2 < \omega << E_{\rm parton} \to \infty$) with the characteristic behavior: $\omega dI/d\omega \simeq \alpha_s \sqrt{\omega_c/\omega}$, $\omega < \omega_c$ is suppressed by $1/N_{\rm coh}$ for $\omega > \omega_{GB}$ with respect to the incoherent Gunion-Bertsch spectrum. For comparison with QED the Landau-Pomeranchuk-Migdal [77–79] (LPM) suppressed photon spectrum behaves as $\omega dI/d\omega \simeq \sqrt{\omega}$.

Opacity expansion: we turn now to the limiting case in which the radiation pattern results from an incoherent superposition of very few $n_0 L$ single hard scattering processes positioned within path length L. Consider a hard partonic projectile which picks up a single transverse momentum μ by interacting with a single hard scatterer. An additional gluon of energy ω decoheres from the projectile wave function if its typical formation time $\bar{t}_{\rm coh} = 2\omega/\mu^2$ is smaller than the typical distance L between the production point of the parton and the position of the scatterer. The relevant phase is

$$\gamma = \frac{L}{\bar{t}_{\rm coh}} \equiv \frac{\bar{\omega}_c}{\omega}\,, \tag{2.8}$$

which indicates a suppression of gluons with energy ω larger than the characteristic gluon energy

$$\bar{\omega}_c = \frac{1}{2}\,\mu^2\,L\,. \tag{2.9}$$

The gluon energy spectrum per unit path length can be estimated in terms of the coherence time $\bar{t}_{\rm coh}$ and of the average number $n_0\,L$ of scattering centres contributing incoherently

$$\omega\frac{dI^{N=1}}{d\omega\,dz} \simeq (n_0\,L)\,\frac{\alpha_s}{\bar{t}_{\rm coh}} \simeq (n_0\,L)\,\alpha_s\,\frac{\mu^2}{\omega}\,. \tag{2.10}$$

This is the typical $1/\omega$-dependence of the non-abelian gluon radiation spectrum in the absence of LPM-type destructive interference effects. It will result again in a quadratic L-dependence of the average energy loss [73].

3.1.2. Quantitative results

C.A. Salgado and U.A. Wiedemann

There are several calculations of the inclusive energy distribution of medium-induced gluon radiation from Feynman multiple scattering diagrams [61–74]. They can be obtained as particular limiting cases of the following compact expression [71, 72]

$$\begin{aligned}\omega\frac{dI}{d\omega} &= \frac{\alpha_s\,C_R}{(2\pi)^2\,\omega^2}\,2{\rm Re}\int_{\xi_0}^{\infty}dy_l\int_{y_l}^{\infty}d\bar{y}_l\int d\mathbf{u}\int_0^{\chi\omega}d\mathbf{k}_T\,e^{-i\mathbf{k}_T\cdot\mathbf{u}}\,e^{-\frac{1}{2}\int_{\bar{y}_l}^{\infty}d\xi\,n(\xi)\,\sigma(\mathbf{u})} \\ &\quad\times\frac{\partial}{\partial\mathbf{y}}\cdot\frac{\partial}{\partial\mathbf{u}}\int_{\mathbf{y}=0}^{\mathbf{u}=\mathbf{r}(\bar{y}_l)}\mathcal{D}\mathbf{r}\exp\left[i\int_{y_l}^{\bar{y}_l}d\xi\frac{\omega}{2}\left(\dot{\mathbf{r}}^2-\frac{n(\xi)\sigma\,(\mathbf{r})}{i\,\omega}\right)\right]\,.\end{aligned} \tag{2.11}$$

Here, $\mathbf{k}_T$ denotes the transverse momentum of the emitted gluon. The limit $k_T = |\mathbf{k}_T| < \chi\,\omega$ on the transverse phase space allows to discuss gluon emission into a finite opening angle Θ, $\chi = \sin\Theta$. For the full angular integrated quantity, χ = 1. The radiation of hard quarks or gluons differs by the Casimir factor $C_R = C_F$ or C_A, respectively.

The two-dimensional transverse coordinates $\mathbf{u}$, $\mathbf{y}$ and $\mathbf{r}$ emerge in the derivation of Eq. (2.11) as distances between the positions of projectile components in the amplitude and complex conjugate amplitude. The longitudinal coordinates y_l, $\bar{y}_l$ integrate over the ordered longitudinal gluon emission points in amplitude and complex conjugate amplitude, which emerge in time-ordered perturbation theory. These internal integration variables play no role in the following discussion. They are explained in more detail in Ref. [71].

The properties of the medium enter Eq. (2.11) in terms of the product of the time-dependent density $n(\xi)$ of scattering centres times the strength of a single elastic scattering $\sigma(\mathbf{r})$. This dipole cross section $\sigma(\mathbf{r})$ is given in terms of the elastic high-energy cross section $|a(\mathbf{q})|^2$ of a single scatterer,

$$\sigma(\mathbf{r}) = 2 \int \frac{d\mathbf{q}}{(2\pi)^2} \, |a(\mathbf{q})|^2 \, \left(1 - e^{i\mathbf{q}\cdot\mathbf{r}}\right) \, . \tag{2.12}$$

The full expression in Eq. (2.11) has been studied in two limiting cases:

1. Multiple soft scattering limit
   For arbitrary many soft scattering centres, the projectile performs a Brownian motion in transverse momentum. This dynamical limiting case can be studied in the saddle point approximation of the path-integral Eq. (2.11), using [63, 66]

$$n(\xi) \, \sigma(\mathbf{r}) \simeq \frac{1}{2} \, \hat{q}(\xi) \, \mathbf{r}^2 \, . \tag{2.13}$$

   Here, $\hat{q}(\xi)$ is the transport coefficient [62] which characterizes the medium-induced transverse momentum squared $\langle q_T^2 \rangle_{\rm med}$ transferred to the projectile per unit path length λ (for details and numerical estimates, see Section 3.1.4.). For a static medium, the transport coefficient is time-independent,

$$\hat{q} = \frac{\langle q_T^2 \rangle_{\rm med}}{\lambda} \, . \tag{2.14}$$

   In the approximation Eq. (2.13), the path integral in Eq. (2.11) is equivalent to that of a harmonic oscillator. Technical details of how to evaluate Eq. (2.11) are given in Ref. [76]. In the multiple soft scattering approximation, the gluon energy distribution (2.11) depends on the characteristic gluon energy ω_c and a dimensionless parameter R,

$$R = \omega_c \, L \, . \tag{2.15}$$

   The spectrum is shown in Fig. 2.6. For the case of medium showing one-dimensional Bjorken expansion, R can be related to the initially produced gluon density [7]. In the limit $R \to \infty$, the full spectrum Eq. (2.11) reduces to a compact analytical expression first derived in [62],

$$\lim_{R\to\infty} \, \omega \frac{dI}{d\omega} = \frac{\alpha_s C_R}{\pi} \, \ln \left[\cosh^2 \sqrt{\frac{\omega_c}{2\omega}} - \sin^2 \sqrt{\frac{\omega_c}{2\omega}} \right] . \tag{2.16}$$

   In the limit of large and small gluon energies, this expression coincides with the qualitative expectations: it shows a characteristic $1/\sqrt{\omega}$-energy dependence for small ω which is suppressed above the characteristic gluon frequency ω_c:

$$\lim_{R\to\infty} \, \omega \frac{dI}{d\omega} \simeq \frac{2\alpha_s C_R}{\pi} \left\{ \begin{array}{ll} \sqrt{\frac{\omega_c}{2\,\omega}} & \text{for} \quad \omega < \omega_c \, , \\ \frac{1}{12} \left(\frac{\omega_c}{\omega}\right)^2 & \text{for} \quad \omega > \omega_c \, . \end{array} \right. \tag{2.17}$$

2. Opacity expansion
   In the opacity expansion [71, 73, 74], the path integral

$$\mathcal{K}(\mathbf{r}(y_l), y_l; \mathbf{r}(\bar{y}_l), \bar{y}_l|\omega) = \int \mathcal{D}\mathbf{r} \exp \left[\int_{y_l}^{\bar{y}_l} d\xi \left(i\frac{\omega}{2}\dot{\mathbf{r}}^2 - \frac{1}{2} n(\xi) \sigma\left(\mathbf{r}\right) \right) \right] \tag{2.18}$$

   in Eq. (2.11) is expanded in powers of the dipole cross section.
   To first order, the entire medium-dependence comes from the interaction of the hard parton with a single static scattering centre, multiplied by the number $n_0 L = L/\lambda$ of scattering centres along

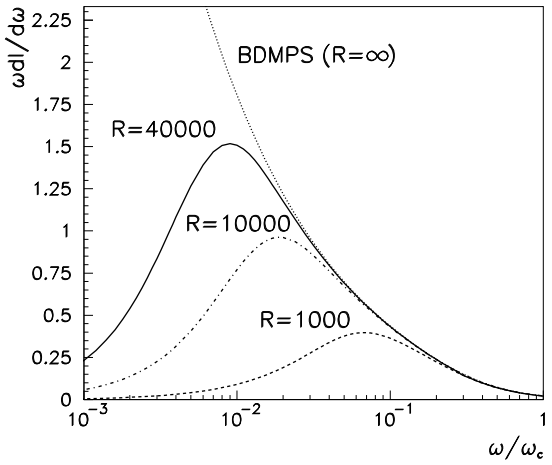

Fig. 2.6: The medium-induced gluon energy distribution $\omega\, dI/d\omega$ in the multiple soft scattering approximation for different values of the kinematic constraint $R = \omega_c\, L$

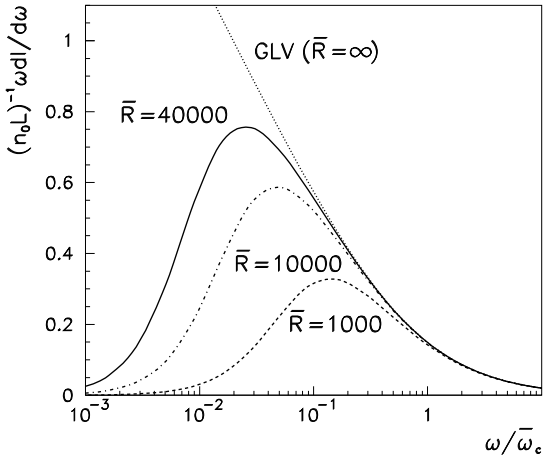

Fig. 2.7: The medium-induced gluon energy distribution $\omega\, dI/d\omega$ for a hard quark in the N = 1 opacity expansion, calculated for different values of the kinematic constraint $\bar{R}$

the path. Modelling the single scatterer by a Yukawa potential with Debye screening mass μ, one finds [80]

$$\omega \frac{dI^{N=1}}{d\omega} = 2\frac{\alpha_s\, C_R}{\pi}\,(n_0 L)\,\gamma \int_0^\infty dr\, \frac{r - sin(r)}{r^2} \times \left(\frac{1}{r+\gamma} - \frac{1}{\sqrt{((\bar{R}/2\gamma) + r + \gamma)^2 - 4r\bar{R}/2\gamma}} \right) . \tag{2.19}$$

This result is also obtained to leading order in opacity from the reaction operator approach (for details, see Section 3.1.3.). The energy distribution Eq. (2.19) depends via the phase factor $\gamma = \frac{\bar{\omega}_c}{\omega}$ on the characteristic gluon energy $\bar{\omega}_c$ in Eq. (2.9), and on the dimensionless quantity $\bar{R} = \bar{\omega}_c\, L$. The energy distribution Eq. (2.19) is plotted in Fig.2.7. In the limit $\bar{R} \to \infty$, the characteristic $1/\omega$-energy dependence of the estimate (2.10) is recovered for sufficiently large gluon energies $\omega > \bar{\omega}_c$,

$$\lim_{\bar{R}\to\infty} \omega \frac{dI^{N=1}}{d\omega} = 2\,\frac{\alpha_s\, C_R}{\pi}\,(n_0\, L)\,\gamma \int_0^\infty dr\, \frac{1}{r+\gamma}\, \frac{r - sin(r)}{r^2} \simeq 2\,\frac{\alpha_s\, C_R}{\pi}\,(n_0\, L) \begin{cases} \log\left[\frac{\bar{\omega}_c}{\omega}\right] & \text{for} \quad \bar{\omega}_c > \omega\,, \\ \frac{\pi}{4}\,\frac{\bar{\omega}_c}{\omega} & \text{for} \quad \bar{\omega}_c < \omega\,. \end{cases} \tag{2.20}$$

In both limiting cases, the multiple soft and the single hard scattering limit, the gluon energy distributions show similar dependencies on the gluon energy and the dimensionless 'kinematic constraint' $R = \omega_c\, L$ ($\bar{R} = \bar{\omega}_c\, L$). In the opacity expansion, one additional model parameter enters since one specifies both the average momentum transfer μ per scattering as well as the average number $n_0\, L$ of scattering centres involved. One can establish, however, a numerical relation between transport coefficient, Debye screening mass and opacity, for which both approximations lead to comparable results [80].

3.1.3. Energy loss in the reaction operator approach

I. Vitev

In this Section we review the finite opacity GLV approach [73, 74] to the computation of the induced gluon radiative energy loss in dense nuclear matter. This calculational framework is well equipped

for practical applications [8, 52, 81] and underlies the numerical results presented in Sections 3.4.3. and 3.4.6. This Section also complements the discussion and numerical results on the opacity expansion in Section 3.1.2.

We first discuss some of the important physical constraints in the case of nucleus–nucleus collisions that lead to the development of the Reaction Operator approach:

- A prerequisite for the consistency of all current theoretical approaches to non-abelian jet energy loss is the path (or time) ordering of the exchanged gluons between the propagating jet+induced gluon system the dense nuclear matter. This approximation holds as long as the range of the typical scattering in the medium, $R = \mu^{-1}$, is much smaller than the mean free path λ_g, in which case diagrams with crossed gluon exchanges are suppressed by $\sim e^{-\mu\lambda_g}$ [61, 82] (see also Section 3.1.1.). This condition by itself puts a theoretical constraint on the applicability of the large number of scattering centres limit for the case of heavy ion reactions where the typical size of the medium $\langle L \rangle \sim 5$ fm. The conclusion is reinforced by the fact that the hot and dense quark-gluon plasma, that is expected to be created in energetic AA reactions, expands in the final state, which leads to additional growth of the mean free path.
- The inherent dynamical nature of heavy ion reactions and the final state expansion of the system require careful treatment of the interference phases along the eikonal line of jet+gluon propagation that are the basis of the LPM destructive interference effect [77–79] in QCD. Symmetry arguments for the exchange gluons *do not* apply since their collective properties, e.g. the Debye screening mass, and correspondingly the transport coefficient $\hat{q} = \mu^2/\lambda_g$ are strongly position dependent. Most of the contribution to the interference phases is accumulated in the early stages of jet propagation. The explicit solution in the GLV reaction operator approach for the medium induced bremsstrahlung spectrum keeps the exact position and momentum information in the jet and gluon phases and propagators, see Eq. (2.24). This particular formulation of the problem of multiple radiative parton scattering can therefore answer the important question about the *rate* at which the transition to the asymptotic large number of interactions limit might takes place [73, 74].
- For phenomenological applications [8, 52, 81] the Reaction Operator solution for the radiative spectrum $\omega dN^g/d\omega$ and the mean energy loss $\langle \Delta E \rangle$ does implement finite kinematic bounds (e.g. $\mu < k_T < \omega$, $\omega_{pl} \sim \mu < \omega < E$ and $q_T^2 < s/4$) [73, 74], where the effective parton mass is determined by the medium properties [83, 84]. In the infrared and collinear regions μ plays the a role similar to the mass of a heavy quark [85–87]. The finiteness of the available phase space is particularly important at RHIC energies, but this also holds true at LHC energies for $p_T < 20$–50 GeV. The analytic solutions discussed in the previous sections and in the sections that follow relax the kinematic constraints. It is difficult to *a posteriori* adequately account for the overestimate of the available phase space even on average. Instead, the integration limits have to be imposed directly in the full solution Eq. (2.24).
- The dominance of the lowest order terms in the opacity expansion series, which has been demonstrated in [73, 74], is not unique to the gluon bremsstrahlung problem. For example, a perturbative expansion of nuclear enhanced power corrections in the number of quark-nucleon scatterings in DIS on nuclei was recently computed and resummed [88]. The full solution is well approximated by the first few terms of the series for a wide parameter range.

A powerful way to address multiple interactions of systems traversing abelian and non-abelian media is to decompose the complex multi-parton dynamics in a product of basic operator insertions that represent the interaction with a single scattering centre [73, 74, 88–90], subject to the assumption that the mean free path of the propagating system significantly exceeds the range of the scattering potential as discussed above. Let $\mathcal{A}_{i_1 \cdots i_{n-1}}(x, \mathbf{k}, c)$ be the amplitude of the propagating jet+gluon system that has already undergone $n-1$ scatterings where $x = k^+/p^+ \approx \omega/E$ is the gluon momentum fraction, $\mathbf{k}$ is its transverse momentum and c – its colour matrix. When the composite system passes by a scattering centre it can miss, which is which leaves its amplitude unchanged ($\hat{\mathbf{1}}$). If the system exchanges a single

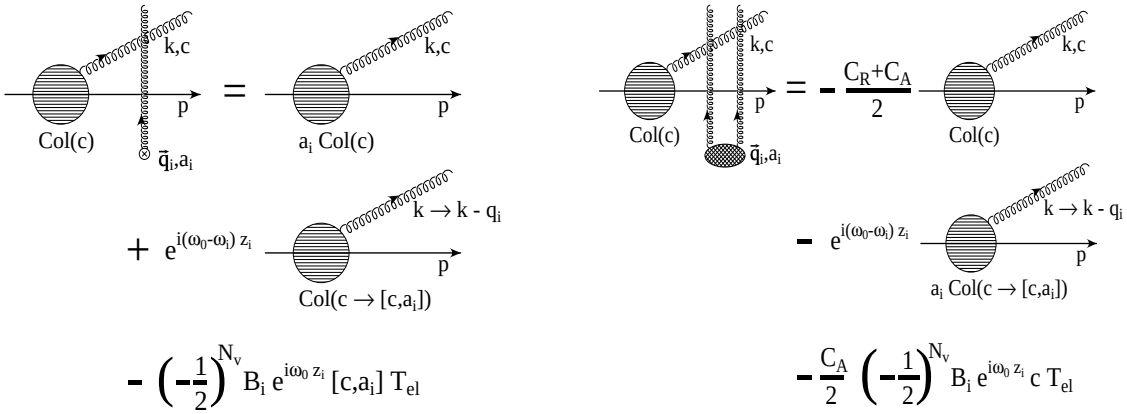

Fig. 2.8: Left panel: diagrammatic representation of the action of the direct insertion operator $\hat{D}_i$ (single hit) at position z_i on a jet+gluon state described by an amplitude $\mathcal{A}$. The generated kinematic modifi cation, colour factors or colour rotation, symmetry factors and phases from the energy difference before and after the momentum exchange are explicitly shown. Right panel: diagrammatic representation of the action of the direct insertion operator $\hat{V}_i$ (double hit) at position z_i. Figure is adapted from Ref. [74].

momentum with the scattering, left panel of Fig. 2.8, their corresponding modification of the colour and kinematics of its amplitude is given by the direct insertion operator $\hat{D}$ and reads:

$$\hat{D}_n \mathcal{A}_{i_1\cdots i_{n-1}}(x,\mathbf{k},c) = a_n \mathcal{A}_{i_1\cdots i_{n-1}}(x,\mathbf{k},c) + e^{i(\omega_0-\omega_n)z_n}\mathcal{A}_{i_1\cdots i_{n-1}}(x,\mathbf{k}-\mathbf{q}_n,[c,a_n])$$
$$-\left(-\tfrac{1}{2}\right)^{N_v(\mathcal{A}_{i_1\cdots i_{n-1}})}\mathbf{B}_n\, e^{i\omega_0 z_n}[c,a_n]\, T_{el}(\mathcal{A}_{i_1\cdots i_{n-1}}) \quad , \tag{2.21}$$

where $\mathbf{B}_n = \mathbf{H} - \mathbf{C}_n = \mathbf{k}/\mathbf{k}^2 - (\mathbf{k}-\mathbf{q}_n)/(\mathbf{k}-\mathbf{q}_n)^2)$ is the so-called Bertsch-Gunion amplitude for producing a gluon with transverse momentum $\mathbf{k}$ in an isolated single collision with scattering centre n. The momentum transfer to the jet is $\mathbf{q}_n$. The notation $\omega_n = (\mathbf{k}-\mathbf{q}_n)^2/2\omega$ is for a gluon with energy ω ($\omega_0 = \mathbf{k}^2/2\omega$) and a_n is the colour matrix in the d_R dimensional representation of the jet with colour Casimir C_R. $N_v = \sum_{m=1}^{n-1}\delta_{i_m,2}$ counts the number of virtual interactions in $\mathcal{A}_{i_1\cdots i_{n-1}}$. $T_{el}(\mathcal{A}_{i_1\cdots i_{n-1}})$ is the elastic colour factor associated with all $n-1$ momentum transfers from the medium to the jet line. Similarly, for the case of two momentum transfers given by the virtual insertion operator $\hat{V}$, right panel of Fig. 2.8,

$$\hat{V}_n \mathcal{A}_{i_1\cdots i_{n-1}}(x,\mathbf{k},c) = -\frac{C_R+C_A}{2}\mathcal{A}_{i_1\cdots i_{n-1}}(x,\mathbf{k},c) - e^{i(\omega_0-\omega_n)z_n} a_n \mathcal{A}_{i_1\cdots i_{n-1}}(x,\mathbf{k}-\mathbf{q}_n,[c,a_n])$$
$$-\left(-\tfrac{1}{2}\right)^{N_v}\frac{C_A}{2}\,\mathbf{B}_n\, e^{i\omega_0 z_n} c\, a_{n-1}^{i_{n-1}}\cdots a_1^{i_1} \quad . \tag{2.22}$$

To build one power of the elastic scattering cross section, or equivalently one power of opacity $\chi = \bar{n} = L/\lambda_g$, two gluon exchanges at a fixed position z_n are needed. Therefore, it is easy to see that the basic operator unit that represents one additional scattering with the medium — the GLV Reaction Operator — has the form:

$$\hat{R}_n = \hat{D}_n^\dagger \hat{D}_n + \hat{V}_n + \hat{V}_n^\dagger \ , \tag{2.23}$$

where $\hat{D}_n$, $\hat{V}_n$ are defined in Eqs.(2.21,2.22). The full solution [74] for the medium induced gluon radiation off jets produced in a hard collisions inside the nuclear medium of length L and *to all orders* in the correlations between the multiple scattering centres is computed via the iterative action of the Reaction Operator on an initial condition given by the vacuum bremsstrahlung and averaging over the

momentum transfers and the positions of the scattering centre, respectively,

$$\sum_{n=1}^{\infty} x\frac{dN^{(n)}}{dx\,d^2\mathbf{k}} = \frac{C_R\alpha_s}{\pi^2}\sum_{n=1}^{\infty}\prod_{i=1}^{n}\int_0^{L-\sum_{a=1}^{i-1}\Delta z_a}\frac{d\Delta z_i}{\lambda_g(i)}\int\prod_{i=1}^{n}\left(d^2\mathbf{q}_i\,\left[|\bar{v}_i(\mathbf{q}_i)|^2-\delta^2(\mathbf{q}_i)\right]\right)$$
$$\times\left(-2\,\mathbf{C}_{(1,\cdots,n)}\cdot\sum_{m=1}^{n}\mathbf{B}_{(m+1,\cdots,n)(m,\cdots,n)}\right.$$
$$\left.\times\left[\cos\left(\sum_{k=2}^{m}\omega_{(k,\cdots,n)}\Delta z_k\right)-\cos\left(\sum_{k=1}^{m}\omega_{(k,\cdots,n)}\Delta z_k\right)\right]\right)\,, \qquad (2.24)$$

where $\sum_2^1 \equiv 0$ is understood. In Eq. (2.24) $\mathbf{C}_{(m,\cdots,n)} = \frac{1}{2}\nabla_{\mathbf{k}}\ln(\mathbf{k}-\mathbf{q}_m-\cdots-\mathbf{q}_n)^2$, $\mathbf{B}_{(m+1,\cdots,n)(m,\cdots,n)} = \mathbf{C}_{(m+1,\cdots,n)} - \mathbf{C}_{(m,\cdots,n)}$ are the colour current propagators, $\omega^{-1}_{(m,\cdots,n)} = 2xE/|C^2_{(m,\cdots,n)}|$ are formation times, and $\Delta z_k = z_k - z_{k-1}$ are the separations of subsequent scattering centres. The momentum transfers $\mathbf{q}_i$ are distributed according to a normalized elastic scattering cross section $|\bar{v}_i(\mathbf{q}_i)|^2 = \sigma_{el}^{-1}d\sigma_{el}/d^2\mathbf{q}_i = \mu^2/\pi(\mathbf{q}_i^2+\mu^2)^2$ for the colour-screened Yukawa type and the radiative spectrum can be evaluated from (2.24) for any initial nuclear geometry with an arbitrary subsequent dynamical evolution of the matter density. It is this stage of the calculation, Eq. (2.24), at which the finite kinematic constraints have to be imposed for the remaining $\mathbf{q}, \mathbf{k}$ and x integrals.

As argued above, the explicit all order solution for the double differential radiative spectrum, Eq. (2.24), provides an unambiguous way to study the convergence of the opacity series and the relative importance of its terms. It can be seen from Fig. 2.9 that at large jet energies the lowest order correlation between the jet production point one of the scatterings that follow gives the dominant contribution to the non-abelian energy loss. It also gives the quadratic dependence of ΔE on the size of the plasma, $\Delta E \propto L^2$ for *static* media [73]. For *realistic* plasmas higher order opacity corrections may become important only for large number of scatterings $n \geq 5$ and small jet energies $E \sim$ 5–10 GeV.

Despite the dominance of the first order in the opacity expansion [73], to improve the numerical accuracy for small parton energies we include corrections up to third order in χ. The left panel of Fig. 2.10 shows the radiation intensity dI/dx with an infrared cut-off at small $x = \omega/E$ given by the plasmon mass μ. The dynamical expansion of the bulk soft matter is assumed to be of Bjorken type. The medium induced radiative energy loss is proportional to the density of the scattering centres in the medium and for the cases of 1+1D and 1+3D expansions it has been shown that a useful to drive the calculation by dN^g/dy [81, 91] since the gluon rapidity density can be related to the hadron multiplicities and the number of participants in AA collisions. The right panel of Fig. 2.10 shows the probability distribution of fractional energy loss $\epsilon = \sum_n \omega_n/E$, numerically computed as in Ref. [5] from the gluon number distribution $dN(x,E)/dx$, in the Poisson approximation [5, 7, 92, 93] of independent gluon emission

$$P(\epsilon,E) = \sum_{n=0}^{\infty}P_n(\epsilon,E)\,, \quad P_{n+1}(\epsilon,E) = \frac{1}{n+1}\int_{x_0}^{1-x_0}dx_n\,\frac{dN(x_n,E)}{dx}P_n(\epsilon-x_n,E)\,. \qquad (2.25)$$

The number of radiated gluons $\langle N^g(E)\rangle$ is finite and small which leads to an explicit finite no-radiation contribution $P_0(\epsilon,E) = e^{-\langle N^g(E)\rangle}\delta(\epsilon)$.

Analytic examples in the one scattering centre limit

In the case of 1+1D Bjorken longitudinal expansion with initial plasma density ρ_0 and formation time τ_0, i.e. $\rho(\tau) = \rho_0\,(\tau_0/\tau)$, it is possible to obtain a closed form analytic formula [81] under the strong asymptotic no kinematic bounds assumption. For a hard jet penetrating the quark-gluon plasma the LPM effect originates from the formation physics function defined in Ref. [81] as

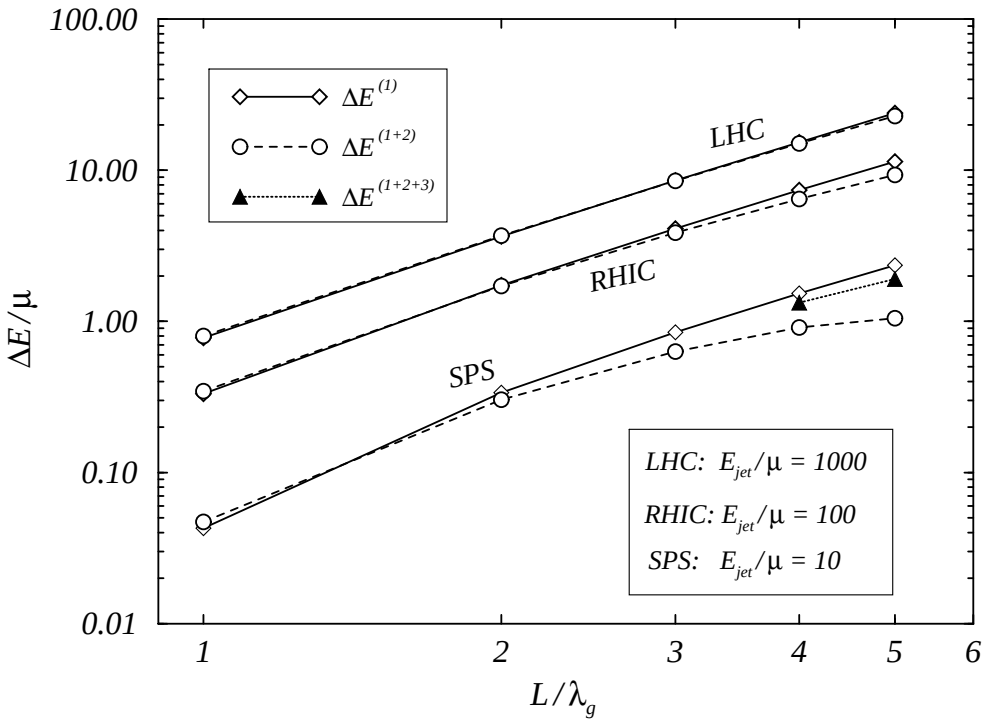

Fig. 2.9: The radiative energy loss of a quark jet with energy E_{jet} = 5,50,500 GeV (at SPS, RHIC, LHC) is plotted as a function of the opacity L/λ_g. for a static medium (λ_g = 1 fm, μ = 0.5 GeV). Solid curves show the first order in opacity results. The dashed curves show results up to second order in opacity, and two third order results are shown by solid triangles for SPS energies. Figure is adapted from Ref. [74].

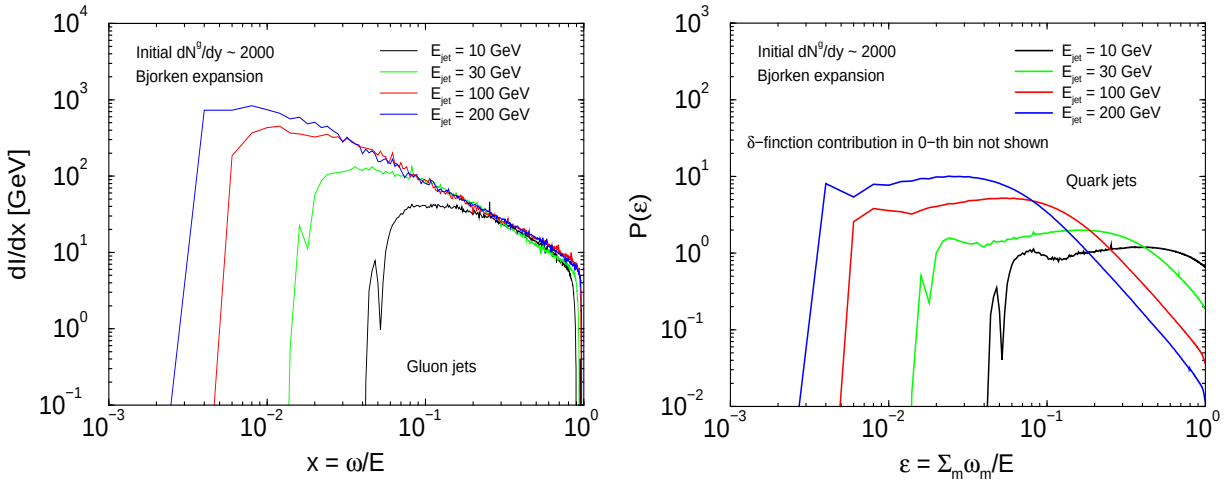

Fig. 2.10: Left panel: the radiative spectrum dI/dx computed numerically up to third order in opacity from Eq. (2.24) in a dynamical Bjorken expansion scenario with a gluon plasma rapidity density dN^g/dy = 2000. Right panel: the fractional energy loss probability distribution $P(\epsilon = \sum_n \omega_n/E)$ of fractional radiative energy loss computed as in [5]. The no-radiation δ-function contribution is not shown.

$f(x,\tau) = \int_0^\infty du\ [1-\cos(uZ(x,\tau))]/[u(1+u)]$. With $Z(x,\tau) = (\tau-\tau_0)\mu^2(\tau)/2xE$ being the local formation physics parameter, two simple analytic limits apply: for $x \gg x_c = L\mu^2(L)/2E$, in which case the formation length is large compared to the size of the medium, the small $Z(x,\tau)$ limit applies, leading to $f(Z) \approx \pi Z/2$. The interference pattern along the gluon path becomes important and accounts for the the non-trivial dependence of the energy loss on L. When $x \ll x_c$, i.e. the formation length is small compared to the plasma thickness, one gets $f(Z) \approx \log Z$. The bremsstrahlung intensity distribution reads:

$$\frac{dI^{(1)}}{dx} = \frac{9C_R\pi\alpha_s^3}{4}\frac{1}{A_T}\frac{dN^g}{dy} \times \begin{cases} \dfrac{L}{x} + \cdots, & x \gg \dfrac{\mu^2(L)L}{2E} \\ \dfrac{6E}{\pi\mu^2(L)}\ln\dfrac{\mu^2(L)L}{2xE} + \cdots, & x \ll \dfrac{\mu^2(L)L}{2E} \end{cases}, \quad (2.26)$$

where $C_R = 4/3\ (3)$ for quark (gluon) jets. In Eq. (2.26) A_T is the transverse size of the medium, e.g. $A_T = \pi R^2$ for central nucleus–nucleus collisions. The mean energy loss (to first order in χ) integrates to

$$\Delta E^{(1)} = \frac{9C_R\pi\alpha_s^3}{4}\frac{1}{A_T}\frac{dN^g}{dy}\,L\,\left(\ln\frac{2E}{\mu^2 L} + \frac{3}{\pi} + \cdots\right). \quad (2.27)$$

We emphasize the linear rather than quadratic dependence of the energy loss on the size of the medium [81] in the Bjorken expansion case. The logarithmic enhancement with energy comes from the $x_c < x < 1$ region [73]. In the case of sufficiently large jet energies ($E \to \infty$) this term dominates.

In the reaction operator approach, medium induced radiative energy loss in transversely expanding plasma is discussed in Ref. [5]. To derive an analytic expression taking transverse flow into account, we consider an asymmetric expanding sharp *elliptic* density profile the surface of which is defined by $x^2(R_x+v_x\tau^{-2}+y^2(R_y+v_y\tau)^{-2} = 1$. The area of this elliptic transverse profile increases with time, τ, as $A_T(\tau) = \pi(R_x+v_x\tau)(R_y+v_y\tau)$. A short calculation for the $\propto \ln E$ term in the opacity series leads to

$$\Delta E^{(1)}(\phi_0) \approx \frac{9}{4}\frac{C_R\alpha_s^3}{R_xR_y}\frac{dN^g}{dy}\,\frac{\log\frac{1+a_x\tau(\phi_0)}{1+a_y\tau(\phi_0)}}{a_x-a_y}\,\log\frac{2E}{\mu^2 L}, \quad (2.28)$$

where $a_x = v_x/R_x, a_y = v_y/R_y$. This expression is a central result for transversely expanding media and provides a simple analytic generalization that interpolates between pure Bjorken 1+1D expansion for small $a_{x,y}\tau$, and 3+1D expansion at large $a_{x,y}\tau$. In the special case of pure Bjorken (longitudinal) expansion with $v_x = v_y = 0$ Eq. (2.28) reduces to Eq. (2.27) with $A_T = \pi R_xR_y$. We also note that for a jet originating near the centre of the medium and *fully penetrating* the plasma the enhanced escape time due to expansion $\tau = R/(1-v_T)$ compensates for the $1/(1+v_T\tau/R)$ dilution factor. Therefore, in this isotropic case, the extra dilution due to transverse expansion has in fact little or no effect of the total energy loss $\Delta E^{(1)}_{1D}(b = 0\ \text{fm}) \approx \Delta E^{(1)}_{3D}(b = 0\ \text{fm})$, modulo logarithmic factors which become sizable only for large v_T. An important consequence of our finding is that the inclusive azimuthally averaged jet quenching pattern in central collisions is approximately independent of the transverse flow.

3.1.4. Estimates for cold nuclear matter transport coefficients

F. Arleo

The modification of high-p_T hadro- and jet production due to multiple medium-induced interactions depends on the spatial extension of the medium, and on the probability and strength of the multiple scatterings which the hard partons suffer. To characterize medium-modifications of high-p_T jets produced in nucleus–nucleus collisions, and to relate them to the properties of hot and dense QCD matter produced in the collision region, knowledge about the multiple scattering strength of cold nuclear matter is a baseline of obvious importance. Several parameterizations, suited for different processes, have

been proposed to characterize this strength of multiple scattering which a hard parton undergoes while propagating through cold nuclear matter. Here we summarize the information currently available from theoretical predictions, as well as from data analysis of processes in which incoming or outgoing quarks propagate through nuclear matter, and we comment on the relation between different parameterizations.

There are two parameters often used for the characterization of the strength of multiple scattering.

- BDMPS transport coefficient $\hat{q}$
  In the approach of Baier, Dokshitzer, Mueller, Peigné, and Schiff (BDMPS) [61, 62, 65], this transport coefficient of the medium is given by $\hat{q} = \mu^2/\lambda_{\rm mfp}$. Here μ is the typical transverse momentum exchanged with the medium and $\lambda_{\rm mfp}$ denotes the parton mean free path in the medium. In the following, $\hat{q}$ will refer to the transport coefficient of a propagating gluon.
  The transport coefficient $\hat{q}$ is a measure of the scattering strength of the QCD medium. It is related to the local density of colour charges. In the BDMPS framework, $\hat{q}$ is related to the elastic scattering cross section σ of a parton on a scattering centre in the medium, see Eq. (2.4). For cold nuclear matter, it is given by the gluon density of the nucleon (see Appendix B of Ref. [62]). This allows for a simple expression of the gluon transport coefficient in terms of the gluon distribution $xG(x)$ and the nuclear density ρ,

$$\hat{q} = \frac{4\,\pi^2 \alpha_s\, N_c}{N_c^2 - 1}\, \rho\, x\, G(x, Q^2)\,. \tag{2.29}$$

  Taking $\alpha_s \simeq 1/2$, $\rho \simeq 0.16$ fm^{-3} and $xG(x) \simeq 1$, Baier et al. have estimated the value for cold nuclear matter, $\hat{q}$ = 0.045 GeV^2/fm. Since also the saturation momentum Q_s of gluons for central gluon-nucleus (radius R_A) collisions at small x is given in terms of the gluon distribution function, there is a linear relation between Q_s and $\hat{q}$, [94]

$$Q_s^2 = 2 R_A\, \hat{q}\,. \tag{2.30}$$

- LQS scale parameter λ
  In the perturbative QCD approach developed by Luo, Qiu, and Sterman (LQS) [95], λ denotes the strength of twist-4 matrix elements. These determine the strength of double parton scattering, see Section 3.5.1.
  To determine a numerical estimate, LQS calculated the momentum imbalance of dijets in photoproduction on nuclei. This is defined as

$$\Delta\langle k_T^2\rangle \;=\; \left(p_{\perp_1}^2 + p_{\perp_2}^2\right) \;\times\; \sin\Delta\Phi\,, \tag{2.31}$$

  where $p_{\perp_i}$ denote the transverse momenta of the partons and $\Delta\Phi$ the angle between the two corresponding jets. Their analysis assumes that the nuclear enhancement seen in the data is due to the rescattering of one of the produced partons (either quark or gluon). Assuming only the rescattering of the quark when x is not too small, they can rewrite the momentum imbalance as

$$\Delta\langle k_T^2\rangle = C_R\, \pi^2\, \alpha_s\, \lambda^2\, A^{1/3}\,. \tag{2.32}$$

  Comparing with the measurements (see Table 2.2) reported at Fermilab by the E683 collaboration,

$$\Delta\langle k_T^2\rangle \;=\; 2 \times 0.216 \ln A \sim 2 \times 0.216 A^{1/3}\,, \tag{2.33}$$

  they extract $\lambda^2 \simeq 0.1$ GeV^2. Assuming moreover the non-perturbative scale λ to be greater than Λ_{QCD}, they conclude λ^2 = 0.05–0.1 GeV^2. The original LQS estimate is based on rescattering of partons in the final state. X.F. Guo [96] gave a different estimate based on the $\langle k_T^2\rangle$ of Drell-Yan pairs produced in h-A collisions. This observable shows a nuclear enhancement due to the multiple scatterings of the incoming quark entering the nucleus,

$$\Delta\langle k_T^2\rangle = \langle k_T^2\rangle_{h\,A} - \langle k_T^2\rangle_{h\,N}\,. \tag{2.34}$$

In a calculation [96] to leading order in α_s but taking into account nuclear enhanced power corrections, this quantity was shown to be proportional to the four-parton correlation function in nuclei, $T_q(x, A)$, given in the Luo, Qiu, and Sterman model by

$$T_q(x, A) \;=\; \lambda^2\, A^{1/3}\, f_q^A(x, A)\,, \tag{2.35}$$

which depends linearly on the length $\sim A^{1/3}$ covered by the hard incoming quark, and where λ is the unknown non-perturbative scale. Assuming only one quark flavor to contribute to the DY process, the LO $\langle k_T^2 \rangle$ broadening Eq. (2.34) reads

$$\Delta\langle k_T^2 \rangle \;=\; \left(\frac{4\,\pi^2\,\alpha_s}{3}\right)\,\lambda^2\,A^{1/3}\,. \tag{2.36}$$

Experimentally, the $\langle k_T^2 \rangle$ broadening has been measured by the NA10 and E772 collaborations in pion and proton induced reactions on nuclei respectively, see Table 2.2. The value

$$\lambda^2 \;=\; 0.01 \;\; \mathrm{GeV}^2 \tag{2.37}$$

has been extracted from a comparison of Eq. (2.36) with these data. This is a factor at least 5 smaller than the original LQS estimate. It may come from the strong interference beyond the leading order for the initial-state interactions [97].

The following discussion focuses on these two parameters. Also, we shall express numerical estimates in terms of the mean energy loss per unit length, $-dE/dz$. Other parameterizations in the literature can be related to them. For example, the product $n_0\,C$ is used in the works of Zakharov [66] and Wiedemann [71, 72] on parton energy loss. It denotes the product of the density n_0 of charges in the medium times their scattering strength C, and can be expressed in terms of the BDMPS transport coefficient, $\hat{q} = 2\,n_0 C$.

Relation between BDMPS transport coefficient, LQS scale parameter and mean energy loss. The BDMPS transport coefficient $\hat{q}$ and the LQS scale parameter λ can be connected assuming the k_T broadening and the dijet momentum imbalance to be directly comparable [62]. In the BDMPS framework, the broadening of an incoming parton (with colour C_R) is given by the transport coefficient and the length it has travelled though the medium,

$$\langle k_T^2 \rangle_{\mathrm{BDMPS}} = \frac{C_R}{C_A}\,\hat{q}\,L\,. \tag{2.38}$$

In the LQS approach to jet broadening [95], it is given by Eq. (2.32). Comparing Eqs. (2.38) and (2.32), a simple expression between $\hat{q}$ and λ is found [62]

$$\hat{q} = C_A\,\pi^2\,\alpha_s\,\frac{A^{1/3}}{L}\,\lambda^2 = \frac{4}{3}\,C_A\,\pi^2\,\alpha_s\;\times\;\left(\frac{1}{r_0}\right)\times\;\lambda^2\,, \tag{2.39}$$

where L = $3/4\;r_0\,A^{1/3}$ with $r_0 \;\simeq$ 1.2 fm. The transport coefficient can also be related to the mean energy loss per unit length $-dE/dz$. This parameter depends linearly on the length L of the medium and is therefore proportional to the atomic mass number $A^{1/3}$ [65]

$$\left(-\frac{dE}{dz}\right)_{\mathrm{out}} = \frac{1}{4}\,\alpha_s\,C_R\,\hat{q}\,L = \frac{1}{4}\,\alpha_s^2\,C_A\,C_R\,\pi^2\,A^{1/3}\,\lambda^2 \tag{2.40}$$

for an outgoing parton, while

$$\left(-\frac{dE}{dz}\right)_{\mathrm{in}} = \frac{1}{12}\,\alpha_s\,C_R\,\hat{q}\,L = \frac{1}{12}\,\alpha_s^2\,C_A\,C_R\,\pi^2\,A^{1/3}\,\lambda^2 \tag{2.41}$$

Table 2.2: Summary of various data analyses to extract the amount of quark energy loss in nuclear matter

		Observable	Data	Reaction
incoming q	Vasiliev *et al.* (E866) [100]	Drell-Yan x_1 dependence	E866	p(800 GeV)- Be, Fe, W
	Johnson *et al.* (E772) [101]	Drell-Yan x_1 and M dependence	E772 E866	p(800 GeV)- D, C, Ca, Fe, W p(800 GeV)- Be, Fe, W
	Arleo [103]	Drell-Yan x_1 dependence	NA3	π^-(150 and 280 GeV)- p, Pt
	Guo [96]	Drell-Yan k_T broadening	NA10 E772	π^- (140 and 280 GeV) - D, W p (800 GeV) - C, Ca, Fe, W
	Gyulassy, Vitev [8]	Hadroproduction Cronin enhancement	E300 E605	p (400 and 800 GeV) - Be, W
outgoing q gluon	Luo, Qiu, Sterman [95]	Photoproduction dijet momentum imbalance	E683	γ - p, D, Be, C, Al, Cu, Sn, Pb $\sqrt{s}$ = 21 GeV
	Wang, Wang [6]	DIS fragmentation functions	HERMES	e- D, N, Kr $\sqrt{s} = 7.2$ GeV

in the case of partons approaching the medium.

For a numerical comparison of estimates for $-dE/dz$ with $\hat{q}$ and λ, we use the mean energy loss $-dE/dz$ in a L = 5 fm nucleus, and obtain the following relations

$$\frac{1}{3}\left(-\frac{dE}{dz}\right)_{\rm out} = \left(-\frac{dE}{dz}\right)_{\rm in} [\mathrm{GeV/fm}] = 1.39\,\hat{q}\ \left[\mathrm{GeV^2/fm}\right] = 22.8\,\lambda^2\ \left[\mathrm{GeV^2}\right]\ , \qquad (2.42)$$

where $\alpha_s \simeq 0.5$ and C_R = 4/3.

Comparison of estimates for multiple scattering in cold nuclear matter

The results of different numerical estimates for the scattering properties of cold nuclear matter are tabulated in Table 2.3 and summarized in Fig. 2.11. In the last subsection, the origin of the estimates of Baier *et al.*, Luo, Qiu and Sterman, as well as X.F. Guo have been reviewed already. Here, we explain how the other estimates were obtained and we give arguments for the discrepancies between different estimates.

Theoretical arguments [62, 98]. The arguments leading Baier *et al.* to relate the energy loss of cold nuclear matter to the gluon distribution in the nucleon are discussed above. Without comparison to experimental data, S. Brodsky and P. Hoyer had suggested an upper bound for parton energy loss [98]. It is based on the argument that the minimum longitudinal momentum transfer to the hard parton due to gluon radiation is set by the uncertainty principle, $\Delta p_z \times L > 1$, where L is the distance between

Table 2.3: Compilation of the different estimates for the magnitude of quark energy loss, given either in terms of $\hat{q}$, λ, or the mean energy loss per unit length for an incoming $(-dE/dz)_{\rm in}$ and outgoing quark $(-dE/dz)_{\rm out}$. The correspondence between the variables has been tempted and is explained in the text. In bold are the original estimates given by the various groups.

		$\hat{q}$	λ^2	$(-dE/dz)_{\rm in}$	$(-dE/dz)_{\rm out}$
theory	Brodsky, Hoyer [98]	≤ 0.72	≤ 0.022	$\leq \mathbf{0.5}$	$\leq \mathbf{0.5}$
	Baier *et al.* [62]	**0.045**	0.0029	0.063	0.19
data analysis	Vasiliev *et al.* (E866) [100]	$\leq \mathbf{0.24}$	≤ 0.014	≤ 0.33	≤ 0.99
	Johnson *et al.* (E772) [101]	$2.0 \pm 0.3 \pm 0.4$	$0.12 \pm 0.02 \pm 0.02$	$\mathbf{2.7} \pm \mathbf{0.4} \pm \mathbf{0.5}$	$8.2 \pm 1.1 \pm 1.5$
	Arleo [103]	$\mathbf{0.14} \pm \mathbf{0.11}$	0.009 ± 0.007	0.20 ± 0.15	0.60 ± 0.45
	Guo [96]	0.16	**0.01**	0.23	0.69
	Gyulassy, Vitev [8]	**0.1**	0.0061	0.14	0.42
	Luo, Qiu, Sterman [95]	0.82–1.6	**0.05–0.1**	1.14–2.28	3.4–6.8
	Wang, Wang [6]	0.12	0.0073	0.17	**0.5**

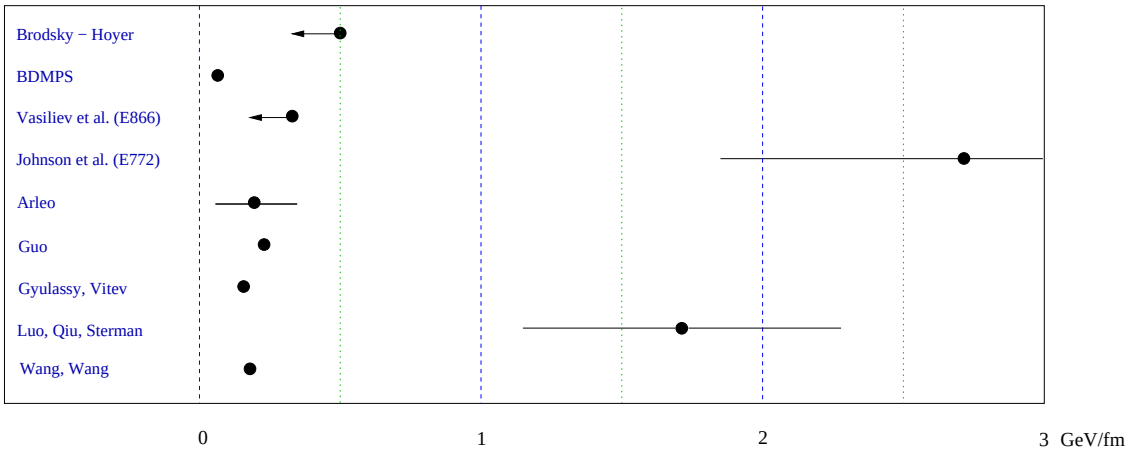

Fig. 2.11: Compilation of the different estimates for the magnitude of an incoming quark mean energy loss per unit length, $(-dE/dz)_{\rm in}$, in a L = 5 fm nucleus (see text and Table 1.3)

two scattering centres. Let ΔE be the energy carried away by the emitted gluon and k_T its transverse momentum. The longitudinal momentum transfer then reads $\Delta p_z \simeq k_T^2 / 2\Delta E$, leading to

$$\frac{k_T^2}{2\,\Delta E} \times L > 1\,. \tag{2.43}$$

While this expression comes directly from the Heisenberg principle, a similar expression has been explicitly derived by Brodsky and Hoyer in a simpler QED model. The maximal radiative energy loss for partons (note that it should apply to both quarks and gluons) now amounts to

$$-\frac{dE}{dz} < \frac{k_T^2}{2}\,, \tag{2.44}$$

where k_T^2 can be related to the typical transverse momentum which partons acquire in the medium. Brodsky and Hoyer mainly emphasize that this radiative energy loss is not proportional to the energy of the scattering particle. They point out that a previous analysis of Drell–Yan data [99] based on $-\frac{dE}{dz} \propto E$ violates the uncertainty principle at large E. With the estimate k_T^2 = 0.1 GeV^2 for partons traversing cold nuclear matter, Brodsky and Hoyer arrive at $-\frac{dE}{dz} \leq 0.5$ GeV/fm, taking into account a similar energy loss as Eq. (2.44) due to elastic scattering. Clearly, this upper bound depends on the choice of k_T^2 and is violated if k_T^2 turns out to be larger. Thus, the analysis of Brodsky and Hoyer does not constrain the scattering properties of cold nuclear matter, but it constrains the energy dependence of $-\frac{dE}{dz}$ in the ultra-relativistic limiting case.

Estimates for outgoing quarks [6, 95]. The original estimate for the LQS scale parameter λ in cold nuclear matter is based on the transverse momentum broadening of dijets measured in photoproduction on nuclei. Another analysis of the energy loss of outgoing quarks in cold nuclear matter was given by E. Wang and X.-N. Wang [6]. In their approach, the multiple scattering of the produced quarks escaping the nucleus modifies the fragmentation functions in nuclei, $D(z, Q^2, A)$. The strength of this modification (here denoted $\tilde{C}$) is again related to nuclear enhanced twist-4 parton correlation functions.

The HERMES collaboration measured hadron production in e-A collisions on D, N, and Kr targets ($\sqrt{s}$ = 7.2 GeV) as a function of the virtual photon energy ν and the momentum fraction carried by the produced hadron, z. These measurements give a direct access to the nuclear dependence of the fragmentation functions. Comparing with these preliminary data, E. Wang and X.-N. Wang found a good agreement provided that

$$\tilde{C}\alpha_s^2 \simeq 0.00065 \;\; \mathrm{GeV}^2. \tag{2.45}$$

They translate this quantity into a mean energy loss of

$$\left(-\frac{dE}{dz}\right)_{\mathrm{out}} = 0.5 \;\; \mathrm{GeV/fm} \tag{2.46}$$

for a L = 5 fm nucleus.

Estimates for incoming quarks [96,100–103]. Several works have attempted to parametrize multiple scattering effects of cold nuclear matter from Drell–Yan measurements in hadron-nucleus collisions. The estimate of X.F. Guo based on the nuclear enhanced transverse momentum broadening of Drell–Yan pairs was reviewed. Three other groups estimated the parton energy loss from the x_1-dependence of Drell–Yan data.

The data analysis of M.A. Vasiliev *et al.* (E866) [100] is based on Drell–Yan measurements in 800 GeV proton induced reactions on Beryllium, Iron, and Tungsten targets. The data cover a wide range in the momentum fraction of the projectile parton, x_1, integrated over the invariant mass interval $4 < M < 8.4$ GeV. The data analysis assumes [100] that the multiple scatterings of the incoming (anti)quark in the nucleus shift the momentum fraction of the hard parton on average by a

$$\Delta x_1 = \frac{\kappa}{s}\, A^{2/3}\,, \tag{2.47}$$

where κ parametrizes the strength of the energy loss. The leading-order Drell–Yan cross section

$$\sigma^{p\,A}(x_1) \sim f^p(x_1 + \Delta x_1) \times f^A(x_2) \times \hat{\sigma} \tag{2.48}$$

is then fitted to the data with κ considered as a free parameter. The effects of nuclear shadowing $f^A(x_2) \neq f^p(x_2)$ in (2.48) have been taking into account using the EKS98 parameterization [15].

The amount of quark energy loss was found to be negligible in these data sets, with a one-standard deviation upper limit $\kappa < 0.10$ GeV^2. Assuming the length covered by the incoming parton to be given by the nuclear radius, $L = 3/4\, r_0\, A^{1/3}$, one can relate easily the κ parameter to the BDMPS transport coefficient. Using Eq. (4.61) in Eq. (2.41), it is given by

$$\hat{q} = \frac{16\,\kappa}{m_p\, r_0^2} \tag{2.49}$$

with $r_0 \simeq 1.2$ fm. The upper limit extracted by this group amounts to

$$\hat{q} \;\leq\; 0.237 \;\; \mathrm{GeV}^2/\mathrm{fm}\,. \tag{2.50}$$

M. Johnson *et al.* (E772) [101,102] performed a different analysis of the E772 and E866 Drell–Yan measurements. They raised the point that E772 Drell–Yan data have also been used in the EKS98 analysis. In principle, the small upper bound Eq. (2.50) could originate from an erroneous attribution of the sizable nuclear dependence to shadowing effects. The authors [101, 102] then attempt to disentangle the effects of quark energy loss and nuclear shadowing on the basis of a light-cone formulation of the Drell–Yan process which allows to calculate shadowing corrections. For the E772 and E866 data sets, they extract

$$\left(-\frac{dE}{dz}\right)_{\mathrm{in}} \;=\; 2.73 \pm 0.37 \pm 0.5 \;\; \mathrm{GeV/fm}\,, \tag{2.51}$$

where the errors are statistics and systematics respectively. This value is an order of magnitude larger than any other estimate for cold nuclear matter and depends entirely on the validity of a theoretical light-cone calculation of nuclear shadowing, whose uncertainties are difficult to evaluate.

As illustrated by the two analyses above, the poorly known shadowing corrections in the Drell–Yan process render the extraction of quark energy loss from Drell–Yan data difficult. F. Arleo [103] emphasized that Drell–Yan production in pion induced reactions at lower beam energy is much less sensitive to shadowing effects [103] mainly for two reasons. First, the pion beam favours the fusion of valence quarks for which shadowing corrections are well fixed from DIS measurements only. Moreover, the low beam energy probes a target momentum fraction range $x_2 \sim 0.1$ where shadowing is known to be small.

The Drell–Yan cross section has been computed in the QCD-improved parton model to leading-order. In these calculations, the energy loss ϵ is modeled by the BDMPS probability distribution [92] $P(\epsilon)$ which was determined from the medium-induced BDMPS gluon energy distribution. The cross section reads

$$\sigma^{\pi^-\,A}(x_1) \sim f^{\pi^-}(x_1 + \epsilon/E_\pi) \times f^A(x_2) \times \hat{\sigma} \times P(\epsilon)\,. \tag{2.52}$$

In the fit of Eq. (2.52) to NA3 data, the transport coefficient was considered a free parameter. It has been found that

$$\hat{q} \;=\; 0.144 \pm 0.108 \;\; \mathrm{GeV}^2/\mathrm{fm}\,, \tag{2.53}$$

which corresponds to a mean energy loss per unit length

$$\left(-\frac{dE}{dz}\right)_{\mathrm{in}} \;=\; 0.20 \pm 0.15 \;\; \mathrm{GeV/fm} \tag{2.54}$$

in a large ($L = 5$ fm) nucleus.

An alternative way to determine the nuclear matter transport coefficient is to analyze the multiple scattering and associated transverse momentum broadening of incoming partons. The Cronin effect observed in pA reactions relative to the Glauber-scaled pp result [35–37] has been analyzed by Gyulassy and Vitev [8] in the framework of multiple initial state scatterings of partons in cold nuclei. Parton broadening due to random elastic scatterings is computable from [90]. The possibility of hard fluctuations along the projectile path leads to a power law tail of the k_T distribution that enhances $\langle \Delta k_T^2 \rangle$ beyond the naive Gaussian random walk result $\mu^2 L/\lambda$. For a high energy parton with transverse momentum p_T produced in a pA reaction $Q^2_{max} \sim p_T^2$. The Cronin effect is modeled by using

$$\langle k_T^2 \rangle_{pA} - \langle k_T^2 \rangle_{pp} \approx \frac{\mu^2}{\lambda} L_A \, \ln(1 + c\, p_T^2/\mu^2) \, . \tag{2.55}$$

Calculations are consistent with the energy, $\sqrt{s}$ = 27.4, 38.8 GeV, and p_T dependence observed in $p + W/p + Be$ reactions with parameters of the nuclear medium set as follows: $c/\mu^2 GeV$ = 0.18^2 and μ^2/λ = 0.05 GeV^2/fm. The corresponding transport coefficient and initial state mean energy loss per unit length using Eq. (10) are:

$$\hat{q} \simeq 0.1 \ \mathrm{GeV}^2/\mathrm{fm} \tag{2.56}$$

and

$$\left(-\frac{dE}{dz} \right)_{\mathrm{in}} \simeq 0.14 \ \mathrm{GeV/fm} \tag{2.57}$$

for a quark jet approaching the nucleus. The uncertainties in the above estimates are correlated with the uncertainties in the fragmentation functions.

3.1.5. The transport coefficient $\hat{q}$ for a hot and expanding medium

R. Baier and U.A. Wiedemann

Various data on DIS electron-nucleus and hadron-nucleus collisions indicate that the multiple scattering properties of cold nuclear matter can be described by a cold nuclear matter transport coefficient $\hat{q}|_{\mathrm{nuclear\ matter}} < 0.5$–1 GeV^2/fm. This information is compiled in the previous Section 3.1.4. For hot equilibrated matter, the estimated dependence of $\hat{q}$ on the energy density ϵ is shown in Fig. 2.12. For example, for a quark gluon plasma, the number density is translated into ϵ as $\rho(T) \sim T^3 \sim \epsilon^{3/4}$. A "smooth" increase of $\hat{q}$ with increasing ϵ is observed, such that

$$\hat{q}|_{\mathrm{QGP}} \gg \hat{q}|_{\mathrm{nuclear\ matter}} \, . \tag{2.58}$$

The QCD phase transition near $\epsilon \simeq 1 \ \mathrm{GeV/fm}^3$ [104] leaves no structure in the ϵ-dependence of $\hat{q}$. In contrast, plotting $\hat{q}$ versus temperature, one would find a sharp increase of the transport coefficient at the critical temperature.

What matters in practice for jet quenching in a heavy ion collision is *for how long* the transport coefficient takes values which are significantly above the cold nuclear matter reference value.

In nucleus–nucleus collisions at collider energies, the produced hard partons propagate through a rapidly expanding medium. The density of scattering centres and thus the transport coefficient $\hat{q}(\tau)$ is expected to reach a maximal value $\hat{q}_d$ around the plasma formation time τ_0, and then decreases with time τ rapidly due to the strong longitudinal and — to a lesser extent — transverse expansion,

$$\hat{q}(\tau) = \hat{q}_d \left(\frac{\tau_0}{\tau} \right)^{\alpha} \, . \tag{2.59}$$

Here, α = 0 characterizes the static medium discussed above. The value α = 1 corresponds to a one-dimensional, boost-invariant longitudinal expansion and approximates the findings of hydrodynamical

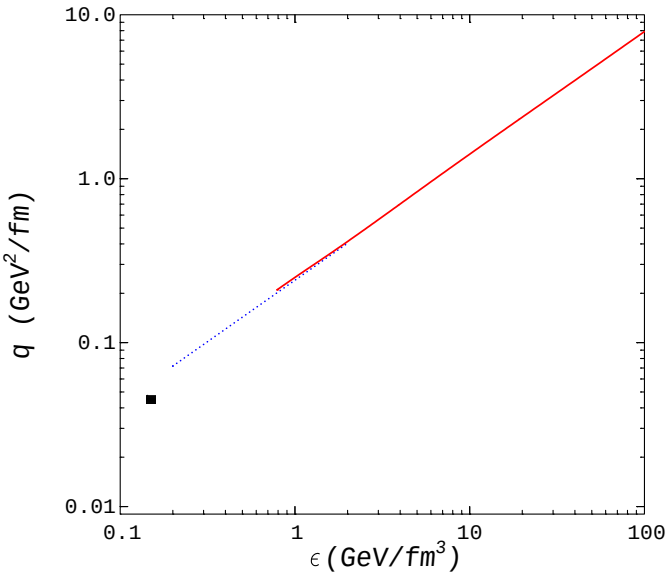

Fig. 2.12: Transport coefficient as a function of energy density for different media: cold, massless hot pion gas (dotted) and (ideal) QGP (solid curve). Figure is taken from Ref. [94].

simulations. The formation time τ_0 of the medium may be set by the inverse of the saturation scale $p_{\rm sat}$ [105] and is $\approx$ 0.2 fm/c at RHIC and $\approx$ 0.1 fm/c at LHC. Since the time difference between the formation of the hard parton and the formation of the medium bulk is irrelevant for the evaluation of the radiation spectrum Eq. (2.11), one can replace in Eq. (2.11) the production time τ_0 of the parton by 0.

For a dynamically evolving medium of the type Eq. (2.59), the path-integral Eq. (2.18) in Eq. (2.11) is the path integral of a 2-dimensional harmonic oscillator with time dependent (imaginary) frequency $\Omega^2(\tau) \equiv \frac{\hat{q}(\tau)}{i2\omega}$ and *mass* ω [106]. In this way, one can calculate the medium-induced gluon energy distribution (2.11) for a dynamically expanding medium [106]. The result is shown in Fig.2.13. The

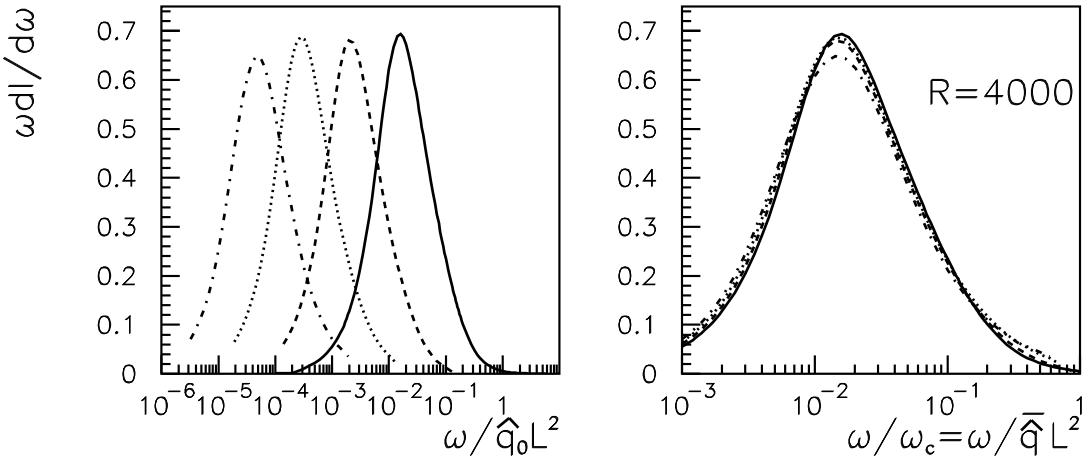

Fig. 2.13: LHS: The medium-induced gluon energy distribution for expanding collision regions (2.59) with expansion parameter α = 0, 0.5, 1.0 and 1.5. The value of the transport coefficient $\hat{q}_0$ is taken at initial time τ_0. RHS: The same gluon radiation spectrum with parameters rescaled according to (2.60). Figure is taken from Ref. [80].

radiation spectrum $\omega \frac{dI}{d\omega}$ satisfies a simple scaling law which relates the radiation spectrum of a dynamically expanding collision region to an equivalent static scenario. The linearly weighed line integral [7]

$$\overline{\hat{q}} = \frac{2}{L^2} \int_{\tau_0}^{\tau_0+L} d\tau \ (\tau - \tau_0) \ \hat{q}(\tau) \simeq \frac{2}{2-\alpha} \, \hat{q}(L) \qquad \text{for} \qquad \tau_0 \to 0 \,, \tag{2.60}$$

defines the transport coefficient of the equivalent static scenario. The linear weight in Eq. (2.60) implies that scattering centres which are further separated from the production point of the hard parton are more effective in leading to partonic energy loss. In contrast to earlier believe that parton energy loss is most sensitive to the hottest and densest initial stage of the collision, this implies for a dynamical expansion following Bjorken scaling (α = 1 in Eq. (2.59)) that all time scales contribute equally to the average transport coefficient. This makes partonic energy loss a valuable tool for the measurement of the quark-gluon plasma lifetime.

3.1.6. Angular dependence of radiative energy loss

R. Baier and U.A. Wiedemann

Hard jets, when produced in a heavy ion collision, will be measured in a typical calorimeter experiment within an angular cone of opening angle $\theta_{\rm cone}$. Here we summarize what is known about the angular dependence of medium-induced radiative energy loss.

Average energy loss. The mean energy loss due to gluons, induced by the medium and radiated outside the cone, has been investigated in [29] and more recently in [72, 80, 107]. The calculations are based on the integrated energy loss *outside* an angular cone of opening angle $\theta_{\rm cone}$,

$$\Delta E(\theta_{\rm cone}) = \int_0^\infty d\omega \int_{\theta_{\rm cone}}^\pi \frac{\omega dI}{d\omega d\theta} d\theta \,. \tag{2.61}$$

Figure 2.14 shows numerical results for this angular dependence obtained from evaluating Eq. (2.11) in the multiple soft scattering approximation with different values for the BDMPS transport coefficient $\hat{q}$ and the in-medium pathlength L. Here, $\frac{\Delta E}{E}(\Theta)$ does not decrease monotonously with increasing Θ but has a maximum at finite jet opening angle. The reason is that the radiative energy loss outside a cone angle Θ receives additional contributions from the Brownian $\mathbf{k}_T$-broadening of the standard DGLAP vacuum radiation,

$$\frac{1}{\mathbf{k}_T^2} \longrightarrow \frac{1}{(\mathbf{k}_T + \mathbf{q}_T)^2} \,. \tag{2.62}$$

This redistribution in transverse momentum space does not affect the total $\mathbf{k}_T$-integrated yield $\frac{\Delta E}{E}(\Theta = 0)$, but shows up as soon as a finite cone size is chosen. Thus, strictly speaking, the total $\mathbf{k}_T$-integrated radiative energy loss $\frac{\Delta E}{E}(\Theta = 0)$ is not the upper bound for the radiative energy loss outside a finite jet cone angle $\frac{\Delta E}{E}(\Theta)$.

To sum up, there is a simple physical reason for the non-monotonic behavior of $\Delta E(\theta_{\rm cone})$ as a function of the jet cone, namely the redistribution of the vacuum component of gluon radiation in transverse phase space. However, the size of the effect remains unclear. First, one may expect that the region of small $\theta_{\rm cone}$ is dominated by higher order QCD contributions which are not yet taken into account. Second, the effect shown in Fig. 2.14 is seen in the multiple soft scattering approximation of Eq. (2.11). However, in the single hard scattering approximation, $\Delta E(\theta_{\rm cone})$ decreases monotonously [80]. Irrespective of these differences for small opening angle, it is worth emphasizing that both approximations agree quantitatively for $\theta_{\rm cone} > 10^\circ$ [80].

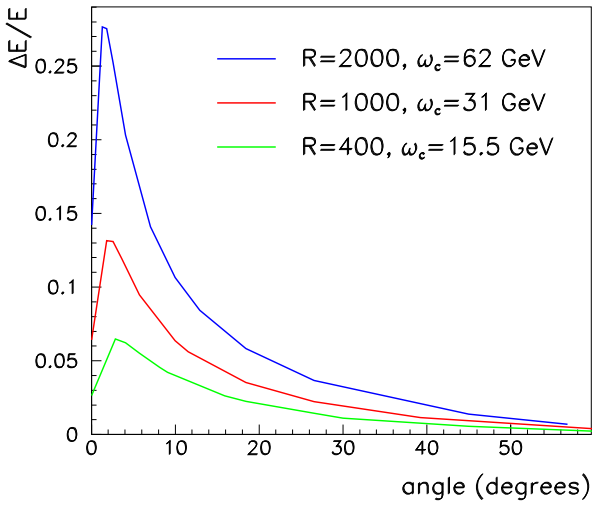

Fig. 2.14: The fraction of the total radiative energy loss $\Delta E/E$ emitted outside a jet cone of fi xed angle Θ. This calculation is for a jet of total energy E = 100 GeV and $R = \frac{1}{2}\hat{q}\,L^3, \omega_c = \hat{q}\,L^2$.

Universality of angular dependence. The integrated mean loss $\Delta E(\theta_{\rm cone})$, normalized to $\Delta E \equiv \Delta E(\theta_{\rm cone} = 0)$, is defined by

$$R(\theta_{\rm cone}) = \frac{\Delta E(\theta_{\rm cone})}{\Delta E} \tag{2.63}$$

with $R(\theta_{\rm cone} = 0)$ = 1. In the BDMPS limiting case, the total energy loss ΔE depends only on the characteristic gluon energy, see Eq. (2.7). In this limit, it was observed that the ratio $R(\theta_{\rm cone})$ depends on a single dimensionless variable, which includes all the medium dependent parameters, namely [29]

$$R(\theta_{\rm cone}) = R(c(L)\theta_{\rm cone})\,, \tag{2.64}$$

where

$$c^2(L) = \frac{N_c}{2C_F}\hat{q}\,(L/2)^3\,. \tag{2.65}$$

The typical dependence on $\theta_{\rm cone}$ is shown in Fig. 2.15. When comparing hot and cold QCD matter we recall that for fixed in-medium pathlength L,

$$c(L)\Big|_{\rm HOT} \gg c(L)\Big|_{\rm COLD}\,. \tag{2.66}$$

This is a consequence of the temperature dependence of the BDMPS transport coefficient $\hat{q}$. $R(\theta_{\rm cone})$ is also universal in the sense that it is the same for an energetic quark and for an energetic gluon jet. In a recent study [80], the ratio $R(\theta_{\rm cone})$ was calculated in the presence of kinematic constraints on the transverse phase space. Small deviations from the universal behaviour in Eq. (2.64) were observed, but for all practical purposes these are negligible.

3.2. Multiple Gluon Emission and Quenching Weights

R. Baier and U.A. Wiedemann

Irrespective of the number of additionally radiated gluons, what matters for the medium modification of hadronic observables is how much *additional* energy ΔE is radiated off a hard parton. In this Section, we first discuss the so called quenching weight which is the probability distribution $P(\Delta E)$ of the additional medium-induced energy loss. For independent gluon emission, this probability is the

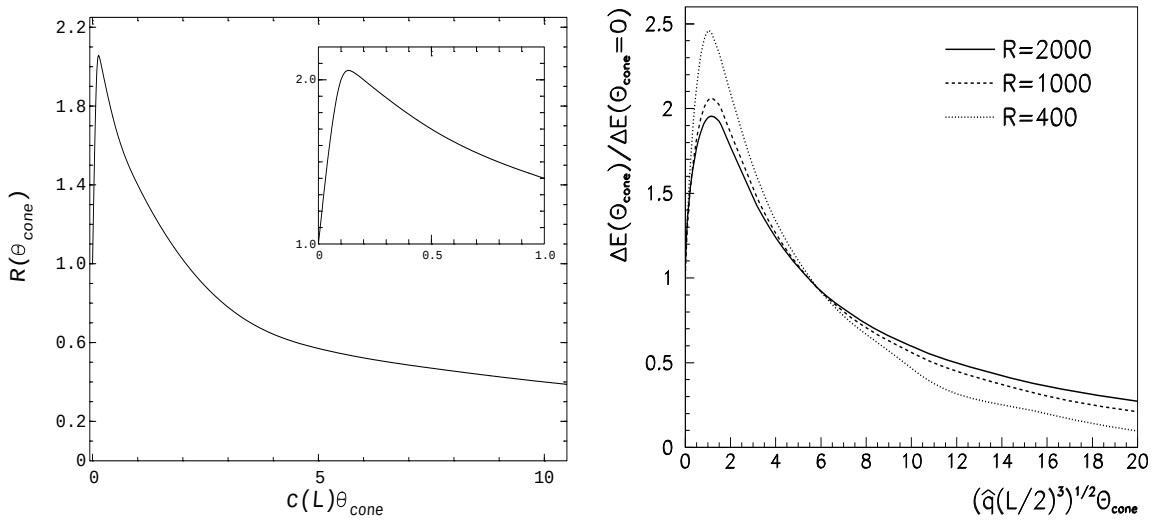

Fig. 2.15: The mean energy loss radiated outside an opening cone $\theta_{\rm cone}$ normalized to the total average energy loss. LHS: in the BDMS calculation [107], the ratio is universal, depending on a single dimensionless variable only. RHS: if the kinematic constraints in transverse phase space are taken into account, deviations from the universal behaviour remain small [80].

normalized sum of the emission probabilities for an arbitrary number of n gluons which carry away a total energy ΔE [92]:

$$P(\Delta E) = \sum_{n=0}^{\infty} \frac{1}{n!} \left[\prod_{i=1}^{n} \int d\omega_i \frac{dI(\omega_i)}{d\omega} \right] \delta \left(\Delta E - \sum_{i=1}^{n} \omega_i \right) e^{-\int d\omega \frac{dI}{d\omega}} . \tag{2.67}$$

In general, the quenching weight, Eq. (2.67), has a discrete and a continuous part, [7]

$$P(\Delta E) = p_0 \, \delta(\Delta E) + p(\Delta E) . \tag{2.68}$$

The discrete weight p_0 emerges as a consequence of a finite mean free path. It determines the probability that no additional gluon is emitted due to in-medium scattering and hence no medium-induced energy loss occurs.

In order to determine the discrete and continuous part of Eq. (2.68), it is convenient to rewrite Eq. (2.67) as a Laplace transformation [92]

$$P(\Delta E) = \int_C \frac{d\nu}{2\pi i} \, \mathcal{P}(\nu) \, e^{\nu \Delta E} , \tag{2.69}$$

$$\mathcal{P}(\nu) = \exp \left[- \int_0^{\infty} d\omega \, \frac{dI(\omega)}{d\omega} \, \left(1 - e^{-\nu \, \omega} \right) \right] . \tag{2.70}$$

Here, the contour C runs along the imaginary axis with $\mathrm{Re}\nu$ = 0.

For the further discussion, it is useful to treat the medium-induced gluon energy distribution $\omega \frac{dI}{d\omega}$ in Eq. (2.11) explicitly as the medium modification of a 'vacuum' distribution [80]

$$\omega \frac{dI^{(tot)}}{d\omega} = \omega \frac{dI^{(vac)}}{d\omega} + \omega \frac{dI}{d\omega} . \tag{2.71}$$

From the Laplace transform Eq. (2.69), one finds the total probability

$$P^{(tot)}(\Delta E) = \int_0^{\infty} d\bar{E} \, P(\Delta E - \bar{E}) \, P^{(vac)}(\bar{E}) . \tag{2.72}$$

This probability $P^{(tot)}(\Delta E)$ is normalized to unity and it is positive definite. In contrast, the medium-induced modification of this probability, $P(\Delta E)$, is a generalized probability. It can take negative values for some range in ΔE, as long as its normalization is unity,

$$\int_0^\infty d\bar{E}\, P(\bar{E}) = p_0 + \int_0^\infty d\bar{E}\, p(\bar{E}) = 1\,. \tag{2.73}$$

We now discuss separately the properties of the discrete contribution p_0 and the continuous one $p(\bar{E})$.

Discrete part of the quenching weight. The discrete part of the quenching weight can be expressed in terms of the total gluon multiplicity,

$$p_0 = \lim_{\nu\to\infty} \mathcal{P}(\nu) = \exp\left[-N(\omega=0)\right]\,, \tag{2.74}$$

where the multiplicity $N(\omega)$ of gluons with energy larger than ω emerges by partially integrating the exponent of (2.70),

$$N(\omega) \equiv \int_\omega^\infty d\omega'\, \frac{dI(\omega')}{d\omega'}\,. \tag{2.75}$$

For the limiting case of infinite in-medium pathlength, the total multiplicity $N(\omega)$ diverges and the discrete part vanishes. In general, however, p_0 is finite. A typical dependence of p_0 on model parameters is shown in Fig. 2.16 for the radiation spectrum calculated in the multiple soft scattering limit. A qualitatively similar behaviour is found in the opacity expansion. Remarkably, p_0 can exceed unity for some parameter range, since the medium modification $\omega\frac{dI}{d\omega}$ to the radiation spectrum Eq. (2.71) can be negative. The value $p_0 > 1$ then compensates a predominantly negative continuous part $p(\Delta E)$ and satisfies the normalization Eq. (2.73). It indicates a phase space region at very small transverse momentum, into which *less* gluons are emitted in the medium than in the vacuum. This effect is more pronounced for gluons than for quarks.

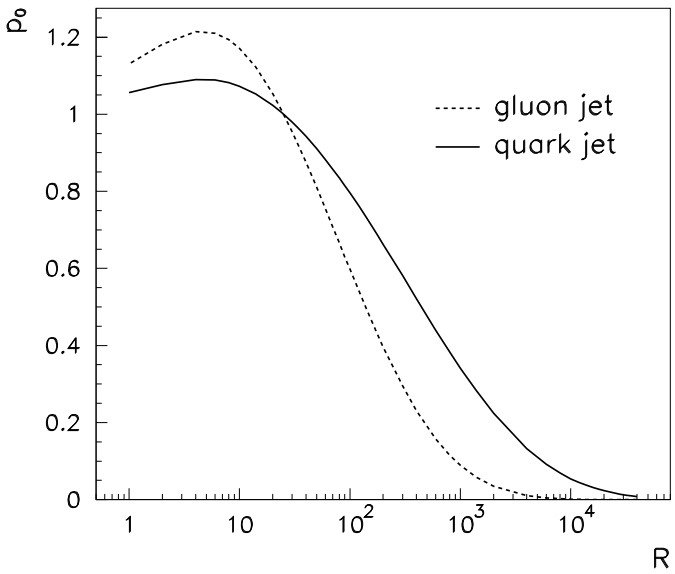

Fig. 2.16: The discrete part p_0 of the quenching weight calculated in the multiple soft scattering limit as a function of R. Figure taken from Ref. [80].

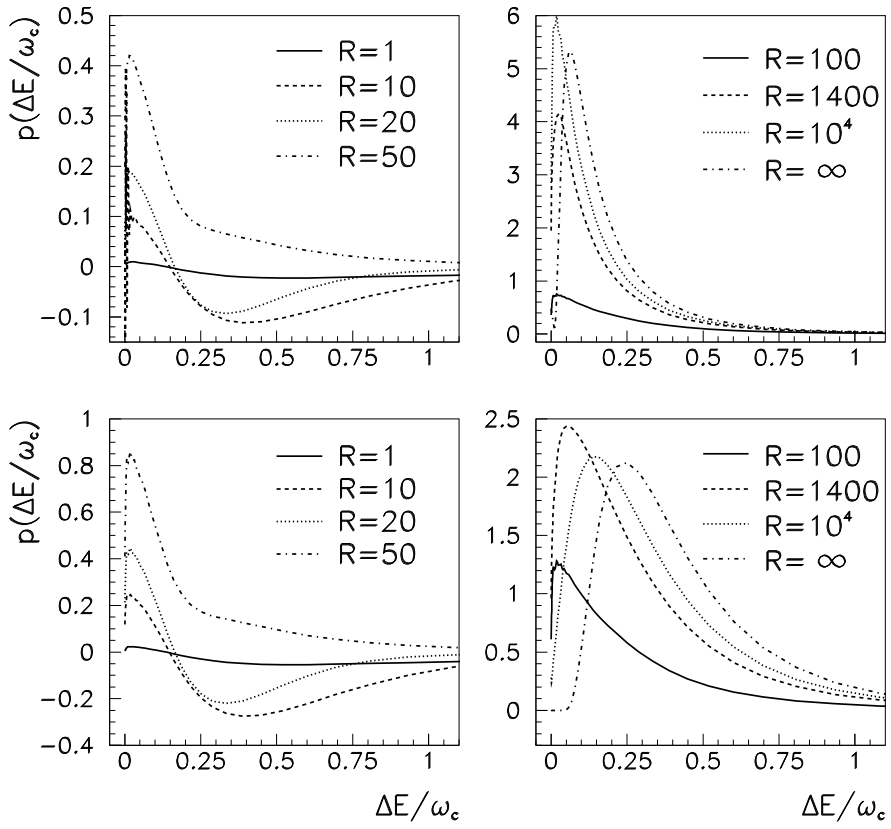

Fig. 2.17: The continuous part of the quenching weight (2.68), calculated in the multiple soft scattering limit for a hard quark (upper row) or hard gluon (lower row). Figure is taken from Ref. [80].

Continuous part of the quenching weight. The continuous part $p(\Delta E)$ of the probability distribution (2.68) is shown in Fig. 2.17 calculated in the multiple soft scattering limit. In the opacity expansion, it looks qualitatively similar. With increasing density of scattering centres (i.e. increasing $R = \frac{1}{2}\hat{q}L^3$) the probability of loosing a significant energy fraction ΔE increases. Also, since the interaction between partonic projectile and medium are larger for a hard gluon than a hard quark, the energy loss is larger for gluons. This can be seen in Fig 2.17 from the larger width of $p(\Delta E)$ for the gluonic case. Finally, as expected from the normalization condition Eq. (2.73), the continuous part $p(\Delta E)$ shows predominantly negative contributions for the parameter range for which the discrete weight p_0 exceeds unity.

In the multiple soft scattering limit and for infinite pathlength, the quenching weight was found to be fit very well by a two-parameter log-normal distribution [93]. Analytically, an estimate of the quenching weight can be obtained [92] in the limit $R \to \infty$ from the small-ω approximation $\omega \frac{dI}{d\omega} \propto \frac{1}{\sqrt{\omega}}$ in the multiple scattering limit

$$P^{\text{approx}}_{\text{BDMS}}(\epsilon) = \sqrt{\frac{a}{\epsilon^3}}\, \exp\left[-\frac{\pi\, a}{\epsilon}\right], \qquad \text{where} \qquad a = \frac{2\,\alpha_s^2\, C_R^2}{\pi^2}\omega_c\,. \tag{2.76}$$

This approximation is known to capture [7] the rough shape of the probability distribution for large system size, but it has an unphysical large ϵ-tail with infinite first moment $\int d\epsilon\, \epsilon\, P^{\text{approx}}_{\text{BDMS}}(\epsilon)$. Remarkably, Equation (2.76) provides a semi-quantitative understanding of the degree of partonic energy loss shown in Fig. 2.17. In particular, comparing for $R \to \infty$ the maxima of the curves in Fig. 2.17 for quarks and gluons, one finds a displacement by a factor ≈ 5. This agrees well with the square of the relative Casimir factors $(C_A/C_F)^2$ by which the maximum of $\epsilon P^{\text{approx}}_{\text{BDMS}}(\epsilon)$ changes.

3.3. Collisional Versus Radiative Energy Loss

I.P. Lokhtin and A.M. Snigirev

The collisional energy loss due to elastic scattering with high-momentum transfer have been originally estimated by Bjorken in [57], and recalculated later in [108, 109] taking also into account the loss with low-momentum transfer dominated by the interactions with plasma collective modes. The method for quantum field-theoretic calculating energy loss in the low exchange momentum region of the collisions (screening effect in the plasma) have been developed by Braaten and Pisarski [83, 110, 111]. It allows one to calculate the hard thermal loop (HTL) corrections to the propagator of the exchanged gluon in the $Qq \to Qq$ and the $Qg \to Qg$ processes.

The average collisional energy loss per mean free path λ can be written as [57]

$$\frac{dE_{\rm coll}}{dz} = \frac{\Delta E_{\rm coll}}{\lambda} = \int d^3k\, \rho(k) \int dt \frac{d\sigma}{dt}\, \frac{t}{2k} \simeq \frac{1}{4T\sigma\,\lambda} \int\limits_{\mu_D^2}^{3TE/2} dt \frac{d\sigma}{dt} t\,. \tag{2.77}$$

Here, $\lambda = 1/\int d^3k \rho(k)\sigma$, and $\rho(k)$ defines the thermal density of partonic scatterers (the sum over which is implicit). The factor $\frac{t}{2k}$ denotes the energy transfer per scattering times the flux factor of the incident participating partons [4]. The dominant contribution to the differential cross section $d\sigma/dt$ for scattering of a parton with energy E off the 'thermal' partons with energy $3T \ll E$ at temperature T is taken to be the LO perturbative scattering cross section [57]

$$\frac{d\sigma}{dt} \cong \frac{2\pi\alpha_s^2(t)}{t^2}\,. \tag{2.78}$$

The integrated parton scattering cross section σ is regularized by the Debye screening mass squared $\mu_D^2 \cong 4\pi\alpha_s T^2(1 + N_f/6)$.

There are marked differences between collisional and radiative energy loss. For collisional energy loss, the scattering centres act incoherently. The value ΔE_{coll} is independent of in-medium path length, and it depends only logarithmically on the initial parton energy. It is determined mainly by the medium temperature [57]

$$\frac{dE_{\rm coll}}{dz} \propto \alpha_s^2\, T^2\, \ln E/T\,. \tag{2.79}$$

The dependence of the total collisional energy loss on in-medium pathlength can be weaker than linear for an expanding medium and it is linear for a static one.

The angular-integrated radiative energy loss of a high energy projectile parton is known to dominate over the collisional energy loss by up to an order of magnitude [51, 112, 113]. However, the angular dependence of the lost (i.e. redistributed) energy is very different for both mechanisms. With increasing parton energy, the maximum of the angular distribution of bremsstrahlung gluons shifts towards the direction of the parent parton. This means that measuring the jet energy as a sum of the energies of final hadrons moving inside an angular cone with a given finite size θ_0 will allow the bulk of the gluon radiation to belong to the jet and thus the major fraction of the initial parton energy to be reconstructed. Therefore, the medium-induced radiation mainly softens the particle energy distributions inside the jet, and increases the multiplicity of secondary particles. Only to a lesser degree does it affect the total jet energy. It is important to notice that the coherent Landau-Pomeranchuk-Migdal radiation induces a strong dependence of the radiative energy loss of a jet (but not a leading parton) on the jet angular cone size [71–73, 106, 114].

On the other hand, collisional energy loss turns out to be practically independent of jet cone size, because the bulk of 'thermal' particles knocked out of the dense matter by elastic scatterings fly away in almost transverse direction relative to the jet axis [114]. In fact, in relativistic kinematics,

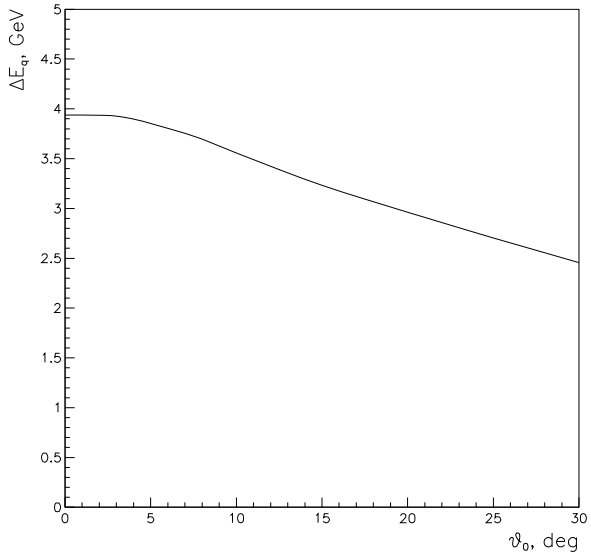

Fig. 2.18: Angular dependence of the collisional energy loss for a 100 GeV quark-initiated jet, according to Ref. [114]. In comparison to the radiative energy loss shown in Fig. 2.14, the contribution is relatively small at small angles, but cannot be neglected at large angles.

$E \gg m_0 = 3\,T$, in the rest system of the target with effective mass m_0 we get the following estimate for the transverse $p_T^{t,i}$ and longitudinal $p_L^{t,i}$ momenta of the incident and "thermal" particles: $p_T^t \simeq \sqrt{t}$, $p_L^t \simeq t/2m_0$; $p_T^i \simeq -\sqrt{t}$, $p_L^i \simeq E - t/2m_0$. Scattering angle θ_i of the incident parton vanishes in the relativistic limit, $\tan\theta_i = p_T^i/p_L^i \simeq \sqrt{t}/E \to 0$. The scattering angle θ_t of a struck "thermal" particle with respect to the initial direction of the fast parton can be estimated as $\tan\theta_t = p_T^t/p_L^t \simeq 2m_0/\sqrt{t}$. The minimal and maximal values of $\tan\theta_t$ are $\tan\theta_t^{max} \simeq 2m_0/\mu_D$ and $\tan\theta_t^{min} \simeq 2m_0/\sqrt{0.5 m_0 E}$ respectively. It is straightforward to evaluate the average $\langle\tan\theta_t\rangle$ as [114]

$$\langle\tan\theta_t\rangle = \left\langle \frac{2m_0}{\sqrt{t}} \right\rangle \simeq \frac{6T}{\sigma} \int\limits_{\mu_D^2}^{3TE/2} dt \frac{d\sigma}{dt} \frac{1}{\sqrt{t}}\,. \tag{2.80}$$

Neglecting a weak $\alpha_s(t)$ dependence we obtain $\langle\tan\theta_t\rangle \simeq \frac{2}{3}\tan\theta_t^{max} \simeq 4m_0/3\mu_D$. Substituting μ_D, we arrive at $< \theta_t > \sim 60^0$ for $T > 200$ MeV. This value exceeds typical cone sizes $\theta_0 \sim 10^0 - 30^0$ used to experimentally define hadronic jets. This means that the major part of 'thermal' particles will fly outside the cone of the jet and thus cause the 'jet energy loss'. This study indicates that radiative energy loss indeed dominates the medium-dependence of jets for small cone opening angles θ_0. However, collisional energy loss may have a significant contribution to jet quenching for larger cone opening angles θ_0, see Fig. 2.18.

Here, we have considered only massless partons propagating through a dense QCD-matter. Although a full description of the coherent gluon radiation from a massive colour charge is still lacking, finite quark mass effects are expected to lead to a relative suppression of medium-induced radiation of heavy (especially b) quarks [85]. In this case the influence of collisional energy loss on experimental observables of 'heavy quark quenching' (such as high-mass dileptons and secondary charmonium production) can be comparable with the effect of medium-induced radiation [114], see Section 3.4.4.

3.4. Observable Consequences of Radiative Energy Loss

3.4.1. E_T-Distributions and p_T-spectra: quenching weights

R. Baier and U.A. Wiedemann

Assume that a hard parton looses an additional energy fraction ΔE while escaping the collision region. The medium-dependence of the corresponding inclusive transverse momentum spectra can be characterized in terms of the quenching factor Q [92]

$$\begin{aligned} Q(p_T) &= \frac{d\sigma^{\rm med}(p_T)/dp_T^2}{d\sigma^{\rm vac}(p_T)/dp_T^2} = \int d\Delta E\, P(\Delta E) \left(\frac{d\sigma^{\rm vac}(p_T+\Delta E)/dp_T^2}{d\sigma^{\rm vac}(p_T)/dp_T^2} \right) \\ &\simeq \int d\Delta E\, P(\Delta E) \left(\frac{p_T}{p_T+\Delta E} \right)^n , \end{aligned} \tag{2.81}$$

where $P(\Delta E)$ is the quenching weight given in Eq. (2.67). Here, the last line is obtained by assuming a powerlaw fall-off of the p_T-spectrum. The effective power n depends in general on energy and p_T. It is $n \simeq 7$ for the kinematic range relevant for RHIC, and it is smaller for LHC. Alternatively, instead of the quenching factor in Eq. (2.81), the medium modification of hadronic transverse momentum spectra is often characterized by a shift factor $S(p_T)$,

$$\frac{d\sigma^{\rm med}(p_T)}{dp_T^2} \simeq \frac{d\sigma^{\rm vac}(p_T+S(p_T))}{dp_T^2} , \tag{2.82}$$

which is related to $Q(p_T)$ by

$$Q(p_T) = \exp\left\{ -\frac{n}{p_T} \cdot S(p_T) \right\} . \tag{2.83}$$

Most importantly, since the hadronic spectrum shows a strong powerlaw decrease, what matters for the suppression is not the average energy loss $\langle \Delta E \rangle$ but the least energy loss with which a hard parton is likely to get away. One concludes that $S(p_T) < \langle \Delta E \rangle$ and depends on transverse momentum [92].

Figure 2.19 shows a calculation of the quenching factor, Eq. (2.81), in the multiple soft scattering limit. A qualitatively similar result is obtained in the opacity expansion. In general, quenching weights increase monotonically with p_T since the medium-induced gluon radiation is independent of the total projectile energy for sufficiently high energies. At very low transverse momenta, the calculation based on Eq. (2.11) is not reliable and the interpretation of the medium modification of hadronic spectra in nucleus–nucleus collisions will require additional input (e.g. modifications due to the Cronin effect). Figure 2.19 suggests, however, that hadronic spectra at transverse momenta $p_T > 10$ GeV, can be suppressed significantly due to partonic final state rescattering.

Finally, Fig. 2.19 allows to comment on the sensitivity of the perturbative calculation of $\omega \frac{dI}{d\omega}$ on uncontrolled non-perturbative soft physics. The gluon energy distribution in Eq. (2.11) allows in principle for the emission of arbitrarily soft gluons. It is clear, however, that the calculation cannot be reliable in this soft regime. To quantify the sensitivity of the calculation to the low momentum region, Baier et al. [92] introduced a sharp cut-off on the $R \to \infty$ gluon energy distribution which was varied between $\omega_{\rm cut}$ = 0 and $\omega_{\rm cut}$ = 500 MeV. However, phase space constraints (i.e. finite R) deplete the gluon radiation spectrum in the soft region, see Fig. 2.6. As seen in Fig. 2.19, this decreases significantly the sensitivity of quenching factors to the uncontrolled infrared properties of the radiation spectrum [80].

3.4.2. Medium-modified fragmentation functions

C.A. Salgado

In proton–proton collisions, the inclusive production of a hadron h of high enough p_T can be described by the factorization (LO) formula (2.1). Both the parton distribution functions and the fragmentation functions entering this expression are obtained from global fits to experimental data. The

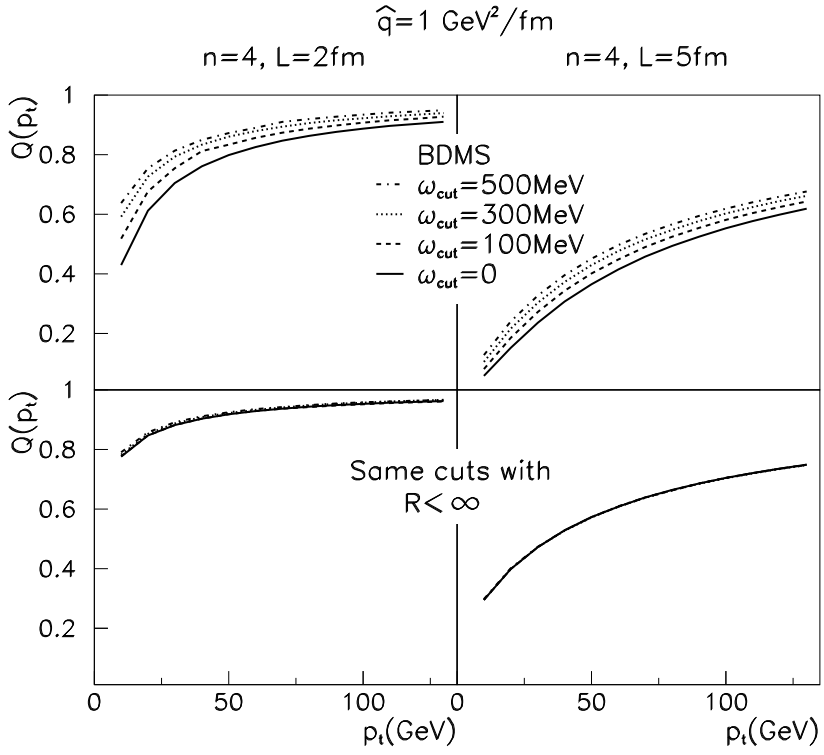

Fig. 2.19: The quenching factor, Eq. (2.81), calculated in the multiple soft scattering limit. Upper row: calculation in the $R \to \infty$-limit but with a variable sharp cut-off on the infrared part of the gluon energy distribution. Lower row: the same calculation is insensitive to infrared contributions if the finite kinematic constraint $R = \omega_c L < \infty$ is included. Figure is taken from Ref. [80].

procedure is well known: an initial condition containing all the non-perturbative information is evolved, by DGLAP equations, to scales Q^2 and μ_F^2 respectively and then fitted, in a recursive procedure, to available data. A third scale, the renormalization scale μ_R^2, is contained in the perturbative cross section $d\sigma^{ij\to k}$ through the running of $\alpha_S(\mu_R^2)$. Equation (2.1) leads to a fair description of the shape of high-p_T hadronic spectra while the normalization has to be adjusted by an energy-dependent K-factor (see Ref. [44]). Also to NLO, the disagreement between theory and experiment lies essentially in an albeit reduced normalization factor [115]. However, the theoretical K-factor σ^{NLO}/σ^{LO} shows, some p_T-dependence.

For proton–nucleus or nucleus–nucleus collisions, Eq. (2.1) is also expected to work, though, due to the enhanced power corrections in the nucleus, the range of validity would be for p_T larger than in proton–proton. Apart from geometrical factors, the generalization to pA or AA collisions needs of nuclear PDF and medium-modified FF. This *medium* that modifies the parton fragmentation could be the nucleus itself (*cold nuclear matter*) in both pA and AA collisions and/or eventually the produced high-dense state (*hot and dense medium*) in AA collisions. The nuclear PDF have been studied in several approaches and global fits similar to the ones for the proton are available (see the pA section in this Yellow Report for the state-of-the-art in the field). The case for the FF is less clear, ideally one should perform a new global fit for these medium-FF using modified evolution equations. These new evolution equations would take care of the evolution, in the medium, of a highly virtual parton to the final hadrons. Whether something like this could be obtain for (factorized) leading twist FF, and how the evolution equations would be modified by the medium, is still very unclear. Finite temperature modifications to DGLAP evolution have been calculated in [116] in the framework of a thermal field theory. The modified splitting functions depend in this case on the temperature of the medium. However, multiple scattering

effects as induced radiation or interference (LPM) are not included. There has been an attempt of constructing medium-modified fragmentation functions from a twist expansion in Refs. [6, 117–119]. In these references, the medium-modifications of the FF are given by one additional collision of the parton with the medium (the first term in an opacity expansion). These terms are of higher-twist nature. On the other hand, the medium induced radiation that could eventually lead to modified leading-twist evolution equations including multiple scattering effects has been computed in several approximations [61, 73]. In summary, a full leading-twist DGLAP-like evolution containing all the relevant features of the problems is still missing. Most of the present approaches using leading twist FF rely on a model proposed in Ref. [120]. The medium-modified fragmentation functions are, in this model, given by

$$D_{k\to h}^{(\mathrm{med})}(z,\mu_F^2) = \int_0^{1-z} d\epsilon\, P_E(\epsilon)\, \frac{1}{1-\epsilon}\, D_{k\to h}(\frac{z}{1-\epsilon},\mu_F^2)\,. \tag{2.84}$$

The picture is the following. The high energetic quark or gluon loses some fraction ϵ of its energy when traveling through the medium and then fragments in the vacuum with the normal vacuum FF, $D_{k\to h}(z/1-\epsilon,\mu_F^2)$, with the corresponding shifted momentum fraction. Any modification of the virtuality dependence of the FF by the medium is neglected. Also, the hadronized remnants of the medium-induced soft radiation are neglected in the definition of (2.84). However, these remnants are expected to be soft, and their inclusion would thus amount to an additional contribution to $D_{k\to h}^{(\mathrm{med})}(z,\mu_F^2)$ for $z<0.1$ say. The only ingredient needed in Eq. (2.84) is the probability distribution $P_E(\epsilon)$ for a parton of energy E to lose a fraction ϵ of this energy. These quenching weights are normally computed in the independent gluon emission approximation (2.67) with $P(\Delta E) = P_E(\epsilon = \Delta E/E)/E$.

Another approximation that has been taken for the quenching weight is just

$$P_E(\epsilon) = \delta\left(\epsilon - \frac{\Delta E}{E}\right)\,. \tag{2.85}$$

It has been argued that using Eq. (2.85) produces a much stronger effect due to the rapid p_T-dependence of the production spectrum (or equivalently to the rapid z-dependence of the FF). This is clearly the case for the multiple soft scattering approximation for which the quenching weight has a sharp maximum. In the hard scattering opacity expansion, the longer tails of the distributions makes the difference between using Eqs. (2.67) and (2.85) smaller.

In Fig. 2.20, medium-modified quark to pion fragmentation functions are plotted for different media [7, 80]. They are calculated from Eq. (2.84) using the multiple scattering approximation for the quenching weights and the LO KKP [121] parametrization of $D_{h/q}(z,Q^2)$. For this calculation, the virtuality Q of $D_{h/q}(z,Q^2)$ is identified with the (transverse) initial energy E_q of the parton. This is justified since E_q and Q are of the same order, and $D_{h/q}(z,Q^2)$ has a weak logarithmic Q-dependence while medium-induced effects change as a function of $\epsilon = \frac{\Delta E}{Q} \approx O(\frac{1}{Q})$. For a collision region expanding according to Bjorken scaling, the transport coefficient can be related to the initial gluon rapidity density [62, 81].

$$R = \frac{1}{2}\,\hat{q}\,L^3 = \frac{L^2}{R_A^2}\,\frac{dN^g}{dy}\,, \tag{2.86}$$

That is what is done in Fig. 2.20. Interestingly, Eq. (2.86) indicates how partonic energy loss changes with the particle multiplicity in nucleus–nucleus collisions. This allows to extrapolate parton energy loss effects from RHIC to LHC energies [7].

In principle, the medium modified fragmentation function should be convoluted with the hard partonic cross section and parton distribution functions in order to determine the medium modified hadronic spectrum. For illustration, however, one may exploit that hadronic cross sections weigh $D_{h/q}^{(\mathrm{med})}(z,Q^2)$ by the partonic cross section $d\sigma^q/dp_\perp^2 \sim 1/p_\perp^{n(\sqrt{s},p_\perp)}$ and thus effectively test $z^{n(\sqrt{s},p_\perp)} D_{h/q}^{(\mathrm{med})}(z,Q^2)$ [44]. The value $n = 6$ which characterizes [44] the power law for typical

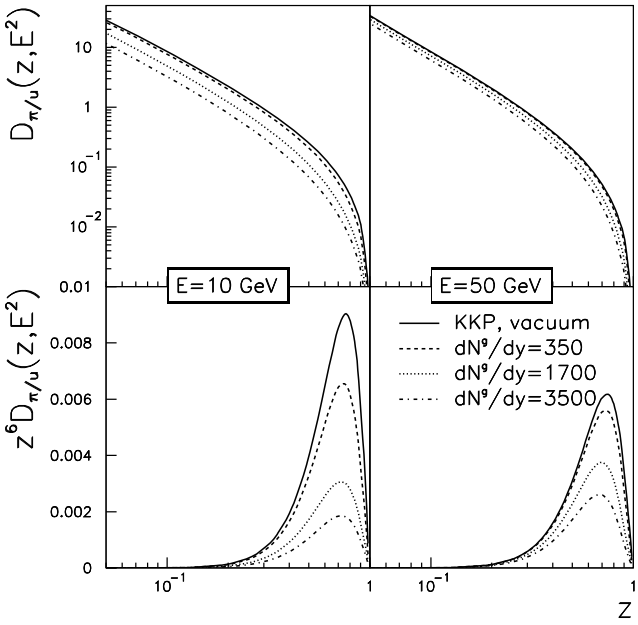

Fig. 2.20: Medium-modified fragmentation functions for media of different densities (upper two panels). Multiplying these FF by z^6 (lower two panels) the position of the maximum gives the relevant z values in the integration of Eq. (2.1). The vacuum fragmentation functions are from Ref. [121].

values at RHIC ($\sqrt{s}$ = 200 GeV and $p_T \sim 10$ GeV). Then, the position of the maximum $z_{\max}$ of $z^6 D_{h/q}^{(\mathrm{med})}(z,Q^2)$ corresponds to the most likely energy fraction $z_{\max}E_q$ of the leading hadron. And the suppression around its maximum translates into a corresponding relative suppression of this contribution to the high-p_T hadronic spectrum at $p_T \sim z_{\max}E_q$. In general, the suppression of hadronic spectra extracted in this way is in rough agreement with calculations of the quenching factor Eq. (2.81).

Medium-modified fragmentation functions have been applied to lepton–nucleus and nucleus–nucleus collisions in this framework. The idea is to compare the strength of the effect in both systems. In this way, information about the relative densities of the media could be obtained. In this Section we summarize the results obtained up to now for both lepton–nucleus and AA collisions.

In the case of cold nuclear matter, experiments of lepton–nucleus scattering measure the inclusive particle cross section for different nuclei. In the kinematic regime of present experiments, the valence quarks give the dominant contribution, so, the ratio of cross sections give direct information about the ratio of FF:

$$R_A^h(z,\nu) = \frac{d\sigma_A^h(z,\nu)/d\nu\, dz}{d\sigma_D^h(z,\nu)/d\nu\, dz} \simeq \frac{D_q^h(z,Q^2,A)}{D_q^h(z,Q^2,D)}\,, \tag{2.87}$$

where ν is the energy of the virtual photon. HERMES experiment has measured the ratios Eq. (2.87) for different nuclei [122]. These data has been studied in [6] in the the twist-expansion previously mentioned and in [123] using the BDMPS [61, 62] gluon radiation spectrum for the energy loss. See Figs. 2.21 and 2.22 for the comparison with data. Though the two approximations are rather different, it is interesting that they both result in a similar average energy loss $dE/dL \sim 0.5$ GeV/fm.

In the case of nucleus–nucleus collisions, the produced medium is expected to be the main source of energy loss for particles produced in the central rapidity region. The new data from RHIC has been used to fix the amount of energy loss needed to reproduce the observed suppression of particles produced at large p_T. The size of the effect is compatible with this *jet quenching* explanation. The fact that the

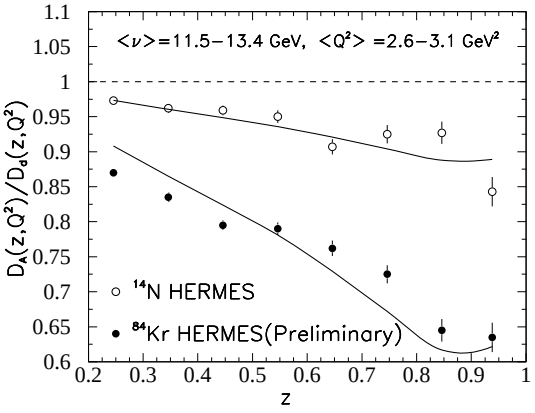

Fig. 2.21: Ratios of medium-induced FF over those for vacuum computed in the twist expansion from Ref. [6]

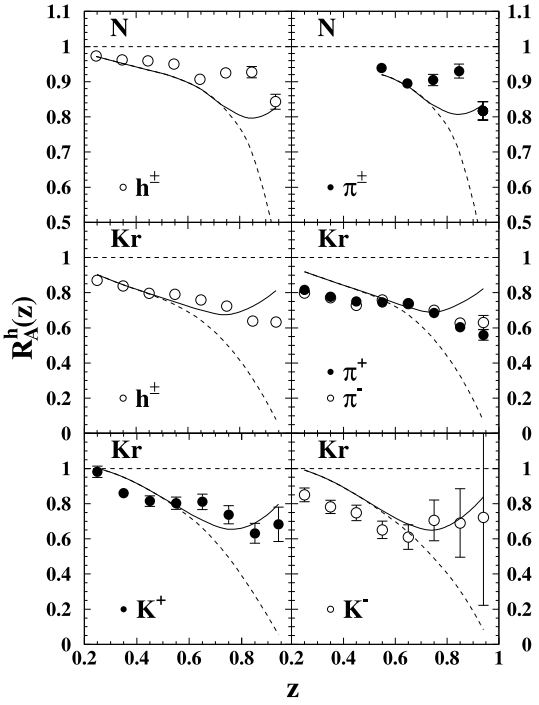

Fig. 2.22: Theoretical calculations with (solid lines) and without (dashed lines) finite formation times are computed [123] in the BDMPS formalism with $\hat{q}$ = 0.72 GeV/fm^2. This corresponds to $\Delta E/L \sim 0.6$ GeV/fm. (See Ref. [123] for details.)

transport coefficient is proportional to the density of the medium allows to estimate the effect for the LHC. This can be read out from the lower two panels in Fig. 2.20. For instance, the suppression for 10 GeV quarks in a medium of 350 gluons per unit rapidity is similar to the one for 50 GeV quarks in a medium of five time larger density. In Fig. 2.23 the suppression using medium-modified fragmentation functions is compared with the experimental data from PHENIX [124].

3.4.3. Nuclear Modification Factors

I. Vitev

Dynamical nuclear effects in pA and AA reactions are detectable through the nuclear modification ratio

$$R_{BA}(p_T) = \begin{cases} \dfrac{d\sigma^{pA}}{dyd^2p_T} \Big/ \dfrac{A\; d\sigma^{pp}}{dyd^2p_T} & \text{in pA} \\ \dfrac{dN^{AA}(b)}{dyd^2p_T} \Big/ \dfrac{T_{AA}(b)\; d\sigma^{pp}}{dyd^2p_T} & \text{in AA} \end{cases} , \tag{2.88}$$

where A and $T_{AA}(b) = \int d^2\mathbf{r}\, T_A(\mathbf{r}) T_B(\mathbf{r}-\mathbf{b})$ in terms of nuclear thickness functions $T_A(r) = \int dz\, \rho_A(\mathbf{r}, z)$ are the corresponding Glauber scaling factors [125] of $d\sigma^{pp}$. We note that in $R_{BA}(p_T)$ the uncertainty associated with the K_{NLO} factors, discussed in the previous Sections, drops out. The reference calculations that follow include shadowing/antishadowing/EMC-effect (here referred to as 'shadowing'), the Cronin effect, and the non-abelian energy loss of jets. The scale dependent nuclear PDFs read: $f_{\alpha/A}(x, Q^2) = S_{\alpha/A}(x, Q^2)\, (Z/A\, f_{\alpha/p}(x, Q^2) + N/A\, f_{\alpha/n}(x, Q^2))$, where we take the isospin effects on average and the EKS'98 parameterization [15] of the shadowing functions $S_{\alpha/A}(x, Q^2)$. Initial state multiple elastic scatterings have been discussed in [23,90,97]. From [90] the transverse momentum distribution of partons that have undergone an average $\chi = L/\lambda$ incoherent interactions in the medium can be evaluated exactly for any initial flux $dN^i(\mathbf{p})$:

$$\frac{dN^f(\mathbf{p})}{d^2\mathbf{p}} = \sum_{n=0}^{\infty} e^{-\chi} \frac{\chi^n}{n!} \int \prod_{i=1}^{n} d^2\mathbf{q}_i \left[\frac{1}{\sigma_{el}} \frac{d\sigma_{el}}{d^2\mathbf{q}_i}\right] \frac{dN^i}{d^2\mathbf{p}}(\mathbf{p} - \mathbf{q}_1 - \cdots - \mathbf{q}_n) \; . \tag{2.89}$$

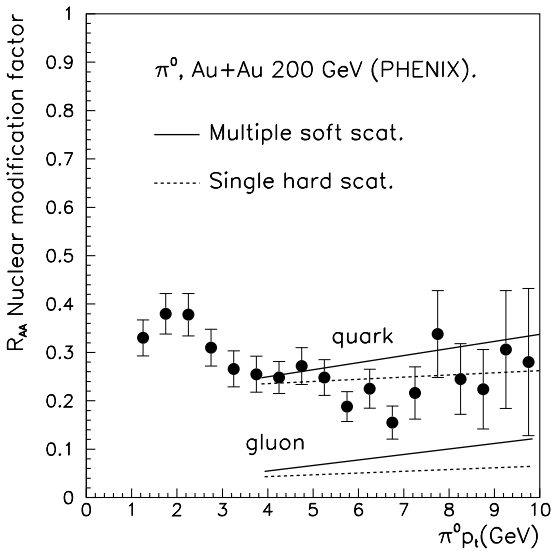

Fig. 2.23: Suppression of π^0 production at high-p_T measured by PHENIX collaboration [124]. Theoretical suppression is estimated [80] from ratios of $z^6 D_i^{med}(z, Q^2)$ at the maximum (see Fig. 2.20). Solid lines are for multiple soft scattering approximation and dashed for single hard scattering in the opacity expansion of Ref. [71].

Numerical estimates of Eq. (2.89) show that for thin media with a few semi-hard scatterings the induced transverse momentum broadening exhibits a weak logarithmic enhancement with p_T and is proportional to $L \propto A^{1/3}$. The transverse momentum transfer per unit length in cold nuclear matter is found to be $\mu^2/\lambda_q \simeq 0.05$ GeV^2/fm [8] from comparison to low energy pA data [35–37]. The left top and bottom panels of Fig. 2.24 show the predicted Cronin+shadowing effect in pPb collisions at $\sqrt{s}$ = 8.8 TeV and central PbPb at $\sqrt{s}$ = 5.5 TeV without final state medium induced energy loss. The 4% (10%) enhancement of R_{BA} at $p_T \simeq 40$ GeV comes from antishadowing and in not related no multiple initial state scattering. The observed difference between π^0 and 0.5 $(h^+ + h^-)$ reflects the different $S_\alpha(x, Q^2)$ for quarks and gluons. Cronin effect at the LHC results in slowing down of the decrease of R_{BA} at small x as seen in the $p_T \to 0$ limit. In contrast, at RHIC one finds $\simeq$ 30% enhancement in central dAu reactions at $\sqrt{s}$ = 200 GeV and $\simeq$ 60% effect in central AuAu relative to the *binary collision* scaled pp result [8,126]. At CERN-SPS energies of $\sqrt{s}$ = 17 GeV the results are most striking, with values reaching 250% in dAu and 400% in central AuAu at $p_T \simeq 4$ GeV. For a summary of results on midrapidity Cronin effect at the LHC see [1, 127].

The manifestation of multiple initial state scattering and nuclear shadowing at forward and backward rapidities $y = \pm 3$ in pPb at the LHC (for CMS $\eta \leq 2.5$) and dAu at RHIC (for BRAHMS $\eta \leq 3$) has also been studied in the framework of a fixed (or slowly varying) initial parton interaction strength [126]. At LHC energies at y = +3 (in the direction of the proton beam) the effect of the sequential projectile interactions is again small (due to the much flatter rapidity and transverse momentum distributions) and is overwhelmed by shadowing, which is found to be a factor of 2–3 times larger than the y = 0 result at small $p_T \sim$ few GeV and vanishes (R_{BA} = 1) at $p_T \simeq 50$ GeV. As previously emphasized, initial state gluon showering can significantly change the low-p_T behaviour of the hadronic spectra at the LHC beyond the current shadowing parameterization. At RHIC in dAu reactions at $\sqrt{s}$ = 200 GeV the nuclear modification ratio is qualitatively different. While near nucleus beam (backward y = –3) rapidity $R_{BA} \simeq$ 0.9–1 at forward rapidities y = +3 the nuclear modification factor exhibits a much more dramatic p_T dependence. At small transverse momenta $p_T \sim 1$ GeV hadron production is suppressed relative to the binary collision scaled pp result, $R_{BA} \leq 0.8$. The maximum Cronin enhancement $R_{BA}^{\max} \simeq 1.3$ (30%)

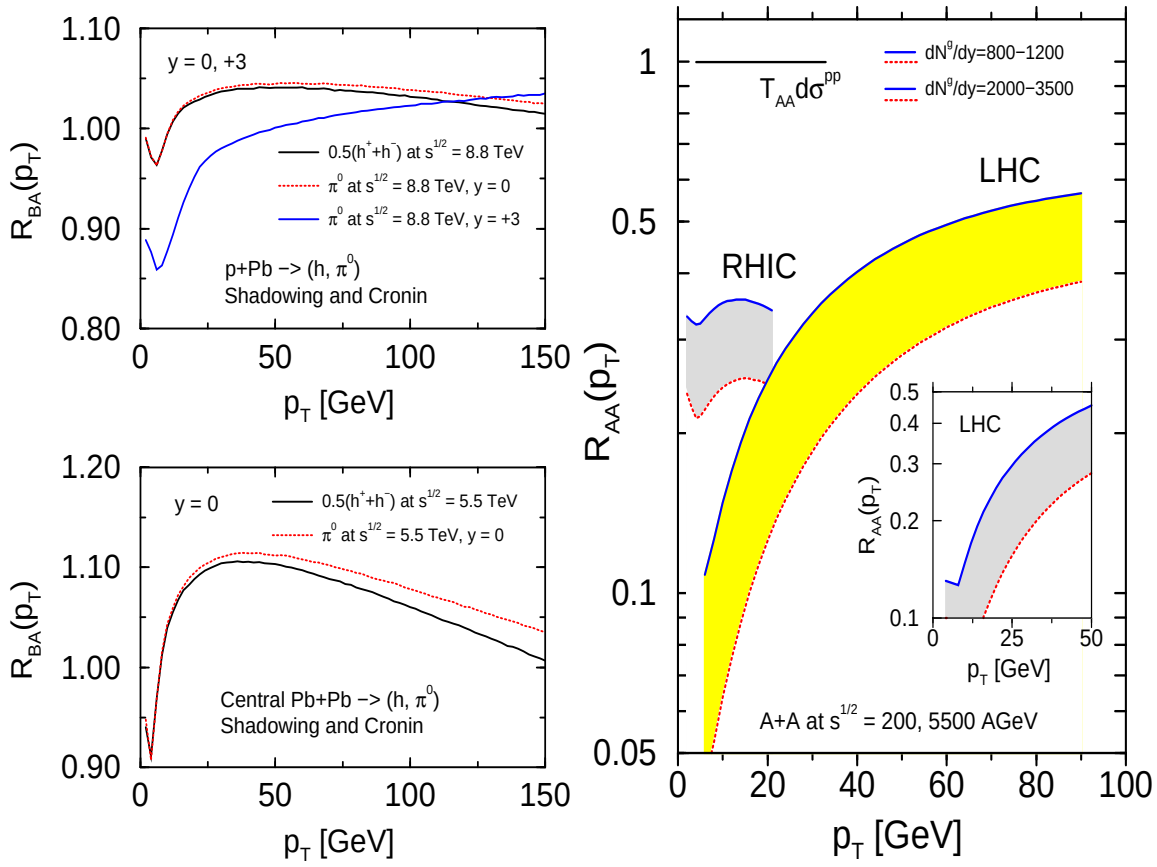

Fig. 2.24: The antishadowing and Cronin effects in pPb and central PbPb without energy loss at the LHC ($\sqrt{s}$ = 5.5 and 8.8 TeV) are shown in the left top and bottom panels. The right panel demonstrates the dominance of final state radiative energy loss effects at the LHC with a much stronger p_T dependence compared to RHIC. The possible restoration of the participant scaling through hydrodynamic-like feedback at $p_T \to 0$ is also shown in Ref. [8].

is essentially the same as at midrapidity but slightly shifted to larger p_T. We emphasize that *both* the suppression and enhancement regions are an integral part of the Cronin effect [35–37] that is understood in terms of probability conservation and momentum redistribution resulting from multiple initial state scattering [1, 8, 23, 43, 90, 97, 125, 127]. At forward (in the direction of the deuteron beam) rapidities a calculation as in [8, 126] demonstrates a *broader* Cronin enhancement region with $R_{BA} \simeq 25\%$ at p_T = 5 GeV. This is understood in terms of the significantly steeper fall-off of the hadron spectra away from midrapidity that enhances the effect of the otherwise similar transverse momentum kicks. While the discussed moderate p_T interval [126] lies at the very edge of BRAHMS acceptance (at y = +3) the same qualitative picture holds at y = +2.

The full solution for the medium induced gluon radiation off jets produced in a hard collision inside the nuclear medium of length L and computed *to all orders* in the correlations between the multiple scattering centres via the GLV reaction operator approach [74] has been discussed in Section 3.1.3. At large jet energies the lowest order correlation between the jet production point one of the scatterings that follow has been shown to dominate and lead to a quadratic mean energy loss dependence on the size of the plasma, $\Delta E \propto L^2$ for *static* media [73]. To improve the numerical accuracy for small parton energies we include corrections to third order in opacity [8] from Eq. (2.24). The dynamical expansion of the bulk soft matter is assumed to be of Bjorken type. In the Poisson approximation of independent gluon emission [5–7, 92] the probability distribution $P(\epsilon, E)$ of the fractional energy loss $\epsilon = \sum_i \omega_i / E$ can be obtained iteratively from the single inclusive gluon radiation spectrum $dN(x, E)/dx$ [5] as in

Eq. (2.25). If a fast parton looses $\epsilon\, E$ of its initial energy prior to hadronization its momentum fraction z_c is modified to $z_c^* = p_h/p_c(1-\epsilon) = z_c/(1-\epsilon)$. The observable suppressed hadron differential cross section can be computed from Eq. (2.1) with the substitution

$$D_{h/c}(z_c, Q^2) \longrightarrow \int d\epsilon\, P(\epsilon, p_c) \frac{z_c^*}{z_c} D_{h/c}(z_c^*, Q^2)\ . \tag{2.90}$$

The nuclear modification factor $R_{AA}(p_T)$ at the LHC is shown on the right panel of Fig. 2.24 and is completely dominated by final state interactions (see left panel). It shows a *significantly stronger* p_T dependence as compared to RHIC, where jet quenching was predicted to be *approximately constant* over the full measured moderate- to high-transverse momentum range [8] — the result of an interplay of shadowing, Cronin effect, and radiative energy loss. The variation of R_{AA} at the LHC is a factor of 5: from 10–20 fold suppression at p_T = 10 GeV to only a factor 2–3 suppression at p_T = 100 GeV. The reason for such a prominent variation is the hardening of the particle transverse momentum spectra (see Fig. 2.4) and the insufficient balancing action of multiple initial state scattering. In fact, the prediction from Fig. 2.24 is that the suppression in central PbPb at $\sqrt{s}_{NN}$ = 5.5 TeV at $p_T \simeq 40$ GeV is comparable to the factor of 4–5 suppression currently observed at RHIC.

The extrapolation of the LHC quenching calculations to small $p_T \to 0$ results in suppression below participant scaling. More careful examination of the mean energy loss of partons, in particular for gluons radiating in nuclear matter at LHC densities, reveals sizeable regions of phase space with $\Delta E \geq E$. This indicates complete absorption of jets in nuclear matter. There is experimental evidence that this regime of extreme *final state* densities may have been achieved at RHIC [128–130]. In this case Eq. (2.90) has to be corrected to include the feedback of the radiated gluons into the system. This hydrodynamic-like feedback is expected to recover the N_{part} scaling in the soft p_T region [8] — also illustrated on the right panel of Fig. 2.24. The effective initial gluon densities derived from the rapidity densities used in Fig. 2.24 are $\rho_g(RHIC)$= 30–50/fm^3 and $\rho_g(LHC)$ = 130–275/fm^3. These are one to two orders of magnitude larger than the density of cold nuclear matter and are suggestive of a deconfined QCD state — the quark–gluon plasma. Interestingly, a recent study of non-equilibrium parton transport in central AuAu and PbPb at $\sqrt{s}_{NN}$ = 200 GeV and $\sqrt{s}$ = 5.5 TeV has found initial parton densities corresponding to the lower bound of the intervals quoted above [131].

At the time of the completion of the CERN Yellow Report experimental data on hadroproduction at RHIC $\sqrt{s}$ = 200 AGeV in dAu and AuAu reactions became available for comparison to theoretical predictions. In the top panel of Fig. 2.25 the Cronin enhancement, resulting from initial state parton broadening [8, 89] is seen to compare qualitatively to the shape of the PHENIX π^0 measurement [132] in minimum bias dAu. Larger enhancement of $h^+ + h^-$ production, consistent with results form low energy pA data, is also shown [133–135]. The bottom panel rules out the scenario for the initial wavefunction origin of moderate and high-p_T hadron suppression, see Fig. 2.26, since in this case $R_{dAu} \approx \sqrt{R_{\rm AuAu}}$. Fig. 2.25 compares the predicted [8] approximately constant suppression of π^0 and $h^+ + h^-$ in $\sqrt{s}$ = 200 AGeV AuAu collisions at RHIC to PHENIX and STAR data [124, 137]. The overall quenching magnitude and its centrality dependence are set by $(\langle L\rangle/A_T)dN^g/dy \propto N_{part}^{2/3}$, dN^g/dy = 1150. We again emphasize that the shape of $R_{\rm AuAu}$ is a result of the interplay of all three nuclear effects: Cronin, shadowing, and jet quenching. The full numerical calculation takes into account the dynamical Bjorken expansion of the medium, finite kinematic bounds, higher order opacity corrections and approximates multiple gluon emission by a Poisson distribution [8]. The remarkably good agreement between the *predicted* nuclear modification factors and the experimental measurements give confidence in projecting the anticipated nuclear effects over a much wider dynamical moderate- and high-p_T range at the LHC.

Conclusions. In central AA reactions the nuclear modification factor $R_{AA}(p_T)$ at the LHC is shown to be completely dominated by final state multi-parton interactions [8]. For comparison, at RHIC Cronin effect and nuclear shadowing also play an important role, leading to an approximately constant

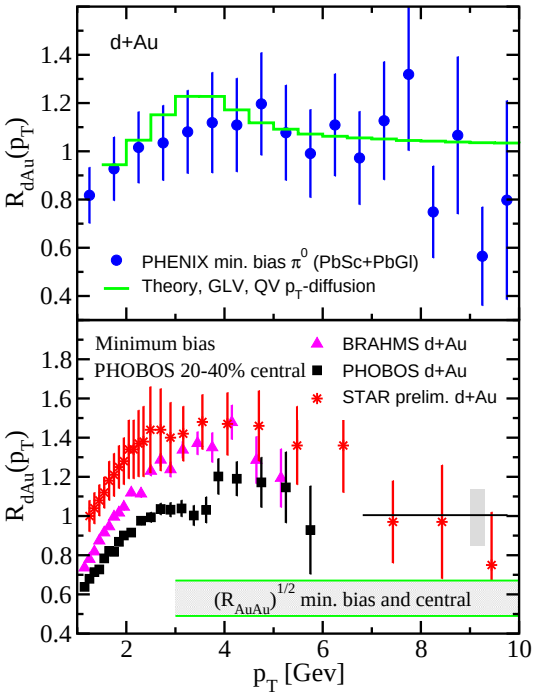

Fig. 2.25: Comparison of the prediced Cronin effect from [8, 126] to the measured small enhancement of single inclusive neutral pion production in dAu at $\sqrt{s}_{NN}$ = 200 GeV. Data is from PHENIX [132]. Bottom panel: a test of a suggested interpretation of high p_T-hadron suppression as a result of initial state wavefunction modification, $R_{dAu} \approx \sqrt{R_{\rm AuAu}}$. Data from BRAHMS, PHOBOS and STAR [133–135] exclude such possibility. Figure adapted from [136].

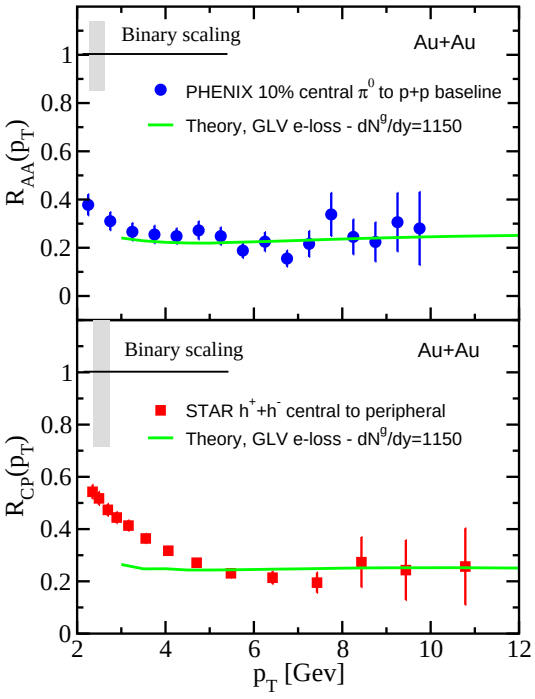

Fig. 2.26: Predicted [8] suppression for π^0 (top panel) and $h^+ + h^-$ (bottom panel) in AuAu compared to PHENIX and STAR data [124, 137]. Similar quenching is found by BRAHMS and PHOBOS [133, 138]. Figure adapted from [136].

suppression ratio. At the SPS initial state multiple elastic scatterings dominate, resulting in a net enhancement of hadron production. At forward (y = +3) rapidities in dAu at RHIC the Cronin enhancement region is predicted to be broader in comparison to the y = 0 case. In contrast in pPb at the LHC nuclear shadowing dominates but in order to detect a sizable reduction relative to the binary collision scaled pp cross section measurements at close to proton rapidity ($y_{\rm max}$ = 9.2 for $\sqrt{s}$ = 8.8 TeV) are needed.

The predicted decreasing $R_{\rm AA}$ with p_T at the LHC, if confirmed, may have important experimental consequences. Comparative large-E_T measurements of the difference in the *full structure* of the jet cone in pp and AA reactions may prove difficult for weak signals and large backgrounds. We emphasize that one of the easiest and most unambiguous approaches for detecting the non-abelian jet energy loss and performing jet-tomographic analysis of the properties of the hot and dense matter created in ultra-relativistic heavy ion reactions is through the suppression pattern of leading hadrons. Therefore these measurements should enter as an important part of the experimental programs at the LHC.

3.4.4. Heavy quark energy loss observables

R. Vogt

Heavy quarks (HQ) are good probes of the QCD medium produced in heavy ion collisions. They are produced perturbatively in the initial hard nucleon–nucleon collisions at timescales on the order of $1/m_Q$. Their production during other stages of the evolution of the system is unlikely, except perhaps in the pre-equilibrium phase of the plasma, because $m_Q \gg T$. (See Refs. [139–142] for some estimates of

thermal charm production.) Thus the initially produced heavy quarks experience the full collision history.

While the heavy quarks are in the medium, they can undergo energy loss by two means: elastic collisions with light partons in the system (collisional) and gluon bremsstrahlung (radiative). We will briefly review some of the predicted results for $-dE/dx$ of heavy quarks for both collisional and radiative loss. We then show the predicted effect on the charm and bottom contributions to the dilepton continuum for both ALICE and CMS using a fixed value of $-dE/dx$.

The collisional energy loss of heavy quarks through processes such as $Qg \to Qg$ and $Qq \to Qq$ depends logarithmically on the heavy quark momentum, $-dE/dx \propto \ln(q_{\max}/q_{\min})$. Treatments of the collisional loss vary with the values assumed or calculated for the cutoffs. These cutoffs are sensitive to the energy of the heavy quark and the temperature and strong coupling constant in the medium. Thus the quoted value of the energy loss is usually for a certain energy and temperature. The calculation was first done by Bjorken [57] who found $-dE/dx \approx 0.2$ GeV/fm for a 20 GeV quark at T = 250 MeV. Further work refined the calculations of the cutoffs [108, 143, 144], with similar results. Braaten and Thoma calculated the collisional loss in the limits $E \ll m_Q^2/T$ and $E \gg m_Q^2/T$ in the hard thermal loop approximation, removing the cutoff ambiguities. They obtained $-dE/dx \approx 0.3$ GeV/fm for a 20 GeV charm quark and 0.15 GeV/fm for a 20 GeV bottom quark at T = 250 MeV [145].

Other models of heavy quark energy loss were presented in the context of J/ψ suppression: could a produced $c\overline{c}$ pair stay together in the medium long enough to form a J/ψ? Svetitsky [146] calculated the effects of diffusion and drag on the $c\overline{c}$ pair in the Boltzmann approach and found a strong effect. The drag stopped the $c\overline{c}$ pair after traveling about 1 fm but Brownian diffusion drove the c and $\overline{c}$ apart quickly. The diffusion effect increased at later times. Essentially he predicted that the heavy quarks would be stopped and then go with the flow. His later calculations of D meson breakup and rehadronization [147] while moving through plasma droplets reached a similar conclusion. Koike and Matsui calculated the energy loss of a colour dipole moving through a plasma using kinetic theory and found $-dE/dx \sim 0.4$–1.0 GeV/fm for a 10 GeV $Q\overline{Q}$ [148].

Thus the collisional loss was predicted to be rather small, less than 1 GeV/fm for reasonable assumptions of the temperature. The loss increases with the energy and temperature. Using the hard thermal loop approach, Mustafa *et al.* found $-dE/dx \approx 1-2$ GeV/fm for a 20 GeV quark at T = 500 MeV [113].

Radiative energy loss of light quarks has been extensively studied and is discussed in detail in the remainder of this chapter. The first application of radiative loss to heavy quarks was perhaps by Mustafa *et al.* [113]. They included the effects of only a single scattering/gluon emission, $Qq \to Qqg$ or $Qg \to Qgg$. In this case, the loss grows as the square of the logarithm $\ln(q_{\max}/q_{\min})$, one power more than the collisional loss, but is of the same order in the strong coupling constant [145]. Thus the radiative loss is guaranteed to be higher than the collisional in this approximation. The heavy quark mass enters their expressions only in the definition of $q_{\max}$ so that the mass dependence of the energy loss is rather weak. They found, for a 20 GeV quark at T = 500 MeV, $-dE/dx \approx 12$ GeV/fm for charm and 10 GeV/fm for bottom.

These large values suggested that energy loss could be quite important for heavy quarks. If true, there would be a strong effect on the $Q\overline{Q}$ contribution to the dilepton continuum. Shuryak [149] was the first to consider this possibility for AA collisions. He assumed that low mass $Q\overline{Q}$ pairs would be stopped in the medium, suppressing the dilepton contribution from these decays substantially. However, the stopped heavy quarks should at least expand with the medium rather than coming to rest, as discussed by Svetitsky [146]. Lin *et al.* then calculated the effects of energy loss at RHIC, including thermal fluctuations, for a constant $-dE/dx$ = 0.5–2 GeV/fm [150]. These results showed that the heavy quark contributions to the dilepton continuum would be reduced albeit not completely suppressed. In any case, the energy loss does not affect the total cross section. The heavy quarks are thus piled up at low

[0]His drag coeffi cient $A(p^2)$ is related to the energy loss per unit length through $A(p^2) = (-dE/dx)/p^2$.

p_T and at midrapidity if stopped completely. The work by Lin *et al.* was extended to the LHC for $-dE/dx$ = 1 GeV/fm [151]. These results are shown here.

Other calculations of effects on the dilepton continuum have focused on higher mass lepton pairs. Lokhtin and Snigirev have calculated the effect of collisional and radiative energy loss on the correlated $b\overline{b}$ contribution to the dilepton continuum in the CMS acceptance [152] and find a large depletion in the mass range $20 < M < 50$ GeV. If the loss is large, the Drell–Yan and thermal dileptons could emerge from under the reduced $b\overline{b}$ decay contribution at large masses. Gallmeister *et al.* [153] have recently considered the amount of energy loss that the RHIC charm data can support.

Before presenting the results of the model calculations of Ref. [151], we note that Dokshitzer and Kharzeev recently pointed out that soft gluon radiation from heavy quarks is suppressed at angles smaller than $\theta_0 = m_Q/E$ [85]. Thus bremsstrahlung is suppressed for heavy quarks relative to light quarks by the factor $(1 + \theta_0^2/\theta^2)^{-2}$, the 'dead cone' phenomenon. The radiative energy loss of heavy quarks could then be quite small. In fact, PHENIX sees little to no energy loss in their charm data [154]. These calculations and their implications are discussed in detail later in this report [2]. We show how the ratio of quenching factors for heavy to light quarks, $Q_H(p_T)/Q_L(p_T)$, depends on L, the path length through the medium, in Fig. 2.27. These results are indicative of how the D/π ratio might be modified in a heavy ion collision.

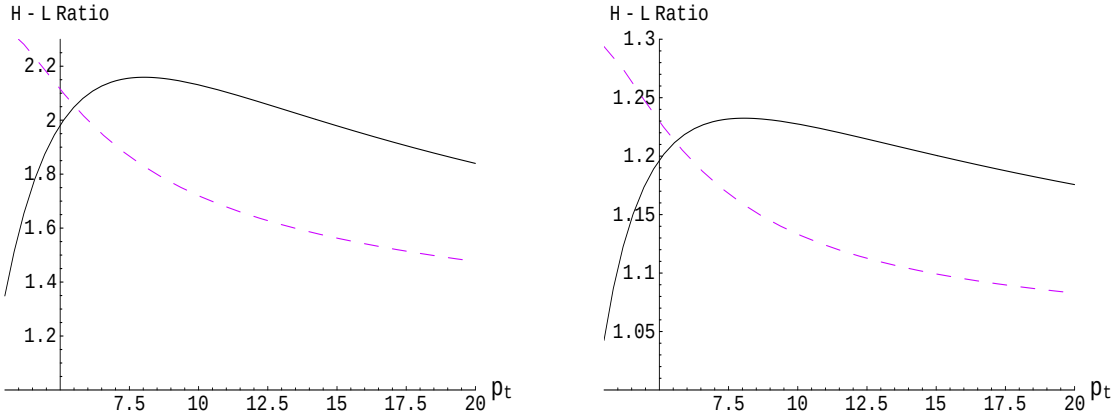

Fig. 2.27: The ratio of quenching factors $Q_H(p_\perp)/Q_L(p_\perp)$ for charm and light quarks in hot matter with $\hat{q}$ = 0.2 GeV^3 (L = 5 fm upper panel, L = 2 fm lower panel). Solid lines correspond to unrestricted gluon radiation, while the dashed lines are based on the calculation with the cut $\omega > 0.5$ GeV on gluon energies. From Ref. [85].

We now turn to an illustration of how a constant 1 GeV/fm energy loss might affect the heavy quark contribution to the dilepton continuum in 5.5 TeV PbPb collisions at the LHC [151]. It is based on the picture that a heavy quark with a transverse path, l_T, and mean-free path, λ, undergoes on average $S = l_T/\lambda$ scatterings. The main model assumption is that the actual number of scatterings, n, is generated from the Poisson distribution, $P(n, S) = e^{-S}S^n/n!$. In the rest frame of the medium, the heavy quark then experiences momentum loss $\Delta p = n\lambda\ dE/dx$ so that its final momentum is $p_T' = p_T - \Delta p$. The heavy quark will thermalize if p_T' is smaller than the average transverse momentum of thermalized heavy quarks with a temperature T. These thermalized quarks are given a random thermal momentum in the rest frame of the fluid and are then transformed back to the centre-of-mass frame of the collision. The calculation assumes $-dE/dx$ = 1 GeV/fm, λ = 1 fm and T = 150 MeV. Even a small energy loss will suppress high p_T and large invariant mass $Q\overline{Q}$ pairs as long as $|dE/dx| \geq \langle p_T\rangle/R_A \sim 0.4$ GeV/fm in PbPb collisions at 5.5 TeV where $\langle p_T\rangle$ is the average transverse momentum of the heavy quark and R_A is the nuclear radius.

The results for $D\overline{D}$ and $B\overline{B}$ decay contributions to the dilepton continuum in ALICE are shown in Fig. 2.28 for the e^+e^-, $\mu^+\mu^-$ and $e\mu$ channels. The pseudorapidity cuts are $|\eta| < 0.9$ for electrons

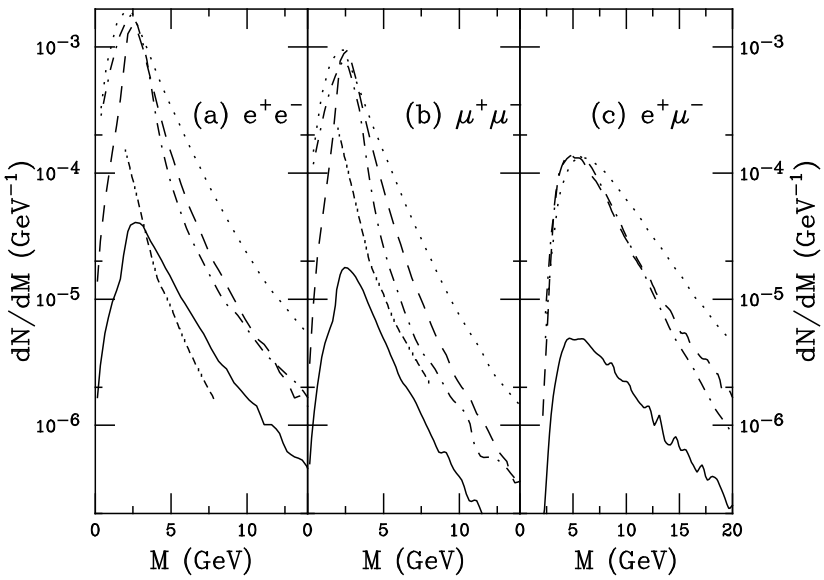

Fig. 2.28: The dilepton invariant mass distributions in the ALICE acceptance. The e^+e^- (a), $\mu^+\mu^-$ (b) and $e\mu$ (c) channels are shown. The dashed and dotted curves are the $D\overline{D}$ and summed single B and $B\overline{B}$ decays respectively without energy loss. The solid and dot-dashed curves are the corresponding results with $-dE/dx$ = 1 GeV/fm. The Drell–Yan rate is given by the dot-dot-dashed curve in (a) and (b). From Ref. [151].

and $2.5 \leq \eta \leq 4$ for muons. A momentum cut of $p_T > 1$ GeV is used for both lepton types. Full azimuthal coverage is assumed for both the central barrel and forward muon arm. Note that the $B\overline{B}$ contribution also includes opposite sign lepton pairs from chain decays of individual B and $\overline{B}$ mesons. In the calculation, 540 $c\bar{c}$ pairs and 7 $b\bar{b}$ pairs were created in central PbPb collisions using the MRS D-' [155] parton densities [151]. More recent parton densities such as MRST HO [13] give smaller charm cross sections, $\sim$ 6 mb, instead of the 17 mb obtained with MRS D-. This would reduce the charm rate relative to the bottom rate by nearly a factor of five. The charm and bottom yields for low mass pairs are similar without loss but energy loss suppresses the charm yield much more strongly than bottom. The moderate loss assumed here still predicts a larger $B\overline{B}$ contribution to the e^+e^- and $\mu^+\mu^-$ continua than the Drell–Yan yield.

The CMS muon acceptance is in the range $|\eta| \leq 2.4$ with a lepton p_T cut of 3 GeV. After these simple cuts are applied, the results are shown in Fig. 2.29 for both $D\overline{D}$ and $B\overline{B}$ decays. Whereas for $M \leq 15$ GeV, the $D\overline{D}$ decays would dominate those of $B\overline{B}$ before the cuts, the measured $B\overline{B}$ decays are everywhere larger than those from charm mesons both before and after energy loss. The generally larger momentum of muons from B decays and the rather high momentum cut result in larger acceptance for $B\overline{B}$ decays. No $D\overline{D}$ decay pairs with $M \leq 5$ GeV survive the momentum cut. A factor of 50 loss in rate at $M \sim 10$ GeV is found before energy loss. A loss in rate by a factor of 100 is obtained when energy loss is included. The corresponding acceptance from $B\overline{B}$ decays is significantly larger, with a loss in rate of a factor of ≈ 8 before energy loss and ≈ 15 with energy loss. Interestingly, the leptons in the decay chain of a single B meson are energetic enough for both to pass the momentum cut, causing the peak at $M \sim 2-3$ GeV. These results suggest that rather than providing an indirect measurement of the charm cross section, as postulated in Ref. [156], the dilepton continuum above the Υ family could instead measure the $b\bar{b}$ production cross section indirectly. A comparison with the spectrum from pp interactions at the same energy would then suggest the amount of energy loss, $-dE/dx$, of the medium. For a calculation of the effects of the dead cone on higher mass dileptons in CMS, see Ref. [157].

We have so far shown results for the dilepton continuum. However, the PHENIX measurement was of single leptons [154]. The single leptons are not as sensitive to the magnitude of the energy loss as

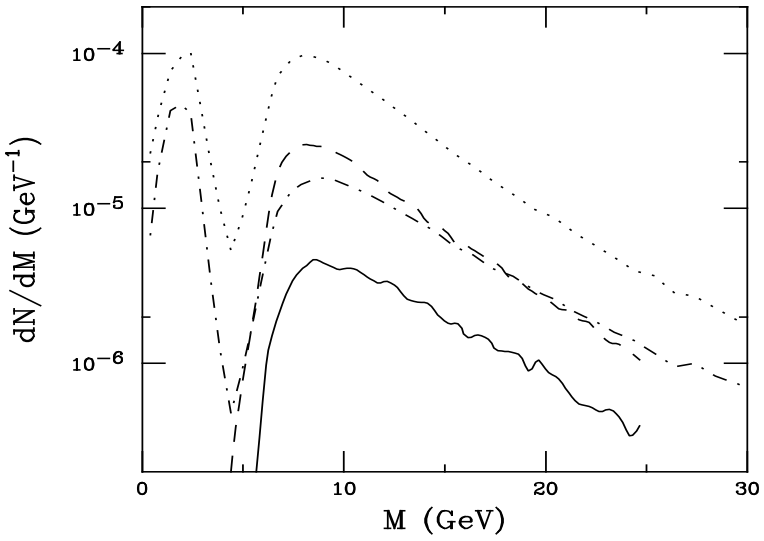

Fig. 2.29: The dilepton invariant mass distributions in the CMS acceptance. The dashed and dotted curves are the $D\overline{D}$ and summed single B and $B\overline{B}$ decays respectively without energy loss. The solid and dot-dashed curves are the corresponding results with $-dE/dx$ = 1 GeV/fm. From Ref. [151].

the dilepton continuum [151].

Single leptons can be categorized as those from thermalized heavy quarks and those from heavy quarks energetic enough to escape after energy loss. The former mainly reflects the effective thermalization temperature while the latter can provide us with information on the energy loss. Single leptons with energies greater than 1–2 GeV are mainly from energetic heavy quarks and thus are more sensitive to the energy loss. Before energy loss, the single leptons from D decays are larger than those from b hadron decays for $p_T < 2.5$ GeV. After energy loss, the b hadron decays dominate the spectra over all p_T.

We show the effect of energy loss on single electrons and muons within the ALICE acceptance in Fig. 2.30. A comparison of the p_T distributions of single muons in the CMS acceptance from the decays of D and B mesons can also provide a measure of the b cross section, shown in Fig. 2.31. The muon p_T distribution is clearly dominated by B decays.

3.4.5. Medium-modified jet shapes and jet multiplicities

C.A. Salgado and U.A. Wiedemann

To discuss the medium-dependence of jet shape observables, one can start from the probability $P_{\rm tot}(\epsilon,\Theta)$ that a fraction $\epsilon = \frac{\Delta E}{E}$ of the total jet energy E is emitted outside the cone angle Θ. Under the assumption that gluon emission follows an independent Poisson process (see Section 3.2.), this probability is given by

$$P_{\rm tot}(\epsilon,\Theta) = \int_C \frac{d\nu}{2\pi i}\, e^{\nu\,\epsilon}\, \exp\left[-\int_0^\infty d\omega\, \left(\frac{dI^{>\Theta}_{\rm vac}}{d\omega} + \frac{dI^{>\Theta}_{\rm med}}{d\omega}\right)\left(1-e^{-\nu\omega}\right)\right]\,. \tag{2.91}$$

The expression (2.91) takes into account the angular energy distribution of the parton fragmentation process in the vacuum, $\frac{dI^{>\Theta}_{\rm vac}}{d\omega}$, as well as its medium-modification $\frac{dI^{>\Theta}_{\rm med}}{d\omega} = \int_\Theta^\pi d\Theta\, \frac{dI_{\rm med}}{d\omega\, d\Theta}$. Since both contributions are additive, the total probability, Eq. (2.91), can be written as a convolution of the vacuum and the medium-induced probability,

$$P_{\rm tot}(\epsilon,\Theta) = \int d\epsilon_1\, P_{\rm vac}(\epsilon_1,\Theta)\, P_{\rm med}(\epsilon-\epsilon_1,\Theta)\,. \tag{2.92}$$

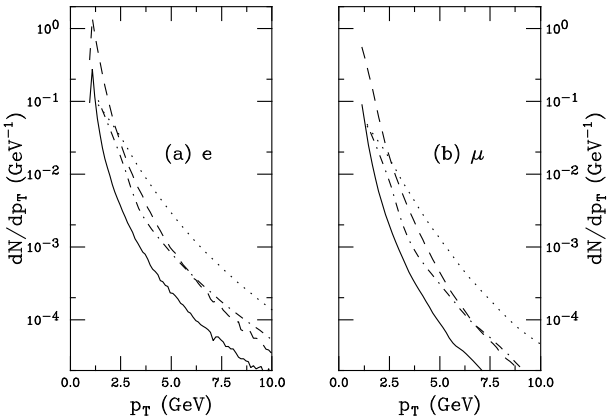

Fig. 2.30: The p_T spectrum of single electrons (a) and muons (b) from charm and bottom decays within the ALICE acceptance. The dashed and dotted curves are the D and B meson decays respectively without energy loss. The solid and dot-dashed curves are the corresponding results with $-dE/dx = 1$ GeV/fm. From Ref. [151].

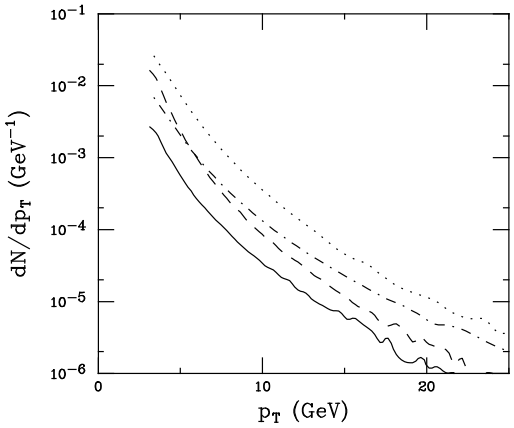

Fig. 2.31: The p_T spectrum of single muons from charm and bottom decays within the CMS acceptance. The dashed and dotted curves are the D and B meson decays respectively without energy loss. The solid and dot-dashed curves are the corresponding results with $-dE/dx = 1$ GeV/fm. From Ref. [151].

We define the vacuum contribution $P_{\rm vac}(\epsilon, \Theta)$ in terms of the jet shape $\rho(r)$. This jet shape is measured in elementary (pp, p$\bar{\rm p}$ or e^+e^-) collisions as the average fraction of calorimeter cell E_T in a jet subcone of radius $r = \sqrt{(\Delta\eta)^2 + (\Delta\Phi)^2}$,

$$\rho(r) \;\; = \;\; \frac{1}{N_{\rm jets}} \sum_{\rm jets} \frac{E_T(r)}{E_T(r=1)} \, . \tag{2.93}$$

We use the Fermilab $D0$ parametrization [158] of $\rho(r)$ which is based on jet shapes measured for average transverse energies of $\approx$ 50–150 GeV. We work in the dijet centre of mass where the jet width in pseudorapidity $\Delta\eta$ and azimuth $\Delta\Phi$ is related to the gluon emission angle Θ of our calculation as $r = \Theta$. In general, $P_{\rm vac}(\epsilon, \Theta)$ is a probability distribution of some width in ϵ whose first moment determines the jet shape. In the presence of medium-effects, however, the vacuum part $\frac{dI_{\rm vac}}{d\omega}$ emits only a fraction $\frac{E-\Delta E}{E}$ of the total energy, and thus we have

$$\langle \epsilon \rangle_{\rm vac}(\Theta) = \int d\epsilon \, \epsilon \, P_{\rm vac}(\epsilon, \Theta) = [1 - \rho(r = \Theta)] \, \frac{E - \Delta E}{E} \, . \tag{2.94}$$

Since we have no experimental data about the width of $P_{\rm vac}(\epsilon, \Theta)$, we choose

$$P_{\rm vac}(\epsilon, \Theta) = \delta \left(\epsilon - \frac{E - \Delta E}{E} \, [1 - \rho(r)] \right) |_{r=\Theta} \, . \tag{2.95}$$

The medium-modified jet shape $\rho_{\rm med}(r) = 1 - \langle \epsilon \rangle_{\rm tot}(\Theta)$ is then defined in terms of the average jet energy fraction radiated outside an angle Θ. One finds

$$\begin{aligned} \rho_{\rm med}(r) \;\; &\equiv \;\; 1 - \langle \epsilon \rangle_{\rm tot}(\Theta) = 1 - \int d\epsilon \, \epsilon \, P_{\rm tot}(\epsilon, \Theta) \\ &= \;\; \rho(r) \; - \frac{\Delta E(\Theta)}{E} + \frac{\Delta E(\Theta = 0)}{E} \, (1 - \rho(r)) \; , \end{aligned} \tag{2.96}$$

where $\frac{\Delta E}{E}(\Theta) = \int d\epsilon \, \epsilon \, P_{\rm med}(\epsilon, \Theta)$. For realistic parameters, one finds that this jet shape is modified by a few percent only [159].

While the jet energy distribution is little affected by the medium, the multiplicity distribution inside the jet cone is expected to change significantly. This is seen from the medium-induced additional number of gluons with transverse momentum $k_\perp = |\mathbf{k}|$, produced within a subcone of opening angle θ_c,

$$\frac{dN^{\rm jet}}{dk_\perp} = \int_{k_\perp/\sin\theta_c}^{E} d\omega \, \frac{dI_{\rm med}}{d\omega \, dk_\perp} \, . \tag{2.97}$$

In Fig. 2.32, this distribution is compared to the shape of the corresponding perturbative component, $\frac{dN^{\rm vac}}{dk_\perp} \propto \frac{1}{k_\perp} \log(E \sin\theta_c / k_\perp)$. The total partonic jet multiplicity is the sum of both components. For realistic values of medium density and in-medium pathlength, medium effects are seen to increase this multiplicity significantly (by a factor $>$ 2–5) in particular in the high-$k_\perp$ tails. Also, the shape and width of the distribution in Eq. (2.138) changes sensitively with the scattering properties of the medium. Moreover, since gluons must have a minimal energy $\omega > k_\perp / \sin\Theta_c$ to be emitted inside the jet cone, this high-$k_\perp$ tail is unaffected by 'background' cuts on the soft part of the spectrum, see Fig. 2.32. This suggests that the measurement of the transverse momentum distribution of hadrons with respect to the jet axis is very sensitive to the transverse momentum broadening of the underlying parton shower and should be detectable above background.

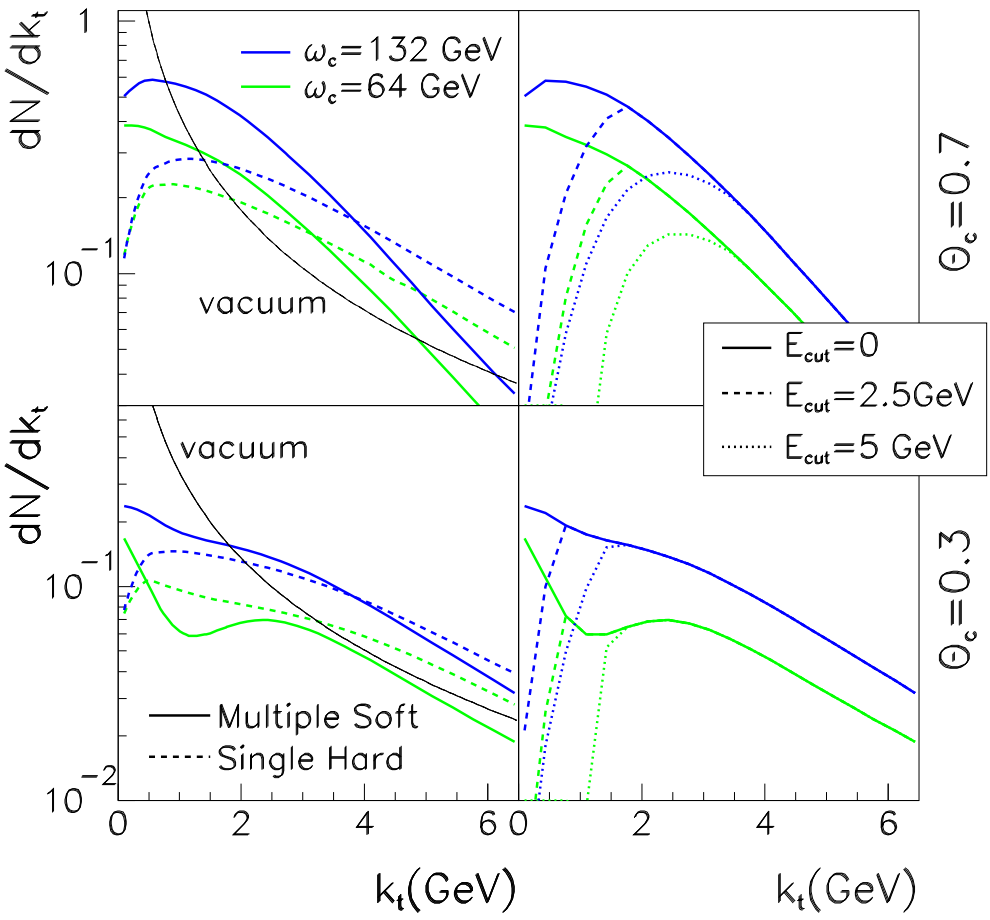

Fig. 2.32: The gluon multiplicity distribution (2.97) inside a cone size $R = \Theta_c$, measured as a function of k_t with respect to the jet axis. Removing gluons with energy smaller than $E_{\rm cut}$ from the distribution (dashed and dotted lines) does not affect the high-k_t tails. Figure is taken from Ref. [159].

3.4.6. Jet quenching and high-p_T azimuthal asymmetry

I.P. Lokhtin, A.M. Snigirev and I. Vitev

The azimuthal anisotropy of high-p_T particle production in non-central heavy ion collisions is among the most promising observables of partonic energy loss in an azimuthally non-symmetric volume of quark-gluon plasma. We discuss the implications of nuclear geometry for the models of partonic energy loss in the context of recent RHIC data and consequences for observation of jet quenching at the LHC.

In order to interpret data on nuclear collisions from current experiments at the Relativistic Heavy Ion Collider (RHIC) and future experiments at the Large Hadron Collider (LHC), it is necessary to have knowledge of the *initial conditions*. There are large uncertainties in the estimates of the initial produced gluon density, $\rho_g(\tau_0) \sim$ 15–50/fm^3 in central AuAu at $\sqrt{s}$ = 130, 200 AGeV and $\rho_g(\tau_0) \sim$ 100–400/fm^3 in central PbPb reactions at $\sqrt{s}$ = 5500 AGeV, since widely different models (e.g. see [105, 160]) seem to be roughly consistent with data [161]. It is, therefore, essential to check the energy dependence of the density of the produced quark-gluon plasma (QGP) with observables complementary to the particle multiplicity dN^{ch}/dy and transverse energy dE_T/dy per unit rapidity. High-p_T observables are ideally suited for this task because they provide an estimate [50] of the energy loss, ΔE, of fast partons, resulting from medium induced non-abelian radiation along their path, as first discussed in [51, 112] in the context of relativistic heavy ion reactions. The approximate linear dependence of ΔE on ρ_g is the key that enables high-p_T observables to convey information about the initial conditions. However, ΔE also depends non-linearly on the size, L, of the medium [65, 73] and therefore differential observables which have well controlled geometric dependences are also highly desirable.

A new way to probe ΔE in variable geometries was recently proposed in Refs. [81, 162]. The idea is to exploit the spatial azimuthal asymmetry of non-central nuclear collisions. The dependence of ΔE on the path length $L(\phi)$ naturally results in a pattern of azimuthal asymmetry of high-p_T hadrons which can be measured via the differential elliptic flow parameter (second Fourier coefficient), $v_2(p_T)$ [163–165]. Before we show the sensitivity of the high-p_T $v_2(p_T > 2$ GeV) to different initial conditions we briefly discuss the various model calculations for the 'elliptic flow' coefficient v_2:

1. The elliptic flow parameter v_2 was first introduced in the context of *relativistic hydrodynamics* [165] and reflects the fact that due to the macroscopic sizes of large nuclei many aspects of AA collisions are driven by nuclear geometry. In non-central collisions the interaction region has a characteristic "almond-shaped" form as shown in Fig. 2.33. Hydro calculations convert the

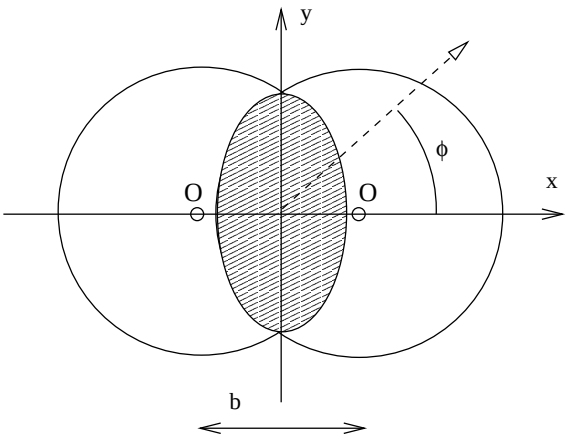

Fig. 2.33: The nuclear overlap region in non-central AA collisions shows the importance of reaction geometry. Model calculation described here convert the spatial anisotropy illustrated above into momentum anisotropy of measured hadrons.

ellipticity of the reaction volume into momentum space azimuthal asymmetry

$$\varepsilon = \frac{\langle x^2\rangle - \langle y^2\rangle}{\langle x^2\rangle + \langle y^2\rangle} \iff \frac{\langle p_x^2\rangle - \langle p_y^2\rangle}{\langle p_x^2\rangle + \langle p_y^2\rangle} = \langle \cos 2\phi\rangle = \frac{\int_0^{2\pi} d\phi\, \cos 2\phi\, \frac{dN^h}{dy\, p_T\, dp_T\, d\phi}}{\int_0^{2\pi} d\phi\, \frac{dN^h}{dy\, p_T\, dp_T\, d\phi}} \tag{2.98}$$

through the higher pressure gradient along the small axis. The elliptic flow is thus perfectly correlated to the reaction plane and can be used for its determination [166]. Hydrodynamic simulations [54, 167] typically describe well data from relativistic nucleus–nucleus collisions at $\sqrt{s}_{NN}$ = 200 GeV up to $p_T \simeq$ 1.5–2 GeV and it is not unlikely that at LHC energies of $\sqrt{s}_{NN}$ = 5.5 TeV the region of validity of those calculations may extend to $p_T \simeq 5$ GeV.

2. Initial conditions can also be mapped onto final state observable distributions by solving covariant Boltzmann transport equations as in *cascade models* (partonic, hadronic, and multi-phase). Elliptic flow in this approach is generated via multiple elastic scatterings. Calculations are sensitive to the choice of initial conditions [168] and are currently limited by statistics to $p_T \sim 6$ GeV. It is interesting to note that they can match the high-p_T behaviour of the v_2 but require extremely large initial gluon rapidity densities $dN^g/dy \simeq 16\,000$ [168] and/or string melting [169].
3. Memory of the initial parton density, reaction geometry, and the consequent dynamical evolution is also retained by large transverse momentum partons (and fragmented hadrons) through their *jet quenching* pattern [81, 162]. While this approach is discussed in more detail below, it is important to emphasize here that at the single inclusive jet (or hadron) level the resulting high-p_T azimuthal asymmetry is also perfectly coupled to the reaction plane. It has been suggested that in the limit of very large energy loss the momentum asymmetry is driven by jet production from the boundary of the interaction volume [170].
4. Recently, a classical computation of the elliptic flow at transverse momenta $k_T^2 > Q_s^2$ in the framework of *gluon saturation* models has been performed [171]. It was found that the azimuthal asymmetry is generated already at proper time $\tau = 0$, i.e. it is built in the coherent initial conditions. The resulting elliptic flow coefficient was found to vanish quickly $v_2(k_T) \propto k_T^{-2}(R_x^{-2} - R_y^{-2})$ above Q_s ($\sim$ 1 GeV for RHIC and $\sim$ 1.4–2 for LHC energies) which is not supported by the current data.
5. An approach that *does not* associate azimuthal asymmetry with the reaction plane has also been presented [172]. Both high-p_T and low-p_T v_2 emerge as a *back-to-back jet correlation bias* (with arbitrary direction relative to the reaction geometry for every p_T bin). For large transverse momenta $v_2 \propto \ln p_T/\mu$ suggest an easily detectable factor of 3 increase in going from p_T = 5 GeV to p_T = 100 GeV at LHC. The p_T-integrated $v_2 \propto 1/Q_s$ at LHC exhibits $\sim$ 50% reduction relative to RHIC. (It can also be deduced that v_2 is larger at the SPS in comparison to RHIC in this model.)

The methods for v_2 analysis can be broadly divided in two categories: two-particle methods discussed, e.g., in [173] and multi-particle methods [174, 175]. In two-particle methods the error on the determined v_2 from non-flow (non-geometric) correlations is $\mathcal{O}(1/(v_2 M))$, where M is the measured multiplicity. With multi-particle methods this error goes down typically to $\mathcal{O}(1/(v_2 M^2))$, i.e., smaller by a factor of order M. Although it is not possible to *completely* eliminate the non-flow components to v_2, experimental techniques based on higher oder cumulant analysis [174, 175] will be able in many cases to *clearly distinguish* between between reaction geometry generated azimuthal asymmetry and back-to-back jet bias.

Parton energy loss and nuclear geometry. For nucleus–nucleus collisions the co-moving plasma produced in an $A + B$ reaction at impact parameter b at formation time τ_0 has a transverse coordinate distribution at mid-rapidity $\rho_g(\mathbf{r}, z = 0, \tau_0)$. In studying jet production and propagation in a nuclear environment it is not always technically possible to perform the Monte-Carlo averaging over the jet production points coincidentally with the simulation of parton fragmentation. It is therefore useful to separate the medium dependence of the mean jet energy loss as a function of the extent of the nuclear

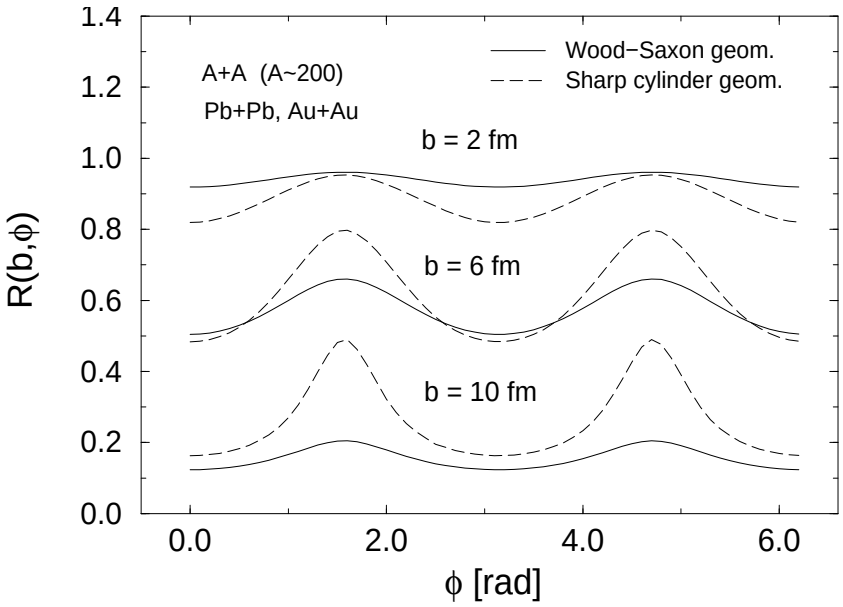

Fig. 2.34: The modulation function $R(b,\phi)$ is plotted versus ϕ for several impact parameters b = 2, 6, 10 fm from Ref. [81]. Diffuse Wood-Saxon versus uniform sharp cylinder geometries are compared. The most drastic difference between these geometries occurs at high impact parameters.

matter traversed and the azimuthal angle ϕ relative to the reaction plane. The total energy loss is proportional to a line integral along the jet trajectory $\mathbf{r}(\tau,\phi) = \mathbf{r} + \hat{v}(\phi)(\tau - \tau_0)$, averaged over the distribution of the jet production points

$$F(b,\phi) \;=\; \int d^2\mathbf{r}\, \frac{T_A(r) T_B(|\mathbf{r}-\mathbf{b}|)}{T_{AB}(b)} \int_{\tau_0}^{\infty} d\tau\; \tau\; \left(\frac{\tau_0}{\tau}\right)^{\alpha} \rho_0(\mathbf{r} + \hat{v}(\phi)(\tau - \tau_0)) \;. \qquad (2.99)$$

$T_A(r) = \int dz\, \rho_A(\mathbf{r},z)$ and $T_{AB}(b) = \int d^2\mathbf{r}\, T_A(\mathbf{r}) T_B(\mathbf{r}-\mathbf{b})$ depend on the geometry. In particular, for a sharp uniform cylinder of radius $R_{\rm eff}$ one readily gets $T_A(r) = (A/\pi R_{\rm eff}^2)\theta(R_{\rm eff} - |\mathbf{r}|)$ and $T_{AB}(0) = A^2/\pi R_{\rm eff}^2$. We can therefore define the effective radius of the sharp cylinder equivalent to a diffuse Wood-Saxon geometry via $F(0,\phi)_{\rm Wood-Saxon} = F(0,\phi)_{\rm Sharp\ cylinder}$. For AuAu collisions and α = 1 the above constraint gives $R_{\rm eff} \approx 6$ fm.

For a non-vanishing impact parameter b and jet direction $\hat{v}(\phi)$, we calculate the energy loss as

$$\frac{\Delta E(b,\phi)}{E} = \frac{F(b,\phi)}{F(0,\phi)} \frac{\Delta E(0)}{E} \equiv R(b,\phi)\, \frac{\Delta E(0)}{E} \;, \qquad (2.100)$$

where the modulation function $R(b,\phi)$ captures in the *linearized* approximation the b and ϕ dependence of the jet energy loss and also provides a rough estimate of the maximum ellipticity generated via correlations to the reaction plane. Figure 2.34 shows the $R(b,\phi)$ modulation factor plotted against the azimuthal angle ϕ for impact parameters b = 2, 6, 10 fm. Note that $R(b,\phi)$ reflects not only the dimensions of the characteristic 'almond-shaped' cross section of the interaction volume but also the rapidly decreasing initial plasma density as a function of the impact parameter.

In order to compare to data at $p_T < 2$ GeV at RHIC and $p_T < 5$ GeV at LHC, one must also take into account the soft non-perturbative component that cannot be computed with the eikonal jet quenching formalism. The hydrodynamic elliptic flow [165] was found in [167] to have the monotonically growing form $v_{2s}(p_T) \approx \tanh(p_T/(10 \pm 2\ \text{GeV}))$ at $\sqrt{s}$ = 200 AGeV and to be less sensitive to the initial conditions than the high-p_T jet quenching studied here. The interpolation between the low-p_T relativistic hydrodynamics region and the high-p_T pQCD-computable region can be evaluated as in [81].

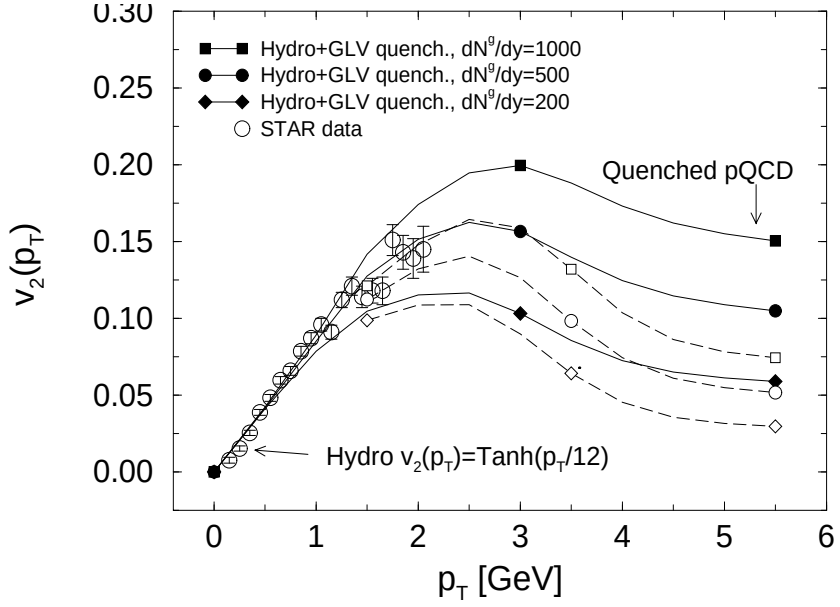

Fig. 2.35: The interpolation of $v_2(p_T)$ between the soft hydrodynamic [167] and hard pQCD regimes is shown for b = 7 fm adapted from Ref. [81]. Solid (dashed) curves correspond to sharp cylindrical (diffuse Wood-Saxon) geometries presented in Fig. 2.34.

Figure 2.35 shows the predicted pattern of high-p_T anisotropy. Note the difference between sharp cylinder and diffuse Wood-Saxon geometries at b = 7 fm approximating roughly 20–30% central events. While the central (b = 0) inclusive quenching is insensitive to the density profile, non-central events clearly exhibit large sensitivity to the actual distribution. We conclude that $v_2(p_T > 2$ GeV $b)$ provides essential complementary information about the geometry and impact parameter dependence of the initial conditions in AA. In particular, the rate at which the v_2 coefficient decreases at high p_T is an indicator of the diffuseness of that geometry. Minimum bias STAR data at RHIC [129, 176] for $p_T \geq 6$ GeV now seem to support the predicted [81, 162] slow decrease of v_2 at large transverse momenta. Recently in Ref. [8] hadron suppression in AuAu (PbPb) relative to the binary scaled pp result at $p_T \simeq 5$ GeV for RHIC conditions $(\sqrt{s}_{NN}, dN^g/dy)$ was found to be approximately equal to the quenching factor at LHC at a much larger transverse momentum scale $p_T \simeq 50$ GeV. One may thus anticipate proportionally large ($\sim$ 10–15%) azimuthal asymmetry for high p_T at the LHC.

Energy loss of jets in transversely expanding medium. We next address the question of the effect of possibly large transverse expansion in relativistic heavy ion reactions on v_2. In non-central collisions, the azimuthal asymmetry of the mean energy loss can be expanded in a Fourier series and characterized as

$$\Delta E^{(1)}_{3D}(\phi) \quad = \quad \Delta E(1 + 2\delta_2(E)\cos 2\phi + \cdots) \; . \tag{2.101}$$

It is correlated to the final measured elliptic 'flow' of jets and hadrons and has been evaluated by using a full hydrodynamic calculation from Ref. [167]. In this case we use the parameterization eBC of Ref. [167] to initialize the system and treat gluon number as conserved current to calculate the density evolution needed in the line integral Eq. (2.99), where it replaces the naive Bjorken $(\tau_0/\tau)^\alpha$ expansion. We average over the jet formation points the density of which is given by the number of binary collisions per unit area as in the Woods-Saxon geometry used in Ref. [81]. We find that the azimuthal asymmetry of the energy loss is strongly reduced for realistic hydrodynamic flow velocities. This implies a much smaller v_2 at high p_T than obtained in Ref. [81] where transverse expansion was not considered and poses questions about the observability of the effect at LHC.

LHC-specific remarks

There are several important aspects in which LHC and RHIC will differ significantly. We briefly discuss the implications of those differences for high-p_T v_2 measurements:

1. Currently at RHIC at $\sqrt{s}$ = 200 AGeV the $p_T \geq$ 2–3 GeV regime is perturbatively computable [8] (modulo uncertainties in the baryonic sector [52]). At LHC the p_T region which is not accessible through the pQCD approach may extend to transverse momenta as high as 5–10 GeV. This would imply the validity of the relativistic hydrodynamics in this domain, the extent of which can be tested by looking for marked deviations in the growth of $v_2(p_T)$, saturation, and turnover.
2. Estimates of the initial gluon rapidity density at LHC vary from dN^g/dy = 2500 to dN^g/dy = 8000. This would imply very large parton energy loss, at least in some regions of phase space. In this case jet production for moderate transverse momenta may be limited to a small shell on the surface of the interaction region, leading to a constant $v_2(p_T)$ purely determined by geometry Ref. [170].
3. Since mean transverse expansion velocities at RHIC have been estimated to be on the order of $v_T \simeq 0.5$ through relativistic hydrodynamics fits, it is natural to expect even larger values at LHC. This may lead to a significant reduction of the observed azimuthal asymmetry as discussed above. An important prediction of the approach put forth in Ref. [81] is that $v_2(p_T)$ exhibits a slow decrease with increasing transverse momentum. This can be used to distinguish azimuthal anisotropy generated through energy loss from alternative mechanisms.

Jet impact parameter dependence at the LHC. In light of the discussion in Section 3.4.6. it is important to assess the feasibility of azimuthal asymmetry measurements for large-E_T jets via detailed simulations. The impact parameter dependence of jet rates in PbPb collisions at the LHC was analysed in Ref. [33]. The initial jet spectra at $\sqrt{s}$ = 5.5 TeV were generated with PYTHIA 5.7 [48]. The initial distribution of jet pairs over impact parameter b of AA collisions (without collective nuclear effects) was obtained by multiplying the corresponding nucleon–nucleon jet cross section, $\sigma_{NN}^{\rm jet}$, by the number of binary nucleon–nucleon sub-collisions [177]:

$$\frac{d^2\sigma_{\rm jet}^0}{d^2b}(b,\sqrt{s}) = T_{AA}(b)\sigma_{NN}^{\rm jet}(\sqrt{s})\left[1-\left(1-\frac{1}{A^2}T_{AA}(b)\sigma_{NN}^{\rm in}(\sqrt{s})\right)^{A^2}\right] \qquad (2.102)$$

with the total inelastic non-diffractive nucleon–nucleon cross section $\sigma_{NN}^{\rm in} \simeq 60$ mb.

The rescattering and energy loss of jets in a gluon-dominated plasma, created initially in the nuclear overlap zone in PbPb collisions at different impact parameters, were simulated. For details of this model one can refer to [33,178]. To be specific, we treated the medium as a boost-invariant longitudinally expanding fluid according to Bjorken's solution [179] and used the initial conditions expected for central PbPb collisions at LHC [180–182]: formation time $\tau_0 \simeq 0.1$ fm/c, initial temperature $T_0 \simeq 1$ GeV, gluon plasma density $\rho_g \approx 1.95$ T^3. For our calculations we have used the collisional part of the energy loss and the differential scattering cross section from [33]; the energy spectrum of coherent medium-induced gluon radiation was estimated using the BDMS formalism [65].

The impact parameter dependences of the initial energy density ε_0 and the averaged over φ jet escape time $\langle\tau_L\rangle$ from the dense zone are shown in Fig. 2.36 [33]. $\langle\tau_L\rangle$ goes down almost linearly with increasing impact parameter b. On the other hand, ε_0 is very weakly dependent of b ($\delta\varepsilon_0/\varepsilon_0 \lesssim 10\%$) up to b on the order of nucleus radius R_A, and decreases rapidly only at $b \gtrsim R_A$. This suggests that for impact parameters $b < R_A$, where $\approx 60\%$ of jet pairs are produced, the difference in rescattering intensity and energy loss is determined mainly by the different path lengths rather than the initial energy density.

Figure 2.37 shows dijet rates in different impact parameter bins for $E_T^{\rm jet} > 100$ GeV and the pseudorapidity acceptance of central part of the CMS calorimeters, $|\eta^{\rm jet}| < 2.5$, for three cases: (i) without energy loss, (ii) with collisional loss only, (iii) with collisional and radiative loss. The total impact parameter integrated rates are normalized to the expected number of PbPb events during a two week LHC

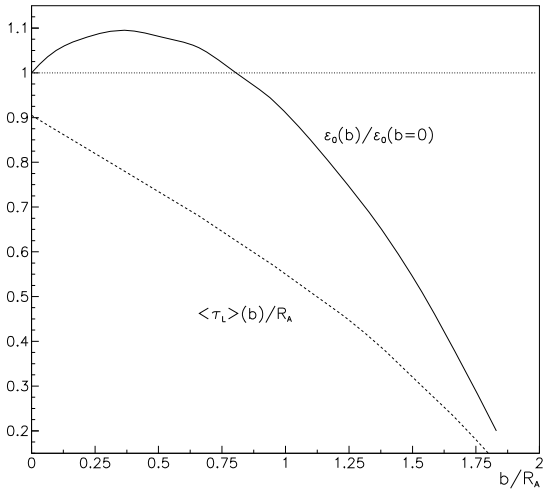

Fig. 2.36: The impact parameter dependence of the initial energy density $\varepsilon_0(b)/\varepsilon_0(b = 0)$ in nuclear overlap zone (solid curve), and the average proper jet escape time $\langle\tau_L\rangle / R_A$ of from the dense matter (dashed curve) [33].

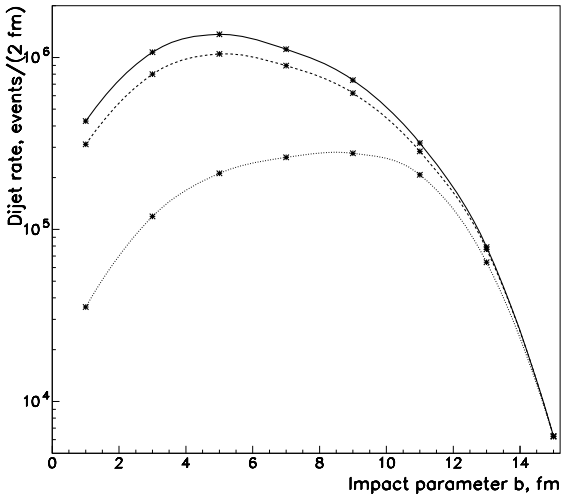

Fig. 2.37: The jet+jet rates for $E_T^{\rm jet} > 100$ GeV and $|\eta^{\rm jet}| < 2.5$ in different impact parameter bins: without energy loss (solid curve), with collisional loss (dashed curve), with collisional and radiative loss (dotted curve) [33].

run, R = 1.2 $\times$ 10^6 s, assuming luminosity L = 5 $\times$ 10^{26} cm^{-2}s^{-1}. The maximum and mean values of $dN^{\rm dijet}/db$ distribution get shifted towards the larger b, because jet quenching is much stronger in central collisions than in peripheral ones. Since the coherent Landau-Pomeranchuk-Migdal radiation induces a strong dependence of the radiative energy loss of a jet on the angular cone size [106, 114], the corresponding result for jets with non-zero cone size θ_0 is expected to be somewhere between (iii) ($\theta_0 \to 0$) and (ii) cases. Thus the observation of a dramatic change in the b-dependence of dijet rates in heavy ion collisions as compared to what is expected from independent nucleon–nucleon reaction pattern, would indicate the existence of medium-induced parton rescattering.

Of course, such kind of measurements require the adequate determination of impact parameter in nuclear collision with high enough accuracy. It has been shown in Ref. [183] that for the CMS experiment the very forward pseudorapidity region $3 \leq |\eta| \leq 5$ can provide a measurement of impact parameter via the energy flow in the very forward (HF) CMS calorimeters with resolution $\sigma_b \sim 0.5$ fm for central and semi-central PbPb collisions (see details in the section on jet detection at CMS).

Jet azimuthal anisotropy at the LHC. While at RHIC the *hadron* azimuthal asymmetry at high-p_T is being analysed, at LHC energies one can hope to observe similar effects for the hadronic jet itself [178] due to the large inclusive cross section for hard jet production on a scale $E_T \sim 100$ GeV.

The anisotropy of the energy loss (ΔE) goes up with increasing b, because the azimuthal asymmetry of the interaction volume gets stronger. However, the absolute value of the energy loss goes down with increasing b due to the reduced path length L (and ε_0 at $b \gtrsim R_A$, see Fig. 2.36). The non-uniform dependence of ΔE on the azimuthal angle φ is then mapped onto the jet spectra in semi-central collisions. Figure 2.38 from Ref. [178] shows the distribution of jets over φ for the cases with collisional and radiative loss (a) and collisional loss only (b) for b = 0, 6 and 10 fm. The same conditions and kinematical acceptance as in Fig. 2.37 were fulfilled. The distributions are normalized by the distributions of jets as a function of φ in PbPb collisions without energy loss. The azimuthal anisotropy becomes stronger in going from central to semi-central reactions, but the absolute suppression factor is reduced with increasing b. For jets with finite cone size one can expect the intermediate result between cases (a)

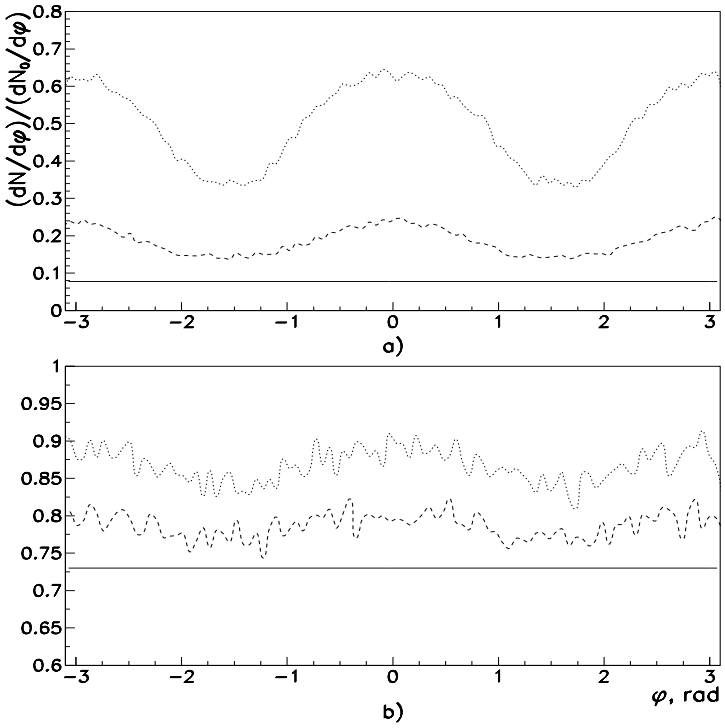

Fig. 2.38: The jet distribution over azimuthal angle for the cases with collisional and radiative loss (a) and collisional loss only (b), $E_T^{\rm jet} > 100$ GeV and $|\eta^{\rm jet}| < 2.5$ [178]. The histograms (from bottom to top) correspond to the impact parameter values $b =$ 0, 6 and 10 fm.

and (b), because, as we have mentioned before, radiative loss dominates at relatively small angular sizes of the jet cone $\theta_0 (\to 0)$, while the relative contribution of collisional loss grows with increasing θ_0.

In non-central collisions the jet distribution over φ is approximated well by the form $A(1 + B\cos 2\varphi)$, where $A = 0.5(N_{\rm max} + N_{\rm min})$ and $B = (N_{\rm max} - N_{\rm min})/(N_{\rm max} + N_{\rm min}) = 2\langle \cos 2\varphi \rangle$. In the model [178] the coefficient of jet azimuthal anisotropy, $v_2^{\rm jet} \equiv \langle \cos 2\varphi^{\rm jet} \rangle_{\rm event}$, increases almost linearly with the impact parameter b and becomes maximum at $b \sim 1.2\, R_A$. After that $v_2^{\rm jet}$ drops rapidly with increasing b: this is the domain of impact parameter values where the effect of decreasing energy loss due to the reduction of the effective transverse size of the dense zone and the initial energy density of the medium is crucial and cannot be compensated by the stronger volume ellipticity. Anther important feature is that the jet azimuthal anisotropy decreases with increasing jet energy, because the energy dependence of medium-induced loss is rather weak (absent in the BDMS formalism and $\sim \ln E$ in the GLV formalism for the radiative part at high E_T).

The advantage of azimuthal jet observables is that one needs to reconstruct only the direction of the jet, not its total energy. It can be done with high accuracy, while reconstruction of the jet energy is more ambiguous. However, analysis of jet production as a function of the azimuthal angle requires event-by-event measurement of the angular orientation of the reaction plane. The methods summarized in Ref. [163, 164, 184] present ways for reaction plane determination. They are applicable for studying anisotropic particle flow in current heavy ion dedicated experiments at the SPS and RHIC, and may be also used at the LHC [178]. Recently a method for measuring jet azimuthal anisotropy coefficients without event-by-event reconstruction of the reaction plane was proposed [185]. This technique is based on the correlations between the azimuthal position of jet axis and the angles of hadrons not incorporated in the jet. The method has been generalized by taking as weights the particle momenta or the energy deposition in the calorimetric sectors. It was shown that the accuracy of the method improves with

increasing multiplicity and particle (energy) flow azimuthal anisotropy, and is practically independent of the absolute values of azimuthal anisotropy of the jet itself.

Conclusions The azimuthal anisotropy of high-p_T hadron production in non-central heavy ion collisions is shown to provide a valuable experimental tool for studying both gluon bremsstrahlung in non-abelian media and the properties of the reaction volume such as its size, shape, initial parton (number and energy) rapidity densities, and their subsequent dynamical evolution. The *saturation* and the *gradual decrease* at large transverse momentum of the reaction geometry generated v_2, predicted as a signature complementary to jet quenching of strong radiative energy loss in a dense QCD plasma [81], seem now supported by preliminary data extending up to $p_T \simeq 10$ GeV at RHIC.

The initial gluon densities in PbPb reactions at $\sqrt{s}_{NN}$ = 5.5 TeV at the Large Hadron Collider are expected to be significantly higher than at RHIC, implying even stronger partonic energy loss. This may result in interesting novel features of jet quenching, such as modification of the jet distribution over impact parameter [33] in addition to the azimuthal anisotropy of the jet spectrum. The predicted large cross section for hard jet production on a scale of $E_T \sim 100$ GeV will allow for a systematic study of the differential nuclear geometry related aspects of jet physics at the LHC.

3.4.7. Rapidity distribution and jets

I.P. Lokhtin, S.V. Shmatov and P.I. Zarubin

Medium-induced parton energy loss may result in observable modifications in the rapidity distributions of the transverse energy flow and charged multiplicity, $dE_T/d\eta$, $dE_T^{\gamma}/d\eta$, and $dn_{ch}/d\eta$ [183, 186].

Indeed, in several Monte Carlo simulations of ultrarelativistic heavy ion collisions, one observes for example the appearance of a wide bump in the pseudo-rapidity interval $-2 \lesssim \eta \lesssim 2$, which is due to jet quenching. Figure 2.39 from [183] demonstrates the evolution of the effect in PbPb collisions as a function of impact parameter (HIJING [160, 187] prediction for $\sqrt{s}$ = 5.5 A TeV). One can see that even peripheral PbPb collisions show the effects of energy loss with the central enhancement still evident at impact parameters up to 12 fm. Since jet quenching due to final state re-interactions is effective only for the mid-rapidity region (where the initial energy density of minijet plasma is high enough), the very forward rapidity region, $|\eta| \gtrsim 3$, remains practically unchanged. A scan of collisions of different nuclear systems provides an additional test of jet quenching. Because smaller nuclei require a shorter transverse distance for the partons to traverse before escaping the system, the central enhancement due to energy loss decreases with system size as obvious from the comparison with and without energy loss. Although the effect has only been shown here for the global E_T distributions $dE_T/d\eta$, qualitatively the same picture is seen when neutral or charged particle production is studied instead of E_T.

The greater the medium-induced energy loss, the more transverse energy is piled up at central η values. This leads to an increase in energy density or 'stopping' in the mid-rapidity region, in contradiction to the assumption of nuclear transparency. Results qualitatively similar to those shown in Fig. 2.39 can be obtained using the VENUS generator [188] or the Parton Cascade Model VNI [189, 190]. However, the physics of the VENUS nucleon rescattering or VNI parton rescattering modes is very different from that of the radiative energy loss mechanism in HIJING. This may be due to the fact that various different nuclear collective effects provide effective forms of 'nuclear stopping'.

One can consider rapidity spectrum of jets itself or high-p$_T$ products of jet fragmentation (the latter case has been discussed for RHIC energy in paper [191]). One expects an anti-correlation between the rapidity distribution of the hard jets and the global $dE_T/d\eta$ spectrum: in the region in which jets are suppressed most, the multiplicity should be the highest. Since jet quenching due to in-medium parton energy loss is strongest in mid-rapidity, the maximal suppression of jet rates as compared to what is expected from independent nucleon–nucleon interactions extrapolation can be observed at central rapidity, while the very forward rapidity domain remains again almost unchanged. Thus analysing the correlation between rapidity distributions of global energy (particle) flow and hard jets, by scanning the

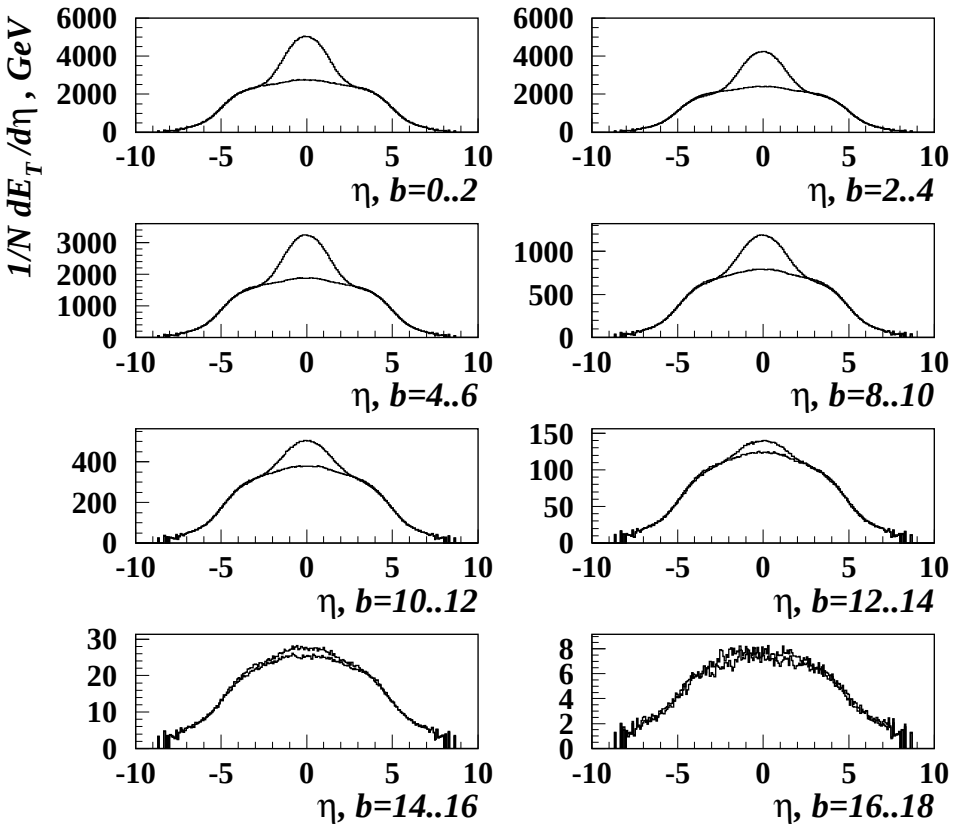

Fig. 2.39: Normalized differential distribution of the total transverse energy $dE_T/d\eta$ over pseudo-rapidity η for 10000 minimum bias PbPb collisions at $\sqrt{s}$ = 5.5 A TeV for various impact parameters [183]. The two cases are included: with jet quenching (the top histogram) and without jet quenching (the lower histogram).

wide rapidity region (up to $|\eta| \leq 5$ under acceptance of CMS experiment [192]), might provide the important information about the pseudo-rapidity size of dense QCD-matter area.

3.5. Medium Enhanced Higher Twist Effects

3.5.1. Formalism of medium enhanced higher twist effects

R.J. Fries

In perturbative QCD the so-called leading twist approximation is widely used to describe a large class of phenomena. There are quantities of non-perturbative nature which cannot be described by perturbation theory, e.g. the bound states of QCD. Nevertheless it is possible to separate perturbative (short range) and non-perturbative (long range) physics in a scattering reaction. Factorization theorems (see e.g. Ref. [193]) enable us to shift non-perturbative physics into a set of well-defined, gauge-invariant (i.e. observable) and universal (i.e. process independent) quantities. These quantities can be expressed by matrix elements of parton operators between hadron states.

It is possible to establish a hierarchy between the matrix elements in terms of an expansion in inverse powers of the momentum transfer. The expansion parameter is λ^2/Q^2, where Q is the perturbative hard scale and λ (for massless QCD) has to be some non-perturbative scale. The leading contribution in this expansion is called leading twist or (in the cases relevant here) twist-2. Factorization theorems can strictly be proved only for certain processes and only up to a certain level of higher twist (see Section 2 of Chapter 1).

The leading twist contribution always consists of one hard scattering on the parton level. In the simple example of deep inelastic scattering, the showcase for pQCD, the hard scattering takes place

between the virtual photon and a quark from the target. The non-perturbative part is described by a matrix element which encodes the process of taking one quark out of the nucleon and putting it back (in the complex conjugated graph). These matrix elements define the well known parton distributions $f_q \sim \langle \bar{q}q \rangle$, $f_g \sim \langle FF \rangle$ for quarks and gluons respectively.

In a nuclear environment, more precisely in AA collisions, the factorization theorems are still valid, but obviously the picture of a dominant single hard scattering process is doubtful. From the point of view of the twist expansion, the matrix elements which are factors in front of the expansion parameter λ^2/Q^2, can be numerically larger compared to the case of the same observable in pp collisions. This is clear since the matrix elements encode the non-perturbative long-range behaviour and will be sensitive to the size of the system. In fact parton distributions are expected to scale roughly with the mass number A of the nucleus, when we neglect shadowing corrections for the moment. However it can happen that some higher twist matrix elements scale more strongly with the nuclear size. They have to contain more operators of parton fields, corresponding to more partons that enter the hard scattering. On the level of twist-4, for example, one has a matrix element of the form $T_{qg} \sim \langle \bar{q}qFF \rangle$ which is a correlator of a quark and a gluon. When the indices of the parton fields are contracted in the right way, this matrix element scales with $A^{4/3}$. Generally, on the level of twist-$(n+2)$, there exists a set of matrix elements that scale with $A^{1+n/3}$. These matrix elements are called nuclear enhanced. The reason for the additional factors of $A^{1/3}$ is, that the different partons can come from different nucleons in the nucleus.

These matrix elements and their nuclear enhancement explain the trivial fact that multiple scatterings are important in collisions of large nuclei. Luo, Qiu and Sterman pointed out some time ago [95, 194, 195], that for large nuclei with $A \gg 1$ one can replace the twist expansion by an effective expansion in $\lambda^2 A^{1/3}/Q^2$, keeping only the nuclear enhanced nuclear effects. These correspond to multiple scatterings on the parton level in the nuclear collision [196].

On the level of twist-4 there exist calculations for jet production in lepton or photon induced reactions on nuclei. They deal with the transverse momentum broadening in jet production [96] and the cross section for dijet production [195]. The twist-4 contributions in these cases correspond to an additional final state interaction of the jets, more precisely a rescattering of the outgoing jet in the nuclear medium. No attempt was made so far to calculate these medium corrections for hadron induced jet production or nucleus–nucleus collisions. For jet production in pA or AA a complete twist-4 calculation would contain both initial and final state interactions of the partons. For an overview of calculations available in the case of pA, see Chapter 1.

In the case of pure final state interactions there are two important mechanisms at the level of twist-4. A parton that already underwent one hard scattering and is on the mass shell afterwards can interact with the soft gluon field of the nucleus, see Fig. 2.40. The second important case is that the parton leaving the primary hard scattering interacts with a hard parton from the nucleus and has to radiate a gluon in order to fall back onto the mass shell. This medium induced radiation is shown in Fig. 2.41.

The factorization formula for the cross section for the twist-4 contribution of hadron induced double scattering takes the form

$$\sigma \sim f_A \otimes H_{AB} \otimes T_B + T_A \otimes H_{BA} \otimes f_B \,, \tag{2.103}$$

where f_A, f_B are parton distributions for nucleus A, B respectively, describing one parton entering the parton cross sections H_{AB}, H_{BA}. T_A, T_B are nuclear enhanced twist-4 matrix elements, describing two partons from the respective nucleus. The generalization of double scattering (twist-4) to arbitrary nuclear enhanced twist is possible in situations where factorization theorems allow, see Chapter 1.

For quantitative estimates models for the twist-4 matrix elements have to be introduced. For soft hard matrix elements the effect of the soft gluon amounts to the appearance of an additional soft energy scale λ. The dependence on the parton momentum fraction of the hard parton is taken to be the same as in the parton distribution of this parton. One therefore sets $T^{SH} = \lambda^2 A^{4/3} f$ where f is the parton distribution of the hard parton normalized to one nucleon. Similarly double hard matrix elements are

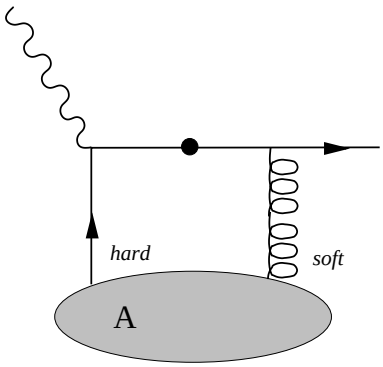

Fig. 2.40: Soft hard scattering: the parton from the primary hard scattering is on the mass shell (indicated by the blob) and scatters off a soft gluon. The soft gluon together with the parton that enters the primary hard scattering from the nucleus is described by a so-called soft hard matrix element T^{SH} of twist-4.

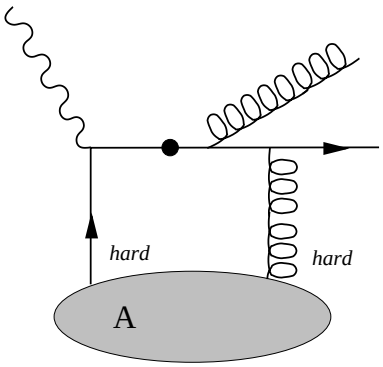

Fig. 2.41: Double hard scattering: the parton from the primary hard scattering is on the mass shell and undergoes an interaction with a second hard parton. It has to radiate a gluon to come back to the mass shell. The two hard partons from the nucleus are described by a so-called double hard matrix element T^{DH} of twist-4.

approximated by the product of the two parton distributions for both partons $T^{DH} = CA^{4/3} f_1 f_2$, C is normalization constant.

3.5.2. Parton energy loss and modified fragmentation functions

E. Wang, X.N. Wang and B. Zhang

The formalism of medium-induced higher twist effects was extended recently to the calculation of medium effects on fragmentation functions [117, 118]. This is of importance for jet physics at LHC since the energy loss of a parton cannot be observed directly. One has to resort to particle distributions within a jet and study the effect of parton energy loss by measuring the modification of the fragmentation function of the produced parton, $D_{a\to h}(z,\mu^2)$ which can be measured directly. This modification can be directly translated into the energy loss of the leading parton.

Here we give an account of this approach which so far includes applications to eA DIS and AuAu collisions at RHIC. The main results will be seen to be consistent with calculations described in Section 3.1.

Parton energy loss in a nuclear medium. As a first example, we consider the process eA DIS [117, 118, 197]. Here, we consider the semi-inclusive processes, $e(L_1) + A(p) \longrightarrow e(L_2) + h(\ell_h) + X$, where L_1 and L_2 are the four-momenta of the incoming and the outgoing leptons, and ℓ_h is the observed hadron momentum. The differential cross section for the semi-inclusive process can be expressed as

$$E_{L_2} E_{\ell_h} \frac{d\sigma^h_{\rm DIS}}{d^3 L_2 d^3 \ell_h} = \frac{\alpha^2_{\rm EM}}{2\pi s} \frac{1}{Q^4} L_{\mu\nu} E_{\ell_h} \frac{dW^{\mu\nu}}{d^3 \ell_h} \ , \tag{2.104}$$

where $p = [p^+, 0, \mathbf{0}_T]$ is the momentum per nucleon in the nucleus, $q = L_2 - L_1 = [-Q^2/2q^-, q^-, \mathbf{0}_T]$ the momentum transfer, $s = (p + L_1)^2$ and $\alpha_{\rm EM}$ is the electromagnetic (EM) coupling constant. $L_{\mu\nu}$ is the leptonic tensor while $W_{\mu\nu}$ is the semi-inclusive hadronic tensor.

In the parton model with the collinear factorization approximation, the leading-twist contribution to the semi-inclusive cross section can be factorized into a product of parton distributions, parton fragmentation functions and the partonic cross section. Including all leading log radiative corrections, the

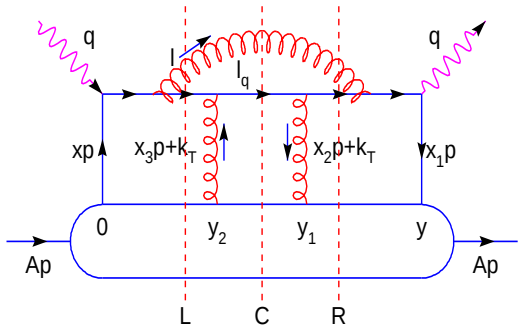

Fig. 2.42: A typical diagram for quark–gluon re-scattering processes with three possible cuts, central (C), left (L) and right (R)

lowest order contribution ($\mathcal{O}(\alpha_s^0)$) from a single hard $\gamma^* + q$ scattering can be written as

$$\frac{dW^S_{\mu\nu}}{dz_h} = \sum_q e_q^2 \int dx f_q^A(x,\mu_I^2) H^{(0)}_{\mu\nu}(x,p,q) D_{q\to h}(z_h,\mu^2)\,. \tag{2.105}$$

Here, $H^{(0)}_{\mu\nu}(x,p,q)$ is the LO hard matrix element. The momentum fraction carried by the hadron is defined as $z_h = \ell_h^-/q^-$ and $x_B = Q^2/2p^+q^-$ is the Bjorken variable. μ_I^2 and μ^2 are the factorization scales for the initial quark distributions $f_q^A(x,\mu_I^2)$ in a nucleus and the fragmentation functions $D_{q\to h}(z_h,\mu^2)$, respectively.

In a nuclear medium, the propagating quark in DIS will experience additional scatterings with other partons from the nucleus. The rescatterings may induce additional gluon radiation and cause the leading quark to lose energy. Such induced gluon radiations will effectively give rise to additional terms in the evolution equation leading to the modification of the fragmentation functions in a medium. These are the so-called higher-twist corrections since they involve higher-twist parton matrix elements and are power-suppressed. We will consider those contributions that involve two-parton correlations from two different nucleons inside the nucleus.

The generalized factorization is usually applied to these multiple scattering processes [95, 194, 195]. In this approximation, the double scattering contribution to radiative correction from processes like the one illustrated in Fig. 2.42 can be written in the following form,

$$\frac{W^{D,q}_{\mu\nu}}{dz_h} = \sum_q \int dx H^{(0)}_{\mu\nu}(xp,q) \int_{z_h}^1 \frac{dz}{z} D_{q\to h}(z_h/z) \frac{\alpha_s}{2\pi} C_A \frac{1+z^2}{1-z} \int \frac{d\ell_T^2}{\ell_T^4} \frac{2\pi\alpha_s}{N_c} T_{qg}^A(x,x_L)\,. \tag{2.106}$$

Here, $T_{qg}^A(x,x_L)$ twist-four parton matrix elements of the nucleus which can be expressed in terms of $\langle A|\bar\psi_q(0)\,\gamma^+\,F_\sigma{}^+(y_2^-)\,F^{+\sigma}(y_1^-)\,\psi_q(y^-)|A\rangle$. The fractional momentum is defined as $x_L = \ell_T^2/2p^+q^-z(1-z)$ and $x = x_B = Q^2/2p^+q^-$ is the Bjorken variable.

Using the factorization approximation [95, 117–119, 194, 195], they can be related to the twist-2 parton distributions of nucleons and the nucleus,

$$T_{qg}^A(x,x_L) = \frac{C}{x_A}(1-e^{-x_L^2/x_A^2})\Big[f_q^A(x+x_L)\,x_T f_g^N(x_T) + f_q^A(x)(x_L+x_T) f_g^N(x_L+x_T)\Big]\,, \tag{2.107}$$

where C is a constant, $x_A = 1/MR_A$, $f_q^A(x)$ is the quark distribution inside a nucleus, and $f_g^N(x)$ is the gluon distribution inside a nucleon. A Gaussian distribution in the light-cone coordinates was assumed

for the nuclear distribution, $\rho(y^-) = \rho_0 \exp(y^{-2}/2R_A^{-2})$, where $R_A^- = \sqrt{2}R_A M/p^+$ and M is the nucleon mass. We should emphasize that the twist-4 matrix element is proportional to $1/x_A = R_A M$, or the nuclear size [119].

Including the virtual corrections and the single scattering contribution, we can rewrite the semi-inclusive tensor in a factorized form with a nuclear modified fragmentation function,

$$\begin{aligned}\widetilde{D}_{q\to h}(z_h,\mu^2) &\equiv D_{q\to h}(z_h,\mu^2) + \int_0^{\mu^2}\frac{d\ell_T^2}{\ell_T^2}\frac{\alpha_s}{2\pi}\int_{z_h}^1\frac{dz}{z}\left[\Delta\gamma_{q\to qg}(z,x,x_L,\ell_T^2)D_{q\to h}(z_h/z)\right.\\ &+ \left.\Delta\gamma_{q\to gq}(z,x,x_L,\ell_T^2)D_{g\to h}(z_h/z)\right], \qquad (2.108)\end{aligned}$$

where $D_{q\to h}(z_h,\mu^2)$ and $D_{g\to h}(z_h,\mu^2)$ are the leading-twist fragmentation functions. The modified splitting functions are given as

$$\Delta\gamma_{q\to qg}(z,x,x_L,\ell_T^2) = \left[\frac{1+z^2}{(1-z)_+}T_{qg}^A(x,x_L) + \delta(1-z)\Delta T_{qg}^A(x,\ell_T^2)\right]\frac{2\pi\alpha_s C_A}{\ell_T^2 N_c \widetilde{f}_q^A(x,\mu_I^2)}, \qquad (2.109)$$

$$\Delta\gamma_{q\to gq}(z,x,x_L,\ell_T^2) = \Delta\gamma_{q\to qg}(1-z,x,x_L,\ell_T^2). \qquad (2.110)$$

To further simplify the calculation, we assume $x_T \ll x_L \ll x$. The modified parton matrix elements can be approximated by

$$T_{qg}^A(x,x_L) \approx \frac{\widetilde{C}}{x_A}(1-e^{-x_L^2/x_A^2})f_q^A(x), \qquad (2.111)$$

where $\widetilde{C} \equiv 2Cx_T f_g^N(x_T)$ is a coefficient which should in principle depend on Q^2 and x_T. Here we will simply take it as a constant.

In the above matrix element, one can identify $1/x_L p^+ = 2q^- z(1-z)/\mu^2$ as the formation time of the emitted gluons. For large formation time as compared to the nuclear size, the above matrix element vanishes, demonstrating a typical LPM interference effect. Additional scattering will not induce more gluon radiation, thus limiting the energy loss of the leading quark.

Since the LPM interference suppresses gluon radiation whose formation time ($\tau_f \sim Q^2/\ell_T^2 p^+$) is larger than the nuclear size MR_A/p^+ in our chosen frame, ℓ_T^2 should then have a minimum value of $\ell_T^2 \sim Q^2/MR_A \sim Q^2/A^{1/3}$. Here M is the nucleon mass. Therefore, the leading higher-twist contribution proportional to $\alpha_s R_A/\ell_T^2 \sim \alpha_s R_A^2/Q^2$ due to double scattering depends quadratically on the nuclear size R_A.

With the assumption of the factorized form of the twist-4 nuclear parton matrices, there is only one free parameter $\widetilde{C}(Q^2)$ which represents quark–gluon correlation strength inside nuclei. Once it is fixed, one can predict the z, energy and nuclear dependence of the medium modification of the fragmentation function. Shown in Fig. 2.21 are the nuclear modification factor of the fragmentation functions for ^{14}N and ^{84}Kr targets as compared to the recent HERMES data [122, 198]. The predicted shape of the z- and ν-dependence agrees well [6] with the experimental data. A remarkable feature of the prediction is the quadratic $A^{2/3}$ nuclear size dependence, which is verified for the first time by an experiment. By fitting the overall suppression for one nuclear target, we obtain the only parameter in our calculation, $\widetilde{C}(Q^2)$ = 0.0060 GeV^2 with $\alpha_s(Q^2)$ = 0.33 at $Q^2 \approx 3$ GeV^2.

We can quantify the modification of the fragmentation by the quark energy loss which is defined as the momentum fraction carried by the radiated gluon,

$$\begin{aligned}\langle\Delta z_g\rangle(x_B,\mu^2) &= \int_0^{\mu^2}\frac{d\ell_T^2}{\ell_T^2}\int_0^1 dz\frac{\alpha_s}{2\pi}z\,\Delta\gamma_{q\to gq}(z,x_B,x_L,\ell_T^2)\\ &= \widetilde{C}\,\frac{C_A\alpha_s^2}{N_c}\,\frac{x_B}{x_A Q^2}\int_0^1 dz\frac{1+(1-z)^2}{z(1-z)}\int_0^{x_\mu}\frac{dx_L}{x_L^2}(1-e^{-x_L^2/x_A^2}), \qquad (2.112)\end{aligned}$$

where $x_\mu = \mu^2/2p^+q^-z(1-z) = x_B/z(1-z)$ if we choose the factorization scale as $\mu^2 = Q^2$. When $x_A \ll x_B \ll 1$ we can estimate the leading quark energy loss roughly as

$$\langle \Delta z_g \rangle(x_B, \mu^2) \approx \widetilde{C}\, \frac{C_A \alpha_s^2}{N_c}\, \frac{x_B}{Q^2 x_A^2}\, 6\sqrt{\pi}\, \ln \frac{1}{2x_B}\,. \tag{2.113}$$

Since $x_A = 1/MR_A$, the energy loss $\langle \Delta z_g \rangle$ thus depends quadratically on the nuclear size.

In the rest frame of the nucleus, $p^+ = m_N$, $q^- = \nu$, and $x_B \equiv Q^2/2p^+q^- = Q^2/2m_N\nu$. One can get the averaged total energy loss as $\Delta E = \nu \langle \Delta z_g \rangle \approx \widetilde{C}(Q^2)\alpha_s^2(Q^2) m_N R_A^2 (C_A/N_c) 3 \ln(1/2x_B)$. With the determined value of $\widetilde{C}$, $\langle x_B \rangle \approx 0.124$ in the HERMES experiment [122, 198] and the average distance $\langle L_A \rangle = R_A\sqrt{2/\pi}$ for the assumed Gaussian nuclear distribution, one gets the quark energy loss $dE/dL \approx 0.5$ GeV/fm inside a Au nucleus (see Section 3.1.4. for a comparison to other cold nuclear matter estimates).

Energy loss and jet quenching in hot medium at RHIC. To extend our study of modified fragmentation functions to jets in heavy-ion collisions and to relate to results obtained in the opacity expansion approach, we can assume $\langle k_T^2 \rangle \approx \mu^2$ (the Debye screening mass) and a gluon density profile $\rho(y) = (\tau_0/\tau)\theta(R_A - y)\rho_0$ for a one-dimensional expanding system. Since the initial jet production rate is independent of the final gluon density which can be related to the parton-gluon scattering cross section [62] [$\alpha_s x_T G(x_T) \sim \mu^2 \sigma_g$], one has then

$$\frac{\alpha_s T_{qg}^A(x_B, x_L)}{f_q^A(x_B)} \sim \mu^2 \int dy \sigma_g \rho(y) [1 - \cos(y/\tau_f)]\,, \tag{2.114}$$

where $\tau_f = 2Ez(1-z)/\ell_T^2$ is the gluon formation time. One can recover the form of energy loss in a thin plasma obtained in the opacity expansion approach [81],

$$\langle \Delta z_g \rangle = \frac{C_A \alpha_s}{\pi} \int_0^1 dz \int_0^{\frac{Q^2}{\mu^2}} du \frac{1+(1-z)^2}{u(1+u)} \int_{\tau_0}^{R_A} d\tau \sigma_g \rho(\tau) \left[1 - \cos\left(\frac{(\tau - \tau_0)\, u\, \mu^2}{2Ez(1-z)}\right)\right]. \tag{2.115}$$

Keeping only the dominant contribution and assuming $\sigma_g \approx C_a 2\pi\alpha_s^2/\mu^2$ (C_a=1 for qg and 9/4 for gg scattering), one obtains the averaged energy loss,

$$\langle \frac{dE}{dL} \rangle \approx \frac{\pi C_a C_A \alpha_s^3}{R_A} \int_{\tau_0}^{R_A} d\tau \rho(\tau)(\tau - \tau_0) \ln \frac{2E}{\tau \mu^2}\,. \tag{2.116}$$

Neglecting the logarithmic dependence on τ, the averaged energy loss in a one-dimensional expanding system can be expressed as $\langle \frac{dE}{dL} \rangle_{1d} \approx (dE_0/dL)(2\tau_0/R_A)$, where $dE_0/dL \propto \rho_0 R_A$ is the energy loss in a static medium with the same gluon density ρ_0 as in a 1-d expanding system at time τ_0. Because of the expansion, the averaged energy loss $\langle dE/dL \rangle_{1d}$ is suppressed as compared to the static case and does not depend linearly on the system size.

In order to calculate the effects of parton energy loss on the attenuation pattern of high p_T partons in nuclear collisions, we use a simpler effective modified fragmentation function [120, 199],

$$\begin{aligned} D'_{h/c}(z_c, Q^2, \Delta E_c) &= (1 - e^{-\langle \frac{\Delta L}{\lambda} \rangle}) \left[\frac{z'_c}{z_c} D^0_{h/c}(z'_c, Q^2) + \langle \frac{\Delta L}{\lambda} \rangle \frac{z'_g}{z_c} D^0_{h/g}(z'_g, Q^2) \right] \\ &+ e^{-\langle \frac{\Delta L}{\lambda} \rangle} D^0_{h/c}(z_c, Q^2)\,, \end{aligned} \tag{2.117}$$

where z'_c, z_g are the rescaled momentum fractions. The first term is the fragmentation function of the jet c after losing energy $\Delta E_c(p_c, \phi)$ due to *medium induced* gluon radiation. The second term is the feedback due to the fragmentation of the $N_g(p_c, \phi) = \langle \Delta L/\lambda \rangle$ radiated gluons. This effective model is

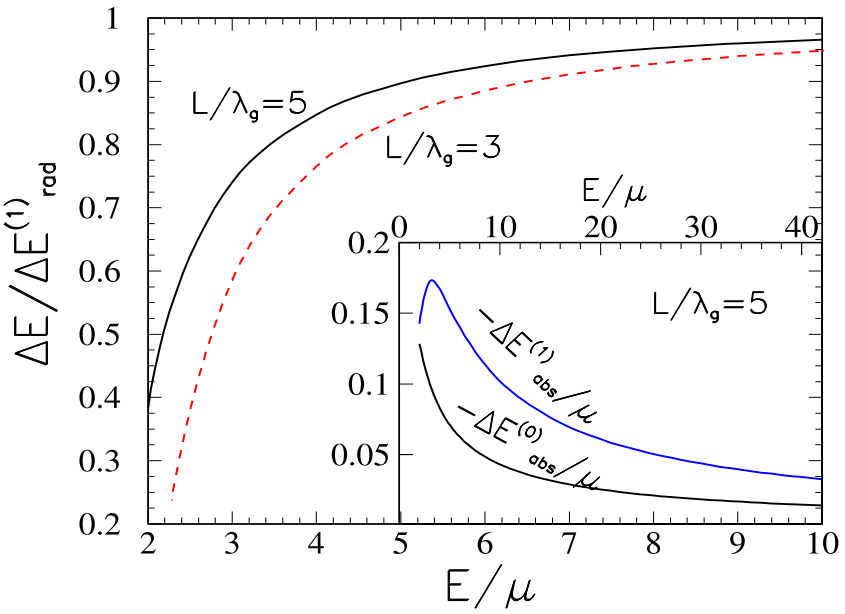

Fig. 2.43: The ratio of effective parton energy loss with ($\Delta E = \Delta E^{(0)}_{abs} + \Delta E^{(1)}_{abs} + \Delta E^{(1)}_{rad}$) and without ($\Delta E^{(1)}_{rad}$) absorption as a function of E/μ. Inserted box: energy gain via absorption with ($\Delta E^{(1)}_{abs}$) and without ($\Delta E^{(0)}_{abs}$) rescattering.

found to reproduce the pQCD result from Eq. (2.108) very well, but only when $\Delta z = \Delta E_c/E$ is set to be $\Delta z \approx 0.6\,\langle z_g\rangle$. Therefore the actual averaged parton energy loss should be $\Delta E/E = 1.6\,\Delta z$ with Δz extracted from the effective model. The factor 1.6 is mainly caused by the unitarity correction effect in the pQCD calculation.

Since gluons are bosons, there should also be stimulated gluon emission and absorption by the propagating parton because of the presence of thermal gluons in the hot medium. Such detailed balance is crucial for parton thermalization and should also be important for calculating the energy loss of an energetic parton in a hot medium [200]. Taking into account such detailed balance in gluon emission, one can then get the asymptotic behaviour of the effective energy loss in the opacity expansion framework [200],

$$\frac{\Delta E}{E} \approx \frac{\alpha_s C_F \mu^2 L^2}{4\lambda_g E}\left[\ln\frac{2E}{\mu^2 L} - 0.048\right] - \frac{\pi\alpha_s C_F}{3}\frac{LT^2}{\lambda_g E^2}\left[\ln\frac{\mu^2 L}{T} - 1 + \gamma_{\rm E} - \frac{6\zeta'(2)}{\pi^2}\right], \quad (2.118)$$

where the first term is from the induced bremsstralung and the second term is due to gluon absorption in detailed balance which effectively reduce the total parton energy loss in the medium.

Shown in Fig. 2.43 are numerical results of the ratios of the calculated radiative energy loss with and without stimulated emission and thermal absorption as functions of E/μ for L/λ_g = 3, 5 and α_s = 0.3. Shown in the inserted box are the energy gain via gluon absorption with ($\Delta E^{(1)}_{abs}$) and without ($\Delta E^{(0)}_{abs}$) rescattering. For partons with very high energy the effect of the gluon absorption is small and can be neglected. However, the thermal absorption reduces the effective parton energy loss by about 30–10% for intermediate values of parton energy. This will increase the energy dependence of the effective parton energy loss in the intermediate energy region. One can parameterize such energy dependence as,

$$\langle\frac{dE}{dL}\rangle_{1d} = \epsilon_0(E/\mu - 1.6)^{1.2}/(7.5 + E/\mu)\,, \quad (2.119)$$

The threshold is the consequence of gluon absorption that competes with radiation that effectively shuts off the energy loss. The parameter μ is set to be 1 GeV in the calculation.

To calculate the modified high p_T spectra in AA collisions, we use a LO pQCD model [201, 202],

$$\frac{d\sigma^h_{AA}}{dyd^2p_T} = K\sum_{abcd}\int d^2bd^2rdx_adx_bd^2k_{aT}d^2k_{bT}t_A(r)t_A(|\mathbf{b}-\mathbf{r}|)g_A(k_{aT},r)g_A(k_{bT},|\mathbf{b}-\mathbf{r}|) \times f_{a/A}(x_a,Q^2,r)f_{b/A}(x_b,Q^2,|\mathbf{b}-\mathbf{r}|)\frac{D'_{h/c}(z_c,Q^2,\Delta E_c)}{\pi z_c}\frac{d\sigma}{d\hat{t}}(ab\to cd)\,, \quad (2.120)$$

with medium modified fragmentation funcitons $D'_{h/c}$ given by Eq. 2.117 and the fragmentation functions in free space $D^0_{h/c}(z_c,Q^2)$ are given by the BBK parameterization [46]. Here, $z_c = p_T/p_{Tc}$, $y = y_c$, $\sigma(ab\to cd)$ are elementary parton scattering cross sections and $t_A(b)$ is the nuclear thickness function normalized to $\int d^2bt_A(b) = A$. We will use a hard-sphere model of nuclear distribution in this paper. The $K \approx 1.5$–2 factor is used to account for higher order pQCD corrections. The parton distributions per nucleon $f_{a/A}(x_a,Q^2,r)$ inside the nucleus are assumed to be factorizable into the parton distributions in a free nucleon given by the MRS D$-'$ parameterization and the impact-parameter dependent nuclear modification factor which will given by the new HIJING parameterization [203]. The initial transverse momentum distribution $g_A(k_T,Q^2,b)$ is assumed to have a Gaussian form with a width that includes both an intrinsic part in a nucleon and nuclear broadening. This model has been fitted to the nuclear modification of the p_T spectra in pA collisions at up to the Fermilab energy $\sqrt{s}$ = 40 GeV [201]. The initial multiple scattering in nuclei can give some moderate Cronin enhancement of the high p_T spectra. Therefore, any suppression of the high p_T spectra in AuAu collisions has to be caused by jet quenching.

We assume a one-dimensional expanding medium with a gluon density $\rho_g(\tau,r)$ that is proportional to the transverse profile of participant nucleons. According to Eq. (2.116), we will calculate impact-parameter dependence of the energy loss as

$$\Delta E(b,r,\phi) \approx \langle\frac{dE}{dL}\rangle_{1d}\int_{\tau_0}^{\Delta L}d\tau\frac{\tau-\tau_0}{\tau_0\rho_0}\rho_g(\tau,b,\vec{r}+\vec{n}\tau)\,, \quad (2.121)$$

where $\Delta L(b,\vec{r},\phi)$ is the distance a jet, produced at $\vec{r}$, has to travel along $\vec{n}$ at an azimuthal angle ϕ relative to the reaction plane in a collision with impact-parameter b. Here, ρ_0 is the averaged initial gluon density at τ_0 in a central collision and $\langle dE/dL\rangle_{1d}$ is the average parton energy loss over a distance R_A in a 1-d expanding medium with an initial uniform gluon density ρ_0. The corresponding energy loss in a static medium with a uniform gluon density ρ_0 over a distance R_A is [6] $dE_0/dL = (R_A/2\tau_0)\langle dE/dL\rangle_{1d}$. We will use the parameterization in Eq. (2.119) for the effective energy dependence of the parton quark energy loss.

Shown in Fig. 2.44 are the calculated nuclear modification factors $R_{AB}(p_T) = d\sigma^h_{AB}/\langle N_{\rm binary}\rangle d\sigma^h_{pp}$ for hadron spectra ($|y| < 0.5$) in AuAu collisions at $\sqrt{s}$ = 200 GeV, as compared to experimental data [124, 204–206]. Here, $\langle N_{\rm binary}\rangle = \int d^2bd^2rt_A(r)t_A(|\vec{b}-\vec{r}|)$. To fit the observed π^0 suppression (solid lines) in the most central collisions, we have used μ = 1.5 GeV, ϵ_0 = 1.07 GeV/fm and $\lambda_0 = 1/(\sigma\rho_0)$ = 0.3 fm. The hatched area (also in other figures in this paper) indicates a variation of $\epsilon_0 = \pm$ 0.3 GeV/fm. The hatched boxes around R_{AB} = 1 represent experimental errors in overall normalization. Nuclear k_T broadening and parton shadowing together give a slight enhancement of hadron spectra at intermediate p_T = 2–4 GeV/c without parton energy loss.

The flat p_T dependence of the π^0 suppression is a consequence of the strong energy dependence of the parton energy loss. The slight rise of R_{AB} at $p_T < 4$ GeV/c in the calculation is due to the detailed balance effect in the effective parton energy loss. In this region, one expects the fragmentation picture to gradually lose its validity and is taken over by other non-perturbative effects, especially for kaons and baryons. As a consequence, the $(K+p)/\pi$ ratio in central AuAu collisions is significant larger than in peripheral AuAu or pp collisions. To take into account this effect, we add a nuclear dependent (proportional to $\langle N_{\rm binary}\rangle$) soft component to kaon and baryon fragmentation functions so that $(K+p)/\pi \approx 2$ at $p_T \sim 3$ GeV/c in the most central AuAu collisions and approaches its pp value

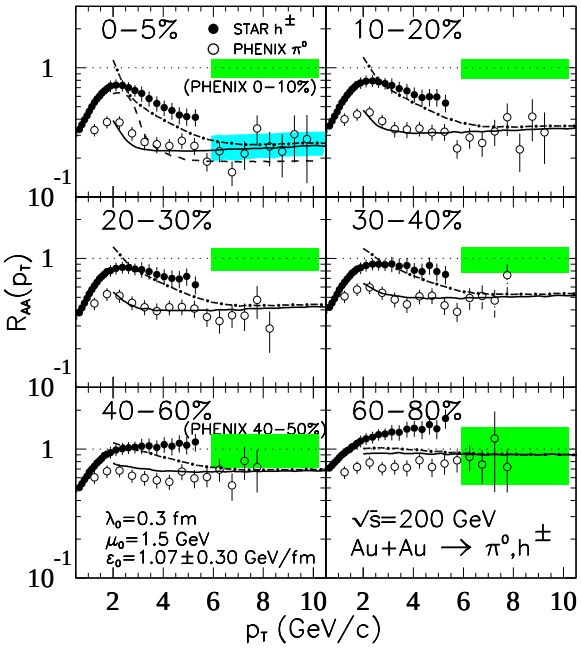

Fig. 2.44: Hadron suppression factors in AuAu collisions as compared to data from STAR [204, 205] and PHENIX [124, 206]. See text for a detailed explanation.

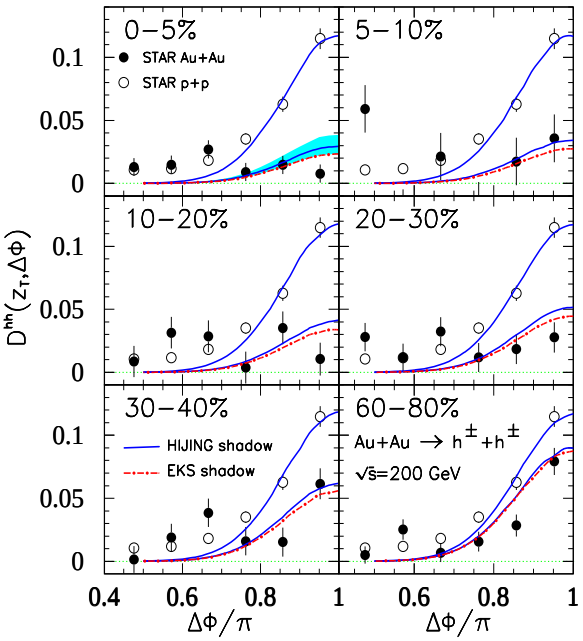

Fig. 2.45: Back-to-back correlations for charged hadrons with $p_T^{\rm trig} > p_T > 2$ GeV/c, $p_T^{\rm trig}$ = 4–6 GeV/c and $|y| < 0.7$ in AuAu (lower curves) and pp (upper curves) collisions as compared to the STAR [207] data.

at $p_T > 5$ GeV/c. The resultant suppression for total charged hadrons (dot-dashed) and the centrality dependence agree well with the STAR data. One can directly relate $h^\pm$ and π^0 suppression via the $(K+p)/\pi$ ratio: $R_{\rm AA}^{h^\pm} = R_{\rm AA}^{\pi^0}[1+(K+p)/\pi]_{AA}/[1+(K+p)/\pi]_{pp}$. It is clear from the data that $(K+p)/\pi$ becomes the same for AuAu and pp collisions at $p_T > 5$ GeV/c. To demonstrate the sensitivity to the parameterized parton energy loss in the intermediate p_T region, we also show $R_{\rm AA}^{h^\pm}$ in 0–5% centrality (dashed line) for μ = 2.0 GeV and ϵ_0 = 2.04 GeV/fm without the soft component.

In the same LO pQCD parton model, one can also calculate di-hadron spectra,

$$
\begin{aligned}
E_1E_2\frac{d\sigma_{AA}^{h_1h_2}}{d^3p_1d^3p_2} \;=\; & \frac{K}{2}\sum_{abcd}\int d^2bd^2rdx_adx_bd^2k_{aT}d^2k_{bT}t_A(r)t_A(|\mathbf{b}-\mathbf{r}|)g_A(k_{aT},r)g_A(k_{bT},|\mathbf{b}-\mathbf{r}|)\\
& \times f_{a/A}(x_a,Q^2,r)f_{b/A}(x_b,Q^2,|\mathbf{b}-\mathbf{r}|)D_{h/c}(z_c,Q^2,\Delta E_c)\\
& \times D_{h/d}(z_d,Q^2,\Delta E_d)\frac{\hat{s}}{2\pi z_c^2z_d^2}\frac{d\sigma}{d\hat{t}}(ab\to cd)\delta^4(p_a+p_b-p_c-p_d)\,, \qquad (2.122)
\end{aligned}
$$

for two back-to-back hadrons from independent fragmentation of the back-to-back jets. Let us assume hadron h_1 is a triggered hadron with $p_{T1} = p_T^{\rm trig}$. One can define a hadron-triggered FF as the back-to-back correlation with respect to the triggered hadron:

$$
D^{h_1h_2}(z_T,\phi,p_T^{\rm trig}) = \frac{d\sigma_{AA}^{h_1h_2}/d^2p_T^{\rm trig}dp_Td\phi}{d\sigma_{AA}^{h_1}/d^2p_T^{\rm trig}}\,, \qquad (2.123)
$$

similarly to the direct-photon triggered FF [120,199] in γ-jet events. Here, $z_T = p_T/p_T^{\rm trig}$ and integration over $|y_{1,2}| < \Delta y$ is implied. In a simple parton model, the two jets should be exactly back-to-back. The initial parton transverse momentum distribution in our model will give rise to a Gaussian-like angular distribution. In addition, we also take into account transverse momentum smearing within a jet using a

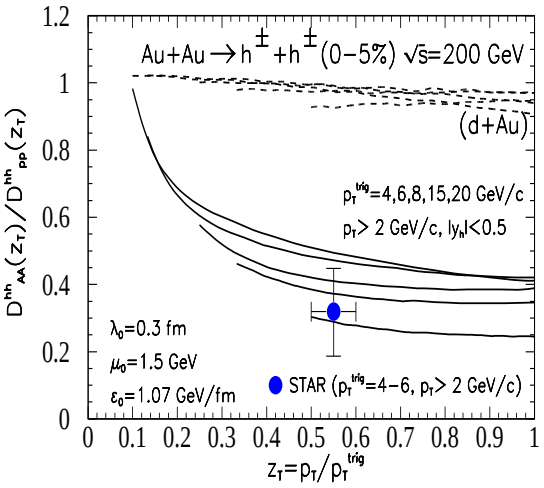

Fig. 2.46: The suppression factor for hadron-triggered fragmentation functions in central (0–5%) AuAu (dAu) collisions as compared to the STAR data [207]

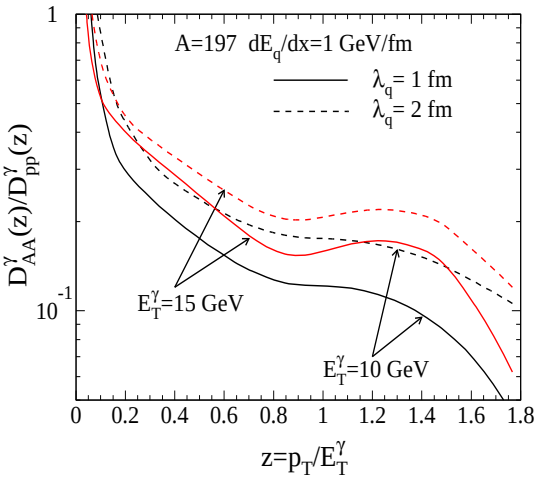

Fig. 2.47: The modification factor of the photon-tagged inclusive jet fragmentation function in central AuAu collisions at $\sqrt{s}$ = 200 GeV for a fixed dE_q/dx = 1 GeV/fm.

Gaussian distribution with a width of $\langle k_T \rangle = 0.6$ GeV/c. Hadrons from the soft component are assumed to be uncorrelated.

Shown in Fig. 2.45 are the calculated back-to-back correlations for charged hadrons in AuAu collisions as compared to the STAR data [207]. The same energy loss that is used to calculate single hadron suppression and azimuthal anisotropy can also describe well the observed away-side hadron suppression and its centrality dependence. In the data, a background $B(p_T)[1+2v_2^2(p_T)\cos(2\Delta\phi)]$ from uncorrelated hadrons and azimuthal anisotropy has been subtracted. The value of $v_2(p_T)$ is measured independently while $B(p_T)$ is determined by fitting the observed correlation in the region $0.75 < |\phi| < 2.24$ rad [207].

With both the single spectra and dihadron spectra, the extracted average energy loss in this model calculation for a 10 GeV quark in the expanding medium is $\langle dE/dL \rangle_{1d} \approx 0.85 \pm 0.24$ GeV/fm, which is equivalent to $dE_0/dL \approx 13.8 \pm 3.9$ GeV/fm in a static and uniform medium over a distance R_A = 6.5 fm. This value is about a factor of 2 larger than a previous estimate, Ref. [6] because of the variation of gluon density along the propagation path and the more precise RHIC data considered .

Integrating over ϕ, one obtains a hadron-triggered FF, $D^{h_1h_2}(z_T, p_T^{\rm trig}) = \int_{\pi/2}^{\pi} d\phi D^{h_1h_2}(z_T, \phi, p_T^{\rm trig})$. Shown in Fig. 2.46 are the suppression factors of the hadron-triggered FFs for different values of $p_T^{\rm trig}$ in central AuAu collisions as compared to a STAR data point that is obtained by integrating the observed correlation over $\pi/2 < |\Delta\phi| < \pi$. The dashed lines illustrate the small suppression of back-to-back correlations due to the initial nuclear k_T broadening in d+A collisions. The strong QCD scale dependence on $p_T^{\rm trig}$ of FFs is mostly cancelled in the suppression factor. The approximately universal shape reflects the weak p_T dependence of the hadron spectra suppression factor in Fig. 2.44, due to a unique energy dependence of parton energy loss. Shown in Fig. 2.47 are the suppresion factors for the direct-photon-tagged jet fragmentation function. They are very similar to the direct-triggered fragmentation function, except that the photon's energy is more closely related to the original jet energy.

3.6. Other Possible Medium-Modifications of High-p_T Hadronic Spectra

3.6.1. Recombination models at the LHC

R.J. Fries

Recent results from RHIC show interesting phenomena in hadron production at intermediate transverse momenta of 2 to 5 GeV/c. This is a region where perturbative QCD starts to be a valid description of hadron dynamics, but non-perturbative effects can still be expected to play a crucial role. The key observations at RHIC are the anomalous enhancement of baryon production, seen e.g. in a p/π^0 ratio of about one and the lack of nuclear suppression for baryons between 1.5 and 4 GeV/c [208] and the different behaviour of elliptic flow for mesons and baryons [209, 210].

These observations have lead to the hypothesis that hadron production at intermediate p_T is dominated by recombination from a hot and dense parton phase instead of fragmentation of fast partons from hard scatterings [56, 211–213]. In the recombination picture a quark–antiquark pair close in phase space can form a meson at hadronization, while three (anti)quarks can find together to be a (anti)baryon. The spectrum of mesons from recombination can be written as [214, 215]

$$E\,\frac{N_M}{d^3P} = C_M \int\limits_{\Sigma} d\sigma \frac{P\cdot u(\sigma)}{(2\pi)^3} \int\limits_0^1 dx\; w_a\big(\sigma; xP^+\big)\;\; |\phi_M(x)|^2\;\; w_b\big(\sigma;(1-x)P^+\big)\;, \tag{2.124}$$

if the energy E of the meson is large compared to $\Lambda_{\rm QCD}$ and the constituent quark masses. Here $\phi_M(x)$ is the meson wave function in light cone coordinates, x is the momentum fraction of one of the quarks, C_M is a degeneracy factor and the $w(\sigma;p)$ are classical phase space distributions of the partons before hadronization. Transverse momenta relative to the hadron momentum have been integrated out in this equation. A similar expression can be found for baryons.

One can easily show that recombination is more effective than fragmentation for an exponential parton spectrum. On the other hand, fragmentation will win over recombination at high P_T if the parton spectrum follows a power law. It has been shown that the shape of the wave function plays only little role if the input parton spectrum is exponential [215]. It is therefore a good approximation to assume that the momentum is equally shared by the valence quarks (1/2 for mesons, 1/3 for baryons). Note that the thermal parton phase at hadronization is assumed to have effective degrees of freedom with constituent quarks and no dynamical gluons.

It turns out that all spectra, the nuclear suppression factors and the anisotropic flow coefficient v_2 for hadrons in AuAu collisions at RHIC for $p_T > 1.5$ GeV/c can be explained by the competition between recombination from a thermalized parton phase with temperature T = 175 MeV and radial flow velocity v_T = 0.55 c (for central collisions) and pQCD fragmentation of hard partons including energy loss [215]. It is worthwhile to note that it is the strong energy loss of partons in the medium that allows recombination to dominate for $p_T < 4$ GeV/c for mesons and for $p_T < 6$ GeV/c for baryons.

Numerical estimates for LHC. In above calculations for RHIC the parameters for the parton phase were determined to match existing data on hadron production. To present estimates for LHC, we fix the temperature of the parton phase at hadronization again at 175 MeV as predicted by lattice QCD [104]. The average radial flow will be increased at LHC compared to RHIC. We choose v_T = 0.75 c as the radial flow velocity in accordance with [216]. The geometric assumptions about the fireball remain the same as those for RHIC [215]. This is certainly a lower bound for LHC.

The contribution from fragmentation is calculated in leading order (LO) pQCD using the parton spectrum given in [217] and KKP fragmentation functions [121]. The partonic energy loss is taken into account as in [215]. Its magnitude is fixed to match the mean nuclear suppression factor of about 0.1 for a 10 GeV pion at LHC estimated in [8].

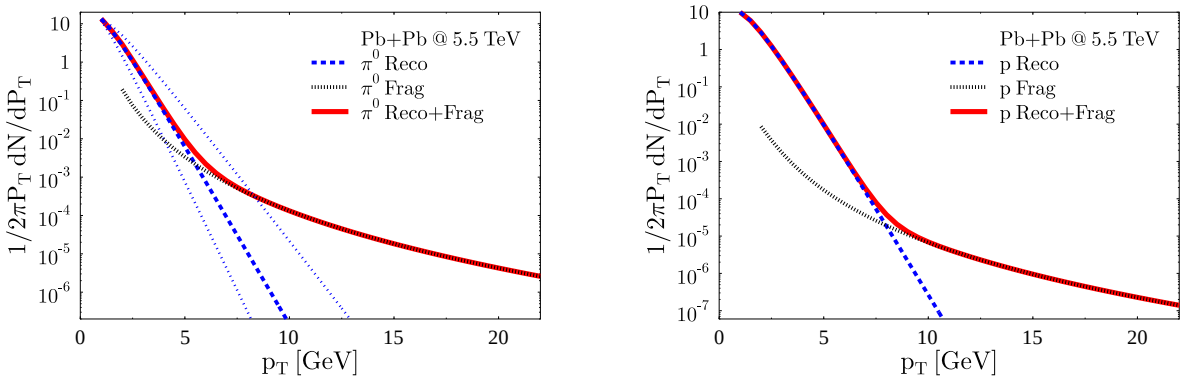

Fig. 2.48: Spectra of π^0 (left) and p (right) as a function of transverse momentum p_T at midrapidity for central PbPb collisions at $\sqrt{s}$ = 5.5 TeV. The recombination from the thermal parton phase (long dashed line), fragmentation with energy loss from LO pQCD (dotted line) and the sum of both (solid line) are shown. For π^0 we also give the recombination contribution for different values of the the radial flow v_T = 0.65 c (lower short dashed line) and v_T = 0.85 c (upper short dashed line).

In Fig. 2.48 we show the spectra for neutral pions and protons for central PbPb collisions at $\sqrt{s}$ = 5.5 TeV. The recombination part for π^0 is also given for two other values of the radial flow to estimate the theoretical uncertainty that is inherent in our ansatz for the parton phase. Larger emission volumes could shift the recombination curve trivially up without changing the slope while leaving the fragmentation contribution nearly unchanged.

The crossover between the fragmentation domain and the recombination domain is at about 6 GeV for pions (4 GeV at RHIC) and 8 GeV for protons (6 GeV at RHIC) using v_T = 0.75 c. A larger hadronization surface, as likely, will shift these values to even higher p_T. In Fig. 2.49 we show the ratio π^0/p from our calculation in comparison with the same quantity calculated for RHIC [215]. We note that the surprising baryon enhancement is shifted to even higher transverse momenta at LHC.

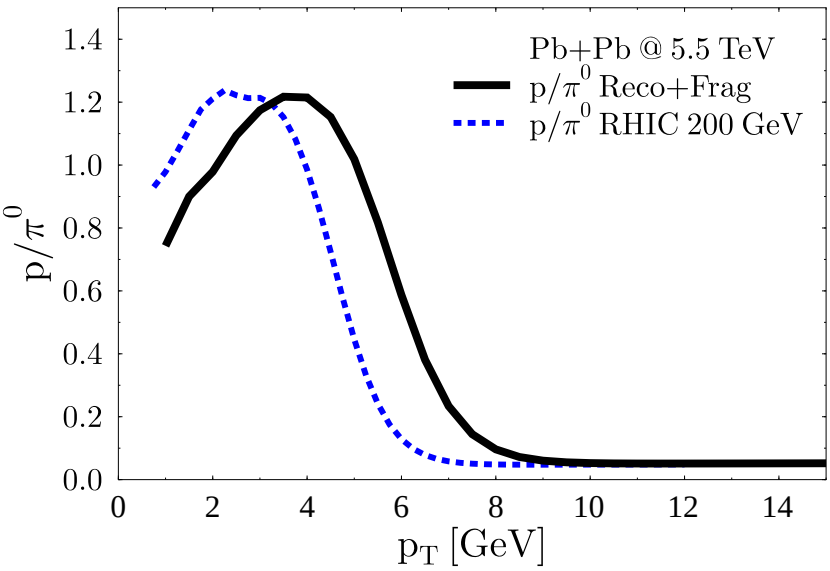

Fig. 2.49: The ratio p/π^0 in central PbPb collisions at LHC, $\sqrt{s}$ = 5.5 TeV, (solid line) and for AuAu collisions at RHIC, $\sqrt{s}$ = 200 GeV, (dashed line) [215]

3.6.2. *Transverse momentum diffusion and the broadening of the back-to-back di-hadron correlation function*

J.W. Qiu and I. Vitev

Multiple parton interactions in relativistic heavy-ion reactions result in transverse momentum diffusion and medium induced non-abelian energy loss of the hard probes traversing cold and hot nuclear matter. The corresponding modification of the single inclusive hadron spectra carries information about the dynamical properties of the medium created in such reactions and constitutes the basis for 'jet tomography' [5–8, 93, 126, 218]. It has been demonstrated that the competition between nuclear shadowing, multiple scattering and jet quenching may lead to distinctly different enhancement/suppression pattern of moderate and high-p_T hadron production in pA and AA collisions at SPS, RHIC and the LHC [8]. Additional experimental tools that can complement the single inclusive measurements, however, are highly desirable. A natural extension of the jet-tomographic technique, first quantitatively discussed in [219], is 'dijet tomography'. In this case the medium response to the propagation of hard partons leads to an associated increase of dijet acoplanarity [220–222], measured via the broadening of the back-to-back di-hadron correlation function [89,136], as well as to a quenching of the away-side Gaussian [136,202,224]. These experimental observables are potentially free of the uncertainties in Glauber scaling of the baseline pp result that are present in the comparison of single inclusive spectra.

Particle production from a single hard scattering with momentum exchange much larger than 1/fm is localized in space-time. It is multiple parton scattering before or after the hard collision that is sensitive to the properties of the nuclear matter. By comparing the high-p_T observables in pp, pA and AA reactions, we are able to study the strong interaction dynamics of QCD in the vacuum, cold nuclear matter and hot dense medium of quarks and gluons, respectively. We here address the elastic (no-radiation) scattering of jets ($\sqrt{p^2}/p^0 \simeq 0$) in nuclear matter [89, 90, 95, 97, 136, 195] that is sensitive to the zeroth line integral moment, $\int dz\ z^0 \rho(z) \propto \langle L \rangle / \lambda = \chi$, of the matter density. A closed form solution can be obtained via the GLV reaction operator approach [90]. Recently, we computed the power corrections due to the recoil of the medium [89] and related the momentum distribution of partons that have traversed nuclear matter to their initial distribution as follows:

$$\begin{aligned}
\frac{d^3N^f(p^+,\mathbf{p}_T)}{dp^+d^2\mathbf{p}_T}\Big|_{p^-=\frac{\mathbf{p}_T^2}{2p^+}} &= \sum_{n=0}^{\infty}\frac{\chi^n}{n!}\int\prod_{i=1}^{n}d^2\mathbf{q}_{i\perp} \\
&\times \left[\frac{1}{\sigma_{el}}\frac{d\sigma_{el}(R,T)}{d^2\mathbf{q}_{i\perp}}\left(e^{-\mathbf{q}_{i\perp}\cdot\vec{\nabla}_{\mathbf{p}_T}}\ e^{\frac{1}{2}(\mathbf{q}_{i\perp}^2/(\sqrt{2}P))\,\partial_{p^+}}-1\right)\right] \\
&\times \frac{d^3N^i(p^+,\mathbf{p}_T)}{dp^+d^2\mathbf{p}_T}\Big|_{p^-=\frac{\mathbf{p}_T^2}{2p^+}}\ .
\end{aligned} \tag{2.125}$$

For any initial jet flux the opacity series in Eq. (2.125) is most easily resummed in the impact parameter space $(b^-,\mathbf{b}_T)$ conjugate to $(p^+,\mathbf{p}_T)$. For the case of a normalized forward monochromatic beam $p^\mu = (P,\mathbf{0}_T,P)$ in the small angle scattering limit we find:

$$\frac{d^3N^f(p^+,\mathbf{p}_T)}{dp^+d^2\mathbf{p}_T}\Big|_{p^-=\frac{\mathbf{p}_T^2}{2p^+}} = \frac{1}{2\pi}\frac{e^{-\frac{\mathbf{p}_T^2}{2\,\chi\,\mu^2\,\xi}}}{\chi\,\mu^2\,\xi}\,\delta\left[p^+-\left(\sqrt{2}P-\frac{1}{2}\frac{2\chi\mu^2\xi}{\sqrt{2}P}\right)\right]\ . \tag{2.126}$$

The medium induced p_T broadening and the corresponding longitudinal momentum reduction can be evaluated from Eq. (2.126):

$$\langle\Delta\mathbf{p}_T^2\rangle \approx 2\xi\int dz\,\frac{\mu^2}{\lambda_{q,g}} = 2\xi\int dz\,\frac{3C_R\pi\alpha_s^2}{2}\rho^g(z) = \begin{cases} 2\xi\,\frac{3C_R\pi\alpha_s^2}{2}\,\rho^g\langle L\rangle\,, & \text{static} \\ 2\xi\,\frac{3C_R\pi\alpha_s^2}{2}\,\frac{1}{A_T}\frac{dN^g}{dy}\,\ln\frac{\langle L\rangle}{\tau_0}\,, & 1+1D \end{cases} \tag{2.127}$$

$$-\frac{dp_\parallel}{dz} \approx -\frac{\Delta p_\parallel}{\langle L\rangle} = \frac{\mu^2\,(2\xi)}{\lambda_{q,g}}\,\frac{1}{2p_\parallel} = \left(\frac{\mu^2}{\lambda_{q,g}}\right)_{eff}\frac{1}{2p_\parallel}\,. \tag{2.128}$$

In Eqs. (2.127) and (2.128) the factor 2 comes from 2D diffusion, $\xi \simeq \mathcal{O}(1)$ and ρ^g is the effective gluon density. For the 1+1D Bjorken expansion scenario A_T is the transverse area of the interaction region, τ_0 is the initial equilibration time and dN^g/dy is the effective gluon rapidity density. We note that $-\Delta p_\parallel$ may mimic small elastic energy loss if the full structure of $d^3N^f/dp^+d^2\mathbf{p}_T$ is not observed.

As an application of the multiple initial and final state elastic scattering formalism elaborated in Refs. [89, 90] we consider the nuclear induced broadening of the back-to-back jet correlations associated with hard QCD $ab \to cd$ partonic subprocesses. We will limit the discussion to the Gaussian 2D random walk approximation, Eq. (2.126), to make use of its additive dispersion property. Measurements of intra-jet correlations find an approximately Gaussian jet cone shape. If one defines $\langle|\mathbf{j}_{T\,y}|\rangle$ to be the average particle transverse momentum relative to the hard scattered parent parton in the plane normal to the collision axis, it can be related to the width σ_{Near} of the near-side ($\Delta\phi < \pi/2$) di-hadron correlation function $C(\Delta\phi) = N^{h_1,h_2}(\Delta\phi)/N_{tot}^{h_1,h_2}$ as follows: $\langle|\mathbf{j}_{T\,y}|\rangle = \langle|\mathbf{p}_T|\rangle \sin(\sigma_{Near}/\sqrt{\pi})$. It is the away-side ($\Delta\phi > \pi/2$) correlation function, however, that measures the dijet acoplanarity. The total vacuum+nuclear induced broadening for the two partons in a plane perpendicular to the collision axis in pA (AA) reads [89]:

$$\langle\mathbf{k}_T^2\rangle = \langle\mathbf{k}_T^2\rangle_{vac} + \begin{matrix}1_{jet}\\(2_{jets})\end{matrix}\left(\frac{\mu^2}{\lambda}\right)_{eff}\langle L\rangle_{IS} + 2_{jets}\left(\frac{1}{2}\right)_{projection}\left(\frac{\mu^2}{\lambda}\right)_{eff}\langle L\rangle_{FS}\,. \tag{2.129}$$

A typical range for the cold nuclear matter transport coefficient for gluons $(\mu^2/\lambda_g)_{eff,\,IS\approx FS}$ = 2 × 0.1 GeV^2/fm – 2 × 0.15 GeV^2/fm is extracted from the analysis of low energy pA data [8, 126]. This can be tested via the predicted Cronin enhancement in dAu collisions at RHIC $\sqrt{s}$ = 200 A GeV [8, 126], which compares well to BRAHMS, PHENIX, PHOBOS and STAR measurements [132–136]. For the case of FS scattering in a 1+1D Bjorken expanding quark–gluon plasma the final state broadening can be evaluated from Eq. (2.127). The relation between $\langle|\mathbf{k}_{T\,y}|\rangle = \sqrt{\langle\mathbf{k}_T^2\rangle_{1\,parton}/\pi}$, $\langle\mathbf{k}_T^2\rangle_{1\,parton} = \langle\mathbf{k}_T^2\rangle/2$, the near-side and away-side widths $\sigma_{Near}, \sigma_{Far}$ and $\langle|\mathbf{p}_T|\rangle$ in the hard fragmentation $z = p_h/p_z \to 1$ limit is approximately given by:

$$\langle|\mathbf{k}_{T\,y}|\rangle = \langle|\mathbf{p}_T|\rangle\cos\left(\frac{\sigma_{Near}}{\sqrt{\pi}}\right)\sqrt{\frac{1}{2}\tan^2\left(\sqrt{\frac{2}{\pi}}\,\sigma_{Far}\right) - \tan^2\left(\frac{\sigma_{Near}}{\sqrt{\pi}}\right)}\,. \tag{2.130}$$

The left panel in Fig. 2.50 shows two measures of the predicted increase in dijet acoplanarity for minimum bias dAu and central AuAu reactions [89]: $\langle|\mathbf{k}_{T\,y}|\rangle$ and the away-side width σ_{Far} of the di-hadron correlation function $C(\Delta\phi) = N^{h_1,h_2}(\Delta\phi)/N_{tot}^{h_1,h_2}$. $C(\Delta\phi)$ is approximated here by near-side and far-side Gaussians for a symmetric $p_T^{h1} \approx p_T^{h2}$ case and the vacuum widths are taken from PHENIX [223]. In the right panel of Fig. 2.50 di-hadron correlations in dAu are shown to be qualitatively similar to the pp case and in agreement with STAR measurements [135, 207]. In AuAu reactions at RHIC dijet acoplanarity is noticeably larger, but this effect alone does not lead to the reported disappearance of the back-to-back correlations [207]. To first approximation the coefficient of the away-side Gaussian (the area under $C(\Delta\phi)$, $\Delta\phi > \pi/2$), is determined by jet energy loss and given by $R_{\rm AA} \propto N_{part}^{2/3}$ in the GLV approach [73–75]. Broadening with and without away-side quenching is shown the bottom right panel of Fig. 2.50. Combined dAu and AuAu experimental data in Fig. 2.50 also rule out the existence of monojets at RHIC. For further discussion on di-hadron correlations, see Refs. [89, 202, 224].

The broadening of the away-side di-hadron correlation function in pPb and PbPb reactions at the LHC is shown in Fig. 2.51. The near side width σ_{Near} at $\langle|\mathbf{p}_T|\rangle$ = 6 GeV, 8 GeV is extrapolated from the PHENIX [223] and STAR [135, 207] measurements. We use two baseline values for the vacuum

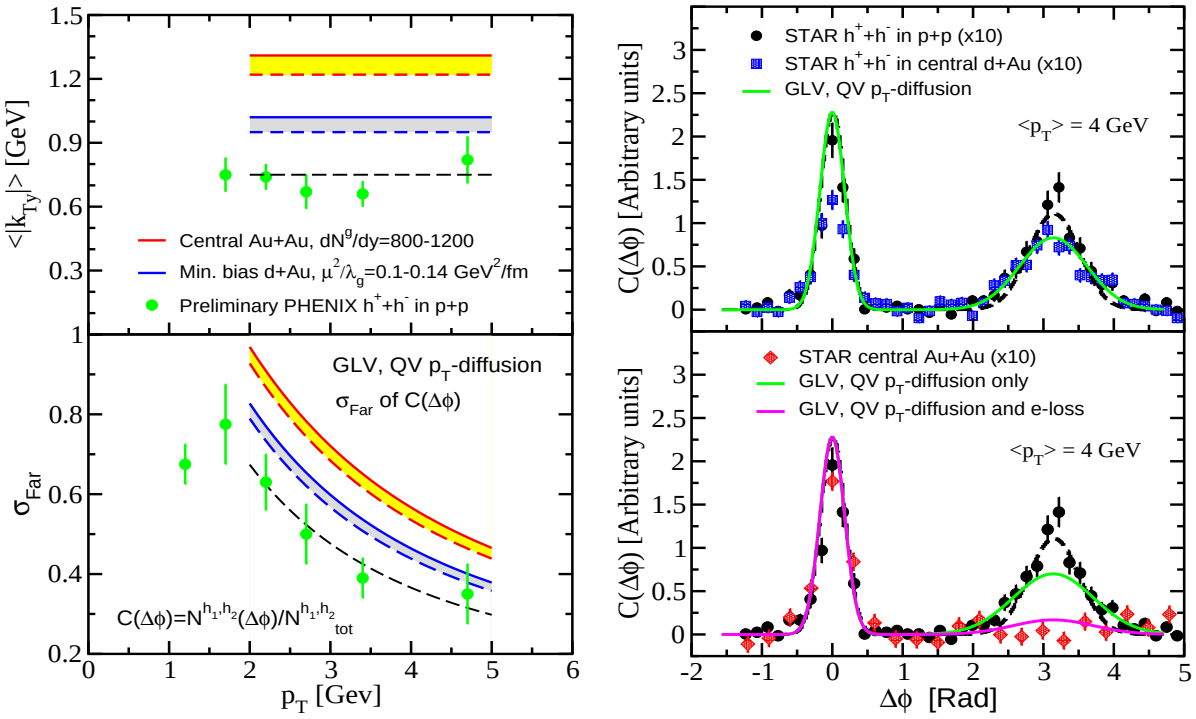

Fig. 2.50: Left panel: predicted enhancement of $\langle|\mathbf{k}_{T\,y}|\rangle$ and σ_{Far} in minimum bias dAu and central AuAu reactions at RHIC from p_T-diffusion [89]. Preliminary pp data is from PHENIX [223]. Right panel: the broadening of the far-side di-hadron correlation function in central dAu and AuAu compared to scaled (x10) STAR data [135, 207]. In the bottom the right panel the broadening with and without suppression, approximately given by $R_{\rm AA}$, are shown. We have used the predicted quenching factor [8], confi rmed by experimental data [124, 137, 138].

radiation induced dijet acoplanarity in pp reactions to account for its possible growth with $\sqrt{s}$ and p_T relative to the PHENIX measurement, $\langle|\mathbf{k}_{T\,y}|\rangle_{vac}$ = 0.8 GeV, 1.2 GeV. In pA reactions the broadening of $C(\Delta\phi)$, $\Delta\phi > \pi/2$ comes from transverse momentum diffusion in cold nuclear matter. The band reflects a range of transport coefficients μ^2/λ = 0.1 GeV^2/fm - 0.14 GeV^2/fm as in Fig. 2.50 with $\sim$ 30% increase of $\langle|\mathbf{k}_{T\,y}|\rangle$ relative to the vacuum case. In central PbPb reactions, where the hot and dense quark–gluon plasma is expected to be formed, the away-side width σ_{Far} grows by approximately a factor of two relative to the pp case. The final state scattering strength in proportional to the gluon rapidity density of the medium and the band represents values in the range dN^g/dy = 2000–3500. In the right panel of Fig. 2.51 the broadening of the di-hadron correlation function in central PbPb with and without the corresponding suppression factor is shown. We note that a direct calculation that does not include the hydrodynamic feedback at the LHC energy and number densities will result in suppression factors $R_{\rm AA} < (N_{part}/2)/N_{bin}$ [8]. In this case the $R_{\rm AA}$ has been set to $(N_{part}/2)/N_{bin} \approx 0.12$ for PbPb at $\sqrt{s}$ = 5.5 TeV. Because of its significantly larger dynamical p_T range, LHC may offer the best possibility to explore the relation between single inclusive hadron suppression and the broadening and disappearance of the back-to-back jet correlations.

3.6.3. High-p_T particle production in saturation models

R. Baier and U.A. Wiedemann

At RHIC, the production of high p_T hadrons in central AuAu collisions shows substantial differences compared to elementary pp collisions, see Section 4. As discussed in previous Sections, the observed depletion/suppression may be explained due to induced multiple gluon radiation off the large

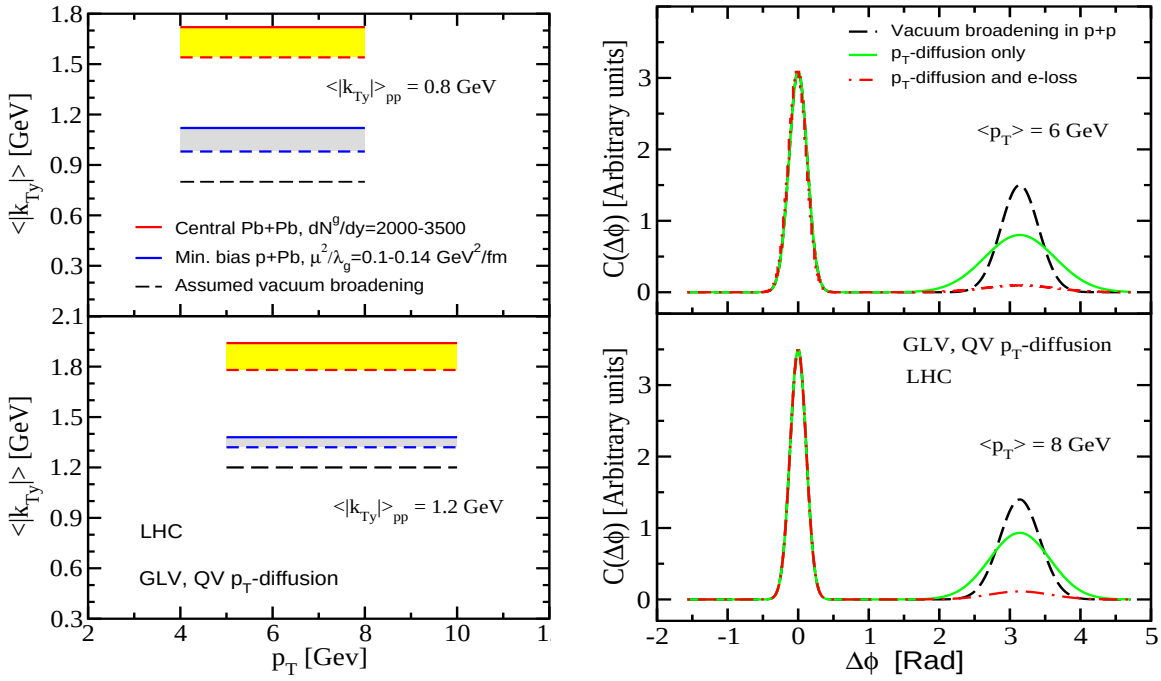

Fig. 2.51: Left panel: dijet acoplanarity quantifi ed via the enhancement of $\langle|\mathbf{k}_{T\,y}|\rangle$ in min. bias pPb and central PbPb reactions at the LHC. Two assumed baseline values for pp vacuum broadening, $\langle|\mathbf{k}_{T\,y}|\rangle_{vac}$ = 0.8 GeV, 1.2 GeV. Right panel: the broadening of the far-side di-hadron correlation function in central PbPb collisions with and without suppression. The quenching factor $R_{\rm AA}$ is taken from Ref. [8].

p_T parton ('jet quenching'). Here, we consider an alternative possibility due to initial state gluon radiation effects, especially saturation effects, put forward first in [225].

Instead of a detailed prediction for hadron production based on saturation models [1], we concentrate in the following on the problem of suppression vs. enhancement of gluon production in AA collisions with shortly mentioning the relevant comparison in pA scattering. This way, we do not include the fragmentation functions of gluons into hadrons and their possible medium dependence discussed in Section 3.4.2. To proceed, we use the k_T factorised formalism for calculating gluon production which is expected to give a qualitatively reasonable description of this process [225–227].

The basic factorised formula for the gluon yield at central rapidity in a collision of identical nuclei is

$$E\frac{dN}{d^3p\,d^2b} = \frac{4\pi^2\alpha_s S_{AA}(b) N_c}{N_c^2-1}\frac{1}{p_T^2}\int d^2k_t\,\phi_A(y,k_t)\,\phi_A(y,p_T-k_t)\,. \tag{2.131}$$

Here $S_{AA}(b)$ is the overlap area in the transverse plane between the nuclei at fixed impact parameter b, and y is the rapidity difference between the central rapidity and the fragmentation region. $\phi_A(y,k_t)$ is the intrinsic momentum dependent nuclear gluon distribution function, related to the standard gluon distribution by

$$\phi_A(y,k_t) = \frac{d(xG_A(x,k_t^2))}{d^2k_t\,d^2b}\,. \tag{2.132}$$

In the following, we will also use the modified gluon distribution

$$h_A(k_t) = k_t^2\,\nabla_{k_t}^2\,\phi_A(k_t)\,, \tag{2.133}$$

which enters some calculations of the gluon yield instead of ϕ_A [228–230]. In general, and especially at low momenta, the distributions h_A and ϕ_A are different. However, they coincide for the leading order

perturbative distribution which at impact parameter b has the shape

$$\phi(k_t, b) \simeq \frac{\alpha_s(N_c^2-1)}{2\pi^2}\frac{\rho_{\rm part}(b)}{2}\frac{1}{k_t^2}\,. \tag{2.134}$$

Here, $\rho_{\rm part}(b)$ is the density of participants, i.e. for central collisions $\rho_{\rm part}(b) \propto A^{1/3}$ and $S_{AA} \propto A^{2/3}$.

Since models for the gluon distribution are reviewed in Chapter 1, we limit the present discussion to shortly reviewing their main features.

McLerran–Venugopalan gluon. The McLerran–Venugopalan model [231, 232] achieves saturation by taking into account the Glauber–Mueller multiple scattering effects. The intrinsic gluon distribution in this model was calculated in [233, 234]:

$$\phi_A^{MV}(k_t) = \frac{N_c^2-1}{4\pi^4\alpha_s N_c}\int\frac{d^2\mathbf{x}}{\mathbf{x}^2}\left(1-e^{-\mathbf{x}^2Q_s^2(\mathbf{x}^2)/4}\right)e^{i\,k_t\cdot\mathbf{x}}\,. \tag{2.135}$$

We will take the saturation momentum to be $\mathbf{x}$-dependent

$$Q_s^2(\mathbf{x}^2, b) = \frac{4\pi^2\alpha_s N_c}{N_c^2-1}\,xG(x, 1/\mathbf{x}^2)\frac{\rho_{\rm part}(b)}{2}\,, \tag{2.136}$$

with $G(x, k_t^2 = 1/\mathbf{x}^2)$ being the *nucleon* gluon distribution:

$$xG(x, 1/\mathbf{x}^2) \simeq \frac{\alpha_s(N_c^2-1)}{2\pi}\ln\left(\frac{1}{\mathbf{x}^2\Lambda_{\rm QCD}^2}\right)\,. \tag{2.137}$$

Evolved gluons. The MV gluon distribution does not contain any evolution in Bjorken x which is necessary to explore the energy dependence of the gluon spectrum. Also, small-x evolution leaves a distinct imprint in the k_t-dependence of the produced gluon. It is argued [235, 236] that in the wide region of momenta $Q_s < |k_t| < \frac{Q_s^2}{Q_0}$ (typically, $Q_0 \sim O(1)$ GeV), the evolved distribution behaves as ('geometric scaling')

$$\phi_A(k_t) \propto \left[\frac{Q_s^2}{k_t^2}\right]^\gamma \tag{2.138}$$

with the anomalous dimension $\gamma = 0.64$. However, it is important to know how the distribution behaves outside this scaling window since this decides about suppression vs. enhancement of large k_t gluon production. This is illustrated by two models in Ref. [227]:

A gluon distribution with *fast* (F) crossover is

$$\phi_A^{\rm F}(k_t) = \frac{N_c^2-1}{4\pi^3\alpha_s N_c}\left(\frac{\hat{Q}_s^2}{k_t^2+\hat{Q}_s^2}\right)^{\gamma(k_t)}\,, \tag{2.139}$$

where $\hat{Q}_s^2 = 2\pi\alpha_s^2 N_c\,\frac{\rho_{\rm part}(b)}{2}$, and $\gamma(k_t)$ is chosen to approach 1 rapidly (like a power law) for $k_t \gg \hat{Q}_s^2/Q_0$ [227].

A *slow* (S) crossover can be modelled by a function with fixed anomalous dimension:

$$\phi_A^{\rm S}(k_t) = \frac{N_c^2-1}{4\pi^3\alpha_s N_c}\left(\frac{\hat{Q}_s^2}{k_t^2+\hat{Q}_s^2}\right)^{0.64}\,. \tag{2.140}$$

The non-linear evolution of the nuclear gluon distributions has recently been calculated numerically [230], using the Balitsky-Kovchegov (BK) evolution equation [237, 238]. The solutions for $h(k_t)$

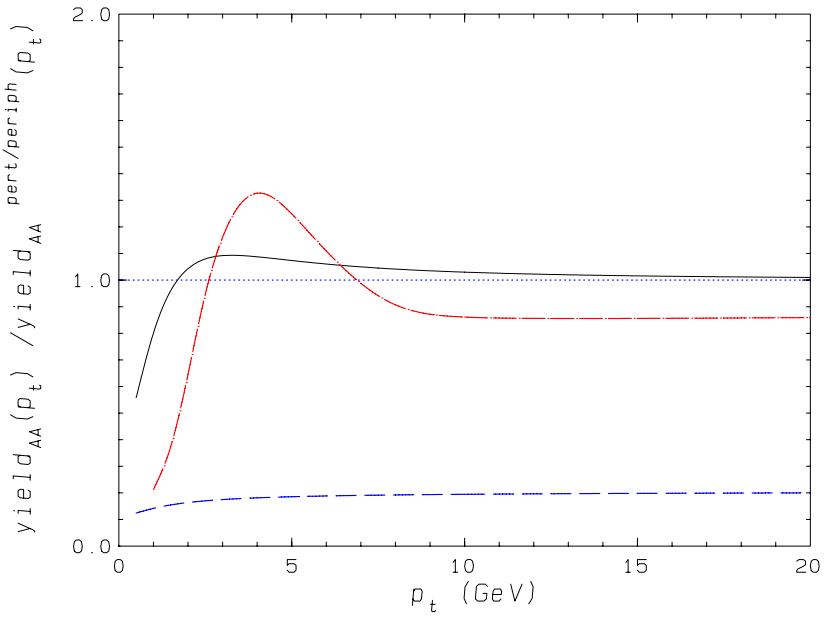

Fig. 2.52: Cronin effect in the p_t-dependence of gluon production yields for head-on AA collisions for Q_s^2 = 2 GeV^2. The solid curve is for the MV-gluon distribution normalized to the perturbative yield, the dot-dashed curve is for the evolved gluon distribution (2.139), and the dashed line is for the evolved gluon distribution (2.140).

plotted versus the scaled variable $\rho = k_t/Q_s(x)$ approach a universal soliton-like shape independent of initial conditions if evolved sufficiently far in rapidity. This numerical solution indicates that Eq. (2.140) provides a more realistic parametrisation of the evolved gluon distribution than Eq. (2.139) with a fast crossover.

Coming to gluon production in AA collisions, one finds with Eq. (2.131) for the perturbative gluon distribution Eq. (2.134),

$$\left.\frac{dN^{\rm pert}(b)}{dy\,d^2p_T}\right|_{y=0} \simeq 2S_{AA}(b)\frac{N_c^2-1}{4\pi^3\alpha_s N_c}\frac{\hat{Q}_s^4(b)}{p_t^4}\left(\ln\frac{p_T^2}{4\Lambda_{\rm QCD}^2}\right) . \tag{2.141}$$

This 'reference' spectrum scales for all transverse momenta with $N_{\rm coll} \sim S_{AA}(b)\,\rho^2_{\rm part}(b)$ ($\sim A^{4/3}$ at b = 0), as expected perturbatively.

In contrast, using the saturated gluon distribution in the MV model, the gluon yield Eq. (2.131) is suppressed at small momenta compared to the perturbative one and scales with the number of participants, $N_{\rm part}(b) = S_{AA}(b)\ \rho_{\rm part}(b)$ ($\sim A$ for $b = 0$). It approaches the perturbative yield (2.141) from above at large p_T.

In Fig. 2.52, we summarize the results for the normalized ratio of central over peripheral (perturbative) yields, corresponding to the nuclear modification factor

$$R_{\rm AA} = \frac{\frac{dN_{AA}}{dyd^2p\,d^2b}}{A^{4/3}\frac{dN_{pp}}{dyd^2p\,d^2b}} ,$$

here quoted at b = 0. For the MV model, one sees a small but clear Cronin enhancement for momenta just above the saturation scale. The distribution $\phi_A^{\rm F}$ displays a clear Cronin effect similar to the MV gluon, while $\phi_A^{\rm S}$ shows uniform suppression for the central/peripheral ratio for all momenta. This illustrates, indeed, that the ratio $R_{\rm AA}$ is very sensitive to the way in which the distribution behaves outside the scaling window.

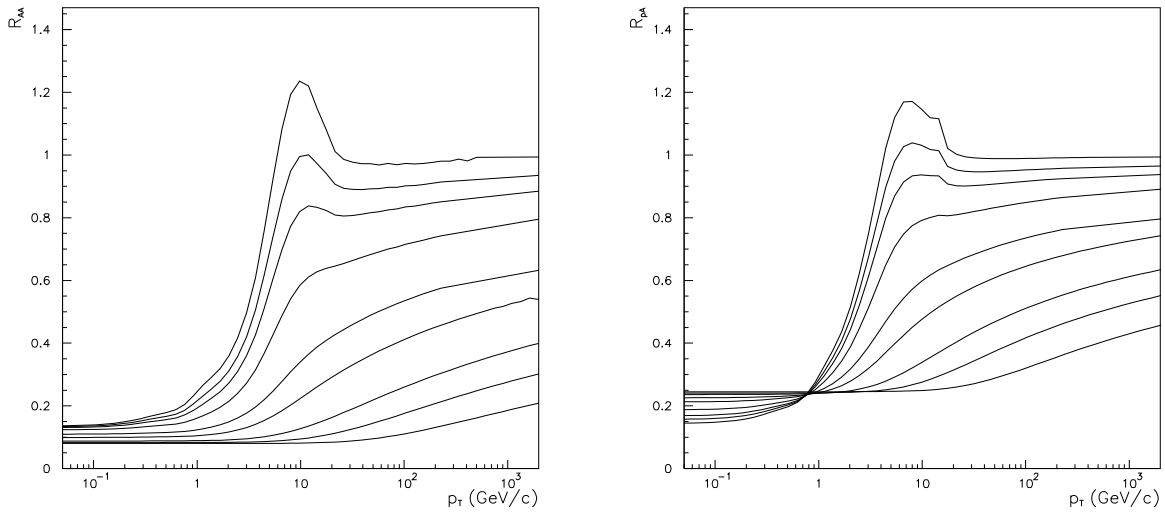

Fig. 2.53: Ratios $R_{\rm AA}$ and R_{pA} of gluon yields in AA (LHS) and pA (RHS) for BK evolution, with MV as initial condition with Q_s^2 = 0.1 GeV^2 for p and 2 GeV^2 for A. Lines from top to bottom correspond to $y = (\alpha_s\, N_c/\pi) \ln 1/x$ = 0, 0.05, 0.1, 0.2, 0.4, 0.6, 1, 1.4 and 2.

For the numerically evolved gluon distribution h, the factor $R_{\rm AA}$ is shown in Fig. 2.53.

The non-linear BK evolution quickly wipes out any initial Cronin enhancement not only on the level of single parton distribution functions but also on the level of particle spectra. Several checks establish that this behaviour is generic [230]. For 'realistic' initial conditions this disappearance occurs within half a unit of rapidity. We note that in our units the evolution from 130 GeV to 200 GeV corresponds to $\delta y \simeq 0.1$ for α_s = 0.2, and thus is not sufficient to completely eliminate an initial enhancement at central rapidity. For forward rapidity, δy is greater. The evolution to the LHC energy corresponds to $\delta y \sim 1$. Thus the BK evolution suggests the reduction of the Cronin effect in d–Au for forward rapidities at RHIC and predicts its disappearance for pA collisions at LHC.

This numerical study [230] strongly indicates that crossover from the scaling regime to the perturbative one is very slow and gradual, and that the Cronin effect which is present in the MV gluon is wiped out by the quantum evolution at high energies. Thus, $\phi_A^{\rm S}$ in Eq. (2.140) seems to provide a more realistic parametrisation of the evolved gluon distribution than $\phi_A^{\rm F}$ in Eq. (2.139).

On the qualitative level, however, we observe that the gluon distributions which lead to the Cronin effect in dAu collisions also lead to the Cronin enhancement in the AuAu collisions (see Fig. 2.53). And vice versa, if no Cronin effect appears in AuAu, none is seen in dAu collisions. Given the recent experimental observation of the Cronin enhancement in dAu collisions at RHIC (see Section 4.), this supports the view that significant final state ('quenching') effects are needed in order to account for the AuAu data.

At LHC, due to higher energies, quantum evolution according to the BK equation will suppress gluon production in pA as well as in AA collisions (see Fig. 2.53).

4. EXPERIMENTAL STATUS AT RHIC

D. d'Enterria

We summarize the main results on hard scattering processes in AuAu, pp, and dAu collisions at $\sqrt{s_{NN}}$ = 200 GeV obtained after three years of operation at the BNL Relativistic Heavy-Ion Collider (RHIC). The main observations so far at RHIC are the following:

- The high p_T yields of inclusive charged hadrons and π^0 in central AuAu at $\sqrt{s_{NN}}$ = 130 [204,206, 239] and 200 GeV [124, 133, 137, 138, 240], are suppressed by as much as a factor 4–5 compared to pp and peripheral AuAu yields scaled by T_{AB} (or N_{coll}).
- At intermediate p_Ts ($p_T \approx$ 2–4 GeV/c) in central AuAu, at variance with mesons (π^0 [124] and Ks [241]) no suppression is seen for baryons (p, $\bar{\rm p}$ [208,242] and Λ, $\bar{\Lambda}$ [241]), yielding an 'anomalous' baryon over meson ratio $p/\pi \sim 1$ much larger than the 'perturbative' $p/\pi \sim$ 0.1–0.3 ratio observed in pp collisions [243, 244] and in e^+e^- jet fragmentation [245].
- The near-side azimuthal correlations of high p_T (leading) particles emitted in central and peripheral AuAu reactions [207,246] are, on the one hand, clearly reminiscent of jet-like parton fragmentation as found in pp collisions. On the other, away-side azimuthal correlations (from back-to-back jets) in central AuAu collisions are found to be significantly suppressed [207].
- At low p_T the strength of the azimuthal anisotropy parameter v_2 is found to be large and consistent with hydrodynamical expectations for elliptic flow. Above $p_T \sim$ 2 GeV/c where the contribution from collective behaviour is negligible, v_2 has still a sizeable value with a flat (or slightly decreasing) behaviour as a function of p_T [209, 241, 247].
- High p_T production in 'cold nuclear matter' as probed in dAu reactions [133–135, 248] not only is not suppressed *enhanced* compared to pp collisions, in a way very much reminiscent of the 'Cronin enhancement' observed in pA collisions at lower centre-of-mass energies [37].

All these results point to strong medium effects at work in central AuAu collisions, and have triggered extensive theoretical discussions based on perturbative or 'classical'-field QCD. Most of the studies on the high p_T suppression are based on the prediction [51, 59, 60] that a deconfined and dense medium would induce multiple gluon radiation off the scattered partons, effectively leading to a depletion of the high-p_T hadronic fragmentation products ('jet quenching'), though alternative interpretations have been also put forward based on initial-state gluon saturation effects ('Colour Glass Condensate', CGC) [225], or final-state hadronic reinteractions [249]. The different behaviour of baryons and mesons at moderately high p_Ts has been interpreted, among others, in terms of 'quark recombination' (or coalescence) effects in a thermalized partonic (QGP-like) medium [211, 213, 250], whereas the disappearance of the back-to-back azimuthal correlations can be explained in both QGP energy loss and CGC monojet scenarios. Finally, the large value of v_2 above 2 GeV/c has been addressed by jet energy loss [81], gluon saturation [172], and quark recombination [251] models.

This summary report presents the p_T, $\sqrt{s_{NN}}$, centrality, particle-species, and rapidity dependence of the inclusive high p_T particle production, plus the characteristics of the produced jets and collective elliptic flow signals extracted from the azimuthal correlations at large p_T, as measured by the four experiments at RHIC (BRAHMS, PHENIX, PHOBOS and STAR) in AuAu, pp, and dAu collisions. The whole set of experimental data puts strong constraints on the different proposed physical explanations for the underlying QCD medium produced in heavy-ion collisions at RHIC and at LHC energies.

4.1. High-p_T Hadron Production in pp Collisions at $\sqrt{s}$ = 200 GeV

pp inclusive cross-sections. Proton–proton collisions are the baseline 'vacuum' reference to which one compares the AuAu results in order to extract information about the QCD medium properties. At $\sqrt{s}$ = 200 GeV, there currently exist three published measurements of high p_T hadron cross-sections in pp($\bar{\rm p}$) collisions: UA1 $p + \bar{p} \rightarrow h^{\pm}$ ($|\eta| < 2.5$, $p_T < 7$ GeV/c) [39], PHENIX $pp \rightarrow \pi^0$ ($|\eta| < 0.35$, $p_T < 14$ GeV/c) [252], and STAR $pp \rightarrow h^{\pm}$ ($|\eta| < 0.5$, $p_T < 10$ GeV/c) [137]. At $\sqrt{s}$ = 130 GeV, an

interpolation between the ISR inclusive charged hadron cross-section and UA1 and FERMILAB data, has been also used as a reference for AuAu at this value of $\sqrt{s}$. Globally the spectra can be reasonably well parametrized by a power-law form $A \cdot (1 + p_T/p_0)^{-n}$ with the parameters reported in Table 2.4. We note that the fit parameters p_0 and n are actually strongly correlated via the mean p_T of the collision: $\langle p_T \rangle = 2p_0/(n-3)$.

Table 2.4: Parameters of the fit $Ed^3\sigma/dp^3 = A \cdot (1 + p_T/p_0)^{-n}$ to the inclusive p_T distributions of all existing pp($\bar{\text{p}}$) hadron (inelastic or non-singly-diffractive) cross-section measurements at $\sqrt{s}$ = 200 GeV

system	$\sqrt{s}$ (GeV)	$p_{\mathrm{T}}^{\mathrm{min}}\left(\frac{\mathrm{GeV}}{c}\right)$	$A\left(\frac{\mathrm{mb\,c^3}}{\mathrm{GeV^2}}\right)$	$p_0\left(\frac{\mathrm{GeV}}{c}\right)$	n
$p+p \to h^{\pm}$ (inel., interpolation [206])	130	0.4	330	1.72	12.4
$p+\bar{p} \to h^{\pm}$ (NSD, UA1) [39]	200	0.25	286	1.8	12.14
$p+p \to h^{\pm}$ (NSD, STAR) [137]	200	0.4	286	1.43	10.35
$p+p \to \pi^0$ (inel., PHENIX) [252]	200	1.0	386	1.22	9.99

In general, all experimental results are consistent within each other, although it is claimed [137] STAR pp inclusive charged yield is smaller by a factor of 0.79 $\pm$ 0.18 compared to UA1 p$\bar{\text{p}}$ results (approximately independent of p_T), the difference due in large part to differing non-singly-diffractive (NSD) cross section measured (35 $\pm$ 1 mb [39] in the first and 30.0 $\pm$ 3.5 mb [137] in the latter). (The PHENIX high p_T π^0 cross-section is inclusive and contains, in principle, all inelastic (including diffractive) channels.) Standard next-to-leading-order (NLO) perturbative QCD calculations describe well the available high p_T pp data at $\sqrt{s}$ = 200 GeV (see Fig. 2.54 for π^0).

pp azimuthal correlations. PHENIX [223] has studied the azimuthal correlations at high p_T in pp collisions at $\sqrt{s}$ = 200 GeV extracting several parameters characterizing the produced jets:

- Mean jet fragmentation transverse momentum: $\langle |j_{\perp y}| \rangle$ = 373 $\pm$ 16 MeV/c, in agreement with previous measurements at ISR [253] and showing no significant trend with increasing $\sqrt{s}$.
- Average parton transverse momentum (fitted to a constant above 1.5 GeV/c): $\langle |k_{\perp y}| \rangle$ = 725 $\pm$ 34 MeV/c. The momentum of the pair $p_\perp$ is related to the individual parton $\langle |k_{\perp y}| \rangle$ via $\sqrt{\langle |p_\perp^2| \rangle_{pair}} = \sqrt{2\pi}\,\langle |k_{\perp y}| \rangle$. The extracted $\sqrt{\langle |p_\perp^2| \rangle_{pair}}$ = 1.82 $\pm$ 0.85 GeV/c is in agreement with the existing systematics of dimuon, diphoton and dijet data in hadronic collisions [254].

4.2. High-p_T Hadron Production in AuAu Collisions

There is a significant amount of high p_T AuAu experimental spectra ($p_T > 2$ GeV/c) measured by the four experiments at RHIC: inclusive charged hadrons at 130 [204, 206, 239] and 200 GeV [133, 137,

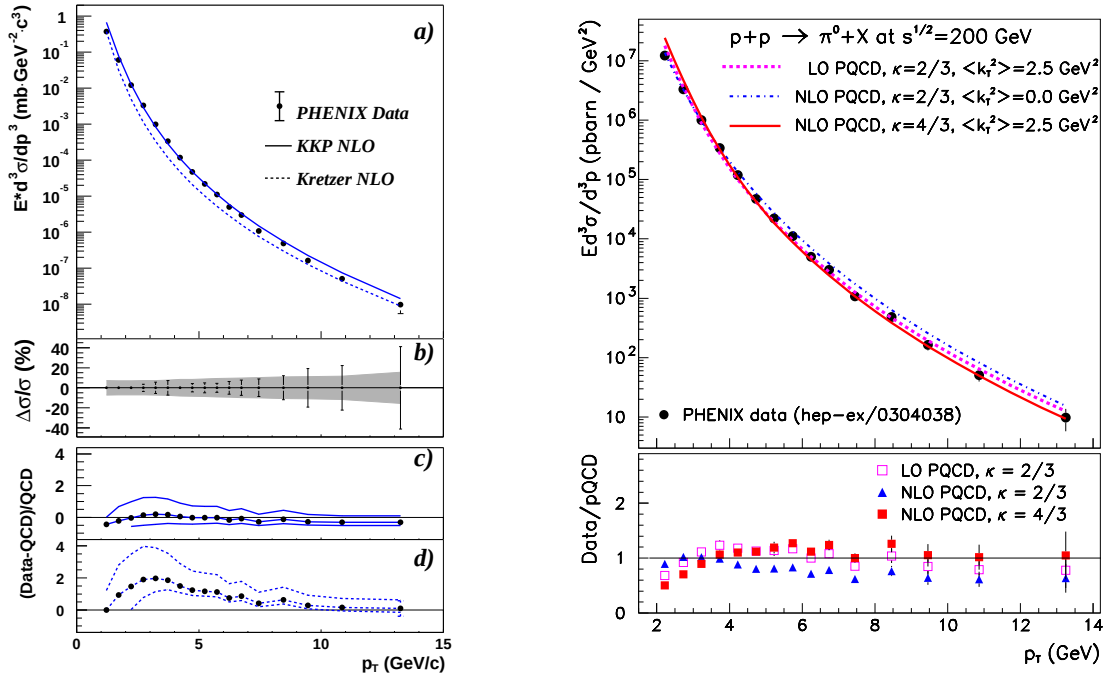

Fig. 2.54: High p_T π^0 cross-section in pp collisions at $\sqrt{s}$ = 200 GeV (PHENIX) compared to the results of two different NLO pQCD calculations: [252] (left), [255] (right)

138, 240], neutral pions at 130 [206] and 200 GeV [124], protons and antiprotons at 130 [242] and 200 GeV [208], K^0_s at 200 GeV [241], and $\Lambda, \bar{\Lambda}$ at 200 GeV [241]. Moreover, all these spectra are measured for different centrality bins and permit to address the impact parameter dependence of high p_T production.

Details on hadron production mechanisms in AA are usually studied via their scaling behaviour with respect to pp collisions. On the one hand, soft processes ($p_T < 1$ GeV/c) are expected to scale with N_{part} [256] (and they actually approximately do [257–259]). On the other hand, in the framework of collinear factorization, hard processes are incoherent and thus expected to scale with N_{coll}. result at RHIC in the high p_T sector is the *breakdown* of this N_{coll} scaling for central AuAu collisions. Figure 2.55 shows the comparison of the pp π^0 spectrum to peripheral (left) and central (right) AuAu spectra, and to pQCD calculations. Whereas peripheral data is consistent with a simple superposition of individual NN collisions, central data shows a suppression factor of 4–5 with respect to this expectation. It is customary to quantify the medium effects at high p_T using the *nuclear modification factor* given by the ratio of the AA to the pp invariant yields scaled by the nuclear geometry (T_{AB}):

$$R_{\rm AA}(p_T) = \frac{d^2N^{\pi^0}_{AA}/dydp_T}{\langle T_{AB}\rangle \times d^2\sigma^{\pi^0}_{pp}/dydp_T}. \qquad (2.142)$$

$R_{\rm AA}(p_T)$ measures the deviation of AA from an incoherent superposition of NN collisions in terms of suppression ($R_{\rm AA}$ <1) or enhancement ($R_{\rm AA}$ >1).

High p_T suppression: magnitude and p_T dependence. Fig. 2.56 shows $R_{\rm AA}(p_T)$ for $h^{\pm}$ (STAR [137], left) and π^0 (PHENIX [124], right) measured in peripheral (upper points) and central (lower points) AuAu reactions at $\sqrt{s_{NN}}$ = 200 GeV. As seen in Fig. 2.55, peripheral collisions are consistent with pp collisions plus N_{coll} scaling as well as with standard pQCD calculations [8, 202], while central AuAu are clearly suppressed by a factor $\sim$ 4–5. (Although peripheral STAR charged hadron

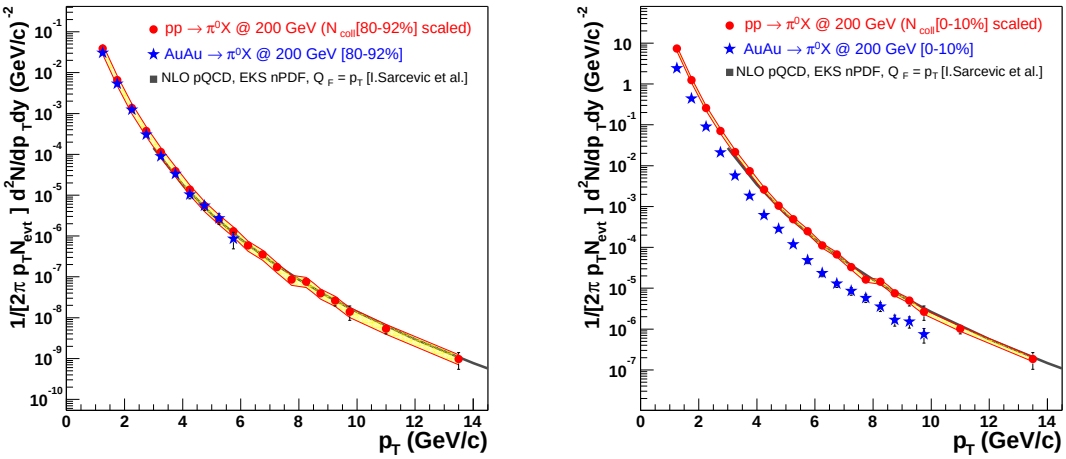

Fig. 2.55: Invariant π^0 yields measured by PHENIX in peripheral (*left*) and in central (*right*) AuAu collisions (stars), compared to the N_{coll} scaled pp π^0 yields (circles) and to a NLO pQCD calculation [260] (gray line). The yellow band around the scaled pp points includes in quadrature the absolute normalization errors in the pp and AuAu spectra as well as the uncertainties in T_{AB}. Updated version of Fig. 1 of [261] with final published data [124, 252].

data seems to be slightly above $R_{\rm AA}$ = 1 and PHENIX π^0 data seems to be below, within errors both measurements are consistent with 'collision scaling'.)

The high p_T suppression in central collisions for both π^0 and $h^{\pm}$ is smallest at p_T = 2 GeV/c and increases to an approximately constant suppression factor of $1/R_{\rm AA} \approx$ 4–5 over p_T = 5–10 GeV/c. *Above* 5 GeV/c the data are consistent within errors with 'participant scaling' given by the dotted line at $R_{\rm AA} \approx 0.17$ in both plots (actually both STAR and PHENIX data are systematically slightly above this scaling). The magnitude and p_T dependence of $R_{\rm AA}$ in the range p_T = 1–10 GeV/c (corresponding to parton fractional momenta $x_{1,2} = p_T/\sqrt{s}(e^{\pm y_1} + e^{\pm y_2}) \approx 2p_T/\sqrt{s} \sim$ 0.02–0.1 at midrapidity), is alone inconsistent with 'conventional' nuclear effects like leading-twist shadowing of the nuclear parton distribution functions (PDFs) [15,262]. Different pQCD-based jet quenching calculations [7,8,80,93,202,255]

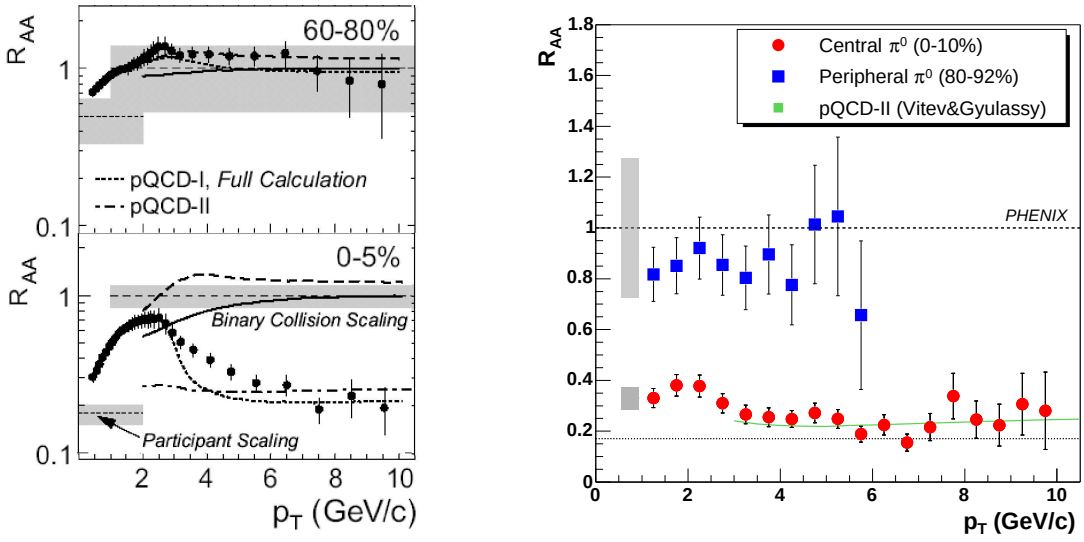

Fig. 2.56: Nuclear modification factor, $R_{\rm AA}(p_T)$, in peripheral and central AuAu reactions for charged hadrons (left) and π^0 (right) measured at $\sqrt{s_{NN}}$ = 200 GeV by STAR and PHENIX respectively. A comparison to theoretical curves: pQCD-I [8], pQCD-II [202], is also shown.

based on medium-induced radiative energy loss, can reproduce the *magnitude* of the π^0 suppression assuming the formation of a hot and dense partonic system characterized by different, but related, properties: i) large initial gluon densities $dN^g/dy \sim 1000$ [8], ii) large 'transport coefficients' $\hat{q}_0 \sim 3.5$ GeV/fm^2 [93], iii) high opacities $L/\lambda \sim 3$–4 [255], or iv) effective parton energy losses of the order of $dE/dx \sim 14$ GeV/fm [202].

The p_T *dependence* of the quenching predicted by all models that include the QCD version of the Landau-Pomeranchuck-Migdal (LPM) interference effect (BDMPS [4] and GLV [73] approaches) is a slowly (logarithmic) increasing function of p_T, a trend not compatible with the data over the entire measured p_T range. Other approaches, such as constant energy loss per parton scattering, are also not supported as discussed in Ref. [260]. Analyses which combine LPM jet quenching together with shadowing and initial-state p_T broadening ("pQCD-II" [8] in Fig. 2.56) globally reproduce the observed flat p_T dependence of $R_{\rm AA}$, as do recent approaches that take into account detailed balance between parton emission and absorption ("pQCD-I" [202] in Fig. 2.56, left).

At variance with parton energy loss descriptions, a gluon saturation calculation [225] is able to predict the magnitude of the observed suppression, although it fails to reproduce exactly the flat p_T dependence of the quenching [137]. Similarly, *semi-quantitative* estimates of final-state interactions in a dense *hadronic* medium [249] yield the same amount of quenching as models based on partonic energy loss, however it is not yet clear whether the p_T evolution of the hadronic quenching factor is consistent with the data or not [137].

The amount of suppression for π^0 [124] and $h^{\pm}$ [137, 240] is the same above $p_T \approx 4$–5 GeV/c for all centrality classes [240]. However, below $p_T \sim 5$ GeV/c, π^0's are more suppressed than inclusive charged hadrons in central collisions (as can be seen by comparing the right and left plots of Fig. 2.56). This is due to the enhanced baryon production contributing to the total charged hadron yield in the intermediate p_T region ($p_T \approx 1$–4 GeV/c) in AuAu collisions [208, 241] (see Section 4.2. below).

High p_T suppression: $\sqrt{s_{NN}}$ dependence. Figure 2.57 shows $R_{\rm AA}(p_T)$ for several π^0 measurements in high-energy AA collisions at different centre-of-mass energies [263]. The PHENIX $R_{\rm AA}(p_T)$ values for central AuAu collisions at 200 GeV (circles) and 130 GeV (triangles) are noticeably below unity in contrast to the enhanced production ($R_{\rm AA} > 1$) observed at CERN-ISR (min. bias $\alpha + \alpha$ [244], stars) and CERN-SPS energies (central PbPb [264], squares) and interpreted in terms of initial-state p_T broadening ('Cronin effect' [37]).

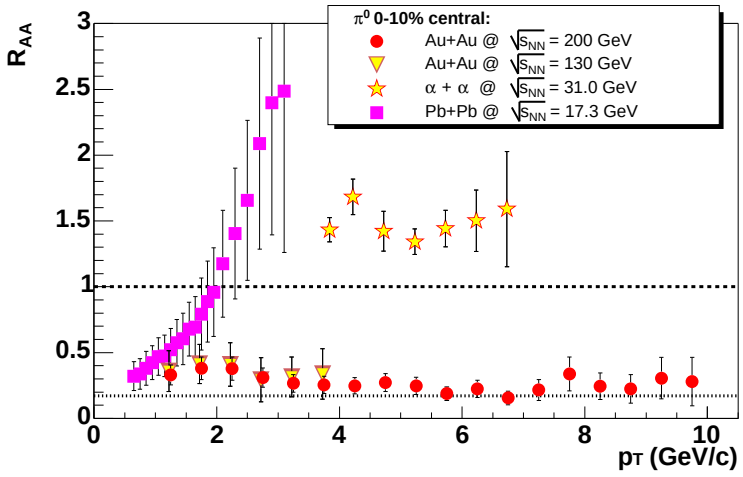

Fig. 2.57: Nuclear modification factor, $R_{\rm AA}(p_T)$, for π^0 measured in central ion-ion reactions at CERN-SPS [264] (squares), CERN-ISR [244] (stars), and BNL-RHIC (triangles [206], circles [124]) energies

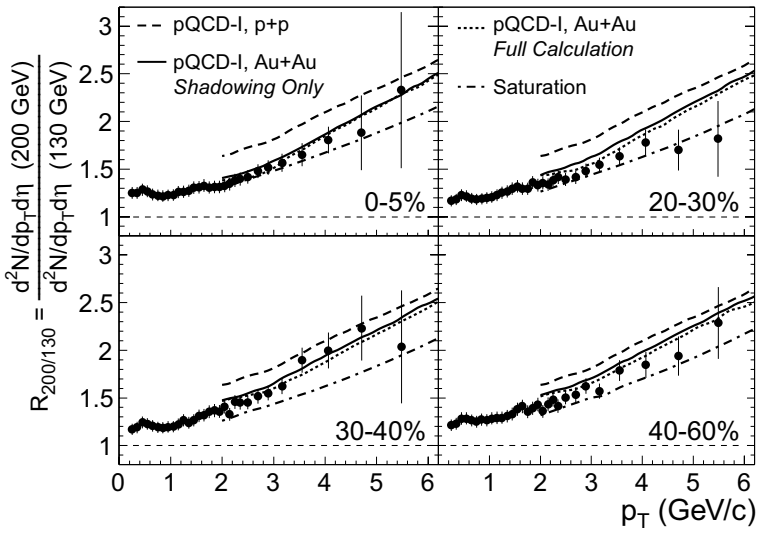

Fig. 2.58: $R_{200/130}(p_T)$ vs. p_T for $(h^+ + h^-)/2$ for four different centrality bins measured by STAR compared to pQCD and gluon saturation model predictions [137]

Figure 2.58 shows $R_{200/130}(p_T)$, the ratio of AuAu charged hadron yields at $\sqrt{s_{\rm NN}}$ = 130 and 200 GeV in 4 centrality classes, compared to pQCD and gluon saturation model predictions [137]. The increase in high p_T yields between the two centre-of-mass energies is a factor ~ 2 at the highest p_Ts, whereas at low p_T, the increase is much moderate, of the order of 15%. The large increment of the hard cross sections is naturally consistent with pQCD expectations due to the increased jet contributions at high transverse momenta. In the saturation model [225] the increase at high p_T is accounted for by the enhanced gluon densities at $\sqrt{s_{\rm NN}}$ = 200 GeV compared to 130 GeV in the 'anomalous dimension' x_T region of the Au parton distribution function.

PHENIX [240] has addressed the $\sqrt{s}$ dependence of high p_T production by testing the validity of 'x_T scaling' in AuAu, i.e. verifying the parton model prediction that hard scattering cross sections can be factorized in two terms depending on $\sqrt{s}$ and $x_T = 2p_T/\sqrt{s}$ respectively:

$$E\frac{d^3\sigma}{dp^3} = \frac{1}{p_T^{n(\sqrt{s})}}\,F(x_T) \implies E\,\frac{d^3\sigma}{dp^3} = \frac{1}{\sqrt{s}^{\,n(x_T,\sqrt{s})}}\,G(x_T)\,. \tag{2.143}$$

In Eq. (2.143), $F(x_T)$ embodies all the x_T dependence coming from the parton distribution (PDF) and fragmentation (FF) functions (PDFs and FFs, to first order, scale as the ratio of p_T at different $\sqrt{s}$.), while the exponent n, related to the underlying parton–parton scattering, is measured to be $n \approx$ 4–8 in a wide range of $pp, \bar{p}$ collisions [240]. Figure 2.59 compares the x_T-scaled hadron yields in $\sqrt{s_{NN}}$ = 130 GeV and 200 GeV AuAu central and peripheral collisions. According to Eq. (2.143), the ratio of inclusive cross-sections at fixed x_T should equal $(200/130)^n$. On the one hand, x_T scaling holds (in the kinematical region, $x_T > 0.03$, where pQCD is expected to hold) in AuAu with the same scaling power $n = 6.3 \pm 0.6$ for neutral pions (in central and peripheral collisions) and charged hadrons (in peripheral collisions) as measured in pp [240]. This is consistent with equal (pQCD-like) production dynamics in pp and AuAu, and disfavours final-state effects described with medium-modified FFs that violate x_T scaling (e.g. constant parton energy losses independent of the parton p_T). Equivalently, models that predict strong initial-state effects (e.g. gluon saturation) respect x_T scaling as long as their predicted modified nuclear PDFs are depleted, independently of $\sqrt{s}$, by the same amount at a given x_T (and centrality). On the other hand, Fig. 2.59 (right) shows that charged hadrons in central collisions (triangles) break x_T scaling which is indicative of a non perturbative modification of particle composition spectra from that of pp at intermediate p_Ts (see Section 4.2. below).

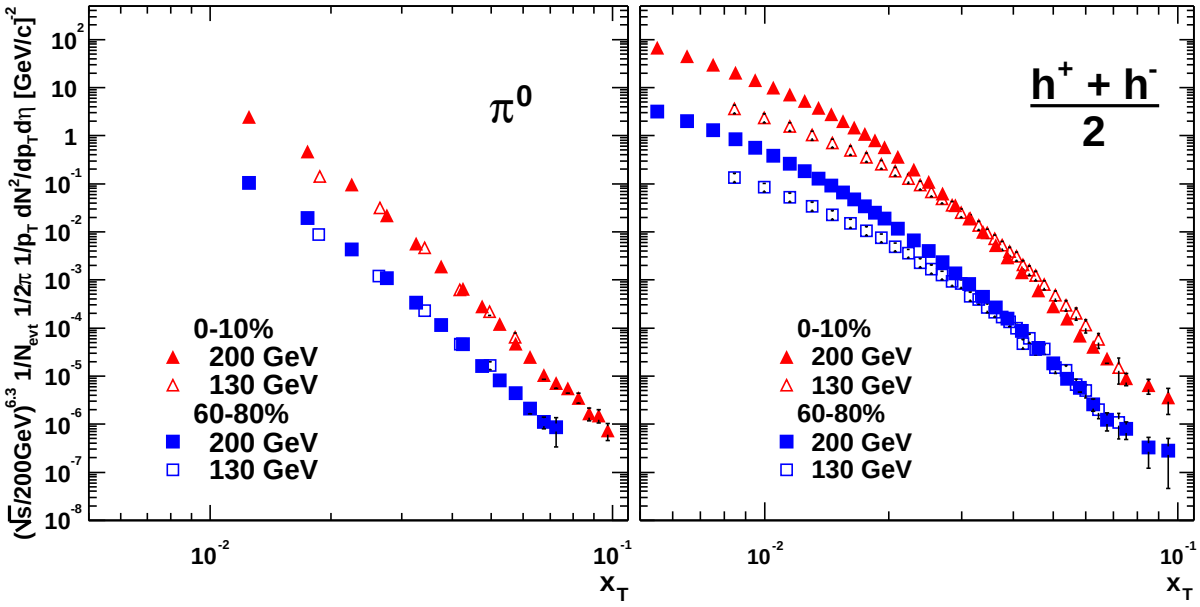

Fig. 2.59: x_T scaled spectra for π^0 (left) and $(h^+ + h^-)/2$ (right) measured in central and peripheral collisions at $\sqrt{s_{NN}}$ = 130 and 200 GeV by PHENIX [240]. Central (Peripheral) x_T spectra are represented by triangles (squares), and solid (open) symbols represent x_T spectra from $\sqrt{s_{NN}}$ = 200 GeV ($\sqrt{s_{NN}}$ = 130 GeV scaled by a factor of $(130/200)^{6.3}$).

High p_T suppression: centrality dependence. In each centrality bin, the value of the high p_T suppression can be quantified by the ratio of AuAu over N_{coll}-scaled pp yields integrated above a given (large enough) p_T. The centrality dependence of the high p_T suppression for π^0 and charged hadrons, given by $R_{\rm AA}(p_T > 4.5$ GeV/$c)$, is shown in Fig. 2.60 (left) as a function of $\langle N_{part}\rangle$ for PHENIX data. The transition from the N_{coll} scaling behaviour ($R_{\rm AA} \sim 1$) apparent in the most peripheral region, $\langle N_{part}\rangle \lesssim 40$, to the strong suppression seen in central reactions ($R_{\rm AA} \sim 0.2$) is smooth. Whether there is an abrupt or gradual departure from N_{coll} scaling in the peripheral range cannot be ascertained within the present experimental uncertainties [263]. The data, however, is inconsistent with N_{coll} scaling (at a 2σ level) for the 40–60% centrality corresponding to $\langle N_{part}\rangle \approx 40$–$80$ [239, 263], whose estimated 'Bjorken' energy density ($\epsilon_{Bj} \approx 1$ GeV/fm^3) [263] is in the ball-park of the expected 'critical' QCD energy density. A similar centrality dependence of the high p_T suppression is seen in STAR $h^\pm$ data (Fig. 2.60, right)

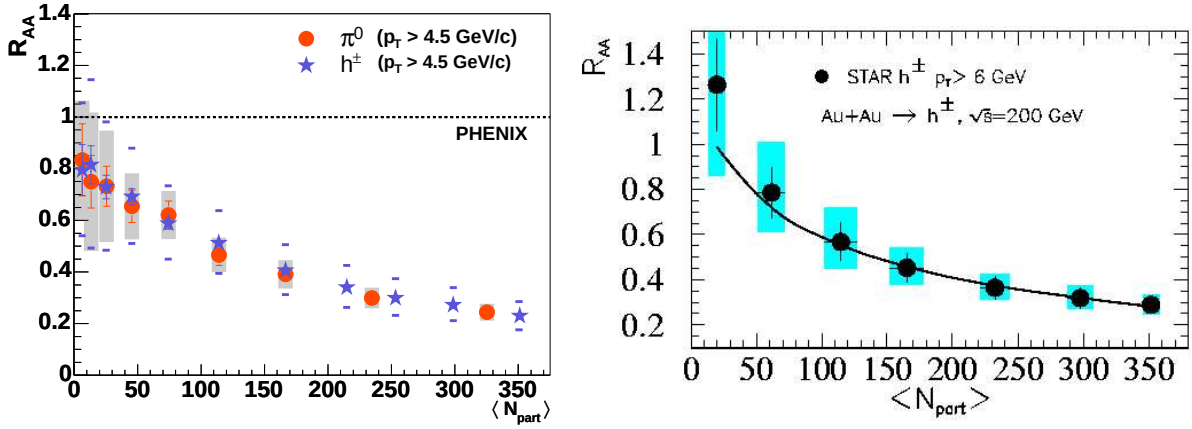

Fig. 2.60: Evolution of the high p_T π^0 and $h^\pm$ suppression, $R_{\rm AA}(p_T > 4.5$ GeV/$c)$, as a function of centrality given by $\langle N_{part}\rangle$ (PHENIX, left). Same evolution shown as $R_{\rm AA}(p_T > 6.0$ GeV/$c)$ for STAR $h^\pm$ data [265] (right).

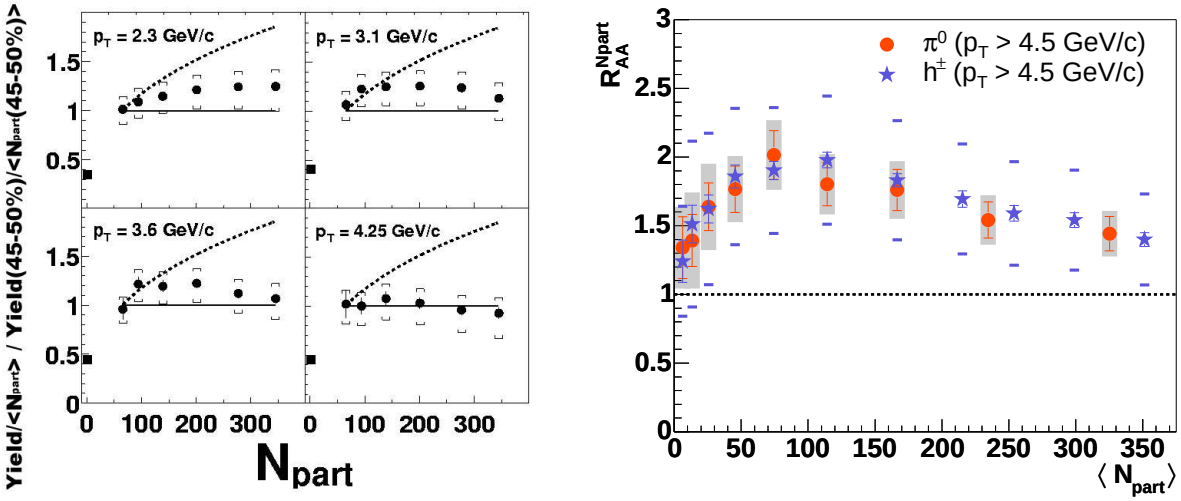

Fig. 2.61: Left: Ratio of central to semi-central $h^{\pm}$ yields normalized by N_{part} in 4 different p_T bins, as a function of N_{part} measured by PHOBOS [138]. The dashed (solid) line shows the expectation for N_{coll} (N_{part}) scaling. Right: Ratio of AuAu over pp π^0 and $h^{\pm}$ yields above 4.5 GeV/c normalized by N_{part} ($R_{\rm AA}^{N_{part}}$) as a function of centrality given by $\langle N_{part} \rangle$ as measured by PHENIX [124, 240]. The dashed line indicates the expectation for N_{part} scaling.

N_{part} (instead of N_{coll}) scaling at high p_T is N_{part}^{pp} = 2) expected in scenarios dominated either by gluon saturation [225] or by surface emission of the quenched jets [266]. "Approximate" N_{part} scaling has been claimed by PHOBOS [138]: the ratio of central to a *fit* to *mid-central* yields in the range $p_T \approx$ 2–4 GeV/c stays flat as a function of centrality (Fig. 2.61, left). However, at higher p_T values, where the suppression is seen to saturate at its maximum value, the centrality dependence of the ratio of N_{part}-scaled AuAu over pp yields for π^0 and $h^{\pm}$ measured by PHENIX (Fig. 2.61, right) does not show a true participant scaling ($R_{\rm AA}^{part} > 1$ for all centralities). Nonetheless, the fact that the production per participant pair above 4.5 GeV/c is, within errors, approximately constant over a wide range of intermediate centralities, is in qualitative agreement with a gluon saturation model prediction [225].

High p_T suppression: particle species dependence. One of the most intriguing results of the RHIC programme so far is the different suppression pattern of baryons and mesons at moderately high p_Ts. Figure 2.62 (left) compares the N_{coll} scaled central to peripheral yield ratios [1] for $(p+\bar{p})/2$ and π^0: $R_{cp} = (yield^{(0-10\%)}/N_{coll}^{0-10\%})/(yield^{(60-92\%)}/N_{coll}^{60-92\%})$. From 1.5 to 4.5 GeV/$c$ the (anti)protons are not suppressed ($R_{cp} \sim 1$) at variance with the pions which are reduced by a factor of 2–3 in this p_T range. If both π^0 and p, $\bar{\rm p}$ originate from the fragmentation of hard-scattered partons that lose energy in the medium, the nuclear modification factor R_{cp} should be independent of particle species contrary to the experimental result. The same discussion applies for strange mesons and baryons as can be seen from the right plot of Fig. 2.62. Whereas the kaon yields in central collisions are suppressed with respect to 'N_{coll} scaling' for all measured p_T, the yield of $\Lambda + \bar{\Lambda}$ is close to expectations from collision scaling in the p_T range 1.8–3.5 GeV/c. Interestingly, above $p_T \sim$ 5.0 GeV/c, the $K_S^0 K^{\pm}$, $\Lambda + \bar{\Lambda}$, and charged hadron yields are suppressed from binary scaling by a similar factor.

Figure 2.63 (left) shows the ratios of $(p+\bar{p})/2$ over π^0 as a function of p_T measured by PHENIX in central (0–10%, circles), mid-central (20–30%, squares), and peripheral (60–92%, triangles) Au+Au collisions [208], together with the corresponding ratios measured in pp collisions at CERN-ISR energies [243, 244] (crosses) and in gluon and quark jet fragmentation from e^+e^- collisions [245] (dashed

[1] Since the 60–92% peripheral AuAu (inclusive and identifi ed) spectra scale with N_{coll} when compared to the pp yields [124, 137, 208], R_{cp} carries basically the same information as $R_{\rm AA}$.

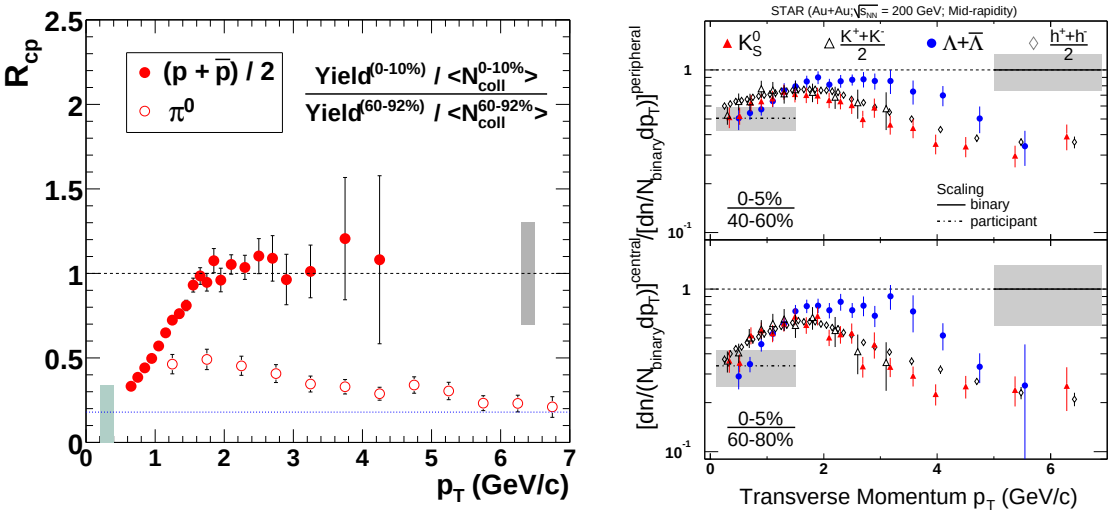

Fig. 2.62: Ratio of central over peripheral N_{coll} scaled yields, $R_{cp}(p_T)$, as a function of p_T for different species measured in AuAu collisions: (p$\bar{\text{p}}$)/2 (dots) and π^0 (circles) by PHENIX [208] (left), and $\Lambda, \bar{\Lambda}$ (circles) and $K^0_s, K^{\pm}$ (triangles) by STAR [241] (right)

and solid lines respectively). Within errors, peripheral AuAu results are compatible with the pp and e^+e^- ratios, but central AuAu collisions have a p/π ratio $\sim$ 4–5 times larger. Such a result is at odds with standard perturbative production mechanisms, since in this case the particle ratios $\bar{p}/\pi$ and p/π should be described by a universal fragmentation function independent of the colliding system, which favours the production of the lightest particle. Beyond $p_T \approx 4.5$ GeV/c, the identification of charged particles is not yet possible with the current PHENIX configuration, however the measured $h/\pi^0 \sim 1.6$ ratio above $p_T \sim 5$ GeV/c in central and peripheral AuAu is consistent with that measured in pp collisions (Fig. 2.63, right). This result together with STAR R_{cp} result on strange hadrons (Fig. 2.62, right) supports the fact that for large p_T values the properties of the baryon production mechanisms approach the (suppressed) meson scaling, thus limiting the observed baryon enhancement in central AuAu collisions to the intermediate transverse momenta $p_T \lesssim 5$ GeV/c.

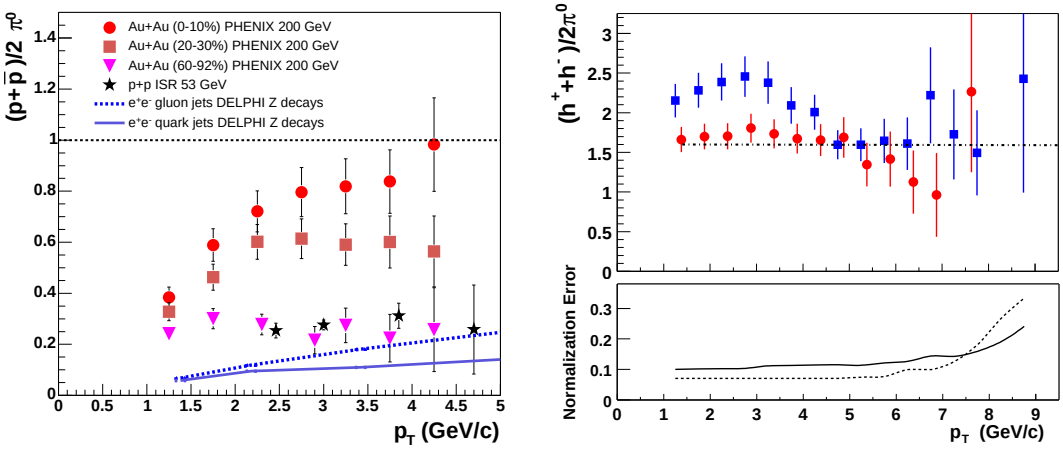

Fig. 2.63: Left: Ratios of (p$\bar{\text{p}}$)/2 over π^0 versus p_T in central (dots), mid-central (squares), and peripheral (triangles) AuAu, and in pp (crosses), and e^+e^- (dashed and solid lines) collisions [208]. Right: Ratio of charged hadron to π^0 in central (0–10% – squares) and peripheral (60–92% – circles) AuAu collisions compared to the $h/\pi \sim 1.6$ ratio (dashed-dotted line) measured in pp collisions [208].

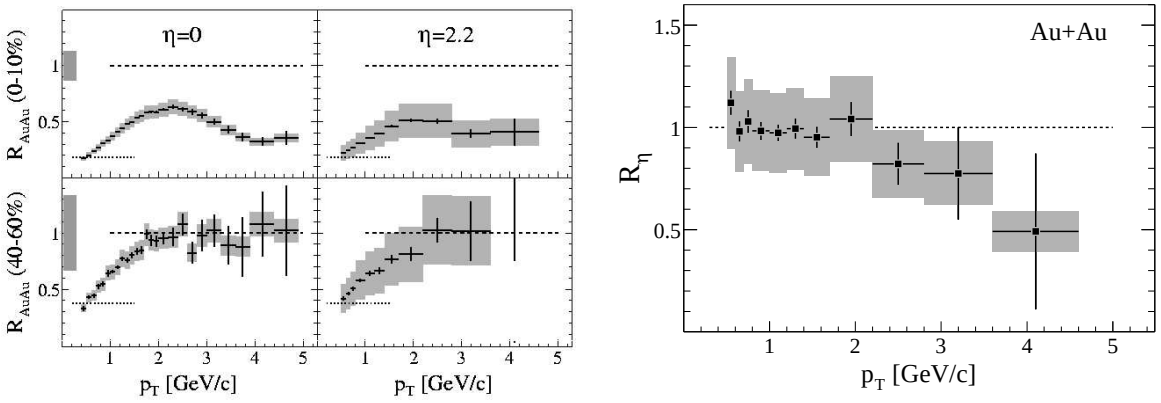

Fig. 2.64: Left: $R_{\rm AA}(p_T)$ measured by BRAHMS at η = 0 and η = 2.2 for 0–10% most central and for semi-peripheral (40–60%) AuAu collisions. Right: Ratio R_η of R_{cp} distributions at η = 2.2 and η = 0. Figures from [133].

Several theoretical explanations (see Refs. [208, 242]) have been proposed to justify the different behaviour of mesons and baryons at intermediate p_Ts based on: i) quark recombination (or coalescence), ii) medium-induced difference in the formation time of baryons and mesons, iii) different 'Cronin enhancement' for protons and pions, or iv) 'baryon junctions'. In the recombination picture [211, 213, 250] the partons from a thermalized system coalesce and with the addition of quark momenta, the soft production of baryons extends to much larger values of p_T than that for mesons. In this scenario, the effect is limited to $p_T < 5$ GeV, beyond which fragmentation becomes the dominant production mechanism for all species.

High p_T suppression: pseudorapidity dependence. BRAHMS is, so far, the only experiment at RHIC that has measured high p_T inclusive charged hadron spectra off mid-rapidity. Fig. 2.64 (left) shows the nuclear modification factors $R_{\rm AA}(p_T)$ for central and semi-peripheral AuAu measurements at mid-pseudorapidity (η = 0) and at η = 2.2 [133]. The high p_T suppression is not limited to central rapidities but it is clearly apparent at forward η's too. Figure 2.64 (right) shows the ratio of suppressions at the two pseudorapidity values, $R_\eta = R_{cp}(\eta = 2.2)/R_{cp}(\eta = 0)$. The high p_T deficit at η = 2.2 is similar to, or even larger than, at η = 0 indicating that the volume causing the suppression extends also in the longitudinal direction.

High p_T azimuthal correlations in AuAu collisions. There are two main sources of azimuthal correlations at high p_T in heavy-ion collisions:

- The *fragmentation* of hard-scattered *partons* results in jets of high p_T hadrons correlated in both rapidity and azimuthal angle. Such correlations are short range ($\Delta\eta \lesssim 0.7$, $\Delta\phi \lesssim 0.75$), involve comparatively large transverse momentum particles ($p_T > 2$ GeV/c), and are unrelated (in principle) to the orientation of the AA reaction plane.
- *Collective (elliptic) flow*: The combination of i) the geometrical asymmetry in non-central AA reactions ('almond'-like region of the overlapping nuclei), and ii) multiple reinteractions between the produced particles in the overlap region results in pressure gradients in the collision ellipsoid which transform the original coordinate-space asymmetry into a momentum–space anisotropy. The amount of elliptic flow (a true collective effect absent in pp collisions) is measured by the second harmonic coefficient, $v_2 \equiv \langle cos(2\phi)\rangle$, of the Fourier expansion of the particles azimuthal distribution with respect to the reaction plane.

Additionally, there are other second-order sources of angular correlations like resonance decays, final state (particularly Coulomb) interactions, momentum conservation, or other experimental effects

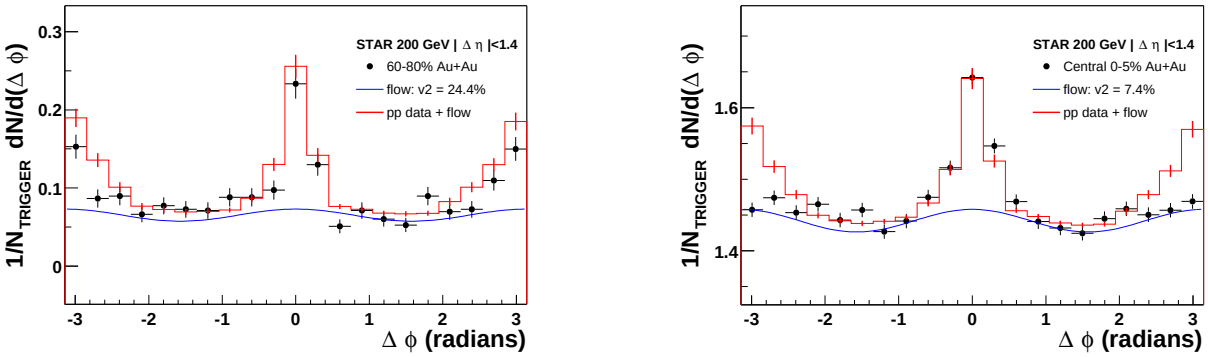

Fig. 2.65: Azimuthal correlations for peripheral (*left*) and central (*right*) AuAu collisions compared to the pedestal and flow-scaled correlations in pp collisions. Figure from Ref. [267].

like photon conversions, which have to be subtracted out in order to extract the interesting 'jet-like' or 'flow-like' signals.

4.3. High-p_T Azimuthal Correlations: Jet Signals

Although, standard jet reconstruction algorithms fail below $p_T \approx 40$ GeV/c when applied to the soft-background dominated environment of heavy-ion collisions, angular correlations of pairs of high p_T particles [207, 246] have been very successfully used to study on a statistical basis the properties of the produced jets. For each event with 'trigger' particle(s) with p_T = 4–6 GeV/c and 'associated' particle(s) with p_T = 2–4 GeV/c and $|\eta| < 0.7$, STAR [207] determines the two-particle azimuthal distribution

$$D(\Delta\phi) \propto \frac{1}{N_{trigger}} \frac{dN}{d(\Delta\phi)} \,. \tag{2.144}$$

Figure 2.65 shows $D(\Delta\phi)$ for peripheral (left) and central (right) AuAu collisions (dots) compared to $D(\Delta\phi)$ from pp collisions (histogram), and to a superposed $cos(2\Delta\phi)$ flow-like term (blue curve). On the one hand, the correlation strength at small relative angles ($\Delta\phi \sim 0$) in peripheral and central AuAu as well as at back-to-back angles ($\Delta\phi \sim \pi$) in peripheral AuAu are very similar to the scaled correlations in pp collisions. The near-side peaks in all three collision systems are characteristic of jet fragmentation [207] (a result also observed by PHENIX using *neutral* trigger particles [246]). On the other hand, the away-side peak ($\Delta\phi \sim \pi$) in central collisions is strongly suppressed.

In order to study the evolution as a function of centrality of the the near-side, $D^{AuAu}(\Delta\phi < 0.75)$, and away-side, $D^{AuAu}(\Delta\phi > 2.24)$, angular correlations in AuAu compared to pp, D^{pp}, STAR has constructed the quantity

$$I_{AA}(\Delta\phi_1, \Delta\phi_2) = \frac{\int_{\Delta\phi_1}^{\Delta\phi_2} d(\Delta\phi)[D^{\mathrm{AuAu}} - B(1 + 2v_2^2 \cos(2\Delta\phi))]}{\int_{\Delta\phi_1}^{\Delta\phi_2} d(\Delta\phi) D^{\mathrm{pp}}} \,, \tag{2.145}$$

where B accounts for overall background and v_2 the azimuthal correlations due to elliptic flow. Figure 2.66 shows I_{AA} for the near-side (squares) and away-side (circles) correlations as a function of the number of participating nucleons (N_{part}). On the one hand, the near-side correlation function is relatively suppressed compared to the expectation from Eq. (2.145) in the most peripheral region (a result not completely understood so far) and increases slowly with N_{part}. On the other hand, the back-to-back correlation strength above the background from elliptic flow, decreases with increasing N_{part} and is consistent with zero for the most central collisions. The disappearance of back-to-back jet-like correlations is consistent with large energy loss effects in a system that is opaque to the propagation of high-momentum partons or their fragmentation products.

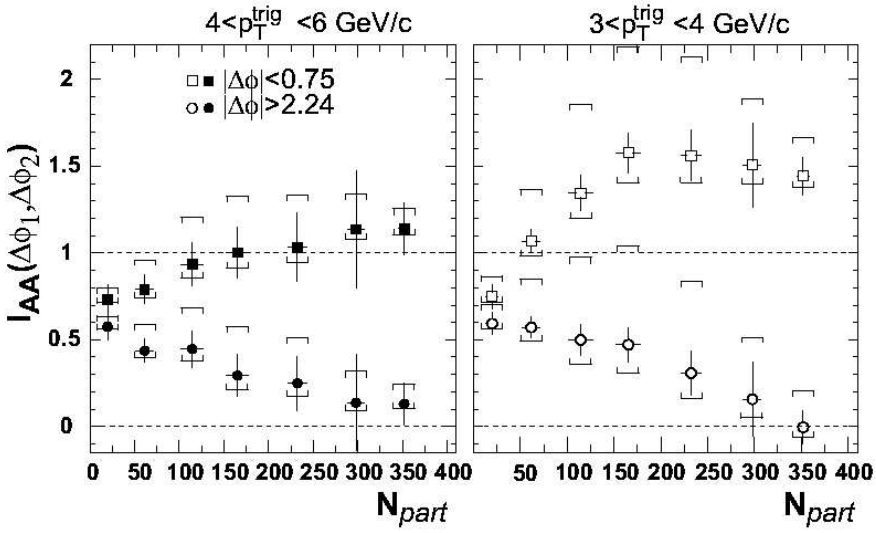

Fig. 2.66: Ratio of AuAu over pp integrated azimuthal correlations, Eq. (2.145), for small-angle (squares, $|\Delta\phi| < 0.75$ radians) and back-to-back (circles, $|\Delta\phi| > 2.24$ radians) azimuthal regions versus number of participating nucleons for trigger particle intervals $4 < p_T^{trig} < 6$ GeV/c (solid) and $3 < p_T^{trig} < 4$ GeV/c (hollow) [207]

High p_T azimuthal correlations: Collective elliptic flow. At low p_T the strength of the elliptic flow signal is found to be large and consistent with hydrodynamics expectations. Above $p_T \sim 2$ GeV/c where the contribution from collective behaviour is negligible, v_2 is found to be still a sizeable signal which saturates and/or slightly decreases as a function of p_T [209,241,247]. The large value $v_2(p_T > 2 \text{ GeV}/c) \sim 0.15$ implies unrealistically large parton densities and/or cross-sections according to standard parton transport calculations [251]. Various interpretations have been proposed to account for such a large v_2 parameter within different physical scenarios. In jet quenching models [81] the resulting momentum anisotropy results from the almond-like density profile of the opaque medium (see, however, [170]). Calculations based on gluon saturation [172] yield a ('non-flow') azimuthal asymmetry component from the fragmentation of the released gluons from the initial-state saturated wave functions of the colliding nuclei. Finally, quark recombination effects [251] can naturally enhance the elliptic flow of the produced hadrons compared to that of partons. The measured $v_2(p_T)$ for mesons and baryons shows a distinct pattern (Fig. 2.67): $v_2^m > v_2^b$ at low p_T, $v_2^m \approx v_2^b$ at $p_T \approx 2$ GeV/c, and $v_2^m < v_2^b$ at higher p_Ts; which further constraints the proposed theoretical explanations.

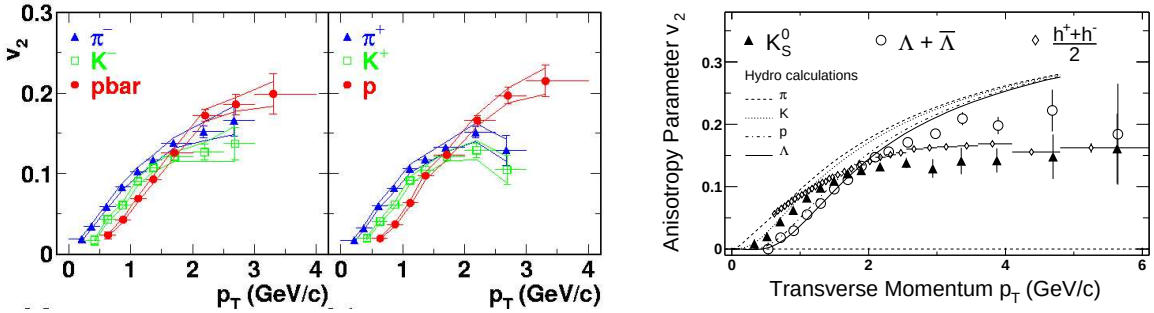

Fig. 2.67: v_2 as a function of transverse momentum for identifi ed particles at RHIC: $\pi^{\pm}$, $K^{\pm}$ and p, $\bar{p}$ from PHENIX (left), and K_s^0 and $\Lambda, \bar{\Lambda}$ from STAR (right)

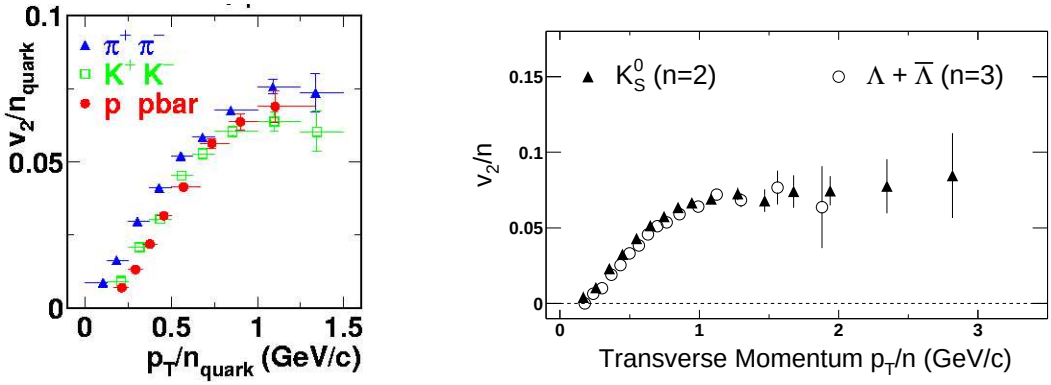

Fig. 2.68: The v_2 parameter scaled by the number of constituent quarks (n) versus p_T/n for $\pi^{\pm}$, $K^{\pm}$ and p, $\bar{\text{p}}$ (PHENIX [209], left) and K^0_s and Λ, $\bar{\Lambda}$ (STAR [241], right)

Quark coalescence models [251] naturally lead to weaker baryon flow than meson flow at low p_T, while the opposite holds above 2 GeV/c. This simple mass ordering expectation recombination models is confirmed by the identified particle data from PHENIX and STAR (Fig. 2.68). The fact that the v_2 parameters scaled by the number of constituent quarks (n = 2 for mesons, n = 3 baryons) versus p_T/n, globally fall in a single curve, supports the scenario where hadrons at moderate p_Ts form by coalescence of co-moving quarks.

4.4. High-p_T Hadron Production in dAu Collisions

Proton- (or deuteron-) nucleus collisions constitute a reference 'control' experiment needed to determine the influence of *cold* nuclear matter effects in high p_T hadro-production. Since final-state medium effects are marginal in p,dAu collisions, they are basic tools to ascertain whether models based on initial- or final- state QCD effects can explain the distinct hard scattering behaviour observed in AuAu collisions at RHIC. During the third year of RHIC operation, the four experiments collected data from dAu collisions at $\sqrt{s_{NN}}$ = 200 GeV. The resulting high p_T results at mid-rapidity from PHENIX [248], STAR [135], PHOBOS [134], and BRAHMS [133] consistently indicate the following:

- High p_T inclusive $h^{\pm}$ [133–135, 248] and π^0 [248] spectra from dAu minimum bias (MB) collisions are not suppressed but are *enhanced* compared to pp collisions (R_{dAu} plots in Fig. 2.69), in a way very much reminiscent of the 'Cronin effect' observed in fixed-target pA collisions at lower $\sqrt{s}$ [37]. As a matter of fact, pAu collisions (from neutron-tagged dAu events [248]) show a similar behaviour as minimum bias dAu collisions.
- Above $p_T \sim$ 2.5 GeV/c the nuclear modification factor of inclusive charged hadrons in MB dAu collisions saturates at [2] $R_{dAu} \sim 1.4$. Above 6 GeV/c, STAR $h^{\pm}$ and PHENIX π^0 results seem to indicate that R_{dAu} decreases as a function of p_T, becoming consistent with 1 at around 8 GeV/c.
- The 'Cronin enhancement' for unidentified hadrons at high p_T ($R^{h^{\pm}}_{dAu} \approx 1.35$) is larger than for neutral pions ($R^{\pi^0}_{dAu} \approx 1.1$) [248].
- The degree of 'enhancement' in dAu compared to pp *increases* with collision centrality [134, 135], an opposite trend to AuAu results.
- The azimuthal correlations in MB and central dAu collisions are very similar to that of pp and do not show the significant suppression of the away-side peak observed in central AuAu reactions [135].

All these results lead to the conclusion that no 'cold' nuclear matter (or initial-state) effects, - like a strong saturation of the nuclear parton distribution functions in the relevant (x, Q^2) kinematical

[2] $R^{\text{PHENIX}}_{dAu}(p_T = 2\text{–}7 \text{ GeV}/c) \sim 1.35$, $R^{\text{STAR}}_{dAu}(p_T = 2\text{–}6 \text{ GeV}/c) \sim 1.45$, $R^{\text{BRAHMS}}_{dAu}(p_T = 2\text{–}5 \text{ GeV}/c) \sim 1.3$.

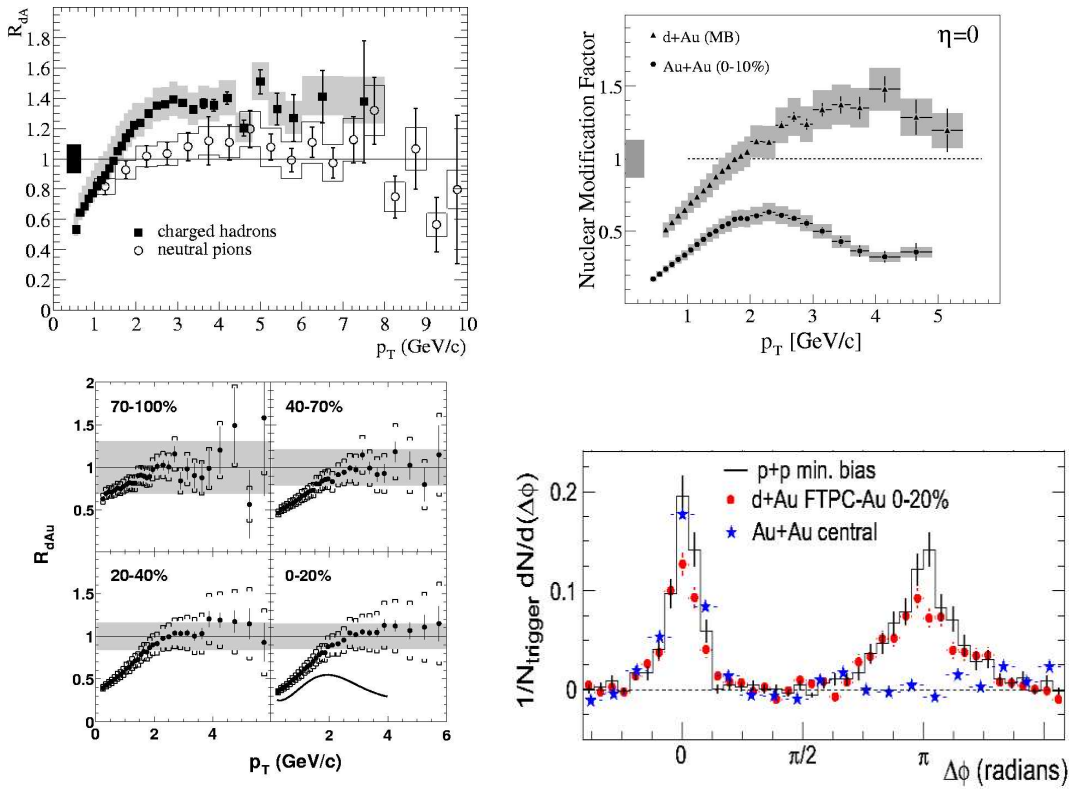

Fig. 2.69: Top: Nuclear modification factor R_{dAu} for MB dAu: $h^{\pm}$ and π^0 (PHENIX, left), $h^{\pm}$ (BRAHMS, right). Bottom: R_{dAu} for $h^{\pm}$ measured by PHOBOS in four different dAu centralities (left), and comparison of two-particle azimuthal distributions for central dAu, pp, and central AuAu collisions (STAR, right).

region probed by the current experimental setups-, can explain the high p_T behaviour in central AuAu. The data suggest, instead, that final-state interactions are responsible of the high p_T suppression and the disappearance of back-to-back dijet correlations observed at mid-rapidity in central AuAu reactions.

In summary, these data put strong experimental constraints on the properties of the underlying QCD medium produced in AuAu reactions at collider energies. Comparison of the energy spectra and angular correlations data to the theoretical calculations globally supports pQCD-based models of final-state parton energy loss in a dense medium, although non-perturbative effects (e.g. quark coalescence) are needed in order to explain the baryon–meson differences in yield and v_2 in the intermediate p_T window ($p_T \approx$ 2–5 GeV/c). Theoretical predictions of a strong saturation of the nuclear wave function at high energies are also in agreement with most of the data but do not seem to explain consistently AuAu and dAu RHIC results at midrapidity. Coming ion–ion runs at RHIC and, in the mid-term, PbPb collisions at LHC energies will help to further strengthen our current understanding of the physics of QCD media at high energy densities.

5. EXPERIMENTAL CAPABILITIES AT LHC

5.1. Jet Physics with the ALICE Detector

A. Morsch

ALICE is a multipurpose heavy ion experiment with excellent tracking and secondary vertex capabilities, electron and muon detection and a high resolution γ-spectrometer [268]. In the barrel part of the experiment ALICE will measure the flavor content and phase-space distribution, event by event, for a large number of particles whose momenta and masses are of the order of the typical energy scale

involved (temperature $\approx \Lambda_{\rm QCD} \approx$ 200 MeV). However, tracking and particle identification capabilities at central rapidity reach also far into the transverse momentum region in which particle production is expected to be dominated by hard processes, the production and fragmentation of high transverse momentum partons, i.e. jets.

Since in its present design complete measurements are restricted to charged particles, the ALICE detector has only limited capabilities to measure the jet energy. However, energy is not the only jet observable. On the contrary, it is likely that the most interesting observables which can reveal the presence and kind of interactions of partons with deconfined partonic matter and the associated radiation of additional gluons (jet quenching) are mainly related to the structure of the jets, i.e. the phase space distribution of particle around the jet axis, fragmentation function and jet shape. Recall also that historically the measurement of particle transverse momenta relative to the jet-axis has been used to show first evidence for gluons radiated from quark jets produced in e^+e^- collisions [269]. Similar distributions can be measured by ALICE down to very low particle momenta and for identified particles. This analysis will be performed as a function of the energy density by varying the centrality and the size of the AA collision system. The study of pA collisions will establish the reference for comparison with cold nuclear matter. Moreover, the observables can be studied as a function of the distance of the jet or leading particle direction to the reaction plane.

The STAR experiment at RHIC has shown [270] that the combination of an electromagnetic calorimeter with a TPC tracking system is functionally equivalent to an ideal jet detector in a heavy ion collision environment. An electromagnetic calorimeter for ALICE (EMCAL) [271] has been proposed by a group of collaborating US institutes. This would provide an opportunity to measure jet energy and the jet structure in heavy ion collisions.

5.1.1. Tracking Particle Identification

ALICE has been designed to measure single- and multi-particle distributions at the highest anticipated charged particle multiplicities for PbPb reactions ($dN/d\eta$ = 8000). The central tracking devices measure particles in the pseudo-rapidity range $|\eta| < 0.9$ with full azimuthal coverage. The inner tracker (ITS) [272] provides secondary vertex reconstruction of charm and hyperon decays, particle identification and tracking of low-momentum particles ($p_{\rm T} > 100$ MeV). The main tracking system is a Time Projection Chamber (TPC) [273] providing robust tracking capability, good momentum resolution and two particle separation, in a high particle density environment. The Transition Radiation Detector (TRD) [274] for electron identification adds additional tracking information at high radii improving the momentum resolution of high-$p_{\rm T}$ particles. The momentum resolution $\Delta p/p$ for particle momenta $<$ 2 GeV is below 1%. It rises almost linearly to up to 16% for p = 100 GeV. Tracking efficiency reaches almost 100% for momenta above 1 GeV. A geometrical inefficiency for high-$p_{\rm T}$ particles of 10% results from dead zones between the TPC read-out chambers.

A Time of Flight System (TOF) [275] based on multi-gap resistive plate chambers (RPCs) extends particle identification in the barrel region to 2 GeV and 3.5 GeV for $\rm K/\pi$ and $\rm K/p$ separation, respectively. Recent studies with an improved TPC tracking algorithm have shown that particle identification on a statistical basis via dE/dx can be extended into the relativistic rise up to $\approx$ 50 GeV. The HMPID (High Momentum Particle IDentification) system [276] using a single-arm Ring Imaging Cerenkov Counter is devoted to the discrimination of hadrons in the hard part of the momentum spectrum. It will enhance the PID capability of ALICE by allowing to identify particles beyond the momentum interval covered by the energy loss measurements and the TOF. The useful range for the identification of $\pi/\rm K$ and K/p of a track by track basis is extended up to 3 GeV and 5 GeV, respectively. The PHOS (PHOton Spectrometer) [277] is a single-arm high-resolution electromagnetic calorimeter of high granularity. It is optimized for measuring photons, π^0s and η mesons in broad energy ranges. The TRD provides excellent e/π-separation in the 1–100 GeV momentum range.

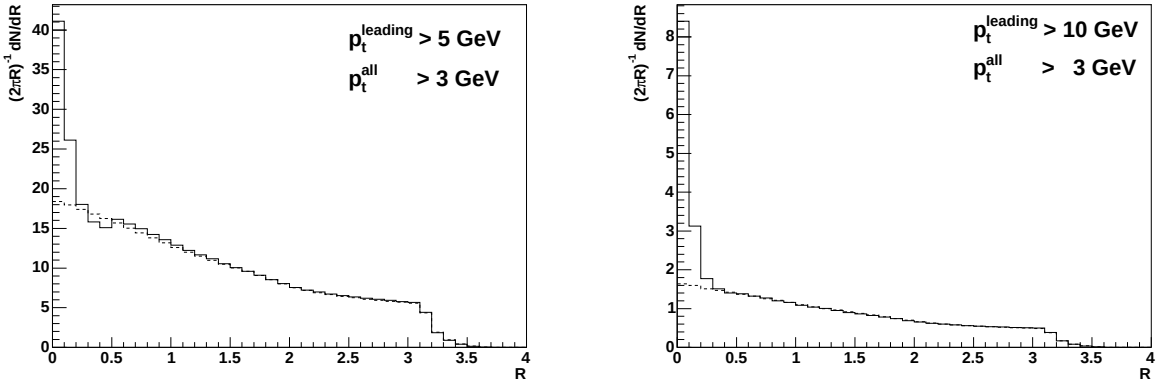

Fig. 2.70: Distance R of particles with $p_{\mathrm{T}}>$ 3 GeV/c to leading particles with $p_{\mathrm{T}}>$ 5 GeV/c (left) and $p_{\mathrm{T}}>$ 10 GeV/c (right). The dashed line describing the uncorrelated background is obtained using randomized leading particle directions.

5.1.2. Event geometry

The combined measurement of energy in the zero-degree calorimeters (ZDC) [278] and the forward electromagnetic calorimeter (ZEM) allows ALICE to determine the collision centrality in five impact parameter bins between 0 and 16 fm. Non-zero impact parameters lead to pressure gradients in the reaction volume producing directed flow that can be observed by ALICE as an anisotropy in the azimuthal distribution of final state particles. The measurement of directed flow allows an unambiguous determination of the event plane. Thus jet observables can be studied as a function of the centrality and the distance of the jet axis to the reaction plane.

5.1.3. Inclusive transverse momentum spectra

As described in Section 3.4.3 transverse momentum spectra are a mean to study final state radiative energy loss via the nuclear modification factor $R_{\mathrm{AA}}(p_{\mathrm{T}})$. Using a sample of 10^7 PbPb minimum bias events and in the absence of quenching ALICE will be able to measure the charged particle transverse momentum spectrum up to $\approx$ 100 GeV and down to $\approx$ 100 MeV. $\mathcal{O}(10)$ events are in the highest momentum bins where jet quenching is expected to reduce the charged particle yield by a factor 2–3. ALICE is planning to use a High Level Trigger (HLT) to increase the statistics in the high momentum region. Moreover, neutral pions will be identified on an event-by-event basis in the high-momentum range from 30–100 GeV.

5.1.4. Rates and the need for triggering

ALICE wants to study the whole spectrum of jet production ranging from mini-jets ($E_{\mathrm{T}} > 2$ GeV) to high-E_{T} jets of several hundred GeV. Concerning the experimental capabilities one has to distinguish four energy regions, which are here discussed for central ($b < 5$ fm) PbPb collisions at $\sqrt{s_{\mathrm{NN}}}$ = 5.5 TeV/nucleon:

- In the region $E_{\mathrm{T}} < 20$ GeV several jets of these energies overlap in one event within the ALICE acceptance. This means jet identification in the traditional sense is not possible. However, their presence reveals in inclusive studies of particle correlations.
- For $E_{\mathrm{T}} < 100$ GeV the jet rate of > 1 Hz is high enough so that even with a read-out rate limited by the TPC to 40 Hz an event sample of $> 10^5$ jets can be collected in one effective month of running (10^6 s).
- For $E_{\mathrm{T}} > 100$ GeV triggering will be necessary to collect enough data.

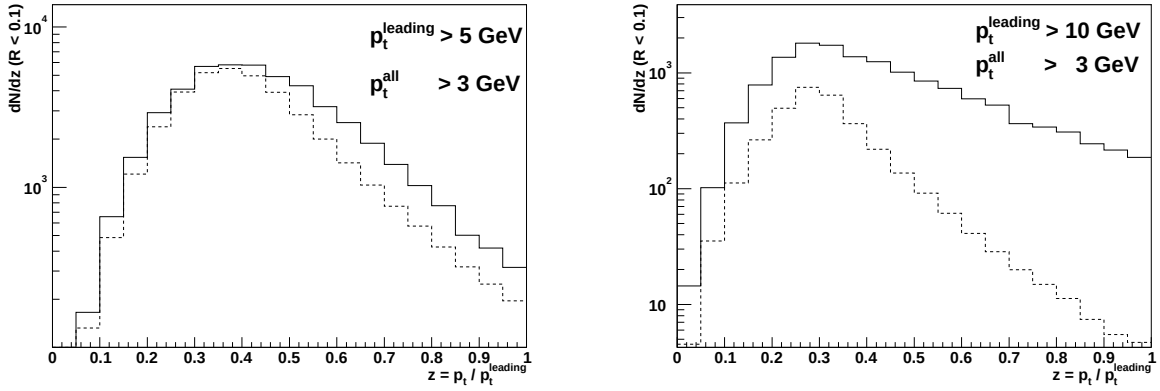

Fig. 2.71: Distribution of $z = p_{\mathrm{T}}/p_{\mathrm{T}}^{\mathrm{leading}}$ for particles within $R < 0.1$ of the leading particle direction (solid line). The contribution of uncorrelated particles obtained from a guard band $1 < R < 2$ has been subtracted and is shown as a dashed line

- Assuming that for a fragmentation function analysis one needs about 10^4–10^5 events the statistics limit is reached at about 250 GeV.

In the absence of calorimetry, triggering on jets is only possible using a High Level Trigger (HLT). Presently ALICE us studying the possibility to trigger on event topologies where two or more high-p_{T} tracks are found in a small area of the $\eta - \phi$ plane. The search has to be performed on track candidates which are themselves the result of a HLT fast clustering and tracking procedure.

5.1.5. Inclusive jets at low E_{T}

In proton–antiproton collisions at 1.8 TeV evidence for low energy charged particle clusters has been seen [279]. These charged particle jets become apparent event by event at a charged jet energy of about 2 GeV with, on the average, two charged particles with $p_{\mathrm{T}} > 0.5$ GeV and grow to, on the average, about 10 charged particles at a charged jet energy of 50 GeV.

In central PbPb collisions at 5.5 TeV with an anticipated charged particle multiplicity of up to 8000 charged particles per unit of rapidity the situation will be completely different. It is expected, that in one central collision about 100 jets with $p_{\mathrm{T}} > 5$ GeV, are produced within the acceptance of the ALICE central tracking system. The jet multiplicity decreases to an average of one, for $p_{\mathrm{T}} > 20$ GeV. The individual structures of these low-p_{T} jets dissolve in the overall event structure and are not distinguishable event by event. Nevertheless, their properties can be studied using inclusive particle correlation distributions as will be shown in the following.

This effort has two main objectives. First the study of the underlying event properties is important for the understanding of the limits of the energy resolution for the reconstruction of high-E_{T} jets in HI collisions, i.e. the underlying event fluctuations. Second, it is expected that in-medium modifications of the jet structure will be stronger for low jet energies. ALICE wants to study changes of the particle momenta parallel to the jet axis (jet quenching) and in the transverse direction (transverse heating).

In order to study inclusive particle correlations, three principle methods can be used:

- Event by event and region by region fluctuations of number of particles or energy;
- Correlations with *leading particles*;
- Spatial spectrum analysis (autocorrelation).

These three methods will be outlined in the following and some feasibility studies will be presented.

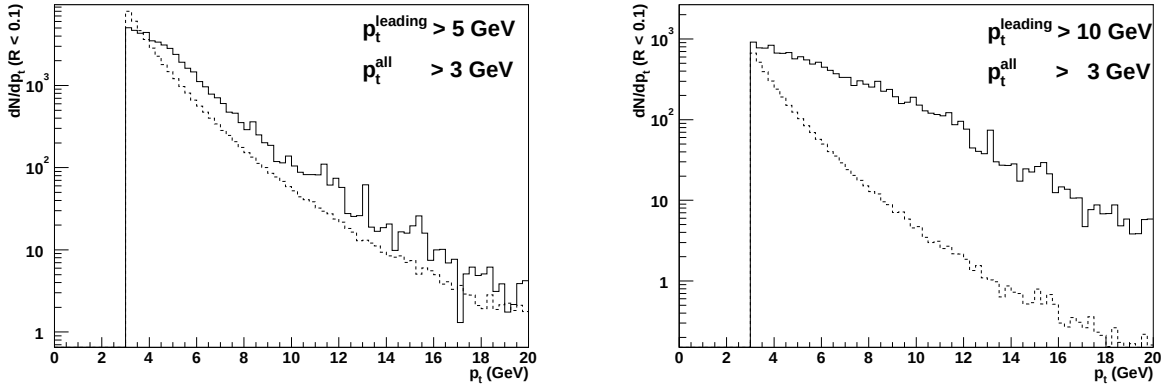

Fig. 2.72: Charged particle transverse momentum distribution for particles within $R < 0.1$ of the leading particle direction (solid line). The contribution of uncorrelated particles obtained from a guard band $1 < R < 2$ has been subtracted and is shown as a dashed line.

Underlying event fluctuations. Here, we will consider fluctuations of the energy contained in a cone of size R_0. These fluctuations limit the energy resolution of high-energy jets obtained with the cone algorithm. For uncorrelated particle production, the relation between the *rms* energy variation ΔE and the number of particles, N, the mean transverse momentum, $< p_{\rm T} >$, and the *rms* of the $p_{\rm T}$-distribution, $\Delta p_{\rm T}$, is $\Delta E = \sqrt{N}\sqrt{< p_{\rm T} >^2 + \Delta p_{\rm T}^2}$. As an example, this value increases by a factor $\sqrt{2}$, if the multiplicity N results from $N/2$ clusters of multiplicity 2. In fact, in central PbPb collisions simulated with HIJING [160, 187], we observe for R_0 = 0.3 fluctuations that are by factors of 1.3–1.5 higher than expected for uncorrelated particles, the exact value depending on the $p_{\rm T}$-cut.

Correlations with leading particles. In order to study correlations with leading particles we apply an algorithm similar to the one used for the CDF charged jet analysis. All particles with a $p_{\rm T} > p_{\rm T}^{\rm seed}$ are leading particle candidates and are ordered according to their $p_{\rm T}$. We start with the highest $p_{\rm T}$ candidate and record the distances R in the $\eta - \phi$-plane between all charged particles and the leading particle. If another candidate is found within a distance $R < R_{\rm sep}$ it is eliminated from the list of leading particles. The procedure continues with the next leading particle until none is left.

This algorithm is a natural extension of the cone algorithm used for jet reconstruction to inclusive studies in the low-$p_{\rm T}$ jet region for heavy ions collisions. To see possible angular correlations we plot the particle density $(2\pi R)^{-1}{\rm d}N/{\rm d}R$. Uncorrelated particle production should result in a flat distribution close to the leading particle direction R = 0.

HIJING simulations of central PbPb collisions at the LHC centre of mass energy have been performed to study these leading particle correlations. Fig. 2.70 shows such distributions for $p_{\rm T}^{\rm seed}$ = 5 and 10 GeV with a cut on all other particles of $p_{\rm T}^{\rm all} > 3$ GeV and $R_{\rm sep}$ = 0.5. The dashed lines are the corresponding distributions for randomized leading particle directions. Clear correlation signals are visible for $R < 0.3$. As expected, the significance of the signal increases with the transverse momentum cut.

Fragmentation function. The distributions of the correlated particle transverse momentum normalized by the leading particle transverse momentum $z = p_{\rm T}/p_{\rm T}^{\rm leading}$ is related to the jet fragmentation function. In Fig. 2.71 we show this distribution for particles with $R < 0.1$. The background distribution obtained from particles in a guard band $1 < R < 2$ has been subtracted and is shown as a dashed line. The signal dominates at high z values. The corresponding 'raw' $p_{\rm T}$ distributions are shown in Fig. 2.72.

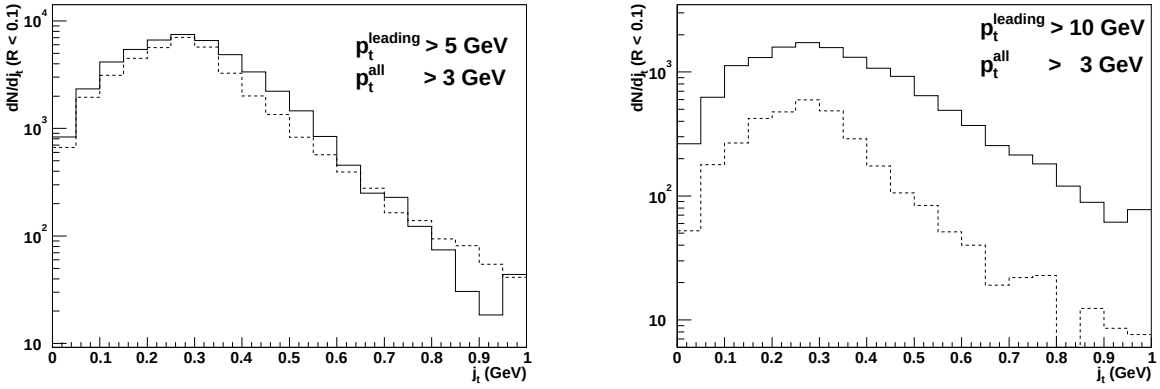

Fig. 2.73: Distributions of the correlated particle momentum perpendicular to the jet axis $j_{\mathrm{T}} = p\ \sin(\theta$(particle, leading particle)) obtained from particles within $R < 0.1$ of the leading particle direction (solid line). The contribution of uncorrelated particles obtained by randomizing the leading particle direction has been subtracted and is shown as a dashed line.

$p_{\mathrm{T}}^{\mathrm{leading}}$ is only a very poor estimator of the jet energy and the dN/dz distribution can only be interpreted as a smeared out 'pseudo'-fragmentation function. This explains the rather modest decrease as z approaches 1. Nevertheless, since in-medium modifications of the fragmentation function are expected to be strong for low energy jets, we expect that the effect can be observed in the measured distribution by comparing pPb to PbPb data.

Momentum transverse to the jet axis. The distributions of the correlated particle momentum perpendicular to the jet axis $j_{\mathrm{T}} = p\ \sin(\theta$(particle, leading particle)) is shown in Fig. 2.73. The background shown as dashed lines is obtained using randomized leading particle direction and has been subtracted. Signal and background have a similar distribution. However, this has to be interpreted in the light of the results of the previous paragraph, where we saw that the signal has a harder p_{T}-spectrum. Ordering of p_{T} in the jet fragmentation leads to limited j_{T} with mean value of about 250 MeV. Higher p_{T} particles are, on the average, closer to the jet axis. It is expected that in-medium effects can significantly broaden the j_{T} distribution of the particles inside the jet. For the expected $S/B > 1$ such changes can be easily measured.

Forward–backward correlations. The backward jets observed through forward-backward ϕ-correlations are more difficult. This is due to the limited η-acceptance of the experiment which reduces the number of two-jet events within the acceptance, especially for low-p_{T} jets. Higher statistics or harder cuts are needed than for the R-correlation to obtain significant signals. In Fig. 2.74 we show the $\Delta\phi$ distribution for particles with $p_{\mathrm{T}} > 5$ GeV with respect to the leading particles direction with $p_{\mathrm{T}}^{\mathrm{leading}} > 10$ GeV. Already for 10^4 HIJING events a significant backward peak is observed indicating that such an analysis is possible at the LHC.

Spatial spectrum analysis. Jets reveal their presence through repeating length scales. It is well known from signal processing that hidden periodicities can be detected using Fourier analysis techniques e.g. the spectral power density *(SPD)* or its back-transformation the autocorrelation function *(ACF)*. For jet analysis the discretized energy density distribution in the $\eta - \phi$ plane is used as an input. The transformations are performed using a two-dimensional discrete fast Fourier transformation algorithm (*DFFT*). In heavy ion collisions the length scales not only repeat inside the same event but also from

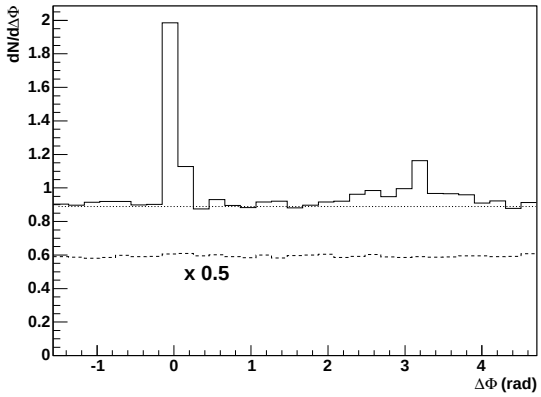

Fig. 2.74: $\Delta\phi$ distribution for particles with $p_{\mathrm{T}} > 5$ GeV/c with respect to the leading particle direction with $p_{\mathrm{T}}^{\mathrm{leading}} > 10$ GeV/c (solid line). The dashed lines represent the uncorrelated background and has been obtained by randomizing the leading particle direction. The dotted line indicates the uncorrelated background level below the signal and has been obtained from fi t to the region between the peaks.

event to event. In order to profit from this fact, the spectral power densities are averaged over many events before the back-transformation is performed to obtain the event averaged auto-correlation function.

5.1.6. Reconstructed jets

Charged jets. Leading particle analysis provides only a very poor energy measurement. It is known from pp data that leading charged particles carry on the average 24% of the charged jet energy. The distribution of this energy fraction has a *rms* of $\approx 50\%$ limiting the jet energy measurement to approximately the same value. Nevertheless, there exists some limited selection power for jet energy classes, since the jet energy can not be lower than the leading particle energy. Due to the steeply falling jet production spectrum a leading particle cut of for example $p_{\mathrm{T}} > 5$ GeV will select low-energy jets mainly in the range $5 < E_{\mathrm{T}} < 25$ GeV. In the low-energy region underlying event fluctuation are of the order of the reconstructible jet energy, i.e. the energy of reconstructed charged particles from the jet in a fixed cone after p_{T}-cuts. Hence, true jet reconstruction is only possible in the high energy region, $E_{\mathrm{T}} > 50$ GeV being our current estimate.

Since the energy resolution will be limited due to the incomplete reconstruction, a simple reconstruction algorithm is sufficient. The cone-algorithm similar to the one developed by the UA1 collaboration [280] has been used to evaluate the jet energy resolution in PbPb collisions using charged particles only. In this algorithm, charged particles above a threshold $p_{\mathrm{T}} > p_{\mathrm{T}}^{\mathrm{seed}}$ are considered as seeds. A jet is defined by all charged particles within a cone $R < R_{\mathrm{max}}$ with respect to the jet axis, which for the first iteration is given by the leading particle direction. In the next iteration a new jet direction is obtained from the sum of the momentum vectors of these jet particles. The procedure is repeated until convergence is reached, i.e. the difference between new and old direction falls below a minimum value. The energy from the underlying event is determined from the particle outside the jet cone and is subtracted from the cone energy. In central PbPb collisions, for a jet E_{T} of 50 GeV the energy resolution is similar to that obtained from the leading particle analysis ($\Delta E_{\mathrm{T}}/E_{\mathrm{T}} \approx 50\%$). For jet energies above 100 GeV the resolution improves to 40%. The resolution is mainly limited by the fluctuation in the part of the jet energy carried by charged particles (30%) and the small cone-size ($R < 0.3$) that is needed to reduce the energy from the underlying event. The latter reduces the reconstructed jet energy and thus increases the ratio $\Delta E/E$.

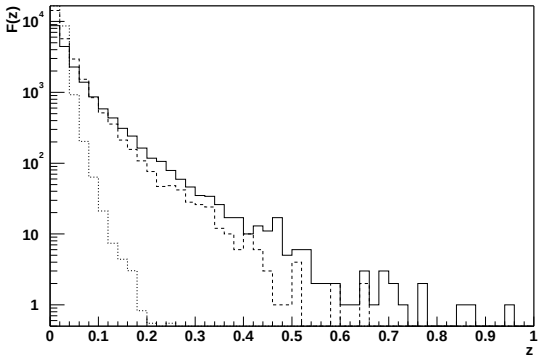

Fig. 2.75: Fragmentation function for jets that have a reconstructed jet energy in the range $95 < E_{\rm T} < 105$ GeV. The solid line is without jet quenching. The dashed line is for a quenching scenario which has been simulated using the superposition of two jets with $E_{\rm T}$ = 80 GeV and $E_{\rm T}$ = 20 GeV, respectively. The dotted line is the z-distribution for charged particles from the underlying event.

Energy resolution with EMCAL. The proposed EMCAL adds additional energy information from neutral particles. A linear combination of the energies of charged particles and calorimeter cells that minimizes the energy dispersion has been found from MC studies and is used to reconstruct the jet energy. In this case jets with $E_{\rm T} > 50$ GeV can be reconstructed. The expected resolution is 34% for $E_{\rm T}$ = 50 GeV and 29% for $E_{\rm T}$ = 100 GeV (preliminary results).

Fragmentation function with reconstructed jets. The fragmentation function represents the average distribution of jet energy among the particles produced in the fragmentation of the initial parton. The effect of additional gluon radiation when the particle is propagating through a deconfined partonic medium will change the fragmentation function in two ways: the relatively low-energetic radiated gluons will increase the number of particle carrying a small fraction z of the jet energy. On the contrary, the high-z part will be depleted. It is important to observe both effects experimentally. The challenge is to obtain a reasonable S/B in the low-z region and enough statistics in the high-z region.

As an example we show in Fig. 2.75 the fragmentation function for jets that have a reconstructed jet energy in the range $95 < E_{\rm T} < 105$ GeV. The solid line is without jet quenching. The dotted line is for a quenching scenario which has been simulated using the superposition of two jets with $E_{\rm T}$ = 80 GeV and $E_{\rm T}$ = 20 GeV, respectively. The dashed line is the underlying event.

Fragmentation function with identified leading particles. Reconstructed D-mesons and high-$p_{\rm T}$ electrons from semi-leptonic heavy-quark decays with large impact parameter are leading particles per se. They tag the production and fragmentation of charm and beauty quarks, respectively. In the past, experiments like UA1 without secondary vertex detection capability for charm and beauty hadrons have used non-isolation cuts as an additional criterion to select these heavy particles, where non-isolation is defined as the energy in a cone around the particle.

In ALICE, the secondary vertex reconstruction capability using the ITS allows to select these particles using impact parameter cuts. D^0 mesons decaying into πK can be reconstructed in the transverse momentum range $0 < p_{\rm T} < 15$ GeV. Electrons from b-hadron decays cover the transverse momentum range $p_{\rm T} > 2$ GeV. Additional particles close to the leading particle come from the fragmentation and decay of the heavy quark. The $j_{\rm T}$ and $p_{\rm T}$ distribution of these particles can be studied in pp, pPb and PbPb collisions. Again, differences between these systems are the result of interactions between partons

and the medium. They are expected to be weaker for heavy quarks than for light quarks, which makes this measurement especially interesting.

Moreover, for identified charmed mesons the inclusive p_{T}-spectra can be studied in the same way as for example charged light hadrons. Comparing $R_{\mathrm{AA}}(p_{\mathrm{T}})$ of light and heavy mesons will show whether energy loss is similar for both particle types. Theory expects a smaller energy loss for heavy quarks (dead-cone effect).

Photon-tagged jets. Photons produced at the earliest stage of the collisions, preserve almost all their energy after traversing through the dense medium. Hence, the attenuation of the jet energy can be measured via comparison of the prompt photon and jet kinematics. Prompt photons accompanied by a jet produced in the opposite direction at high p_{T} can be studied as a probe of the dense medium formed in heavy-ion collisions. ALICE will be able to detect and identify prompt photons using the PHOS detector, while hadrons from jets will be detected by the TPC and, optionally, by the EMCAL.

5.2. Jet Physics with the CMS Detector

O.L. Kodolova, I.P. Lokhtin, S.V. Petrushanko, C. Roland, L.I. Sarycheva, S.V. Shmatov and I.N. Vardanian

5.2.1. CMS Detector

The Compact Muon Solenoid (CMS) is a general purpose detector designed primarily to search for the Higgs boson in proton–proton collisions at LHC [281]. The detector is optimized for accurate measurements of the characteristics of high-energy leptons and photons as well as hadronic jets in a large acceptance, providing unique capabilities for 'hard probes' in both pp and AA collisions. In particular, jet quenching studies of hard jets, high-mass dimuons and high-p_T hadrons are primary goals of the CMS Heavy Ion Programme [192].

A detailed description of the detector elements can be found in the corresponding Technical Design Reports [282–285]. The longitudinal view of the CMS detector is presented in Fig. 2.76.

The central element of CMS is the magnet, a 13 m long solenoid with an internal radius $\approx$ 3 m, which will provide a strong 4 T uniform magnetic field. The 4π detector consists of a 6 m long and 1.3 m radius central tracker, electromagnetic (ECAL) and hadronic (HCAL) calorimeters inside the magnet and muon stations outside. The tracker and muon chambers cover the pseudorapidity region $|\eta| < 2.4$, while the ECAL and HCAL calorimeters reach $|\eta| = 3$. A pair of quartz-fiber very forward (HF) calorimeters, located $\pm$ 11 m from the interaction point, cover the region $3 < |\eta| < 5$ and complement the energy measurement. The tracker is composed of pixel layers and silicon strip counters. The CMS muon stations consist of drift tubes in the barrel region (MB), cathode strip chambers in the end-cap regions (ME), and resistive plate chambers in both barrel and endcap dedicated to triggering. The electromagnetic calorimeter is made of almost 76000 scintillating $PbWO_4$ crystals. The hadronic calorimeter consists of scintillator sandwiched between brass absorber plates. The main characteristics of the calorimeters, such as energy resolution and granularity are presented in Table 2.5.

5.2.2. Dijet, γ+jet and Z+jet production at CMS

The following signals of jet quenching by medium-induced parton energy loss have been identified as being measurable in heavy ion collisions with CMS [192].

Jet pairs are produced in the initial scattering processes in pp and AA collisions through reactions such as

$$gg \to gg\,, \quad qg \to qg\,, \quad qq \to qq\,, \quad gg \to q\overline{q}\,,$$

where the $gg \to gg$ process is dominant. High p_T jet pairs produced in nucleus–nucleus collisions can be

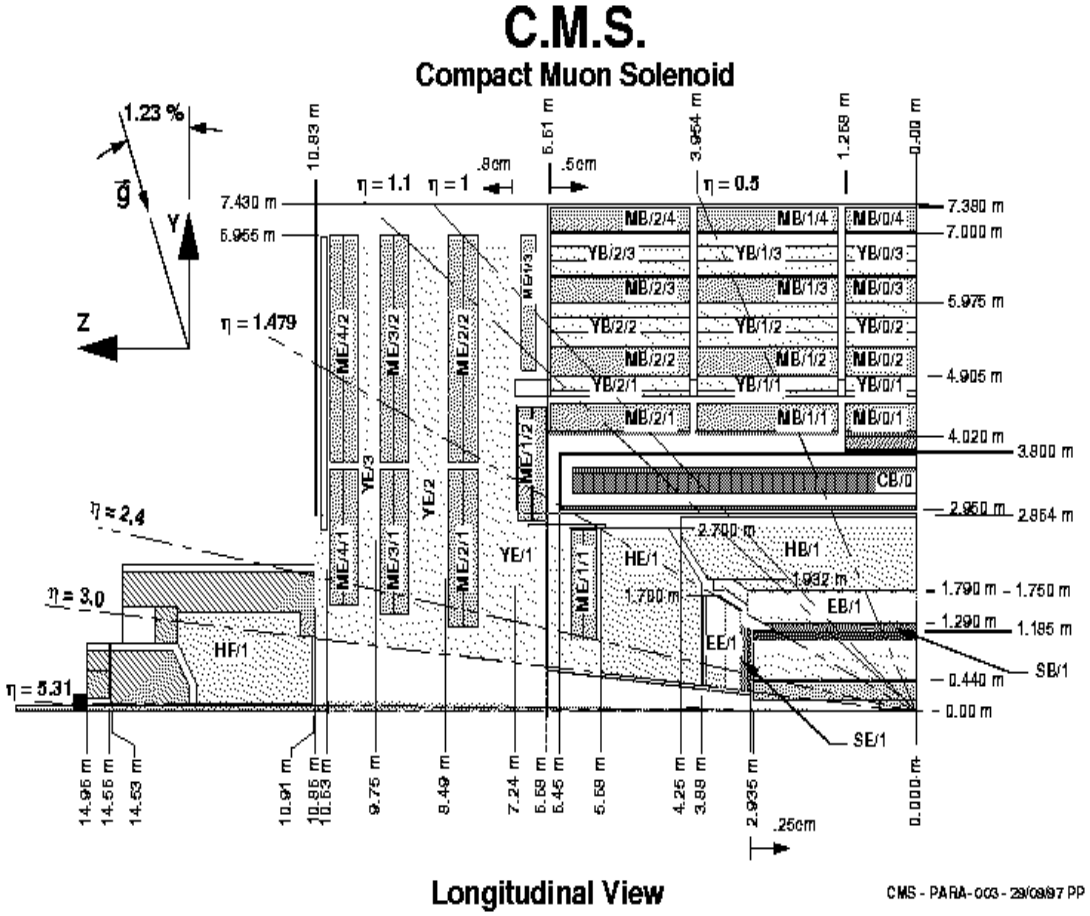

Fig. 2.76: The longitudinal view of CMS detector

suppressed relative to their production in independent nucleon–nucleon interactions [59]. The dijet rates depend on impact parameter [33] and may exhibit azimuthal anisotropy in non-central collisions [178].

Single jets may be produced opposite a gauge boson in γ+jet [120, 199] and Z+jet [286] final states, dominantly through processes such as

$$qg \to q\gamma \ , \qquad qg \to qZ \ .$$

In heavy ion collisions, the relative p_T between the jet and the boson becomes imbalanced due to interactions of the jet within the medium. The Z is detected in the dimuon channel, $Z \to \mu^+\mu^-$.

In this Section, we will consider mainly production and measurement of hard jets, the two points described above. Although not discussed in detail here, CMS can also measure parton energy loss in two other channels, leading particles and heavy quarks. Leading particles in a jet may have their momentum suppressed due to medium modifications of the jet fragmentation functions [50]. The capability of the CMS tracker to measure the momenta of charged particles in heavy ion collisions is discussed later. Heavy quark energy loss, particularly b quark loss, can be measured in two channels. Semileptonic B and D decays contribute to the high mass dimuon spectra and hadronic B decays to J/ψ are a substantial contribution to secondary charmonium production [151, 152].

Table 2.5: Energy resolution, σ/E, and granularity of the CMS calorimeters in the barrel (HB, EB), endcap (HE, EE) and very forward (HF) regions. The energy resolution is shown for the total energy of electrons and photons (ECAL) and transverse energy of hadronic jets (HCAL, HF).

Rapidity coverage	**$0 < \lvert\eta\rvert < 1.5$**		**$1.5 < \lvert\eta\rvert < 3.0$**		**$3.0 < \lvert\eta\rvert < 5.0$**
Subdetector	HCAL (HB)	ECAL (EB)	HCAL (HE)	ECAL (EE)	HF
$\frac{\sigma}{E} = \frac{a}{\sqrt{E}} \bigoplus b$					
a	1.16	0.027	0.91	0.057	0.77
b	0.05	0.0055	0.05	0.0055	0.05
granularity					
$\Delta\eta \times \Delta\varphi$	0.087×0.087	0.0174×0.0174	0.087×0.087	0.0174×0.0174 to 0.05×0.05	0.175×0.175

By considering 'jet energy loss' here, we concentrate on the energy that falls outside the jet cone and is truly lost to the jet, see Refs. [106, 114]. In fact, since coherent radiation induces a strong dependence of the radiative energy loss of a jet on the angular cone size, it will soften particle energy distributions inside the jet, increase the multiplicity of secondary particles, and, to a lesser degree, affect the total jet energy. On the other hand, collisional energy loss turns out to be practically independent of jet cone size and causes the loss of total jet energy. Moreover, the total energy loss of a jet will be sensitive to the experimental capabilities for low-p$_T$ particles, products of soft gluon fragmentation. In CMS, most of these low-p_T hadrons may be cleared out of the central calorimeters by the strong magnetic field.

Table 2.6 presents the event rates for various channels, including hard jets, in a one-month PbPb run (assuming two weeks of data taking), T = 1.2 $\times$ 10^6 s, with luminosity L = 5 $\times$ 10^{26}cm^{-2}s^{-1} so that

$$N_{\rm ev} = T\sigma^h_{AA}L \ .$$

The production cross sections in minimum bias nucleus–nucleus collisions were obtained from those in pp interactions at the same energy, $\sqrt{s}$ = 5.5 TeV, using the simple parameterization $\sigma^h_{AA} = \sigma^h_{pp}A^2$. The pp cross sections were evaluated using PYTHIA 6.1 [48] with the CTEQ5L parton distributions. The jet production cross sections in the CMS acceptance will be large enough to carefully study the dijet rate as a function of impact parameter as well as the azimuthal angle and rapidity distributions of jet pairs. The estimated statistics for γ+jet production are satisfactory for studying the E_T-imbalance of the process but the large background from jet+jet($\rightarrow \pi^0$) is still under investigation. The corresponding statistics for $Z(\rightarrow \mu^+\mu^-)$+jet are rather low, but the background is less than 10% in this case.

Table 2.6: Expected rates for jet production channels in a one-month PbPb run

Channel	**Barrel**	**Barrel + Endcap**
jet+jet, $E_T^{\rm jet} > 100$ GeV	2.1 $\times$ 10^6	4.3 $\times$ 10^6
γ+jet, $E_T^{{\rm jet},\gamma} > 100$ GeV	1.6 $\times$ 10^3	3.0 $\times$ 10^3
$Z(\rightarrow \mu^+\mu^-)$+jet, $E_T^{\rm jet}, p_T^Z > 100$ GeV	30	45
$Z(\rightarrow \mu^+\mu^-)$+jet, $E_T^{\rm jet}, p_T^Z > 50$ GeV	180	300

Of course, there are some theoretical uncertainties in the absolute jet rates in pp collisions due to the choice of parton distribution functions, the importance of next-to-leading order of α_s corrections, etc. Thus jet measurements in pp or dd collisions at the same or similar energies per nucleon as in the heavy ion runs are strongly desirable to determine the baseline rate precisely. One complementary way to reduce uncertainties in the analysis of jet quenching is the introduction of a reference process unaffected by medium-induced energy loss and with a production cross section proportional to the number of nucleon–nucleon collisions, such as $Z(\rightarrow \mu^+\mu^-)$ production [192, 286].

5.2.3. Jet reconstruction

The main difficulty of jet recognition in heavy ion collisions arises from the 'false' jet background — transverse energy fluctuations coming from the high multiplicity of 'thermal' secondary particles in the event [287]. Predictions give between 3000 to 8000 charged particles per unit rapidity in central PbPb collisions at the LHC. In these circumstances, reconstruction of 'true' QCD jets resulting from hard parton–parton scatterings is very important. The definition of an object like a jet is quite non-trivial even

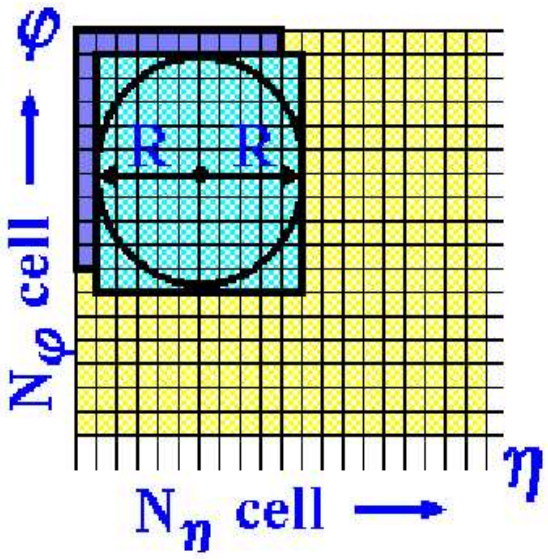

Fig. 2.77: Sliding window-type jet finding algorithm

in pp collisions. In particular, the energy and spatial resolution of hard jets are sensitive to the parameters of the jet finding algorithm, see Ref. [288].

In the CMS heavy ion physics programme, the modified sliding window-type jet finding algorithm has been developed to search for 'jet-like' clusters above the average energy and to subtract the background from the underlying event [192, 289], see Fig. 2.77 for an illustration. The algorithm is described step-by-step here.

- As a function of pseudorapidity η, one calculates for each event the average transverse energy, $\overline{E_T^{\rm cell}(\eta)}$, and the dispersion, $D_T^{\rm cell}(\eta) = \sqrt{\overline{(E_T^{\rm cell}(\eta))^2} - \left(\overline{E_T^{\rm cell}(\eta)}\right)^2}$, in all the calorimeter cells. The superscript 'cell' means averaging over the calorimeter cells in the given event.
- All possible rectangular windows, with overlaps, in the calorimeter map of $\eta - \varphi$ space are constructed. Each window consists of an integer number of calorimeter cells. The numbers of cells per window in η, $N_\eta^{\rm wind}$, and φ, $N_\varphi^{\rm wind}$, are calculated separately,

$$\begin{aligned} N_\eta^{\rm wind} &= RN_\eta^{\rm tot}/\eta_{\rm max}\,, \\ N_\varphi^{\rm wind} &= RN_\varphi^{\rm tot}/2\pi\,, \end{aligned}$$

  where $N_\eta^{\rm tot}$ and $N_\varphi^{\rm tot}$ are the total number of calorimeter cells in η and φ, $\eta_{\rm max}$ is the maximum pseudorapidity and R is the jet cone radius, an external parameter of the algorithm.
- The window energy is calculated as a sum of the call energies exceeding background, which is 1σ, $D_T^{\rm cell}(\eta)$, above the averaged energy, $E_T^{\rm cell}$. If the transverse energy of the cell is negative after background subtraction, it is set to zero.
- The search for jets and the evaluation of their energies is started from the window with the maximum transverse energy.
- Non-overlapping windows with energy $E_T^{\rm wind} > E_T^{\rm cut}$ are considered to be jet candidates.
- The centre of gravity of the window is considered as a centre of the jet.
- For correction of the jet axis a cell with maximum transverse energy in cone is found and considered as a new geometrical centre of this jet. Cells within radius R around the new geometrical centre are collected and centre of gravity of jet is recalculated.

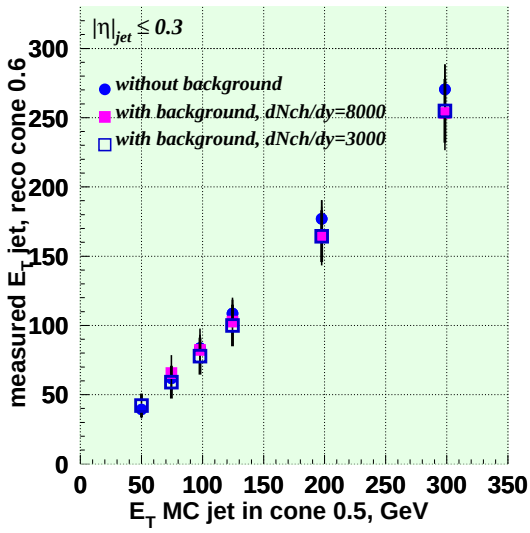

Fig. 2.78: Correlation between reconstructed and generated jet transverse energies in PbPb and pp events

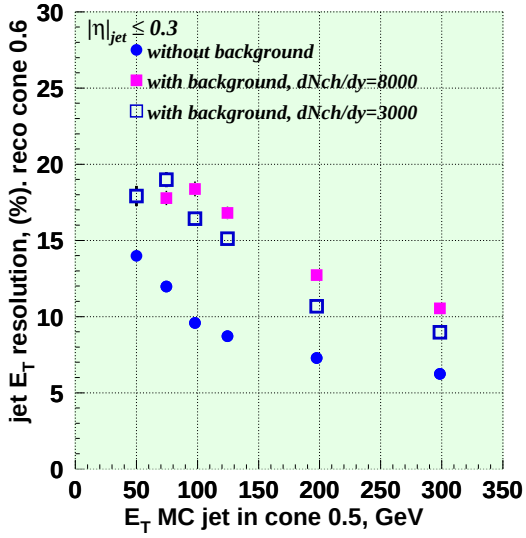

Fig. 2.79: Jet energy resolution in PbPb and pp events. (See text for explanation)

- Cells in a cone with radius R around jet centre are collected.
- The values of $\overline{E_T^{\rm cell}(\eta)}$ and $D_T^{\rm cell}(\eta)$ are recalculated using cells which were not included in the jets.
- The jet energy is then the difference between energies in collected cells, $E_T^{\rm cell}$, and the background energy per cell,

$$E_T^{\rm jet} = \sum_{n_c} \{E_T^{\rm cell} - [\overline{E_T^{\rm cell}(\eta)} + D_T^{\rm cell}(\eta)]\} \, .$$

Table 2.7: Purity, noise (contamination levels, false jets / generated jets) and jet transverse energy resolution in central Pb+Pb collisions with $dN^{\pm}/dy$ (y = 0) = 3000 and 8000

E_T min	Purity		Noise		$\sigma(E_T)/E_T(\%)$	
(GeV)	3000	8000	3000	8000	3000	8000
75	0.96 ± 0.03	0.88 ± 0.03	0.021 ± 0.006	0.083 ± 0.009	19.0	17.8
100	0.99 ± 0.03	0.97 ± 0.03	0.002 ± 0.001	0.011 ± 0.003	16.4	18.4
125	1.00 ± 0.03	0.99 ± 0.03	0.000 ± 0.000	0.004 ± 0.002	15.1	16.8
200	1.00 ± 0.03	0.99 ± 0.03	0.000 ± 0.000	0.001 ± 0.001	10.7	12.7

Jet reconstruction was studied in the barrel calorimeters, $|\eta| < 1.5$, with the GEANT-based package CMSIM_123 (CMS simulation package, version 123) adapted to heavy ion collisions. The initial jet distributions in the nucleon–nucleon sub-collisions at $\sqrt{s}$ = 5.5 TeV were generated using PYTHIA 6.1 [48], as described before. This dijet event is then superimposed on the PbPb event, obtained using a hydrodynamical model of the hadron spectrum [287] as a superposition of thermal hadron distributions

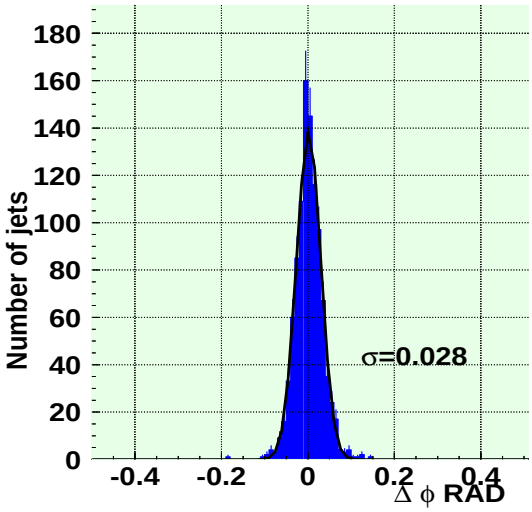

Fig. 2.80: Distribution of differences in azimuthal angle φ between generated and reconstructed jets with E_T = 100 GeV in pp events

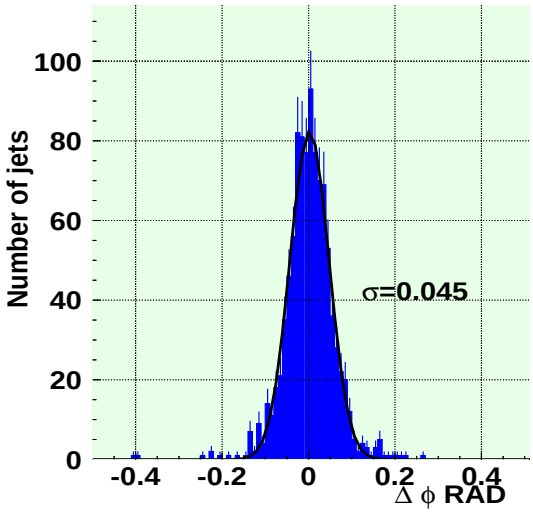

Fig. 2.81: The same as in Fig. 2.80 but for PbPb events at $dN^{\pm}/dy$ (y = 0) = 8000

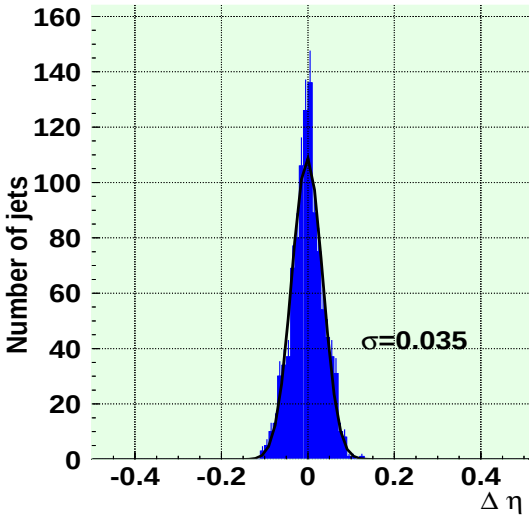

Fig. 2.82: Distribution of differences in pseudorapidity η between generated and reconstructed jets with E_T = 100 GeV in pp events.

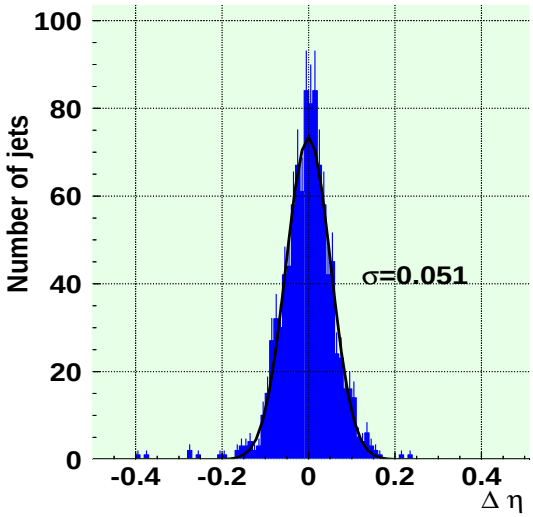

Fig. 2.83: The same as in Fig. 2.82 but for PbPb events at $dN^{\pm}/dy$ (y = 0) = 8000

and collective flow. The average hadron transverse momentum, $\langle p_T^h \rangle$ = 0.55 GeV/c, was fixed in the model. The analysis was done for two estimates of the charged particle multiplicity at y = 0 in central collisions, $dN^{\pm}/dy$ (y = 0) = 3000 and 8000. The calorimeter occupancy is high enough in these cases: mean energy per tower is about 4.4 (1.7) GeV for $dN^{\pm}/dy$ (y = 0) = 8000 (3000) in the barrel part, and it increases by a factor $\sim$ 2 in endcaps. Fig. 2.78 shows the correlation between reconstructed and generated transverse energies of jets in PbPb and pp events. The generated jet cone has a radius R = 0.5 while the radius of the reconstructed cone is larger, R = 0.6. Since the average measured jet energy in PbPb collisions is the same as in pp, the pp interactions are a baseline for jet physics in heavy ion collisions. However, the jet transverse energy resolution is degraded by a factor $\sim$ 2 in the high multiplicity central PbPb collisions compared to pp interactions, as shown in Fig. 2.79. The jet energy resolution is defined here as $\sigma(E_T^{\rm reco}/E_T^{\rm gen})/ < E_T^{\rm reco}/E_T^{\rm gen} >$, where $E_T^{\rm reco}$ is the reconstructed transverse energy, and $E_T^{\rm gen}$ is the transverse energy of all generated particles inside the given cone radius R. The resolution of 75 GeV jets with $dN^{\pm}/dy$ (y = 0) = 8000 is smaller than for 100 GeV jets (as well as the resolution of 50 GeV jets with $dN^{\pm}/dy$ (y = 0) = 3000 is smaller than for 75 GeV jets) since the background is not fully subtracted and, as a result, the reconstructed jet energy is larger in PbPb than pp. We can define the purity of jet reconstruction as the number of events with a true QCD jet divided by the number of events with reconstructed jets. Then, for example, the purity is $\sim$ 50% for 50 GeV jets for $dN^{\pm}/dy$ (y = 0) = 8000, because the average energy of the false jets in the background events is also $\sim$ 50 GeV. The purity increases rapidly with increasing $E_T^{\rm reco}$ and becomes $\sim$ 100% at 100 GeV. Table 7 summarizes the purity, contamination levels (false jets /generated jets) and jet transverse energy resolution in central PbPb collisions with $dN^{\pm}/dy$ (y = 0) = 3000 and 8000.

Since the azimuthal angle and rapidity distribution of jets are of particular interest for jet quenching observables, the angular resolution is important. Figures 2.80 and 2.81 show the differences in azimuthal angle φ between generated and reconstructed 100 GeV jets in events without and with PbPb background. Even in the most pessimistic case, $dN^{\pm}/dy$ (y = 0) = 8000, the φ resolution is degraded only by a factor of $\sim$ 1.6 in PbPb compared to pp collisions. The resolution is still less than the azimuthal size of a calorimeter tower, $\Delta\varphi$ = 0.087. A similar result is also found for the η resolution (shown in Figs. 2.82 and 2.83), which is however somewhat worse than the φ resolution. The reason for that is the vertex was not fixed here and there was not correction of η due to fluctuation of Z coordinate in 'pile up' subtraction algorithm (the latest version of the algorithm included this facility).

Figures 2.84 and 2.85 shows the energy dependence of the spatial resolution for pp and PbPb events with $dN^{\pm}/dy$ (y = 0) = 3000 and 8000. Thus the spatial position of a hard jet can be reconstructed in heavy ion collisions at CMS with high enough accuracy for analysis of jet production as a function of azimuthal angle and pseudorapidity.

The Level 1 single jet and electron/photon trigger rates in PbPb collisions have been estimated using the trigger algorithms developed for pp collisions with a parameterization of HIJING results for the background [192]. The dominant contribution to the trigger rate comes from the single jet trigger which uses the transverse energy sums (electromagnetic + hadronic) computed in the calorimeter regions (4 $\times$ 4 trigger cells) $\Delta\eta \times \Delta\phi$ = 0.348 $\times$ 0.348. For a threshold of 40–50 GeV it gives an acceptable output rate of about 400–200 Hz and is fully efficient for most central collisions. Assuming that with the high level trigger full jet reconstruction is possible, the rate can be further reduced to a level lower than 10 Hz for jets with reconstructed transverse energies greater than 100 GeV. The rate of the single photon trigger is less than 1 Hz for a threshold of 50 GeV. With such a threshold, the trigger efficiency is close to 10% for γ+jet events useful for off-line analysis.

5.2.4. Tracking

Track finding in heavy ion collisions is difficult due to the large number of tracks in an event. We consider heavy ion multiplicities up to the worst case, 8000 charged particles per unit rapidity in a central PbPb event. In addition to the primary tracks, the CMS tracker is occupied by secondaries produced by

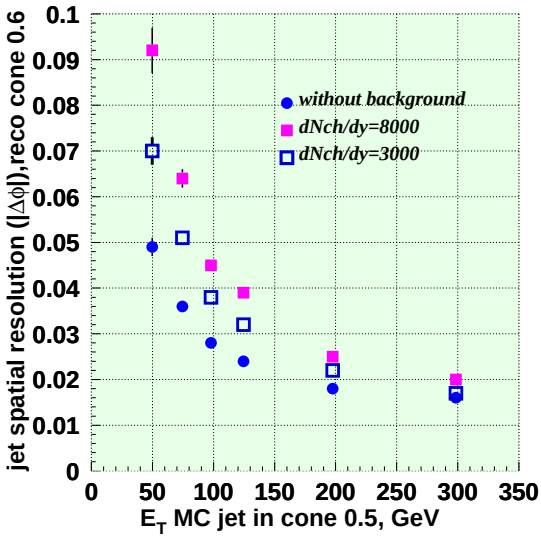

Fig. 2.84: Energy dependence of jet azimuthal angle resolution in PbPb and pp events

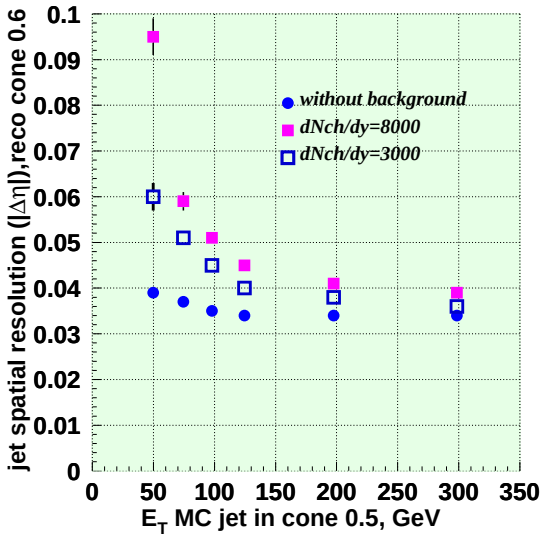

Fig. 2.85: Energy dependence of jet pseudorapidity resolution in PbPb and pp events

interactions with the detector material. The CMS track reconstruction algorithm, originally developed for pp collisions, is based on Kalman Filtering and includes seed generation, track propagation, trajectory updating and smoothing. However, this track finder, optimized for the highest efficiency at low density, fails when dealing with central PbPb events due to the large hit combinatorics. Therefore, modification of the algorithm is necessary [290].

The essential difference for heavy ion collisions is that the primary vertex can be determined with dispersion of 200 μm using only two barrel layers before any tracking. Using this constraint reduces the combinatorial background during track seeding. Thus these two features, primary vertex finding and restriction of the vertex region, were added to the standard package.

In order to achieve good rejection power to fake tracks from random hit combinations we need to require the track to have as many hits as possible. Only tracks that leave the tracker through the outermost layer are considered. This requirement leads to a minimum transverse momentum cutoff of $p_T > 1$ GeV for the track to be considered reconstructable.

Given this constraint the modified pp reconstruction algorithm gives about $\approx 80\%$ geometrical acceptance and close to $\approx 100\%$ algorithmic reconstruction efficiency in a low multiplicity environment. The acceptance varies slightly $\pm$ 10% over the η-coverage of the tracker and is independent of p_T.

We have tested track propagation algorithms for the case of high occupancy using Monte Carlo tracks seeds. The estimated efficiency under these conditions appears high enough, $\approx 80\%$. The momentum resolution is less than 1% at $p_T < 100$ GeV. Thus track propagation at high density is quite effective. The reconstruction time is around 1500 s per event. We have also investigated using a regional track reconstruction in a limited $\eta - \varphi$ area. This option is essentially needed for jet finding and correcting. The efficiency is very high, $\gtrsim 95\%$, but we see a large number of fake tracks.

Thus we believe that pattern recognition is possible in heavy ion collisions with the CMS tracking system. The existing pp track reconstruction package has been shown to be a valuable framework, but needs major restructuring to reduce combinatorics and computation time.

5.2.5. *Impact parameter determination*

It is important to study hard jet and high-p_T hadron production in heavy ion collisions as a function of centrality. In CMS, the best way to determine the impact parameter, b, event-by-event is the transverse energy deposited in the calorimeters, $E_T^{\rm tot}$, which strongly decreases from central to peripheral collisions [192]. The jet production rates, $N^{\rm jet}$, can be measured in bins of $E_T^{\rm tot}$. Then the $b-$ and $E_T^{\rm tot}-$ dependencies of $N^{\rm jet}$ can be related by the $E_T^{\rm tot}-b$ correlation functions C_{AA},

$$N^{\rm jet}(E_T^{\rm tot}) = \int d^2b N^{\rm jet}(b) C_{AA}(E_T^{\rm tot},b), \;\; C_{AA}(E_T^{\rm tot},b) = \frac{1}{\sqrt{2\pi}\sigma_{E_T}(b)} \exp\left(-\frac{\left(E_T^{\rm tot} - \overline{E_T^{\rm tot}}(b)\right)^2}{2\sigma^2_{E_T}(b)}\right),$$

$$N^{\rm jet}(b) = \int dE_T^{\rm tot} N^{\rm jet}(E_T^{\rm tot}) C_{AA}(b,E_T^{\rm tot}), \;\; C_{AA}(b,E_T^{\rm tot}) = \frac{1}{\sqrt{2\pi}\sigma_b(E_T^{\rm tot})} \exp\left(-\frac{\left(b - \overline{b}(E_T^{\rm tot})\right)^2}{2\sigma^2_b(E_T^{\rm tot})}\right).$$

Since very forward rapidity region, $|\eta| \gtrsim 3$, is almost free of final state interactions, the (transverse) energy deposition in HF is determined mainly by the initial nuclear geometry of a collision rather than by final state dynamics. Determining the impact parameter via (transverse) energy deposition in the HF calorimeter thus avoids some possible uncertainties [183, 192]. The impact parameter dependence of the total transverse energy produced in the pseudorapidity interval $3 \leq |\eta| \leq 5$ obtained with HIJING [160, 187] is presented in Fig. 2.86 from Ref. [183] for PbPb interactions. The $E_T - b$ correlation is diffuse due to fluctuations in the nucleus–nucleus collision dynamics, including fluctuations in the number of nucleon–nucleon sub-collisions at a given b and fluctuations of transverse energy flow in each nucleon–nucleon interaction. The correlation of the total energy flow is of similar shape. Most of the energy produced in the very forward direction is between 10 and 100 TeV. It is then possible to measure the total energy with high accuracy, reducing uncertainties in b. The impact parameter distribution at fixed values of E_T is Gaussian-like with a width, σ_b, dependent on impact parameter, see Fig. 2.87 from Ref. [183]. The absolute accuracy is defined here as $\pm 2\sigma_b$, about ~ 1 fm for PbPb collisions with $1 \lesssim b \lesssim 13$ fm. It is degraded by a factor of ~ 2 for very peripheral events, $b \gtrsim 13$ fm, due to the diminution of the produced energy in the pseudorapidity region. At the same time, we see that the relative error is minimal for peripheral collisions since the statistics are increased.

To summarize, we note that although these results were obtained on the particle level, similar conclusions are expected to be valid when detector effects are taken into account. It has been shown that the finite energy and spatial resolution of the HF calorimeter do not substantially degrade the accuracy of the impact parameter determination in heavy ion collisions [183].

5.2.6. *Reconstruction of nuclear reaction plane*

The azimuthal anisotropy of jet and high-p_T particle production in semi-central heavy ion collisions is predicted to be a signal of partonic energy loss in an azimuthally asymmetric volume of quark–gluon plasma [73, 74, 162, 178]. The advantage of azimuthal jet observables is that one needs to reconstruct only the azimuthal position of jet, not its total energy. It can be done easily and with high accuracy while reconstruction of the jet energy is more ambiguous. The methods summarized in Refs. [163, 164] present ways to determine the reaction plane. They are applicable to the study of anisotropic flow of soft and semi-hard particles in the current dedicated heavy ion experiments at the SPS [291] and RHIC [292] and may also be used at the LHC [178]. When the azimuthal distribution of particles is described by the elliptic form,

$$\frac{dN}{d\varphi} = \frac{N_0}{2\pi}\left[1 + 2v_2 \cos 2(\varphi - \varphi_{\rm reac})\right], \quad N_0 = \int\limits_{-\pi}^{\pi} d\varphi \, \frac{dN}{d\varphi},$$

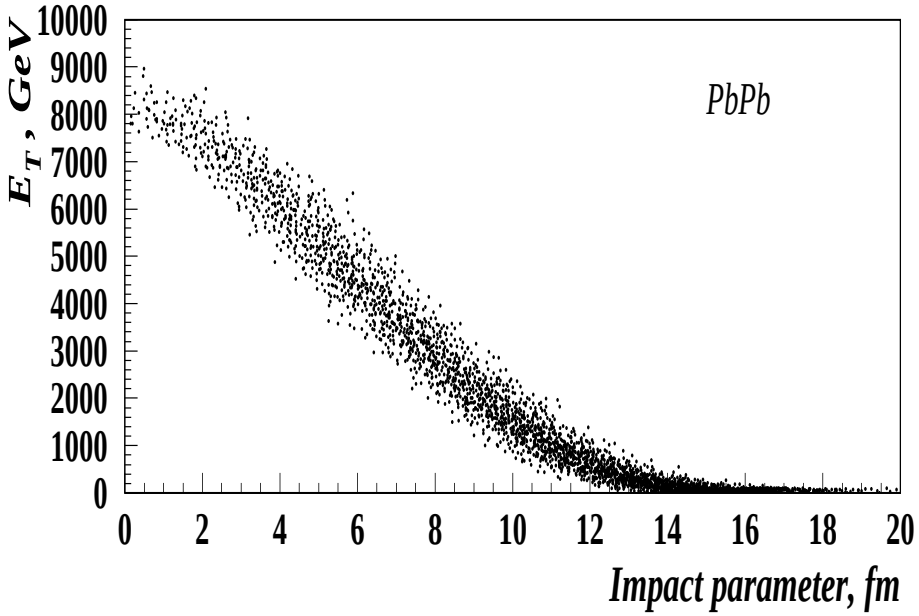

Fig. 2.86: Correlation between the transverse energy flow, E_T, and impact parameter b at very forward rapidities, $3 \leq |\eta| \leq 5$, for 10000 minimum bias PbPb collisions [183]

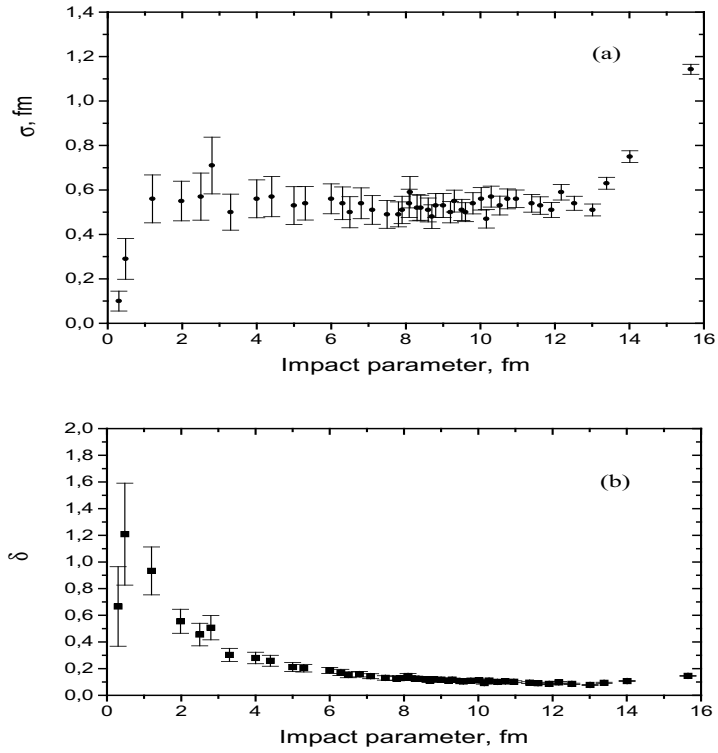

Fig. 2.87: Impact parameter dependence of (a) the Gaussian width σ_b and (b) the relative error $\delta = 2\sigma_b/b$ for PbPb collisions [183]

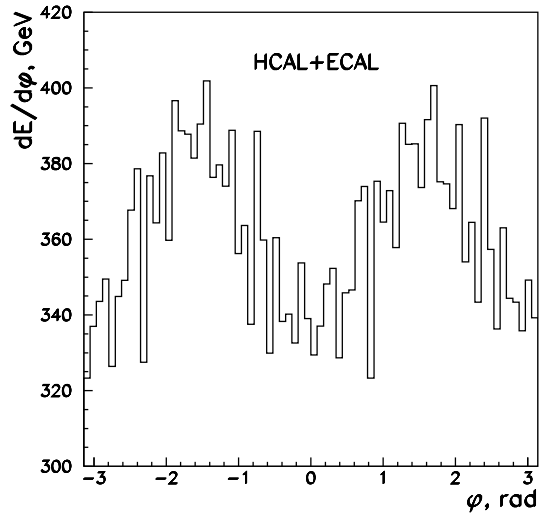

Fig. 2.88: Energy deposition in the barrel and endcap regions of the CMS hadronic (HCAL) and electromagnetic (ECAL) calorimeters for PbPb collisions at b = 6 fm (hydrodynamics with CMSIM_125)

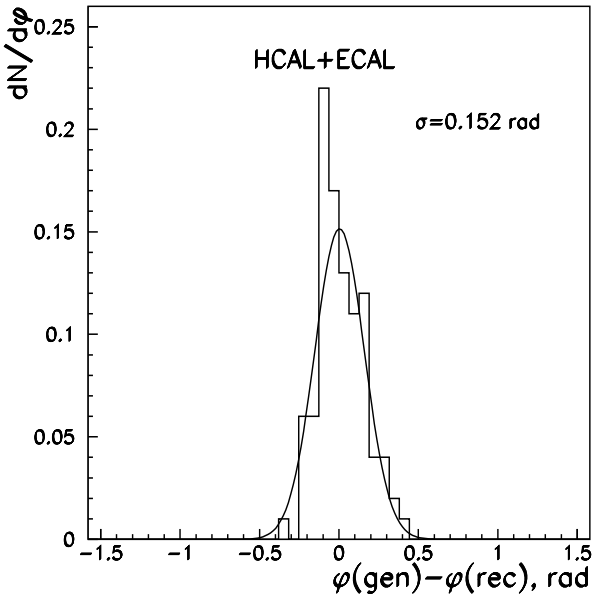

Fig. 2.89: Distribution of differences in the generated and reconstructed azimuthal angles of the PbPb reaction plane for b = 6 fm (hydrodynamics with CMSIM_125)

the nuclear reaction plane angle, $\varphi_{\rm reac}$, is

$$\tan\left(2\varphi_{\rm reac}\right) = \frac{\sum_i \omega_i \sin 2\varphi_i}{\sum_i \omega_i \cos 2\varphi_i} \,,$$

where the weights, ω_i, are selected to optimize the resolution. The coefficient v_2 of the azimuthal anisotropy of particle flow is an average over $\cos(2\varphi)$. In CMS, the weights can be introduced [293] as energy deposition in calorimeter sector i of position φ_i, $\omega_i = E_i(\varphi_i)$. Figure 2.88 illustrates the energy deposition in sectors of the barrel and endcap regions of the CMS hadronic and electromagnetic calorimeters, $|\eta| < 3$, for generated with hydro-code [185, 287] PbPb events at b = 6 fm. The detector response is obtained with CMSIM_125. The estimated resolution of the $\varphi_{\rm reac}$ determination, $\sigma_{\varphi\ \rm reac}$ = 0.15 rad, see Fig. 2.89, allows measurement of the coefficient of the jet azimuthal anisotropy with $\sim 90\%$ accuracy, defined as the ratio of the average of $\langle \cos 2\varphi_{\rm jet} \rangle$ over all events "measured" to its "true" value. The estimates obtained are quite optimistic because hydrodynamic models give rather large values of elliptic flow at high-p_T. On the other hand, the majority of microscopic Monte Carlo models underestimate flow. For example, under the same conditions HIJING [160, 187] with jet quenching predicts much less anisotropic flow and yields $\sigma_{\varphi\ \rm reac}$ = 0.8 with only $\sim$ 20% accuracy.

Recently a method was also suggested [185] for measuring the jet azimuthal anisotropy coefficients without event-by-event reconstruction of the reaction plane. This technique is based on the correlations between the azimuthal position of the jet axis and the angles of particles not incorporated in the jet. Then

$$v_2^{\rm jet} \equiv \langle \cos 2\varphi_{\rm jet} \rangle_{\rm event} = \left\langle \frac{\langle \cos 2(\varphi_{\rm jet} - \varphi)\ \omega(\varphi) \rangle}{\sqrt{\langle \cos 2(\varphi_1 - \varphi_2)\ \omega_1(\varphi_1)\ \omega_2(\varphi_2) \rangle}} \right\rangle_{\rm event} \,,$$

where the weights ω_i are defined as before. In some sense, this represents the development and generalization of the well-known method for measuring the azimuthal anisotropy of particle flow originally considered in a number of works, see for example Refs. [163–166, 173]. The accuracy of the method improves with increasing multiplicity and particle (energy) azimuthal anisotropy and is practically independent of the absolute value of the azimuthal anisotropy of the jet itself [185]. The accuracy of $v_2^{\rm jet}$

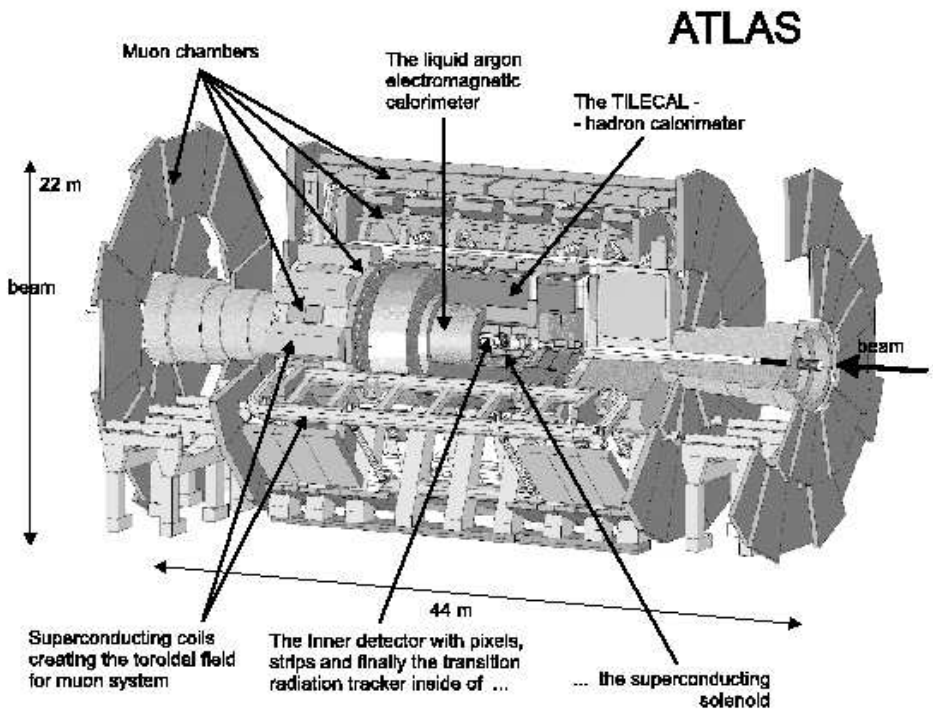

Fig. 2.90: The overall layout of the ATLAS detector

achieved by such a method are estimated to be 94% for hydrodynamics and 30% for HIJING, somewhat better than those obtained from direct reconstruction of the reaction plane angle.

5.3. Jet Physics with the ATLAS Detector

S. Aronson, K. Assamagan, B.Cole, M. Dobbs, J. Dolesji, H. Gordon, F. Gianotti, S. Kabana, M. Levine, F. Marroquim, J. Nagle, P. Nevski, A. Olszewski, L. Rosselet, P. Sawicki, H. Takai, S. Tapprogge, A. Trzupek, M.A.B. Vale, S. White, R. Witt, B. Wosiek and K. Wozniak

The ATLAS detector is designed to study high p_T physics in proton–proton collisions at high LHC machine luminosity. Most of the detector subsystems will be available for the study of heavy ion collisions. One of the highlights of the ATLAS detector is its calorimeter subsystem. Both the electromagnetic and hadronic compartments are finely segmented and well suited for jet quenching studies. RHIC results suggest that partons may radiate gluons in the dense matter formed in heavy ion collisions. This phenomena can be certainly be well explored in the ATLAS detector. We report on early assessment of the detector capabilities in the heavy ion environment.

5.3.1. The ATLAS detector

The ATLAS detector is designed to study proton–proton collisions at the LHC design energy of 14 TeV in the centre of mass. The physics pursued by the collaboration is vast and includes: Higgs boson search, searches for SUSY, and other scenarios beyond the Standard Model, as well as precision measurements of process within (and possibly beyond) the Standard Model. To achieve these goals at a full machine luminosity of 10^{34} cm^{-2}s^{-1}. ATLAS will have a precise tracking system (Inner Detector) for charged particle measurements, an as hermetic as possible calorimeter system, which has an extremely fine grain segmentation, and a stand-alone muon system. An overview of the detector is shown in Fig. 2.90.

The Inner Detector is composed of (1) a finely segmented silicon pixel detector, (2) silicon strip detectors (Semiconductor Tracker (SCT)) and (3) the Transition Radiation Tracker (TRT). The segmentation is optimized for proton–proton collisions at design machine luminosity. The inner detector system is designed to cover a pseudo-rapidity of $\mid \eta \mid < 2.5$ and is located inside a 2 T solenoid magnet.

The calorimeter system in the ATLAS detector surrounds the solenoid magnet is divided into electromagnetic and hadronic sections and covers pseudo-rapidity $\mid \eta \mid < 4.9$. The EM calorimeter is an accordion liquid argon device and is finely segmented longitudinally and transversely for $\mid \eta \mid \leq 3.1$. The first longitudinal segmentation has a granularity of 0.003 $\times$ 0.1 ($\Delta\eta \times \Delta\phi$) in the barrel and slightly coarser in the endcaps. The second longitudinal segmentation is composed of $\Delta\eta \times \Delta\phi$ = 0.025 $\times$ 0.025 cells and the last segment $\Delta\eta \times \Delta\phi$ = 0.05 $\times$ 0.05 cells. In addition a finely segmented (0.025 $\times$ 0.1) presampler system is present in front of the electromagnetic (EM) calorimeter. The overall energy resolution of the EM calorimeter determined experimentally is 10%/$\sqrt{E}\oplus$ 0.5%. The calorimeter also has good pointing resolution, 60 mrad/$\sqrt{E}$ for photons and timing resolution better than 200 ps for showers of energy larger than 20 GeV.

The hadronic calorimeter is also segmented longitudinally and transversely. Except for the endcaps and the forward calorimeters, the technology utilized for the calorimeter is a lead-scintillator tile structure with a granularity of $\Delta\eta \times \Delta\phi$ = 0.1 $\times$ 0.1. In the endcaps the hadronic calorimeter is implemented in liquid argon technology for radiation hardness with the same granularity as the barrel hadronic calorimeter. The energy resolution for the hadronic calorimeters is 50%/$\sqrt{E}\oplus$ 2% for pions. The very forward region, up to η = 4.9 is covered by the Forward Calorimeter implemented as an axial drift liquid argon calorimeter. The overall performance of the calorimeter system is described in Chapter 1.

The muon spectrometer in ATLAS is located behind the calorimeters, thus shielded from hadronic showers. The spectrometer is implemented using several technologies for tracking devices and a toroidal magnet system, which provides a field of 4 T strength to have an independent momentum measurement outside the calorimeter volume. Most of the volume is covered by MDTs, (monitored drift tubes). The forward region where the rate is high, Cathode Strip Chamber technology is chosen. The stand-alone muon spectrometer momentum resolution is of the order of 2% for muons with p_T in the range 10–100 GeV. The muon spectrometer coverage is $\mid \eta \mid < 2.7$.

The trigger and data acquisition system of ATLAS is a multi-level system, which has to reduce the beam crossing rate of 40 MHz to an output rate to mass storage of $\mathcal{O}(100)$ Hz. The first stage (LVL1) is a hardware based trigger, which makes use of coarse granularity calorimeter data and dedicated muon trigger chambers only, to reduce the output rate to about 75 kHz, within a maximum latency of 2.5 μs.

The performance results mentioned have been obtained using a detailed full simulation of the ATLAS detector response with GEANT and have been validated by an extensive programme of testbeam measurements of all components.

5.3.2. Jet physics and ATLAS

The ATLAS calorimer coverage and its fine segmentation will be an asset for jet studies in the heavy ion environment. Signatures of jet quenching in central heavy ion collisions could manifest as a larger jet cone (as compared to proton–proton collision) and/or modifications in the jet fragmentation function. The finely segmented (longitudinally and transversely) electromagnetic calorimeter will allow us to reconstruct EM clusters in the jet environment and in particular measure the π^0 containt in the jet.

There is excellent opportunity in ATLAS to measure $\gamma - jet$, jet-jet and Z-jet events where one can more fully characterize the modified fragmentation functions. In particular, the γ(or Z) in $\gamma(orZ)$–jet processes provides a 'control' over the away-side jet energy and direction that will allow the physics of quenching to be studied quantitatively and in great detail [199]. The effects of hard gluon radiation on the photon/jet energy imbalance and angular distribution can be studied in great detail using the high-statistics pp data set. The $\gamma - jet$ channel requires the identification of a photon. In proton–proton

collisions the rejection of γ/π^0 is about a factor of three up to a p_T of 50 GeV. However, the heavy ion environment presents considerable more challenge. Z_0 production rates have been estimated by Wang and Huang [199]. For p_T larger than 40 GeV, we expect of the order of $\sim$ 500 $Z_0 \rightarrow \mu^+\mu^-$ events for a one-month run. Therefore multiple runs may be required to extract relevant information on jet fragmentation.

5.3.3. Expected detector performance for jet studies

The ATLAS calorimeter granularity is shown in Table 2.8. The calorimeter system is not only segmented in η and ϕ, but also longitudinally. The calorimeter is fully segmented to η = 5. The electromagnetic calorimeter is in most places 25 X_0 deep and designed to fully contain a 1 TeV electron or photon. The hadronic calorimeter is more than 10 λ_{int} deep and contains all of the hadrons in typical pp high luminosity runs.

Table 2.8: ATLAS calorimeter system segmentation. Listed are the number of longitudinal and the size of the transverse segmentation in the different calorimeters

Calorimeter System	**η coverage**	**Long.**	**Transversal segmentation**
LAr Electromagnetic	$0.0 < \eta < 3.2$	3	0.003×0.1, 0.025×0.025, and 0.05×0.05
LAr Hadronic	$1.5 < \eta < 3.2$	4	0.1×0.1 for $1.5 < \eta < 2.5$ and 0.2×0.2 otherwise
Hadronic Tile	$0.0 < \eta < 1.7$	3	0.1×0.1, 0.1×0.1, and 0.2×0.1
Forward Calorimeter	$3.1 < \eta < 4.9$	4	0.2×0.2

The jet energy resolution for high luminosity proton–proton run is $50\%/\sqrt{E} \oplus$ 2% and the jet reconstruction threshold approximately $E_T \sim$ 20 GeV for proton–proton run. These numbers are expect to be different for the heavy ion environment. Preliminary simulations indicate that the detection thresholds should be at around 40 $\sim$ 50 GeV. We expect a worsening of the energy resolution because of the soft background but the energy scale should remain untouched, unless the ratio of EM to Hadronic components in the jet changes substantially.

Preliminary figures for energy deposition in the EM calorimeter from full HIJING central events indicate that approximately 4 GeV of transverse energy is deposited in a tower $\eta \times \phi$ = 0.1 $\times$ 0.1. This number is consistent with reported by CMS. However, due to the longitudinal segmentation and predominantly low p_T ($<$ 1 GeV)nature of the particles in the background, we do expect that most of the energy to be deposited in the first compartament of the calorimeter. Thus jets could be reconstructed on the basis of the remaining compartaments. Detailed studies are under way.

To study jet quenching in a direct way is to measure its fragmentation function and possible changes in the jet cone radius. The fragmentation function can only be measured if particles are identified within the jet. The segmentation of the ATLAS calorimeter is such that allows, in principle, for the identification of π^0s. In spite of the soft background preliminary studies shows encouraging results. However, we have observed a significant worsening of the EM cluster energy resolution. Studies performed in proton–proton collisions do have not addressed the issue of EM cluster reconstruction, specially for π^0s at low energy.

Acknowledgements

The following sources of funding are acknowledged:

Alexander von Humboldt Foundation: R. Fries;

CERN TH Division, Visitor Programme:

A. Accardi, F. Arleo, R. Baier, R.J. Fries, J.W. Qiu, I. Vitev, R. Vogt;

CICYT of Spain under contract AEN99-0589-C02: N. Armesto;

European Commission IHP program, Contract HPRN-CT-2000-00130: A. Accardi;

German Science Foundation (DFG), Contract FOR 329/2-1: R. Baier;

Marie Curie Fellowship of the European Community programme TMR,

Contract HPMF-CT-2000-01025: C.A. Salgado;

United States Department of Energy,

Contract No. DE-FG02-93ER40764: A. Accardi, I. Vitev;

Contract no. DE-FG02-96ER40945: R. Fries;

Contract No. DE-FG02-87ER40371: J.W. Qiu, I. Vitev;

Contract No. DE-AC03-76SF00098: R. Vogt;

Contract No. DE-AC03-76SF00098: X.N. Wang;

United States NSFC project Nos. 19928511 and 10135030: X.N. Wang;

Universidad de Córdoba: N. Armesto.

References

[1] K.J. Eskola (ed.), Chapter 1, in *'Hard Probes in Heavy-Ion Collisions at the LHC'*, CERN-2004-009 (2004), hep-ph/0308248.

[2] R. Vogt and S. Frixione (eds.), Chapter 3, in *'Hard Probes in Heavy-Ion Collisions at the LHC'*, CERN-2004-009 (2004).

[3] P. Aurenche (ed.), Chapter 4, in *'Hard Probes in Heavy-Ion Collisions at the LHC'*, CERN-2004-009 (2004).

[4] R. Baier, D. Schiff and B. G. Zakharov, *Ann. Rev. Nucl. Part. Sci.* **50** (2000) 37, hep-ph/0002198.

[5] M. Gyulassy, P. Levai and I. Vitev, *Phys. Lett.* **B538** (2002) 282, nucl-th/0112071.

[6] E. Wang and X.N. Wang, *Phys. Rev. Lett.* **89** (2002) 162301, hep-ph/0202105.

[7] C.A. Salgado and U.A. Wiedemann, *Phys. Rev. Lett.* **89** (2002) 092303, hep-ph/0204221.

[8] I. Vitev and M. Gyulassy, *Phys. Rev. Lett.* **89** (2002) 252301, hep-ph/0209161.

[9] T. Affolder *et al.* (CDF Collaboration), *Phys. Rev.* **D64** (2001) 032001, Erratum: **D65** (2002) 039903, hep-ph/0102074.

[10] S. Frixione, Z. Kunszt and A. Signer, *Nucl. Phys.* **B467** (1996) 399, hep-ph/9512328.

[11] S. Frixione, *Nucl. Phys.* **B507** (1997) 295, hep-ph/9706545.

[12] S. Frixione and G. Ridolfi, *Nucl. Phys.* **B507** (1997) 315, hep-ph/9707345.

[13] A.D. Martin, R.G. Roberts, W.J. Stirling and R.S. Thorne, *Eur. Phys. J.* **C4** (1998) 463, hep-ph/9803445.

[14] K.J. Eskola, V.J. Kolhinen and P.V. Ruuskanen, *Nucl. Phys.* **B535** (1998) 351, hep-ph/9802350.

[15] K.J. Eskola, V.J. Kolhinen and C.A. Salgado, *Eur. Phys. J.* **C9** (1999) 61, hep-ph/9807297.

[16] S. Catani, Y.L. Dokshitzer, M.H. Seymour and B.R. Webber, *Nucl. Phys.* **B406** (1993) 187.

[17] S.D. Ellis and D.E. Soper, *Phys. Rev.* **D48** (1993) 3160, hep-ph/9305266.

[18] N. Armesto and C. Pajares, *Int. J. Mod. Phys.* **A15** (2000) 2019, hep-ph/0002163.

[19] F. Carminati, Y. Foka, P. Giubellino, G. Paic, J.-P. Revol, K. Šafařik and U.A. Wiedemann (eds.), *ALICE Physics Performance Report, Chapter IV: Monte Carlo generators and simulations*, ALICE Internal Note 2002-033 (2002).

[20] J. Huston (CDF Collaboration), *Int. J. Mod. Phys.* **A16S1** (2001) 219.

[21] R. Field (CDF Collaboration), *Int. J. Mod. Phys.* **A16S1** (2001) 250.

[22] A. Accardi and D. Treleani, *Nucl. Phys.* **A699** (2002) 82.

[23] A. Accardi and D. Treleani, *Phys. Rev.* **D64** (2001) 116004, hep-ph/0106306.

[24] L. Ametller, N. Paver and D. Treleani, *Phys. Lett.* **B169** (1986) 289.

[25] F. Abe *et al.* (CDF Collaboration), *Phys. Rev.* **D56** (1997) 3811.

[26] F. Abe *et al.* (CDF Collaboration), *Phys. Rev. Lett.* **79** (1997) 584.

[27] A. Capella *et al.*, *Phys. Lett.* **B107** (1981) 106, Erratum: **B109** (1982) 510.

[28] M. Braun and C. Pajares, *Nucl. Phys.* **A532** (1991) 678.

[29] R. Baier, Y.L. Dokshitzer, A.H. Mueller and D. Schiff, Phys. Rev. C **60** (1999) 064902, hep-ph/9907267.

[30] M. Arneodo, A. Bialas, M.W. Krasny, T. Sloan and M. Strikman, hep-ph/9610423.

[31] A. Deshpande, R. Milner and R. Venugopalan (eds.), *EIC White Paper*, preprint BNL-68933.

[32] H. Abramowicz *et al.* (TESLA-N Study Group Collaboration), DESY-01-011.

[33] I.P. Lokhtin and A.M. Snigirev, *Eur. Phys. J.* **C16** (2000) 527, hep-ph/0004176.

[34] J.F. Owens, *Rev. Mod. Phys.* **59** (1987) 465.

[35] J.W. Cronin *et al.*, *Phys. Rev.* **D11** (1975) 3105.

[36] P.B. Straub *et al.*, *Phys. Rev. Lett.* **68** (1992) 452.

[37] D. Antreasyan *et al.*, *Phys. Rev.* **D19** (1979) 764.

[38] B. Alper *et al.* (British-Scandinavian ISR Collaboration), *Phys. Lett.* **B44** (1973) 521.

[39] C. Albajar *et al.* (UA1 Collaboration), *Nucl. Phys.* **B335** (1990) 261.

[40] M. Banner *et al.* (UA2 Collaboration), *Z. Phys.* **C27** (1985) 329.

[41] G. Bocquet *et al.*, *Phys. Lett.* **B366** (1996) 434.

[42] F. Abe *et al.* (CDF Collaboration), *Phys. Rev. Lett.* **61** (1988) 1819.

[43] Y. Zhang *et al.*, *Phys. Rev.* **C65** (2002) 034903, hep-ph/0109233.

[44] K.J. Eskola and H. Honkanen, *Nucl. Phys.* **A713** (2003) 167, hep-ph/0205048.

[45] M. Gluck, E. Reya and A. Vogt, *Eur. Phys. J.* **C5** (1998) 461, hep-ph/9806404.

[46] J. Binnewies, B.A. Kniehl and G. Kramer, *Z. Phys.* **C65** (1995) 471, hep-ph/9407347.

[47] X.N. Wang, *Phys. Rev.* **C58** (1998) 2321, hep-ph/9804357.

[48] T. Sjostrand, *Comput. Phys. Commun.* **82** (1994) 74.

[49] K.J. Eskola *et al.*, hep-ph/0211239.

[50] X.N. Wang and M. Gyulassy, *Phys. Rev. Lett.* **68** (1992) 1480.

[51] M. Gyulassy and X.N. Wang, *Nucl. Phys.* **B420** (1994) 583, nucl-th/9306003.

[52] I. Vitev and M. Gyulassy, *Phys. Rev.* **C65** (2002) 041902, nucl-th/0104066.

[53] I. Vitev and M. Gyulassy, hep-ph/0208108.

[54] D. Teaney, J. Lauret and E.V. Shuryak, nucl-th/0110037.

[55] X.F. Zhang, G. Fai and P. Levai, hep-ph/0205008.

[56] R.C. Hwa and C.B. Yang, *Phys. Rev.* **C67** (2003) 034902, nucl-th/0211010.

[57] J.D. Bjorken, FERMILAB-PUB-82-59-THY.

[58] M.H. Thoma, hep-ph/9503400.

[59] M. Gyulassy and M. Plumer, *Phys. Lett.* **B243** (1990) 432.

[60] R. Baier, Y.L. Dokshitzer, S. Peigne and D. Schiff, *Phys. Lett.* **B345** (1995) 277, hep-ph/9411409.

[61] R. Baier *et al.*, *Nucl. Phys.* **B483** (1997) 291, hep-ph/9607355.

[62] R. Baier *et al.*, *Nucl. Phys.* **B484** (1997) 265 hep-ph/9608322.

[63] B.G. Zakharov, *JETP Lett.* **63** (1996) 952 hep-ph/9607440.

[64] B. G. Zakharov, *JETP Lett.* **65** (1997) 615, hep-ph/9704255.

[65] R. Baier, Y.L. Dokshitzer, A.H. Mueller and D. Schiff, *Nucl. Phys.* **B531** (1998) 403, hep-ph/9804212.

[66] B.G. Zakharov, *Phys. Atom. Nucl.* **61** (1998) 838 [*Yad. Fiz.* **61** (1998) 924], hep-ph/9807540.

[67] B.G. Zakharov, *JETP Lett.* **70** (1999) 176, hep-ph/9906536.

[68] B.G. Zakharov, *JETP Lett.* **73** (2001) 49 [*Pisma Zh. Eksp. Teor. Fiz.* **73** (2001) 55], hep-ph/0012360.

[69] U.A. Wiedemann and M. Gyulassy, *Nucl. Phys.* **B560** (1999) 345, hep-ph/9906257.

[70] U.A. Wiedemann, *Nucl. Phys.* **B582** (2000) 409, hep-ph/0003021.

[71] U.A. Wiedemann, *Nucl. Phys.* **B588** (2000) 303, hep-ph/0005129.

[72] U. A. Wiedemann, *Nucl. Phys.* **A690** (2001) 731, hep-ph/0008241.

[73] M. Gyulassy, P. Levai and I. Vitev, *Phys. Rev. Lett.* **85** (2000) 5535, nucl-th/0005032.

[74] M. Gyulassy, P. Levai and I. Vitev, *Nucl. Phys.* **B594** (2001) 371, nucl-th/0006010.

[75] M. Gyulassy, I. Vitev, X.N. Wang and B.W. Zhang, nucl-th/0302077.

[76] A. Kovner and U.A. Wiedemann, hep-ph/0304151.

[77] L.D. Landau and I. Pomeranchuk, *Dokl. Akad. Nauk Ser. Fiz.* **92** (1953) 735.

[78] L. D. Landau and I. Pomeranchuk, *Dokl. Akad. Nauk Ser. Fiz.* **92** (1953) 535.

[79] A.B. Migdal, *Phys. Rev.* **103** (1956) 1811.

[80] C.A. Salgado and U.A. Wiedemann, *Phys. Rev.* **D68** (2003) 014008, hep-ph/0302184.

[81] M. Gyulassy, I. Vitev and X.N. Wang, *Phys. Rev. Lett.* **86** (2001) 2537, nucl-th/0012092.

[82] M. Gyulassy, P. Levai and I. Vitev, *Nucl. Phys.* **B571** (2000) 197, hep-ph/9907461.

[83] E. Braaten and R.D. Pisarski, *Phys. Rev. Lett.* **64** (1990) 1338.

[84] J.P. Blaizot, E. Iancu and A. Rebhan, *Phys. Rev.* **D63** (2001) 065003, hep-ph/0005003.

[85] Y.L. Dokshitzer and D.E. Kharzeev, *Phys. Lett.* **B519** (2001) 199, hep-ph/0106202.

[86] M. Djordjevic and M. Gyulassy, *Phys. Lett.* **B560** (2003) 37, nucl-th/0302069.

[87] M. Djordjevic and M. Gyulassy, nucl-th/0305062.

[88] J. Qiu and I. Vitev, hep-ph/0309094.

[89] J.W. Qiu and I. Vitev, nucl-th/0306039.

[90] M. Gyulassy, P. Levai and I. Vitev, *Phys. Rev.* **D66** (2002) 014005, nucl-th/0201078.

[91] M. Gyulassy, I. Vitev, X.N. Wang and P. Huovinen, *Phys. Lett.* **B526** (2002) 301.

[92] R. Baier, Y.L. Dokshitzer, A.H. Mueller and D. Schiff, *JHEP* **0109** (2001) 033, hep-ph/0106347.

[93] F. Arleo, *JHEP* **0211** (2002) 044, hep-ph/0210104.

[94] R. Baier, *Nucl. Phys.* **A715** (2003) 209, hep-ph/0209038.

[95] M. Luo, J.W. Qiu and G. Sterman, *Phys. Rev.* **D49** (1994) 4493.

[96] X.F. Guo, *Phys. Rev.* **D58** (1998) 114033, hep-ph/9804234.

[97] J.W. Qiu and G. Sterman, hep-ph/0111002.

[98] S.J. Brodsky and P. Hoyer, *Phys. Lett.* **B298** (1993) 165, hep-ph/9210262.

[99] S. Gavin and J. Milana, *Phys. Rev. Lett.* **68** (1992) 1834.

[100] M.A. Vasilev *et al.* (FNAL E866 Collaboration), *Phys. Rev. Lett.* **83** (1999) 2304, hep-ex/9906010.

[101] M.B. Johnson *et al.* (FNAL E772 Collaboration), *Phys. Rev. Lett.* **86** (2001) 4483, hep-ex/0010051.

[102] M.B. Johnson *et al.*, *Phys. Rev.* **C65** (2002) 025203, hep-ph/0105195.

[103] F. Arleo, *Phys. Lett.* **B532** (2002) 231, hep-ph/0201066.

[104] F. Karsch, *Nucl. Phys.* **A698** (2002) 199, hep-ph/0103314.

[105] K.J. Eskola *et al.*, *Nucl. Phys.* **B570** (2000) 379, hep-ph/9909456.

[106] R. Baier *et al.*, *Phys. Rev.* **C58** (1998) 1706, hep-ph/9803473.

[107] R. Baier *et al.*, *Phys. Rev.* **C64** (2001) 057902, hep-ph/0105062.

[108] S. Mrowczynski, *Phys. Lett.* **B269** (1991) 383.

[109] M.H. Thoma, *Phys. Lett.* **B269** (1991) 144.

[110] E. Braaten and R.D. Pisarski, *Nucl. Phys.* **B337** (1990) 569.

[111] J. Frenkel and J.C. Taylor, *Nucl. Phys.* **B334** (1990) 199.

[112] X.N. Wang, M. Gyulassy and M. Plumer, *Phys. Rev.* **D51** (1995) 3436, hep-ph/9408344.

[113] M.G. Mustafa *et al.*, *Phys. Lett.* **B428** (1998) 234, nucl-th/9711059.

[114] I.P. Lokhtin and A.M. Snigirev, *Phys. Lett.* **B440** (1998) 163, hep-ph/9805292.

[115] P. Aurenche *et al.*, *Eur. Phys. J.* **C13** (2000) 347, hep-ph/9910252.

[116] J.A. Osborne, E. Wang and X.N. Wang, *Phys. Rev.* **D67** (2003) 094022, hep-ph/0212131.

[117] X.F. Guo and X.N. Wang, *Phys. Rev. Lett.* **85** (2000) 3591, hep-ph/0005044.

[118] X.N. Wang and X.F. Guo, *Nucl. Phys.* **A696** (2001) 788, hep-ph/0102230.

[119] J. Osborne and X.N. Wang, *Nucl. Phys.* **A710** (2002) 281, hep-ph/0204046.

[120] X.N. Wang, Z. Huang and I. Sarcevic, *Phys. Rev. Lett.* **77** (1996) 231, hep-ph/9605213.

[121] B.A. Kniehl, G. Kramer and B. Potter, *Nucl. Phys.* **B582** (2000) 514, hep-ph/0010289.

[122] A. Airapetian *et al.* (HERMES Collaboration), *Eur. Phys. J.* **C20** (2001) 479, hep-ex/0012049.

[123] F. Arleo, hep-ph/0306235.

[124] S.S. Adler *et al.* (PHENIX Collaboration), *Phys. Rev. Lett.* **91** (2003) 072301, nucl-ex/0304022.

[125] R.J. Glauber and G. Matthiae, *Nucl. Phys.* **B21** (1970) 135.

[126] I. Vitev, *Phys. Lett.* **B562** (2003) 36.

[127] A. Accardi and M. Gyulassy, nucl-th/0308029.

[128] S. Mioduszewski (PHENIX Collaboration), nucl-ex/0210021.

[129] P. Jacobs, hep-ex/0211031.

[130] G.J. Kunde, nucl-ex/0211018.

[131] F. Cooper, E. Mottola and G.C. Nayak, hep-ph/0210391.

[132] S.S. Adler *et al.* (PHENIX Collaboration), nucl-ex/0306021.

[133] I. Arsene *et al.* (BRAHMS Collaboration), nucl-ex/0307003.

[134] B.B. Back *et al.* (PHOBOS Collaboration), *Phys. Rev. Lett.* **91** (2003) 072302, nucl-ex/0306025.

[135] J. Adams *et al.* (STAR Collaboration), nucl-ex/0306024.

[136] I. Vitev, nucl-th/0308028.

[137] J. Adams *et al.* (STAR Collaboration), nucl-ex/0305015.

[138] B.B. Back *et al.* (PHOBOS Collaboration), nucl-ex/0302015.

[139] A. Shor, *Phys. Lett.* **B215** (1988) 375.

[140] A. Shor, *Phys. Lett.* **B233** (1989) 231.

[141] B. Müller and X.N. Wang, *Phys. Rev. Lett.* **68** (1992) 2437.

[142] P. Levai and R. Vogt, *Phys. Rev.* **C56** (1997) 2707, hep-ph/9704360.

[143] M.H. Thoma and M. Gyulassy, *Nucl. Phys.* **B351** (1991) 491.

[144] M.H. Thoma, *Phys. Lett.* **B273** (1991) 128.

[145] E. Braaten and M.H. Thoma, *Phys. Rev.* **D44** (1991) 2625.

[146] B. Svetitsky, *Phys. Rev.* **D37** (1988) 2484.

[147] B. Svetitsky and A. Uziel, *Phys. Rev.* **D55** (1997) 2616, hep-ph/9606284.

[148] Y. Koike and T. Matsui, *Phys. Rev.* **D45** (1992) 3237.

[149] E. Shuryak, *Phys. Rev.* **C55** (1997) 961, nucl-th/9605011.

[150] Z.W. Lin, R. Vogt and X.N. Wang, *Phys. Rev.* **C57** (1998) 899, nucl-th/9705006.

[151] Z.W. Lin and R. Vogt, *Nucl. Phys.* **B544** (1999) 339, hep-ph/9808214.

[152] I.P. Lokhtin and A.M. Snigirev, *Eur. Phys. J.* **C21** (2001) 155, hep-ph/0105244.

[153] K. Gallmeister, B. Kampfer and O.P. Pavlenko, nucl-th/0208006.

[154] K. Adcox *et al.* (PHENIX Collaboration), *Phys. Rev. Lett.* **88** (2002) 192303, nucl-ex/0202002.

[155] A.D. Martin, W.J. Stirling and R.G. Roberts, *Phys. Lett.* **B306** (1993) 145;
Erratum: **B309** (1993) 492.

[156] S. Gavin, P.L. McGaughey, P.V. Ruuskanen and R. Vogt, *Phys. Rev.* **C54** (1996) 2606.

[157] I.P. Lokhtin, hep-ph/0210010.

[158] B. Abbott *et al.* (D0 Collaboration), FERMILAB-PUB-97-242-E.

[159] C.A. Salgado and U.A. Wiedemann, hep-ph/0310079.

[160] X.N. Wang and M. Gyulassy, *Phys. Rev.* **D44** (1991) 3501.

[161] B.B. Back *et al.* (PHOBOS Collaboration), *Phys. Rev. Lett.* **85** (2000) 3100, hep-ex/0007036.

[162] X.N. Wang, *Phys. Rev.* **C63** (2001) 054902, nucl-th/0009019.

[163] S. Voloshin and Y. Zhang, *Z. Phys.* **C 70** (1996) 665, hep-ph/9407282.

[164] A.M. Poskanzer and S.A. Voloshin, *Phys. Rev.* **C58** (1998) 1671, nucl-ex/9805001.

[165] J.Y. Ollitrault, *Phys. Rev.* **D46** (1992) 229.

[166] J.Y. Ollitrault, *Phys. Rev.* **D48** (1993) 1132, hep-ph/9303247.

[167] P.F. Kolb *et al.*, *Nucl. Phys.* **A696** (2001) 197, hep-ph/0103234.

[168] D. Molnar and M. Gyulassy, *Nucl. Phys.* **A697** (2002) 495, [Erratum **A703** (2002) 893], nucl-th/0104073.

[169] Z.W. Lin and C.M. Ko, *Phys. Rev.* **C65** (2002) 034904, nucl-th/0108039.

[170] E.V. Shuryak, *Phys. Rev.* **C66** (2002) 027902, nucl-th/0112042.

[171] D. Teaney and R. Venugopalan, *Phys. Lett.* **B539** (2002) 53, hep-ph/0203208.

[172] Yu.V. Kovchegov and K.L. Tuchin, *Nucl. Phys.* **A708** (2002) 413, hep-ph/0203213.

[173] S. Wang *et al.*, *Phys. Rev.* **C44** (1991) 1091.

[174] N. Borghini, P.M. Dinh and J.Y. Ollitrault, *Phys. Rev.* **C64** (2001) 054901, nucl-th/0105040.

[175] N. Borghini, P.M. Dinh and J.Y. Ollitrault, nucl-ex/0110016.

[176] K. Filimonov (STAR Collaboration), nucl-ex/0210027.

[177] R. Vogt, *Heavy Ion Phys.* **9** (1999) 339, nucl-th/9903051.

[178] I.P. Lokhtin *et al.*, *Pramana* **60** (2002) 1045, hep-ph/0112180.

[179] J.D. Bjorken, *Phys. Rev.* **D27** (1983) 140.

[180] K.J. Eskola, K. Kajantie and P.V. Ruuskanen, *Phys. Lett.* **B332** (1994) 191, hep-ph/9404237.

[181] K.J. Eskola, *Prog. Theor. Phys. Suppl.* **129** (1997) 1, hep-ph/9708472.

[182] K.J. Eskola, *Comments Nucl. Part. Phys.* **22** (1998) 185, nucl-th/9705027.

[183] I. Damgov *et al.*, *Part. Nucl. Lett.* **107** (2001) 93.

[184] J.Y. Ollitrault, nucl-ex/9711003.

[185] I.P. Lokhtin, L.I. Sarycheva and A.M. Snigirev, *Phys. Lett.* **B537** (2002) 261, hep-ph/0203144.

[186] M.V. Savina, S.V. Shmatov, N.V. Slavin and P.I. Zarubin, *Phys. Atom. Nucl.* **62** (1999) 2084 [*Yad. Fiz.* **62** (1999) 2263], hep-ph/0007130.

[187] M. Gyulassy and X. N. Wang, *Comput. Phys. Commun.* **83** (1994) 307, nucl-th/9502021.

[188] K. Werner, *Phys. Rept.* **232** (1993) 87.

[189] K. Geiger, *Phys. Rept.* **258** (1995) 237.

[190] K. Geiger, *Comput. Phys. Commun.* **104** (1997) 70, hep-ph/9701226.

[191] A. Polleri and F. Yuan, nucl-th/0108056.

[192] G. Baur *et al.*, *'Heavy Ion Physics Programme in CMS'*, CERN CMS Note 2000/060.

[193] J.C. Collins, D.E. Soper and G. Sterman, *Adv. Ser. Direct. High Energy Phys.* **5** (1988) 1.

[194] M. Luo, J. Qiu and G. Sterman, *Phys. Lett.* **B279** (1992) 377.

[195] M. Luo, J.W. Qiu and G. Sterman, *Phys. Rev.* **D50** (1994) 1951.

[196] R.J. Fries, hep-ph/0201311.

[197] B.W. Zhang and X.N. Wang, *Nucl. Phys.* **A720** (2003) 429, hep-ph/0301195.

[198] V. Muccifora (HERMES Collaboration), *Nucl. Phys.* **A715** (2003) 506, hep-ex/0106088.

[199] X.N. Wang and Z. Huang, *Phys. Rev.* **C55** (1997) 3047, hep-ph/9701227.

[200] E. Wang and X.N. Wang, *Phys. Rev. Lett.* **87** (2001) 142301, nucl-th/0106043.

[201] X.N. Wang, *Phys. Rev.* **C61** (2000) 064910, nucl-th/9812021.

[202] X.N. Wang, nucl-th/0305010.

[203] S.y. Li and X.N. Wang, *Phys. Lett.* **B527** (2002) 85, nucl-th/0110075.

[204] C. Adler *et al.*, *Phys. Rev. Lett.* **89** (2002) 202301, nucl-ex/0206011.

[205] J.L. Klay (STAR Collaboration), *Nucl. Phys.* **A715** (2003) 733, nucl-ex/0210026.

[206] K. Adcox *et al.* (PHENIX Collaboration), *Phys. Rev. Lett.* **88** (2002) 022301, nucl-ex/0109003.

[207] C. Adler *et al.* (STAR Collaboration), *Phys. Rev. Lett.* **90** (2003) 082302, nucl-ex/0210033.

[208] S.S. Adler *et al.* (PHENIX Collaboration), nucl-ex/0305036.

[209] S.S. Adler *et al.* (PHENIX Collaboration), nucl-ex/0305013.

[210] R. Snellings (STAR Collaboration), nucl-ex/0305001.

[211] R.J. Fries *et al.*, Phys. Rev. Lett. **90** (2003) 202303, nucl-th/0301087.

[212] S.A. Voloshin, *Nucl. Phys.* **A715**, 379c (2003), nucl-ex/0210014.

[213] V. Greco, C.M. Ko and P. Levai, nucl-th/0301093.

[214] R.J. Fries, B. Müller, C. Nonaka and S.A. Bass, nucl-th/0305079.

[215] R.J. Fries, B. Müller, C. Nonaka and S.A. Bass, nucl-th/0306027.

[216] P.F. Kolb, J. Sollfrank and U.W. Heinz, *Phys. Rev.* **C62** (2000) 054909, hep-ph/0006129.

[217] D.K. Srivastava, C. Gale and R.J. Fries, *Phys. Rev.* **C67** (2003) 034903, nucl-th/0209063.

[218] P. Levai *et al.*, *Nucl. Phys.* **A698** (2002) 631.

[219] M. Gyulassy, *Lect. Notes Phys.* **583** (2002) 37.

[220] D.A. Appel, *Phys. Rev.* **D33** (1986) 717.

[221] J.P. Blaizot and L.D. McLerran, *Phys. Rev.* **D34** (1986) 2739.

[222] G.T. Bodwin, S.J. Brodsky and G.P. Lepage, *Phys. Rev.* **D39** (1989) 3287.

[223] J. Rak (PHENIX Collaboration), nucl-ex/0306031.

[224] T. Hirano and Y. Nara, nucl-th/0301042.

[225] D. Kharzeev, E. Levin and L. McLerran, *Phys. Lett.* **B561** (2003) 93, hep-ph/0210332.

[226] L.V. Gribov, E.M. Levin and M.G. Ryskin, *Phys. Rept.* **100** (1983) 1.

[227] R. Baier, A. Kovner and U.A. Wiedemann, *Phys. Rev.* **D68** (2003) 054009, hep-ph/0305265.

[228] M.A. Braun, *Phys. Lett.* **B483** (2000) 105, hep-ph/0003003.

[229] D. Kharzeev, Yu.V. Kovchegov and K. Tuchin, hep-ph/0307037.

[230] J.L. Albacete *et al.*, hep-ph/0307179.

[231] L.D. McLerran and R. Venugopalan, *Phys. Rev.* **D49** (1994) 2233, hep-ph/9309289.

[232] L.D. McLerran and R. Venugopalan, *Phys. Rev.* **D49** (1994) 3352, hep-ph/9311205.

[233] Yu.V. Kovchegov, *Phys. Rev.* **D54** (1996) 5463, hep-ph/9605446.

[234] J. Jalilian-Marian, A. Kovner, L.D. McLerran and H. Weigert, *Phys. Rev.* **D55** (1997) 5414, hep-ph/9606337.

[235] E. Iancu, K. Itakura and L. McLerran, *Nucl. Phys.* **A708** (2002) 327, hep-ph/0203137.

[236] A.H. Mueller and D.N. Triantafyllopoulos, *Nucl. Phys.* **B640** 331 (2002), hep-ph/0205167.

[237] I. Balitsky, *Nucl. Phys.* **B463**, 99 (1996), hep-ph/9509348.

[238] Yu.V. Kovchegov, *Phys. Rev.* **D60** (1999) 034008, hep-ph/9901281.

[239] K. Adcox *et al.* (PHENIX Collaboration), *Phys. Lett.* **B561** (2003) 82, nucl-ex/0207009.

[240] S.S. Adler (PHENIX Collaboration), nucl-ex/0308006.

[241] J. Adams *et al.* (STAR Collaboration), nucl-ex/0306007.

[242] K. Adcox *et al.* (PHENIX Collaboration), *Phys. Rev. Lett.* **88** (2002) 242301, nucl-ex/0112006.

[243] B. Alper *et al.* (British-Scandinavian Collaboration), *Nucl. Phys.* **B100** (1975) 237.

[244] A.L. Angelis *et al.* (BCMOR Collaboration), *Phys. Lett.* **B185** (1987) 213.

[245] P. Abreu *et al.* (DELPHI Collaboration), *Eur. Phys. J.* **C17** (2000) 207, hep-ex/0106063.

[246] M. Chiu (PHENIX Collaboration), *Nucl. Phys.* **A715** (2003) 761, nucl-ex/0211008.

[247] C. Adler *et al.* (STAR Collaboration), *Phys. Rev. Lett.* **90** (2003) 032301, nucl-ex/0206006.

[248] S.S. Adler *et al.* (PHENIX Collaboration), hep-ex/0307019.

[249] K. Gallmeister, C. Greiner and Z. Xu, *Phys. Rev.* **C67** (2003) 044905 hep-ph/0212295.

[250] R.C. Hwa and C.B. Yang, *Phys. Rev.* **C67** (2003) 064902, nucl-th/0302006.

[251] D. Molnar and S.A. Voloshin, *Phys. Rev. Lett.* **91** (2003) 092301, nucl-th/0302014.

[252] S.S. Adler *et al.* (PHENIX Collaboration), hep-ex/0304038.

[253] A.L. Angelis *et al.* (CERN-Columbia-Oxford-Rockefeller Collaboration), *Phys. Lett.* **B97** (1980) 163.

[254] L. Apanasevich *et al.*, *Phys. Rev.* **D59** (1999) 074007, hep-ph/9808467.

[255] G.G. Barnafoldi, P. Levai, G. Papp, G. Fai and Y. Zhang, nucl-th/0212111.

[256] A. Bialas, M. Bleszynski and W. Czyz, *Nucl. Phys.* **B111** (1976) 461.

[257] K. Adcox *et al.* (PHENIX Collaboration), *Phys. Rev. Lett.* **86** (2001) 3500, nucl-ex/0012008.

[258] B.B. Back *et al.* (PHOBOS Collaboration), *Phys. Rev.* **C65** (2002) 061901, nucl-ex/0201005.

[259] D. d'Enterria, nucl-ex/0302016.

[260] S.Y. Jeon, J. Jalilian-Marian and I. Sarcevic, *Phys. Lett.* **B562** (2003) 45, nucl-th/0208012.

[261] D. d'Enterria (PHENIX Collaboration), *Nucl. Phys.* **A715** (2003) 749, hep-ex/0209051.

[262] S.R. Klein and R. Vogt, *Phys. Rev.* **C67** (2003) 047901, nucl-th/0211066.

[263] D. d'Enterria (PHENIX Collaboration), nucl-ex/0306001.

[264] M.M. Aggarwal *et al.* (WA98 Collaboration), *Eur. Phys. J.* **C23** (2002) 225, nucl-ex/0108006.

[265] X.N. Wang, nucl-th/0307036.

[266] B. Muller, *Phys. Rev.* **C67** (2003) 061901, nucl-th/0208038.

[267] P. Jacobs and J. Klay, nucl-ex/0308023.

[268] ALICE Collaboration, Technical Proposal, CERN/LHCC/95–71;
ALICE Collaboration, Technical Proposal, Addendum 1, CERN/LHCC/96–32;
ALICE Collaboration, Technical Proposal, Addendum 2, CERN/LHCC/99–13.

[269] R. Brandelik *et al.* (TASSO Collaboration), *Phys. Lett.* **B86** (1979) 243.

[270] W. Kristie and K. Schestermanov, STAR Note 196.

[271] T. Cormier, *'Jet Physics in ALICE and the Proposed New Electromagnetic Calorimeter'*, Proc. of the IV Symposium on LHC Physics and Detectors, Fermilab 2003, to be published in EPJdirect(2003).

[272] ALICE Collaboration, Technical Design Report of the Inner Tracking System, CERN/LHCC/1999–12.

[273] ALICE Collaboration, Technical Design Report of the Time Projection Chamber, CERN/LHCC/2000–01.

[274] ALICE Collaboration, Technical Design Report of the Transition Radiation Detector, CERN/LHCC/2001–21.

[275] ALICE Collaboration, Technical Design Report of the Time Of Flight Detector, CERN/LHCC/2000–12.

[276] ALICE Collaboration, Technical Design Report of the High Momentum Particle Identification Detector, CERN/LHCC/1998–19.

[277] ALICE Collaboration, Technical Design Report of the Photon Spectrometer, CERN/LHCC/1999–04.

[278] ALICE Collaboration, Technical Design Report of the Zero Degree Calorimeter, CERN/LHCC/1999–05;

[279] T. Affolder *et al.* (CDF Collaboration), *Phys. Rev.* **D65** (2002) 092002.

[280] G. Arnison *et al.* (UA1 Collaboration), *Phys. Lett.* **B132** (1983) 214.

[281] CMS Collaboration, Technical Proposal, CERN/LHCC/1994–38.

[282] CMS HCAL Design Report, CERN/LHCC/1997–31.

[283] CMS MUON Design Report, CERN/LHCC/1997–32.

[284] CMS ECAL Design Report, CERN/LHCC/1997–33.

[285] CMS Tracker Design Report, CERN/LHCC/1998–6.

[286] V. Kartvelishvili, R. Kvatadze and R. Shanidze, *Phys. Lett.* **B356** (1995) 589.

[287] N.A. Kruglov, I.P. Lokhtin, L.I. Sarycheva and A.M. Snigirev, *Z. Phys.* **C 76** (1997) 99.

[288] B. Flaugher and K. Meier, *'A compilation of jet finding algorithms'*, Proc. of the Snowmass Summer Studies (1990), FERMILAB-CONF-90/248-E.

[289] O.L. Kodolova, S. Kunori and I.N. Vardanian, CERN CMS Internal Note 2002/020.

[290] C. Roland, CERN CMS Rapid Note 2003/003.

[291] H. Appelshauser *et al.* (NA49 Collaboration), *Phys. Rev. Lett.* **80** (1998) 4136, nucl-ex/9711001.

[292] K.H. Ackermann *et al.* (STAR Collaboration), *Phys. Rev. Lett.* **86** (2001) 402, nucl-ex/0009011.

[293] I.P. Lokhtin, L.I. Sarycheva, A.M. Snigirev and S.V. Petrushanko, CERN CMS Note 2003/019.